Thèse

présentée devant
L'Institut National des Sciences Appliquées de Lyon

Préparée au sein du groupe de Microélectronique du Laboratoire Européen pour la Recherche Nucléaire (CERN)

Etude et caractérisation d'un capteur en silicium amorphe hydrogéné déposé sur circuit intégré pour la détection de particules et de rayonnements

pour obtenir
le grade de docteur

Ecole doctorale : Electronique, Electrotechnique, Automatique

Par

Matthieu DESPEISSE
Soutenue le 03 mars 2006 devant la Commission d'examen

Jury

GONTRAND Christian	Professeur	Directeur de thèse
GUILLOT Gerard	Professeur	Président
BALLIF Christophe	Professeur	Rapporteur
DABROWSKI Wladyslaw	Professeur	Rapporteur
DUSSEAU Laurent	Professeur	Rapporteur
ANELLI Giovanni	Docteur	Resp. de thèse CERN

A mes parents.

Acknowledgements

This thesis offered me the opportunity to work in a highly motivating and international research environment. I am grateful to many people for the help, the trust or the support they offered me during the past years.

First of all I would like to thank Pierre Jarron, who gave me the opportunity to work in such environment on an innovative project. I want to thank Pierre especially for his trust, his support and involvement in the project and for the different discussions we shared about this always “surprising” amorphous material. Mike Letheren is also acknowledged for having accepted me in the MIC group, as well as Roger Rusack, who kindly received me in his group of the University of Minnesota for the achievement of my work.

My very special thanks go to Giovanni Anelli, who was a perfect supervisor of my thesis at CERN and from who I learned a lot. From the design of my first circuit to the completion of this thesis he has offered me a very grateful help, always in a friendly atmosphere and with great humor. Grazie mille maestro to have read and corrected so carefully my thesis (thanks and apologizes to Federica!) and for having been such a good friend and support in these past years! I would like to thank Christian Gontrand who was my supervisor at INSA, always with his nice humor and passion for science. I would like to also thank Wladek Dabrowski, Laurent Dusseau and Christophe Ballif who corrected this manuscript and helped to improve its quality.

Further, I want to thank the persons directly involved in the work on the TFA technology. Thanks to Danielle Moraes (amazing samba dancer and player!) for her help and support and to Jan Kaplon. Special thanks go to Shahyar Saramad from who I learned a lot! I have shared very nice moments with him trying to put order in the disorder of a-Si:H properties and always in a very friendly atmosphere, متشکرم (motshakeram)! Big thanks to Francois Powolny for his important help and his strong support and friendship (and also for standing my sometimes not-very-good-mood while writing!). It was a very great pleasure to share the office with you Francois, and good luck to you now! Thanks to Diana, Martin, Mélanie and Klaus for their help in measurements (on this “stuff” as would say Martin!) Thanks to Ausias Garrigos with who I started this work and who was a very good friend, muchas gracias! I want to thank the different collaborators at the IMT of Neuchatel, ETH Zurich and University of Minnesota. I express special thanks to John Morse for his contribution to this work by accepting me for some days at the ESRF in Grenoble, thanks to John and Irina! Finally, thanks to Ian Mc Gill and Francoise Cossey at CERN, to whom

I have given tricky problems to connect the detectors and who impressed me by the quality of their work! For similar reasons, thanks to Sandra and to Ernest!

I want to express special thanks to Werner Riegler, who was always here to answer my questions. Thanks a lot for the time spent with you which permitted a much deeper understanding of the work presented in the thesis! Big thanks also to Lukas Tlustos and Erik Heijne for their precious help on detectors. High radiation levels environment is a very specific world, to which I have been introduced by two persons who manipulate and understand with great dexterity radioactivity and radiation effects as well as humor and "joie de vivre", merci à Maurice Glaser et Federico Ravotti! Very big thanks to Nicolas Pelloux who taught me microelectronic design as well as climbing and with whom I had really great time! I also thank gratefully Rafael Ballabriga for his appreciated help in electronics, for his great support and his sincere friendship in the difficult times, moltes gràcies Rafa! Finally, as these acknowledgements already get very long, I want to thank all the persons of the MIC group that I have not cited yet, with whom it was a great pleasure to work as everyone permitted a very nice working atmosphere, thanks to all of you!

I would like to thank especially Victor Tiny Ignasi and Nico, Barnabé and Angela who made me laugh every day I think, Joelma and Maria, Hervé Rafa Fred Francois Bruno Sandra et Pierre (quelle équipée…), Alessandro, Stefanos (efkaristo poly for the conclusion), Ausias Maria Delhia and Oscar, Nuno, Giulia, Hugo, Sandro, Peder and many others for having made my stay at CERN a great pleasure.

In order to forget work, to relax and to let go away a thesis stress, I found a very good method which I advise to anyone reading this: playing percussions in a batucada "live section" (samba)! Thanks to Gael, mestre, to all musicians and dancers of Sambaloelek (vous êtes tous géniaux et remplis d'"energia"), to my "surdo" and to my drum sticks!

Finally and most important, I would like to thank my wonderful parents and sister's family whose support during the writing of this thesis was invaluable, Joy for her support, and all my friends in Ardèche (merci mes ptao!). I love you all, merci pour votre soutien, compréhension et patience.

As it is the custom for a thesis, these acknowledgements were written in a hurry, so that I am pretty sure to have forgotten many people who helped me a lot to achieve this work during the past years. I would thus also like to thank all these people, who while reading these acknowledgements, think they have been forgotten!

Table of contents

Résumé

Malgré la complexité du monde qui nous entoure, ses fondations peuvent être expliquées de manière simplifiée à l'aide d'un petit nombre de particules élémentaires régies par quelques forces fondamentales. L'étude de ces constituants de base de la matière de l'univers et de leurs interactions a cependant nécessité tout au long du dernier siècle la construction et l'utilisation d'une instrumentation de plus en plus complexe nécessitant toujours les technologies les plus avancées. Cette riche période de théories, de découvertes et d'expérimentations a mené au développement du modèle standard des particules et des forces et à la confirmation expérimentale de certaines des théories qu'il englobe. Cependant, certaines théories restent encore à étudier expérimentalement et la recherche et l'établissement d'une nouvelle physique au-delà du modèle standard seront bientôt nécessaires. Une nouvelle machine, le « Large Hadron Collider » (LHC), est en cours de construction au Laboratoire européen de physique des particules [CERN]. Le LHC sondera la matière plus profondément que jamais auparavant, ouvrant les portes à de nouvelles découvertes, et sera un outil fondamental pour l'étude de certaines des théories du modèle standard et pour l'établissement d'une nouvelle physique. Il sera constitué principalement d'accélérateurs et de détecteurs. Les accélérateurs sont d'énormes machines qui permettent d'accélérer jusqu'à des vitesses proches de la lumière des particules avant de les précipiter sur d'autres particules accélérées dans un sens inverse ou appartenant à une cible fixe. Autour des points où les "collisions" se produisent, des expériences sont montées qui consistent en des instruments, parfois gigantesques, constitués de plusieurs sortes de détecteurs de particules et utilisant les technologies les plus avancées pour pouvoir étudier précisément les produits des collisions.

La physique des particules de par ses exigences toujours plus poussées est ainsi un fort précurseur de nouvelles technologies de détection pouvant trouver des applications dans diverses autres domaines de la science. De nombreux domaines profitent par exemple aujourd'hui du développement des détecteurs silicium piloté par les exigences du LHC au CERN [Wer05, MED]. Les futures expériences du CERN, qui seront consécutives au LHC, sont déjà à l'étude et nécessiteront de nouvelles technologies de détection alternatives aux détecteurs silicium actuels pour pouvoir remplir des conditions plus strictes et restreintes que pour le LHC. Le travail présenté dans cette thèse a été effectué dans le groupe de Microélectronique du CERN et s'inscrit dans ce contexte de recherche et de développement de nouvelles solutions de détection pour les futures expériences de physique des hautes énergies et de caractérisation de ces solutions pour d'autres

applications. Le potentiel d'une nouvelle technologie pour la détection de radiation ionisante est présenté dans cette thèse. Cette technologie appelée « Thin-Film on ASIC » (TFA) est basée sur la déposition d'un capteur en silicium amorphe hydrogéné directement sur circuit intégré.

La présentation effectuée dans ce résumé vise dans un premier temps à introduire plus précisément le contexte dans lequel s'inscrit le travail et à comprendre les différentes questions et défis associés au développement de cette nouvelle technologie. Les différents travaux effectués et les principaux résultats obtenus sont expliqués, en soulignant l'apport original important fourni par cette thèse et l'aspect pluridisciplinaire du travail effectué. Le texte fait référence à certaines figures, certaines équations ou indications bibliographiques correspondant au corps de la thèse écrit en anglais.

I. Détection de radiations pour la physique des hautes énergies

Le LHC est actuellement en construction au CERN pour fournir à la physique des particules son instrument le plus important pour sonder la matière et percer certains de ses multiples secrets. Les expériences ATLAS, CMS, LHCb et ALICE verront chacune en leur centre des collisions de faisceaux de hadrons à des énergies jamais obtenues auparavant (collisions de protons à une énergie de 14 TeV ou de noyaux de plomb à une énergie de 1150 TeV). Dans chaque expérience, plusieurs détecteurs ayant chacun un but particulier sont disposés autour du point d'impact pour étudier les produits de la collision. Des détecteurs de trace (regroupés dans le « traceur ») permettent de reconstruire la trajectoire des particules, des calorimètres permettent de mesurer leur énergie, et des chambres à muons permettent la détection de muons. Les composants des particules collisionnées peuvent être ainsi identifiés tout comme de nouvelles particules créées, révélant la nature des interactions agissant entre elles. L'expérience ATLAS est représentée comme exemple en Figure 1.

Dans ces expériences, de très hauts niveaux de radiation seront atteints, spécialement dans le traceur qui est disposé au plus proche des points d'interaction (quelques centimètres). Les exigences des détecteurs du traceur sont très strictes et représentent d'importants défis, de grandes aires de détection devant être couvertes avec des résolutions spatiales de quelques microns et temporelles de 25 ns dans un milieu soumis à de très hautes doses. Les détecteurs silicium remplissent ces différentes exigences et seront ainsi utilisés dans les différents traceurs du LHC. Ils pourront être utilisés pour les 10 ans de fonctionnement du LHC, i.e. jusqu'à des fluences de 10^{15} cm^{-2} (1 MeV neutron équivalent) et des doses maximales d'environ 500 kGy.

La formation d'un signal électrique correspondant au passage d'une radiation au travers d'un détecteur est tout d'abord détaillée pour apporter les bases à la compréhension du travail présenté dans cette thèse (Chapitre 1). Le principe de détection d'un détecteur semi-conducteur est basé sur l'établissement d'une zone de charge libre dans le détecteur où un champ électrique règne. Une radiation va interagir avec le détecteur en créant des paires electron-trou. Les mécanismes d'interaction diffèrent selon le type de radiation, que l'on peut alors diviser en :

- Particules chargées: elles interagissent principalement au travers d'interactions Coulombiennes entre la particule primaire et les électrons orbitaux des atomes du détecteur. Une ionisation directe est donc produite dans le matériau. Le pouvoir de ralentissement dE/dx est exprimé par l'équation de Bethe-Bloch (équation 1.1). Chaque type de particule présente pour une certaine énergie un minimum dans son pouvoir de ralentissement, et cette particule à cette énergie est appelée particule à minimum d'ionisation (MIP). La quantité moyenne d'énergie W nécessaire pour créer une paire électron-trou dans un détecteur semi-conducteur dépend de la largeur de sa bande interdite (Figure 1.2) et vaut 3.6 eV pour le silicium.
- Neutrons et photons : dans un premier temps un neutron ou un photon interagit respectivement avec un noyau et un électron. Celui-ci est mis en mouvement selon l'énergie transférée par le photon ou le neutron et provoque dans un deuxième temps des ionisations ou excitations dans le matériau. On parle donc d'ionisations indirectes. Le type d'interaction primaire du photon dépend de son énergie et du nombre atomique Z du matériau de détection (Figure 1.3). Contrairement à une particule chargée qui interagit tout le long de son trajet dans le détecteur, l'interaction du photon est localisée et statistique (équation 1.2).

Les charges libres créées par une radiation dans un détecteur semi-conducteur sont accélérées par le champ électrique interne du détecteur jusqu'à leur collection aux électrodes. Leur mouvement induit un signal électrique image sur les électrodes du détecteur. Le courant est donc induit dès la création des paires et ce jusqu'à la collection des charges mouvantes. Ce courant induit a été calculé par Ramo et Schockley [Sho38, Ram39] et est égal au produit de la charge mouvante par la vitesse de déplacement et par un champ dit de pondération. Ce dernier correspond au champ électrique équivalent qui règnerait dans le détecteur pour une tension de 1 V appliquée à l'électrode de référence et de 0 V à toutes les autres électrodes (ce champ est un facteur purement géométrique du détecteur qui représente le couplage électrostatique de la charge et de l'électrode et est exprimé en m^{-1}). Différentes extensions du théorème de Ramo [Cav71, Rie04] permettent de nos jours l'application de ce concept à tout type de détecteurs semi-conducteurs. Ce courant induit par l'interaction d'une radiation avec le détecteur peut être faible et une pré-amplification est primordiale pour obtenir un signal électrique qui puisse être traité et analysé. Un détecteur est ainsi directement connecté à un amplificateur de charge ou de courant [Gat86], et à l'interaction d'une radiation dans le détecteur correspond un pulse de tension en sortie de l'électronique de pré-amplification. Un schéma résumant la création d'un signal électrique dans le système détecteur-électronique est représenté dans la Figure 1.6.

Les détecteurs silicium utilisés dans les traceurs des expériences LHC sont segmentés en plusieurs zones actives, sous la forme de barrettes ou de pixels. Chaque élément est connecté séparément à son électronique de lecture associée par soudage filaire (wire-bonding) ou par de petites billes métalliques. Cette dernière technologie, dite « bump-bonding » ou « flip-chip » est utilisée pour les détecteurs pixels hybrides. Les détecteurs silicium à barrettes et hybrides sont respectivement représentés en Figure 1.7 et Figure 1.8. Les détecteurs pixels hybrides permettent d'obtenir directement une information bidimensionnelle. Les limitations actuelles de ces détecteurs sont principalement un coût élevé associé à la connexion par les billes métalliques et une tenue aux radiations qui est insuffisante pour une application dans les futures expériences de physique des hautes énergies.

En effet, malgré le fait que le LHC ne soit pas encore opérationnel, le potentiel pour la physique des particules et les défis technologiques associés à une évolution du LHC (Super LHC ou SLHC) vers une luminosité 10 fois plus importante (10^{35} $cm^{-2} \cdot s^{-1}$) ont déjà été étudiés [Gia02]. Un important besoin de recherche et de développement a été identifié pour les détecteurs, les détecteurs silicium actuels ne pouvant survivre aux plus fortes doses d'irradiations (10 fois supérieures) associées à l'évolution de la machine [Mol05]. Cette évolution conduit donc à une intense période de recherche de solutions alternatives aux détecteurs existants, allant de l'amélioration des technologies existantes à l'étude de nouvelles technologies. De nombreux avantages parallèles peuvent être associés à cette recherche car les technologies étudiées peuvent également révéler un fort potentiel pour des applications dans d'autres domaines de la science. Le travail présenté dans cette thèse s'inscrit dans ce contexte et présente la caractérisation d'une nouvelle technologie pour la détection directe de radiation. Cette technologie consiste en la déposition de capteurs en silicium amorphe hydrogéné directement sur un circuit intégrant l'électronique de lecture.

II. Silicium amorphe hydrogéné et technologie TFA

Les solides amorphes sont par nature non cristallins. Ils ne présentent pas d'ordre à longue portée dans l'arrangement des atomes. Cependant, l'ordre règne dans ce désordre au niveau microscopique entre un atome et ses proches voisins et permet à des matériaux tels que le silicium amorphe hydrogéné (a-Si :H) de disposer de caractéristiques électriques proches de celles de sa contrepartie cristalline. Un premier effet fondamental du désordre structurel est d'induire une forte incertitude dans le moment k des électrons et des trous du réseau et dans une énergie potentielle non périodique. Le matériau ne peut donc être étudié et caractérisé directement par la résolution de l'équation de Schrödinger ou par les relations E(k) comme dans le silicium cristallin, et la description est développée à partir des liaisons chimiques entre les atomes et par la densité d'état des bandes d'énergie N(E). La notion de bande interdite est conservée pour le a-Si:H et la bande interdite ou bande de mobilité vaut environ 1.8 eV. Un atome de silicium dans le silicium amorphe présente avec ses proches voisins en moyenne une longueur et un angle de liaison similaire au cas du silicium cristallin. Les fluctuations dans ces valeurs cependant provoquent des liaisons dites « faibles » ou « étirées » qui présentent une faible densité induisant des états d'énergie dits localisés, c'est-à-dire qu'aucune conduction des porteurs libres n'est attendue pour ces états. Ces états localisés forment des queues de bandes dans la distribution de densité d'état (Figure 2.4). Les défauts dans l'a-Si:H correspondent à des défauts de coordination, quand un atome a trop ou pas assez de voisins. Le défaut prépondérant du silicium amorphe correspond au cas où un atome de silicium ne dispose que de 3 voisins, présentant ainsi une liaison pendante qui va induire un état énergétique dans la bande interdite du matériau. Ces défauts de coordination induisent des états localisés près du milieu de la bande interdite (Figure 1.4). L'ajout d'hydrogène dans le silicium amorphe permet la passivation de presque 99 % de ces défauts, l'hydrogène venant saturer les liaisons pendantes. L'a-Si:H peut ainsi être défini par sa bande interdite et ses états localisés dans les queues de bande et au milieu du gap, induits par la structure amorphe du matériau, et par la passivation des défauts profonds par l'hydrogène qui permet l'utilisation de ce matériau.

Les différents états localisés influent sur le transport électrique. Les états profonds causés par les défauts de coordination sont des centres de recombinaison métastables. Leur densité n'est pas fixée et peut être changée par diverses perturbations. Une dégradation du matériau a ainsi été observée à la lumière, effet appelé Staebler-Wronski [Sta77, Bra98] totalement réversible. Les états des queues de bande influent sur la conduction et provoquent le piégeage des porteurs libres. La conductivité est ainsi limitée par ces états et est définie par le phénomène de « piégeage multiple», c'est-à-dire de consécutifs piégeages et dé-piégeages (Figure 2.8). A température ambiante, le transport des électrons est considéré comme non dispersif, de telle manière qu'une mobilité constante des électrons entre 1 et 5 $cm^2 \cdot V^{-1} \cdot s^{-1}$ est observée. Les états localisés sont en plus grande concentration dans la queue de bande de valence et induisent un transport dispersif des trous à température ambiante, c'est-à-dire une mobilité faible (de l'ordre de 0.1 à 0.01 $cm^2 \cdot V^{-1} \cdot s^{-1}$) qui varie avec le temps (équation 5.1).

Différents travaux effectués les 30 dernières années ont contribué à l'établissement d'un modèle du matériau mais différentes questions controversées subsistent encore. Cependant, le silicium amorphe hydrogéné est de nos jours largement commercialisé, que ce soit sous la forme de systèmes photovoltaïques (Figure 2.12) ou de transistors (TFT, Figure 2.13). Il est déposé aujourd'hui principalement par déposition vapeur-chimique assistée par plasma (PE-CVD, Figure 2.11) ou par filaments chauds (HW-CVD).

La déposition du matériau présente d'importants avantages car elle peut être effectuée sur de grandes surfaces, sur des surfaces non planes, à faible coût et à des températures inférieures à 250 °C. Cette dernière propriété permet la déposition de ce matériau directement sur circuit intégré sans dégradation de l'électronique intégrée. Des capteurs en a-Si:H peuvent ainsi être directement déposés sur un circuit intégrant l'électronique de lecture (Figure 2.15). Cette technologie dite « Thin-Film on ASIC » (TFA) a été proposée et déjà étudiée et développée pour des imageurs [Fis92, Sch99]. Les capteurs sont généralement structurés sous la forme n-i-p. Les couches dopées n et p présentent des densités de défauts importantes qui induisent une forte recombinaison de porteurs libres. Une couche intrinsèque est ainsi utilisée comme élément actif. Les couches dopées sont produites très fines (environ 30 à 60 nm) et permettent uniquement de déserter la couche i et d'induire un champ électrique dans cette zone active. Les applications commerciales utilisent de nos jours des couches d'épaisseur maximale d'environ 1 µm et des couches similaires ont été utilisées dans les premiers dispositifs TFA développés.

La technologie présente différents avantages pour la physique des hautes énergies ou pour d'autres éventuelles applications de détection de particules, provenant de la structuration du système de détection et des caractéristiques du matériau :

- Intégration capteur-circuit intégré : le haut degré d'intégration de la technologie TFA permet une réduction des coûts de fabrication en éliminant le procédé de connexions par billes métalliques utilisé pour les détecteurs silicium hybrides. L'intégration verticale permet également à l'électronique de lecture de pouvoir avoir la même aire que le pixel et d'obtenir un facteur de remplissage proche de 100 %, l'électronique et le capteur ne partageant pas exactement le même substrat.
- Déposition sur circuit après sa production : le capteur et l'électronique de lecture peuvent être séparément construits et optimisés. Différentes technologies ou procédés peuvent ainsi etre également utilisés au niveau du circuit intégré, et différentes configurations et épaisseur du capteur peuvent être utilisées selon l'application.
- Résistance aux radiations : différentes études de la résistance aux radiations de l'a-Si:H ont été effectuées dans le cadre d'utilisation de cellules solaires pour des applications spatiales et ont démontré une intéressante résistance aux radiations supérieure à celle du silicium cristallin [Sro98, Kis98, Kun03].

Cependant, une épaisseur de 1 µm du capteur est insuffisante pour la création par le passage d'une radiation ionisante d'un signal pouvant être lu par l'électronique de lecture. Des capteurs avec une épaisseur supérieure sont ainsi requis [Dub91, Fou01, Per87]. La notion de diode « épaisse » comme il est fait référence dans la thèse est très relative. En effet, en comparaison à des dispositifs a-Si:H standards, les diodes de 20 à 30 µm déposées peuvent être considérées comme épaisses. Cependant, elles peuvent être considérées comme fines en comparaison des épaisseurs standard des détecteurs silicium

(de 150 à 500 µm), et vont ainsi conduire à de faibles signaux créés par une particule. Une étude présente par exemple un signal d'une amplitude de 770 electrons créé par un MIP dans un capteur a-Si:H de 21 µm d'épaisseur [Ale91].
L'avantage principal de la technologie TFA provient de l'intégration du capteur et de l'électronique mais soulève également différentes questions et différents problèmes relatifs à la segmentation du détecteur et à l'interface circuit intégré-a-Si:H.
Les différentes limitations de la technologie et les importants défis associés au développement d'un dispositif TFA pour la détection de particules sont ainsi :

- La déposition de diodes a-Si:H épaisses au dessus de l'électronique. Ces diodes doivent présenter de faibles courants de fuite et une faible densité de défauts pour permettre la déplétion totale de la partie active.
- L'optimisation d'une électronique de lecture bas bruit capable de traiter les petits signaux créés par une particule dans le capteur en a-Si:H
- L'étude détaillée des mécanismes de création du signal dans un capteur en a-Si:H
- L'étude de l'interface a-Si:H-circuit intégré et de la segmentation du détecteur.

Le travail effectué dans cette thèse représente la première étude du potentiel de la technologie TFA pour la détection de radiations ionisantes, que ce soit pour la physique des hautes énergies ou pour d'éventuelles autres applications. La thèse ainsi implique un plus large domaine d'investigation et comprend l'optimisation et le développement de circuits intégrés dédiés à cette nouvelle technologie, l'étude et la caractérisation de la création d'un signal dans un capteur a-Si:H « épais » et l'étude du système TFA complet. Les contributions du travail présenté sont ainsi multiples et résumées dans les sections suivantes.

III. Développement de circuits intégrés pour la technologie TFA

La première importante contribution du travail présenté dans cette thèse est l'optimisation et le développement d'un circuit intégré adapté à la technologie « Thin-Film on ASIC ». L'optimisation est basée sur 2 principaux pôles directeurs qui sont le développement d'électrodes intégrées dans le circuit définissant l'interface capteur-électronique de lecture, et le développement de préamplificateurs bas bruits (centaines d'électrons) et rapides (dizaines de nanosecondes) pour permettre respectivement l'étude des faibles signaux créés par une radiation ionisante dans le capteur en a-Si:H déposé sur le circuit intégré et la caractérisation de la vitesse de ce signal.

Les technologies CMOS sont beaucoup utilisées dans le domaine de la physique des hautes énergies. Elles offrent une haute densité d'intégration, une faible consommation de puissance et permettent l'intégration de blocs analogiques et digitaux sur le même circuit. De plus, une technique de dessin spéciale permet d'élever la résistance des circuits aux radiations [Ane01]. Les circuits intégrés développés durant le travail de cette thèse l’ont ainsi été sur une technologie CMOS commerciale 0.25 µm. Deux circuits intégrés ont été développés et sont présentés dans cette section :

- l’AFP
- l’aSiHtest

L’AFP a été développé pour pouvoir caractériser différents détecteurs et n’est pas dédié à la technologie TFA. Cependant, les premiers détecteurs TFA ont été construits à partir de ce circuit, permettant de démontrer la faisabilité du concept TFA mais également de révéler différents problèmes liés à cette technologie. Ces premiers résultats ont ainsi amené au développement du circuit aSiHtest, totalement dédié à l’étude détaillée de la technologie TFA.

Architecture des préamplificateurs :

Les préamplificateurs intégrés dans les puces électroniques développées sont des amplificateurs transimpédance utilisant une boucle de retour active [Jar96]. Cette architecture est présentée dans la Figure 3.1. Elle comprend un étage amplificateur qui permet la création pour un pulse de courant en entrée d’un échelon de tension en sortie. Un transistor NMOS est placé entre l’entrée et la sortie et agit comme une résistance permettant la décroissance de l’échelon et ainsi l’obtention d’un pulse de tension en sortie. L’utilisation d’une résistance amènerait à une perte d’espace et à d’importantes capacités parasites par rapport au substrat. L’utilisation de la boucle de retour active permet donc d’obtenir une bande passante plus importante, et également de pouvoir contrôler la résistance du retour à l’aide d’un courant d’alimentation (Figure 3.1). Ce circuit peut aussi être aisément intégré dans un technologie CMOS en n’utilisant que des transistors MOS, et son implémentation dans une telle technologie est représentée dans la Figure 3.2. Le préamplificateur intégré comprend également un étage d’adaptation d’impédance utilisant un transistor monté en drain commun. Celui-ci permet de lire le signal de sortie directement sur un oscilloscope sans impact important sur la bande passante du système, malgré la charge de 50 Ω et la capacité de 9 à 12 pF alors chargeant la sortie du préamplificateur.

Le préamplificateur utilisé a tout d’abord été étudié théoriquement en détail. Ce travail a été effectué dans le but de maîtriser tout d’abord plus en profondeur les capacités et limitations du circuit et surtout pour fournir les outils nécessaires à une analyse plus poussée des résultats expérimentaux de la caractérisation des détecteurs TFA. En effet, l’étage de pré-amplification amplifie le signal créé par une radiation ionisante dans le capteur en a-Si:H mais change aussi sa forme. L’estimation du signal réel induit sur l’électrode du capteur demande ainsi une compréhension détaillée des mécanismes d’amplification. Les différents calculs effectués sont présentés en détail dans la section 3.1

de la thèse. Les différents models développés ainsi que certaines équation établies sont listés ci après:

- Modèle « simple » de la fonction de transfert calculé dans le domaine fréquentiel considérant les 2 pôles dominant du circuit et définissant le gain de l'étage d'adaptation d'impédance : équations 3.10 et 3.15. L'amplitude du pic de sortie et le temps de montée sont définis par les équations 3.18 et 3.19.
- Modèle « complet » de la fonction de transfert calculé dans le domaine fréquentiel : résultats représentés dans la Figure 3.6.
- Modèle « complet » de la fonction de transfert calculé dans le domaine temporel illustrant les limitations de la linéarité du circuit en fonction du signal d'entrée : équations 3.23, 3.24 et 3.25 et Figures 3.8 et 3.9.
- Stabilité : équations 3.26 à 3.30.
- Bruit exprimé en charge équivalente rapportée à l'entrée du circuit (ENC). La source dominante de bruit est le bruit thermique du transistor d'entrée (bruit série): équation 3.47. Une des sources secondaires est le bruit thermique du transistor de la boucle de retour (bruit parallèle) : équation 3.50.

Ces différents calculs mettent en évidence le compromis qui doit être choisi lors de l'optimisation du circuit entre les performances de vitesse, de bruit, de sensibilité à la capacité d'entrée du circuit et de gain. Les calculs présentés sont validés par différentes comparaisons avec des résultats de simulation HSPICE ou expérimentaux.

Le circuit AFP :

Le premier circuit développé, caractérisé et utilisé pour un détecteur TFA est l'AFP (Active Feedback Pre-amplifier). Une photo du circuit et le schéma de l'architecture des pré-amplificateurs intégrés sont présentés dans la Figure 3.14. Le circuit comprend 32 canaux de pré-amplificateurs similaires optimisés pour présenter une réponse rapide (~ 5 ns temps de montée) pour une capacité du détecteur en entrée de 2 à 5 pF. Les différentes caractéristiques mesurées expérimentalement sont listées dans le tableau ci-dessous.

Pré-amplificateur	*Electrode*	*Temps de montée*	*Gain*	*Bruit*
AFP	94 µm × 68 µm Square pixel	5 ns	2.77 mV/fC	450 e^- rms

Les caractéristiques des préamplificateurs intégrés rendent ce circuit attractif pour la caractérisation de la technologie TFA et les plots métalliques connectés aux entrées des pré-amplificateurs sont disposés au centre du circuit, facilitant la déposition du capteur a-Si :H. Les premières détections de particule ont été effectuées sur un détecteur basé sur ce circuit, démontrant la faisabilité du concept proposé. Cependant, ces premières mesures ont également montré différentes limitations de la technologie et ont amené le développement d'une seconde puce dédiée à une étude globale de la technologie TFA et du capteur en a-Si:H.

Le circuit aSiHtest :

Une des principales contributions apportée par le travail présenté dans cette thèse est le développement d'un circuit complet de test de la technologie TFA. Ce circuit, appelé aSiHtest, offre différentes possibilités de caractérisations d'un capteur pouvant être déposé sur sa surface. Le dessin et une photo du circuit sont présentés à la Figure 3.23. Le circuit présente en son centre une multitude de structures métalliques dessinées dans le dernier niveau de métal de la technologie CMOS utilisée. Le capteur en a-Si:H est déposé sur cette zone pour la construction du détecteur TFA et les différentes structures métalliques définissent les différentes électrodes segmentant le détecteur.

Dans les technologies CMOS une dernière étape lors de la construction d'un circuit consiste en la déposition de couches de passivation recouvrant totalement le circuit pour le protéger. Des ouvertures sont ensuite faites pour pouvoir permettre le contact des plots métalliques dessinés dans le dernier niveau de métal de la technologie. Ces ouvertures sont faites à l'intérieur des différents plots métalliques, et sont ainsi plus petites que les plots dessinés. Cependant, cette propriété des étapes de construction du circuit entraîne une surface non plane du circuit qui va induire différents problèmes au niveau d'un détecteur TFA et de l'interface circuit-capteur, comme il sera présenté en IV. Certaines structures métalliques intégrées dans le circuit aSiHtest présentent des ouvertures faites autour du plot métallique et permettent ainsi d'étudier l'influence de ces ouvertures sur les performances du détecteur. Les structures métalliques intégrées présentent différentes formes, différentes tailles et donc des ouvertures dans les couches de passivation soit à l'intérieur de la structure (comme il est généralement fait) soit autour de la structure (Figure 3.24). Chacune de ces différentes structures est connectée à un amplificateur de courant composé de miroirs de courant, permettant une amplification de courant pouvant être variée de 10^2 à 10^5. Ces structures permettent l'étude des courants de fuite du capteur quand il est déposé sur circuit et la caractérisation de la segmentation du détecteur.

De plus, certaines structures métalliques, sous la forme de pixels ou de barrettes, sont intégrées et connectées à un des 2 préamplificateurs transimpédance de la puce aSiHtest. Ces 2 circuits sont basés sur la même architecture que les amplificateurs de l'AFP et ont été optimisés pour de faibles capacités de détecteur (~ 250 fF). Les structures permettent l'étude des performances et des limitations d'un détecteur à pixel ou d'un détecteur à barrettes (strip) basé sur la technologie TFA. Les 2 préamplificateurs, respectivement nommés MiBeDo et aSiScope, permettent par leurs différentes optimisations une étude de la vitesse de création du signal dans le capteur ou une étude de l'efficacité de détection de radiation ionisante. Les performances de ces 2 électroniques de lecture ont été caractérisées expérimentalement et les résultats obtenus sont résumés dans le tableau ci-dessous.

Pré-amplificateur	*Electrode*	*Temps de montée*	*Gain*	*Bruit*
MiBeDo	- Pixel octogonal :2070 µm^2 - barrettes larges de 6.6 µm avec un espacement allant de 4 à 23.4 µm	5 ns	14.5 mV/fC	160 e$^-$ rms
aSiScope	- Pixel octogonal :2070 µm^2 - barrettes larges de 6.6 µm avec un espacement allant de 4 à 23.4 µm	25 ns	73 mV/fC	70 e$^-$ rms

Les 2 puces électroniques développées, l'AFP et l'aSiHtest, permettent par leurs différents préamplificateurs et leurs différentes structures métalliques un large champ de possibilité de caractérisation du potentiel de la technologie TFA pour la détection de particules et de rayonnements.

IV. Propriétés électriques et segmentation des détecteurs TFA

Les performances et limitations de détecteurs basés sur la déposition de capteurs en silicium amorphe hydrogéné sur circuit intégré ont été étudiées sur des détecteurs développés à partir des puces AFP et aSiHtest. Les capteurs ont été déposés à l'Institut de Micro Technologie de Neuchâtel [IMT] sous la forme de structures n-i-p. Les dépositions ont été faites par VHF PE-CVD, une technique similaire à une déposition standard PE-CVD mais utilisant une haute fréquence d'alimentation du plasma. Cette méthode permet l'obtention d'une vitesse de déposition plus élevée et les différents détecteurs caractérisés dans cette thèse ont été déposés avec une vitesse de 1.56 nm/s.

Les capteurs en a-Si:H présentant une épaisseur supérieure à 1 µm et leur fonctionnement représentent un domaine peu étudié et propice à différentes questions. Les caractérisations effectuées dans cette thèse contribuent à renforcer certaines théories et à proposer de nouvelles explications quant aux mécanismes physiques et aux propriétés électriques du matériau, tout en soulevant également de nouvelles interrogations.

Différentes structures « test » ont tout d'abord été déposées sur un substrat en verre pour caractériser les diodes a-Si:H épaisses. Une électrode commune en chrome est d'abord déposée, au dessus de laquelle est construite la structure n-i-p. Finalement, la zone active est définie par la déposition d'une électrode au sommet de la structure en oxyde conducteur transparent (TCO). Ces structures test sont représentées dans la Figure 4.1.

Les détecteurs TFA sont eux construits par la déposition selon le même procédé des couches n-i-p au dessus d'un circuit intégré, puis d'une électrode en TCO commune. Différentes structures métalliques du circuit intégré définissent les zones actives du détecteur. Ces structures sont reliées entre elles par le capteur, et une couche n spéciale présentant une haute résistivité a été utilisée pour permettre l'isolation des pixels (10^5-10^6 Ω·cm). Les photos de détecteurs TFA AFP et aSiHtest sont présentées dans la Figure 4.2. Le capteur a-Si:H est alimenté en inverse en appliquant une tension négative sur l'électrode commune connectée à la couche p, la couche n étant au potentiel d'entrée des préamplificateurs intégrés aux puces (~ 1.7 V).

Un premier paramètre fondamental pour l'optimisation du détecteur est l'obtention de faibles courant de fuites (ou courants d'obscurité). De forts courants amènent tout d'abord à un bruit plus élevé et peuvent également empêcher la déplétion totale du capteur. De plus, dans les détecteurs TFA développés, le courant de fuite a pour effet direct de décharger le miroir de courant alimentant le transistor de boucle de retour du préamplificateur, modifiant ainsi le courant circulant dans ce transistor et par là même sa transconductande et la fonction de transfert du circuit (Figure 4.3). Les diodes épaisses développées pour la détection directe de radiation ionisante requièrent une importante tension inverse d'alimentation (centaines de volts) entraînant de forts champs électriques dans le capteur (10^4 à 10^5 V/cm). Ceux-ci provoquent tout d'abord de fortes augmentations du courant de fuite comme il en a été mesuré sur des structures test (Figure 4.4). Ces courants peuvent être attribués à une génération thermique augmentée par le champ électrique par effets Poole-Frenkel. De forts champs contribuent en effet à une libération plus aisée de porteurs piégés en abaissant l'énergie d'activation, et contribuent à faciliter la génération thermique de porteurs, comme l'exprime l'équation 4.2.

Les premiers tests effectués sur les détecteurs TFA basés sur les puces AFP ont démontré une première importante limitation de cette technologie. Des capteurs ont été déposés avec une épaisseur maximale de 32 μm, et des tensions maximales de 300 V ont pu être appliquées. Cependant, de plus fortes tensions sont supposées nécessaires pour la déplétion d'un capteur de cette épaisseur. En effet, la tension de déplétion peut être estimée par les calculs découlant de l'équation de Poisson (équation 2.30) et dépend de la densité de défauts profonds et de l'épaisseur d de l'échantillon (équation 2.31). Cette tension peut être estimée comme $V_f \sim 0.45 \times d^2$, et une tension de 460 V est alors attendue pour dépléter le capteur de 32 μm. De forts courants de fuite limitent la tension applicable. Ces courants ont été mesurés et sont présentés à la Figure 4.6, en comparaison avec les courants mesurés sur un capteur similaire déposé sur verre. De très grandes différences sont observées, les courants étant jusqu'à 3 ordres de magnitude plus importants pour le détecteur TFA. Ces premières mesures démontrent donc de forts courants d'obscurité associés à la déposition sur puce.

La compréhension et la réduction de ces courants de fuite liés à l'intégration du capteur sur circuit intégré sont d'une importance primordiale, et de multiples tests ont été effectués sur les différents détecteurs TFA développés. Une première méthode d'investigation proposée dans cette thèse est la caractérisation de la zone active d'un pixel et la recherche de zones à forts champs électriques en utilisant le faisceau d'électrons d'un microscope électronique à balayage (SEM). Les électrons d'une énergie d'environ 20 keV balaient la surface active du détecteur sous test. Un signal électrique est créé correspondant à l'épaisseur de déplétion, au champ électrique, à la quantité de charges libres créées et à l'amplitude du champ de pondération du détecteur à l'endroit du balayage. Ce signal électrique peut être soit directement lu sur un oscilloscope soit réinjecté dans le système d'exploitation du SEM qui peut construire une image ayant pour contraste l'amplitude du signal créé. Cette méthode expérimentale est présentée en détail dans la section 4.2 et permet ainsi l'observation directe d'une cartographie de l'amplitude du signal créé selon l'endroit d'injection de charges.

Des premières mesures ont été effectuées sur des structures test, et les résultats sont présentés Figures 4.9 et 4.10. Ils démontrent une bonne homogénéité du signal induit même sur les bords des pixels. Une très faible induction latérale de signal est par ailleurs observée, suggérant un très faible effet de bord sur les capteurs a-Si:H. Des secondes mesures effectuées sur un pixel d'un détecteur AFP démontrent un tout autre comportement. De forts signaux sont induits à la périphérie et aux coins du pixel, suggérant des zones à forts champs électriques. Ces zones correspondent aux ouvertures dans les couches de passivation. Les effets géométriques créés par les fronts de 4 à 6 µm des couches de passivation (Figures 4.11 et 4.12) sur la forme du capteur induisent donc des zones à forts champs électriques (Figure 4.13) qui peuvent expliquer les forts courants de fuite mesurés sur ces détecteurs TFA.

Les détecteurs TFA développés sur des puces aSiHtest présentent des électrodes au niveau de la puce avec différentes formes, tailles et ouvertures dans la passivation. Ces différentes structures ont permis une étude détaillée des courants de fuite d'un détecteur TFA et de démontrer l'existence de courants de fuite importants additionnels à la périphérie et aux coins des pixels:

- la densité de courant de fuite décroît pour une taille croissante du pixel. Le rapport périmètre sur aire d'un pixel est plus faible pour de grands pixels, et les coins du pixel ne dépendent pas de l'aire du pixel. Les courants additionnels expliquent donc les densités mesurées
- des pixels longs et fins induisent des courants supérieurs par rapport à des pixels carrés ou octogonaux de même aire. Ici encore, le périmètre pour les structures longues est plus important et les courants additionnels expliquent les résultats obtenus

- Des structures avec une ouverture dans les couches de passivation en dehors du plot métallique présentent une densité de courants de fuite inférieure d'un facteur 3 à 10 par rapport à de similaires structures ayant une ouverture à l'intérieur de la structure métallique. La réduction du courant est également proportionnelle à la distance bord du plot métallique-ouverture.

La surface non plane de la puce sur laquelle est déposé le capteur en a-Si:H induit donc de forts effets géométriques à l'endroit des ouvertures dans les couches de passivation et entraîne la création de forts courants de fuite périphériques. Une première méthode de réduction des courants de fuite consiste donc en l'ouverture de larges fenêtres dans la passivation au dessus des structures métalliques.

Les mécanismes physiques responsables du courant de fuite ont également été étudiés sur les détecteurs développés sur les puces aSiHtest en mesurant l'évolution des courants de fuite en fonction de la température. Les résultats présentés Figures 4.25 et 4.26 démontrent une multiplication du courant de fuite par un facteur 1.5 tous les 10 degrés. Les résultats expérimentaux obtenus sont en accord avec une génération thermique augmentée par effets Poole-Frenkel et démontrent que pour une tension de 160 V appliquée à un capteur de 20 μm, l' énergie d'activation est abaissée à 0.42 eV (contre ~ 0.9 eV à faibles champs électriques).

V. Induction et vitesse du signal dans les détecteurs TFA

L'induction et la vitesse du signal dans un détecteur TFA ont été étudiées en utilisant une technique expérimentale de temps de vol présentée en détail dans la section 5.1. Un laser de 660 nm de longueur d'onde a été utilisé pour photo générer en environ 3 ns des paires électron-trou dans le capteur (Figure 5.4). L'a-Si:H présente un coefficient d'absorption de 10^4 cm^{-1} pour ces photons, de telle manière que les paires sont créées très près de l'interface p-i du détecteur. Les charges libres sont alors séparées et accélérées par le champ électrique interne, les trous dérivant vers la zone p et les électrons vers la limite de la zone déplétée du capteur (Figure 5.3). Le mouvement des charges induit un signal électrique négatif sur l'électrode intégrée dans la puce et connectée à l'électronique de lecture.

Le champ électrique interne du capteur peut être estimé en considérant une charge d'espace déterminée par la densité de défauts profonds ionisés. Le champ s'étend depuis l'interface p-i et décroît linéairement dans la zone déplétée (équation 5.4). Le mouvement des porteurs libres créés est également fonction de leur mobilité. A température ambiante, les électrons ont un transport non dispersif et une mobilité pouvant être considérée quasi-constante. Cependant, les trous présentent eux un transport dispersif. Leur mobilité varie avec le temps (équation 5.1). De plus, un fort champ électrique entraîne un abaissement de l'énergie d'activation des porteurs piégés, favorisant ainsi la conductivité du matériau en abaissant les temps de relaxation des trous piégés (équation 5.7). Le mouvement des trous est donc une complexe fonction du temps et du champ électrique.

Le signal créé par les porteurs libres générés par le pulse laser de 660 nm va donc être principalement déterminé par la dérive des électrons à travers la totalité de l'épaisseur déplétée. Les électrons ont une vitesse décroissante le temps de leur dérive (équation 5.6) et vont induire un signal croissant durant le temps de création des charges et décroissant pendant la dérive du paquet de charge créé (Figure 5.6). Les signaux créés dans 2 détecteurs constitués respectivement d'un capteur en a-Si :H de 13 µm et de 32 µm d'épaisseur et d'une puce AFP sont présentés dans les Figures 5.7 et 5.8 pour différentes tensions inverses appliquées. Le front de montée déterminé par le temps de montée de 5 ns du préamplificateur est proche du temps de génération des charge de 3 ns. Le pic correspond donc approximativement au courant induit par la dérive du paquet d'électrons au niveau du champ maximum. La décroissance rapide des signaux ensuite observée est attribuée à la décroissance du courant induit due à une vitesse de dérive décroissante des électrons. Les pulses observés présentent ainsi une décroissance rapide de 16 ns (échantillon 30 µm) à 20 ns (échantillon 13 µm), constante pour les différentes tensions d'alimentation. En augmentant la tension appliquée, la distance de dérive est augmentée mais le champ électrique aussi, et le temps de collection et donc la durée du signal induit sont constants pour un capteur partiellement déplété. Une longue queue de signal (> 600 ns) variant fortement selon la tension appliquée est aussi observée, et peut être attribuée à la lente dérive des trous fortement dépendante du champ électrique (la distance de dérive des trous ne varie pas avec la tension appliquée) et (ou) à un profil non linéaire du champ électrique à la frontière entre les zones déplétée et non déplétée.

Un modèle simplifié du transport des charges libres et du signal induit par leur mouvement a été établi dans cette thèse. Le signal induit par des électrons créés proche de l'interface p-i et dérivant dans la totalité de l'épaisseur déplétée a été démontré décroissant exponentiellement avec le temps selon l'équation 5.13. La vitesse du signal est caractérisée par la constante de temps τ_c (équation 5.9) qui dépend de l'inverse du produit de la mobilité par la densité de défauts ionisés ($\mu_d \times N_{db}^*$). Ce modèle développé, même si simplifié, a permis d'expliquer avec succès les formes des signaux observés, et des simulations utilisant un signal d'entrée de l'AFP basé sur l'équation 5.13 permettent de retrouver les mêmes formes de signaux de sortie que mesurées expérimentalement (Figure 5.12). Le paramètre τ_c a ainsi été extrait. Une méthode similaire a été utilisée sur un échantillon de 20 µm déposé sur une puce aSiHtest et a également permis l'extraction du paramètre τ_c. Les différents paramètres du transport des électrons ainsi mesurés sont listés dans le tableau ci-après.

Echantillon	τ_c	*Temps collection*	$\mu_d \times N_{db}{}^*$	μ_d
13 µm AFP	4 ns	12 ns	1.65×10^{15} cm$^{-1}\cdot$V$^{-1}\cdot$s^{-1}	2.75 cm$^2\cdot$V$^{-1}\cdot$s^{-1}
30 µm AFP	5.6 ns	16.8 ns	1.18×10^{15} cm$^{-1}\cdot$V$^{-1}\cdot$s^{-1}	2 cm$^2\cdot$V$^{-1}\cdot$s^{-1}
20 µm aSiHtest	6 ns	18 ns	1.1×10^{15} cm$^{-1}\cdot$V$^{-1}\cdot$s^{-1}	1.80 cm$^2\cdot$V$^{-1}\cdot$s^{-1}

Les différentes caractérisation faites dans cette thèse démontrent ainsi que le signal induit par les électrons dans un capteur épais en a-Si:H finit après un temps allant de 12 à 18 ns. De plus, pour un capteur « sur-déplété », un signal plus rapide est attendu, le champ électrique étant encore augmenté alors que la longueur de dérive reste la même. Cet effet a été observé sur l'échantillon de 20 µm déposé sur aSiHtest, pour lequel un τ_c constant de 6 ns est mesuré jusqu'à une tension d'environ 180 V, alors que pour une tension de 200 V il est estimé à 5 ns.

Un modèle qualitatif a aussi été développé pour expliquer la longue queue de signal observée expérimentalement. Le modèle est basé sur le signal induit par les trous et tient en compte le transport dispersif des trous et la mobilité variant avec le champ électrique (équation 5.19). Le courant induit par les trous calculé par le modèle devient de plus en plus rapide pour des tensions d'alimentation croissantes et correspond qualitativement aux variations mesurées des queues de signaux avec la tension. De plus, il a également été démontré que ces queux de signaux peuvent être expliquées par le transport d'électrons dans la zone proche de la zone non déplétée, où un champ électrique faible et décroissant lentement peut être présent.

Le travail présenté dans cette thèse a ainsi contribué à l'élaboration d'un modèle simplifié du transport des charges dans un capteur en a-Si:H épais et du signal induit par ce mouvement sur les électrodes. Le travail présenté démontre une limitation des signaux induits par les épaisseurs non déplétées du capteur. Contrairement à un détecteur en silicium cristallin, la partie non déplétée d'un capteur en a-Si:H présente une haute résistivité (~ 10^{10} Ω·cm) qui affecte l'amplitude du courant induit. En effet, le courant dépend alors du rapport épaisseur déplétée d sur épaisseur totale ($d+d_2$) (équation 5.13, [Rie04]). Une déplétion partielle du capteur a ainsi pour effet de diminuer l'induction du signal en diminuant le couplage électrostatique entre les charges mouvantes et l'électrode connectée au préamplificateur.

VI. Détection de radiation ionisante avec des détecteurs TFA

La détection de radiation ionisante a été étudiée sur différents détecteurs TFA et les mécanismes participant à la création du signal ont été appréciés en détail pour permettre la compréhension des performances et des limitations de la technologie TFA.

La faisabilité de la détection de particules avec un détecteur TFA a tout d'abord été démontrée sur un échantillon de 32 µm déposé sur la puce AFP. Des électrons d'énergie allant de 10 à 50 keV ont été détectés avec un temps de montée du signal de sortie de 5 à 10 ns, démontrant la possibilité de détecter des particules avec cette technologie dans un temps court. Ces résultats sont présentés Figure 6.2. Des tests ont également été effectués pour la détection de particules à minimum d'ionisation (MIP), mais aucun signal n'a été mesuré. Ces résultats montrent que le signal créé par un MIP dans un capteur de 32 µm alimenté par 300 V est inférieur à 1300 électrons (Figure 6.5).

Génération du signal :

Un modèle du signal généré par une radiation ionisante dans un capteur a-Si:H a été développé et est proposé dans cette thèse. Le signal induit dépend dans un premier temps de l'interaction de la radiation ionisante avec le capteur et de la création de porteurs libres associée, et dans un deuxième temps du mouvement de ces charges libres et de l'induction d'un courant sur les électrodes du détecteur. La création des porteurs par la radiation ionisante est définie par :

- L'énergie déposée par la radiation ionisante: une particule chargée dépose son énergie tout le long de son trajet dans le capteur et la distribution de l'énergie perdue par la particule est définie par la fonction de génération. Un photon dépose son énergie localement dans un espace restreint et l'endroit d'interaction est statistique.
- L'énergie moyenne pour la création de paires electron-trou dans l'aSi:H : de 4.6 à 6 eV.

Les fonctions de génération des électrons dans l'a-Si:H ont été étudiées et sont présentées dans les équations 6.3 et 6.4 ainsi que dans la Figure 6.6. La probabilité d'interaction d'un photon dans l'a-Si:H a également été étudiée et est représentée pour des rayons X d'énergie de 6, 10 et 20 keV dans la Figure 6.6.
Un courant est donc induit par le mouvement des charges libres générées par la radiation ionisante dans la zone déplétée du capteur. Le modèle simple présenté dans cette thèse permet de calculer le courant induit par un électron ou un trou créé à une position x_0 dans le capteur (Figures 6.7, 6.8 et 6.9) :

- électrons : le courant induit est présenté dans l'équation 6.6. Une charge totale Q_e est induite en un temps inférieur à 20 ns, comme il a été démontré auparavant. Cette charge dépend de l'épaisseur déplétée d et N électrons créés à une position x_0 induisent une charge $Q_e = (q \cdot N/d_{tot}) \cdot (d-x_0)$, d_{tot} étant l'épaisseur totale du capteur. Un signal maximum est ainsi obtenu pour une déplétion complète du capteur.
- Trous : le courant induit est beaucoup plus difficile à calculer à cause des variations de la mobilité des trous avec le temps et avec le champ électrique. Cependant, les calculs ont pu être aboutis et le courant induit est exprimé dans

l'équation 6.13 et nécessite l'utilisation de l'expression présentée dans l'équation 6.12. Les temps de dérive des trous sont beaucoup plus lents et fortement dépendant du champ électrique. Ainsi, pour un temps de montée de l'électronique de lecture rapide, seule une partie du signal est intégrée. Ces temps de montée étant au maximum de 50 ns dans les préamplificateurs utilisés pour le travail de cette thèse, aucune recombinaison n'est attendue mais les trous dérivent sur une très faible distance et induisent une charge correspondant à 5-15 % de la charge totale attendue des trous. De forts champs électriques permettent une augmentation de ce signal. Ainsi, d'épais capteurs ou une « sur-déplétion » conduisent à l'établissement de champs plus importants et permettent une augmentation du signal.

La charge totale Q créée par une radiation ionisante traversant le capteur sur une électrode peut finalement etre exprimée par l'équation 6.16.

Déplétion du capteur :

La déplétion du capteur est un paramètre fondamental pour optimiser la détection. En effet, dans le cas du a-Si:H, la déplétion partielle non seulement amène à une zone active plus faible (donc à une plus faible création de charges libres pour des particules traversant totalement le capteur) mais également à un couplage électrostatique charges - électrode plus faible qui réduit le signal induit. La condition de déplétion dans un capteur a-Si:H ne peut être étudiée en mesurant ses variations de capacité avec la tension appliquée, sa capacité étant constante à cause de la haute résistivité de la zone non déplétée. Une méthode expérimentale basée sur le laser de 660 nm est proposée dans cette thèse. La charge induite par les N charges créées par le laser est en effet égale à $q \cdot N \cdot d/d_{tot}$. En utilisant un préamplificateur disposant d'un temps de montée supérieur à 20 ns (ce temps correspondant au temps maximum nécessaire à la création totale de la charge) on peut ainsi observer l'évolution du pic créé en sortie de l'amplificateur en fonction de la tension appliquée. Les résultats expérimentaux obtenus sur des échantillons déposés sur puce aSiHtest et en utilisant les préamplificateurs aSiScope sont présentées dans les Figures 6.11 et 6.12 et démontrent que la zone de déplétion peut être évaluée par cette méthode. Une tension de 180 V à 196 V a ainsi été mesurée comme nécessaire pour la déplétion d'un capteur de 20 µm. La densité moyenne de défauts ionisés peut également être extraite par cette méthode expérimentale, et des valeurs de $6.15\text{-}6.5 \times 10^{15}$ cm^{-3} ont été mesurées.

Détection :

L'efficacité de détection a été caractérisée sur des échantillons de 20 µm déposés sur puce aSiHtest, en utilisant les préamplificateurs présentant un bruit de 70 électrons rms.

Une efficace détection d'électrons basse énergie (~ 15 à 50 keV) a été démontrée, avec un signal créé de quelques milliers d'électrons. La détection a été étudiée sur des pixels de 2070 μm^2 et également sur des structures barrettes ayant une largeur de 6.6 µm et un espacement minimum de 4 µm. Les résultats de charges créées ont été analysés et comparés aux charges calculées par le modèle présenté dans cette thèse et une énergie moyenne de création de paires electron-trou W de 5.4 ± 0.8 eV a été extraite. Une très faible induction latérale a été démontrée par les mesures sur les structures à barrettes. Les résultats expérimentaux présentés dans les Figures 6.14 et 6.15 montrent que quand un signal est lu sur une barrette, aucun signal n'est lu sur les barrettes voisines. Ces mesures ainsi que les mesures effectuées avec le microscope électronique démontrent une intéressante faible induction latérale des détecteurs TFA, rendant cette technologie attractive pour des applications nécessitants une haute résolution spatiale.

Cependant, aucune claire détection de MIP n'a été démontrée. Le banc de test permettait la mesure avec un rapport signal sur bruit de 10 pour des charges d'entrée de 700 électrons. Aucun signal pouvant être clairement attribué à la détection d'un MIP n'a pu être détecté avec ce banc de test, démontrant qu'un MIP crée moins de 700 électrons dans un capteur de 20 µm totalement déplété et avec une électronique de lecture ayant un temps de montée de 25 ns. Ce faible signal créé par un MIP représente une forte limitation de la technologie TFA pour des applications dans la physique des hautes énergies.

Finalement, la détection de rayons X avec un détecteur TFA a été démontrée avec succès dans cette thèse. Des rayons X de 5.9 keV ont été détecté, créant un signal maximum de 1000 électrons et un pic à 650 électrons pour un échantillon de 15 µm d'épaisseur (Figure 6.20).

VII. Effets des irradiations sur un capteur en a-Si:H

Les effets de hauts niveaux d'irradiation sur les performances d'un détecteur sont fondamentaux et déterminants pour des applications dans la physique des hautes énergies. En effet, comme il a été présenté précédemment, les futures expériences prévues au CERN nécessitent des détecteurs capables de résister à un niveau de radiation encore jamais obtenu jusqu'à aujourd'hui. Les traceurs d'éventuelles expériences pour le super-LHC devront ainsi survivre à une fluence totale de hadrons d'environ 1.6×10^{16} cm^{-2}.

Les effets des irradiations sur le silicium amorphe ont été peu étudiés par le passé, et représentent ainsi un domaine compliqué et vaste. Le travail effectué dans cette thèse à ce propos ne constitue pas une étude systématique du sujet, et présente uniquement quelques résultats expérimentaux montrant les propriétés basiques du matériau. Ces résultats peuvent donc être considérés comme préliminaires et contribuent à la connaissance générale sur ce sujet.

Des premiers tests de diodes épaisses en silicium amorphe hydrogéné sous irradiation de protons d'énergie 23 GeV ont été effectués dans cette thèse jusqu'à des fluences de 1.6×10^{16} cm^{-2}.

Les structures testées sont des diodes n-i-p de 32 µm et de 20 µm d'épaisseur déposées sur verre. Les diodes présentent des surfaces actives de 2 mm × 2 mm et ont été placées dans un faisceau de protons 23 GeV provenant du synchrotron (PS) du CERN. Ces protons vont provoquer dans le détecteur des défauts de déplacements et également des défauts liés à l'ionisation, cependant plus faibles que les dommages que pourraient créer des protons de plus faible énergie. Divers paquets de protons traversent ainsi le détecteur sous test, un paquet durant environ 400 ms et 2 à 3 paquets étant injectés durant un cycle de 16.8 s. Le signal créé par chaque paquet de proton a été mesuré durant l'expérience et est référé comme PSIC. L'évolution des caractéristiques du détecteur a ainsi été étudiée en direct sous le faisceau, en observant le PSIC pour les différentes fluences ou doses accumulées sur le détecteur. Les résultats obtenus sur les 2 échantillons testés sont présentés dans les Figures 7.3, 7.5 et 7.6. Le travail effectué permet d'extraire différentes tendances :

- le courant de fuite est augmenté par l'irradiation. Il est multiplié par un facteur 2 après une fluence de 5×10^{14} protons/cm^2 (équivalent à une dose d'environ 145 kGy)
- les effets sur le courant de fuite sont totalement réversibles et après un traitement thermique du capteur pendant 24 heures à 100 °C le courant de fuite de la diode irradiée est équivalent au courant de fuite post-déposition
- le signal induit (PSIC) est stable et augmente même légèrement (facteur 0.5) jusqu'à une fluence d'environ 10^{14} protons/cm^2
- le PSIC diminue d'une manière log-log linéaire avec la fluence accumulée et est un facteur 4 plus faible après une fluence de 10^{16} protons/cm^2

Ces résultats démontrent une intéressante résistance à une irradiation de protons de 23 GeV de la diode a-Si:H, ce qui en partie provient d'une capacité de réarrangement du matériau permettant de passiver certains des défauts engendrés par collision et est liée à la capacité de réparation thermique du matériau.

Des irradiations ont également été faites sous fortes fluences d'électrons de 26 keV. Les résultats sont présentés dans les Figures 7.7 et 7.9, démontrant une importante dégradation du matériau. Des mesures sous ce même faisceau d'électrons et au laser après irradiation et après différents traitements thermiques à 100 °C démontrent également que les dégradations apportées par l'irradiation peuvent être totalement récupérées (Figures 7.11 et 7.13).

Les effets des irradiations sur un capteur en a-Si:H sont donc principalement une création de défauts profonds liée à l'ionisation. Les importants effets associés sont une augmentation du courant de fuite et une diminution de la zone déplétée et donc du signal induit. Cependant, une diminution de la densité de défauts est provoquée par un traitement thermique, et ce même à température ambiante, démontrant l'importante métastabilité des défauts profonds. La technologie TFA présente donc une intéressante résistance aux radiations liée à la métastabilité du matériau, et la dégradation du détecteur et du signal dépend fortement du taux d'irradiation.

VIII. Conclusions

Le travail présenté dans cette thèse a tout d'abord apporté la démonstration de la faisabilité de la détection de particules et de rayonnements avec un détecteur basé sur la technologie « Thin-Film on ASIC ».

Une première contribution importante du travail effectué consiste dans l'optimisation et le développement d'un circuit intégré adapté à la caractérisation de capteurs pouvant être déposés sur sa surface. Le circuit intégré aSiHtest permet ainsi la caractérisation des courants de fuite du capteur, de la segmentation du détecteur (interface capteur/circuit intégré), de la vitesse du signal créé dans le capteur (à l'aide de préamplificateurs rapides présentant un temps de montée de 5 ns) et de l'efficacité de détection (à l'aide de préamplificateurs bas bruit ayant un bruit rapporté à l'entrée de 70 électrons).

Le travail présenté apporte d'importantes contributions à une compréhension des mécanismes gouvernant les courants de fuite dans un détecteur TFA, ces courants pouvant fortement limiter l'efficacité de détection. Les différents travaux présentés démontrent une création de courant dirigée par une génération thermique augmentée par le champ électrique par effet Poole-Frenkel. Cette génération assistée est également accrue au niveau de l'interface p-i du capteur. De plus, d'importantes sources de courant ont été identifiées à la périphérie et dans les coins d'un pixel d'un détecteur TFA. Ces courants sont induits par la surface de la puce nivelée par les couches de passivation et par les ouvertures dans ces couches pour accéder aux plots métalliques intégrés. Le capteur ainsi déposé épouse la forme de la surface du circuit intégré et de fortes zones de champs et donc de forts courants de fuite sont créés à la périphérie et dans les coins d'un pixel. Une ouverture dans ces couches autour des plots métalliques permet une importante réduction de ces courants.

La création de signal dans un capteur a-Si:H a également été spécialement étudiée. Il a été démontré qu'une déplétion partielle du capteur a un double effet amenant à la réduction du signal. D'une part la zone active est réduite, mais le couplage électrostatique charges créées – électrode est également limité et réduit le signal par un facteur correspondant au rapport épaisseur déplétée sur épaisseur totale du capteur. Une méthode expérimentale est proposée dans cette thèse pour déterminer la déplétion d'un capteur a-Si:H.

Le travail effectué démontre que les électrons libres créés par une radiation ionisante dans un capteur a-Si:H participent à l'induction d'un signal en un maximum de temps d'environ 18 ns. Le signal induit par les trous a été quant à lui démontré être fortement dépendant du champ électrique pour des temps d'analyse de l'ordre de dizaines de nanosecondes. Seulement une faible proportion du signal attendu des trous est vue dans des temps pareils (~ 5 à 15 % en 25 ns).

La détection d'électrons de faibles énergies (15 à 50 keV) a été prouvée avec succès par ce travail, ainsi qu'une très faible induction latérale de signal. Cette étude démontre un fort potentiel de cette technologie pour des applications nécessitant un détecteur d'électrons avec une haute résolution spatiale. La détection de rayons X avec des énergies minimum de 6 keV a également été démontrée avec succès.

Cependant, une importante limitation subsiste pour cette technologie de détection et réside dans la faiblesse du signal créé par une particule à minimum d'ionisation (MIP). Les travaux présentés démontrent une trop grande difficulté de détection de MIP pour des capteurs ayant une épaisseur de 20 µm. L'utilisation de capteurs de 40 µm totalement déplétés pourrait permettre l'obtention d'une charge d'environ 1400 électrons pour un MIP, qui pourrait ainsi être aisément lue par un préamplificateur tel que ceux intégrés dans la puce aSiHtest.

Les performances de la technologie TFA pour la détection de particules ont ainsi été adressées pour la première fois. Les études menées ont soulevé différents problèmes liés à l'aspect novateur de la technologie. Certains de ces problèmes ont pu être estimés et résolus par le travail présenté. Les résultats obtenus sont prometteurs pour cette nouvelle technologie, mais différents problèmes subsistent encore et doivent être adressés pour l'application de cette technologie à la physique des hautes énergies.

INTRODUCTION

The world around us presents a tremendous complexity, but its foundations can be explained with a handful of elementary particles which can attract or repel each other according to different forces. The study of these basic constituents of matter and of their interactions has however necessitated all through the past century the construction and the operation of increasingly complex instrumentation requiring advanced technologies. The standard model has been developed during this intensive research period and incorporates a number of theories which can explain the nature and the consistency of matter. In order to confirm some theories of this model which have not been tested yet by experiments, and in order to probe into matter deeper than ever before, a new complex machine, the Large Hadron Collider (LHC), is currently being built at the European Laboratory for Particle Physics [CERN].

CERN is one of the world's largest scientific laboratories. It has been founded in 1954 and involves international collaborations of physicists and engineers to build and operate the complex instruments necessary for particle physics experiments. These instruments are basically particle accelerators and detectors. Accelerators are used to accelerate beams of charged particles up to a speed close to the speed of light. When the particles have reached the desired energy, they collide with another bunch of particles coming from the opposite direction or hit a fixed target. The LHC accelerator will collide protons or heavy ions at energies never attained before (14 TeV at the centre of mass for protons and 1148 TeV for lead ions). A detector is built around the collision point in order to study the products of the collision. It is a complex system formed by several sub-detectors organized in a cylindrical part called a barrel closed at the two ends by two end-caps. A detector and its infrastructure are called experiment and four experiments are involved with the LHC, CMS (Compact Muon Solenoid), ATLAS (A Torroidal LHC ApparatuS), LHCb (LHC beauty) and ALICE (A Large Ion Collider Experiment). In each of these experiments, two hadron bunches will thus enter the detectors from two opposite sides and collide head-to-head in its centre. The information taken for each collision by the sub-detectors allows the analysis of the physics of the collision, each sub-detector having a specific task. The tracker reconstructs the trajectory of the particles, the calorimeters measure the energy and the muon chambers detect the muons. A part of the detector is surrounded by an electromagnet which generates a very strong magnetic field to bend charged particle trajectories. From the curvature one can extract the momentum and the charge sign of a particle. The ATLAS experiment detector is represented as example in Figure 1.

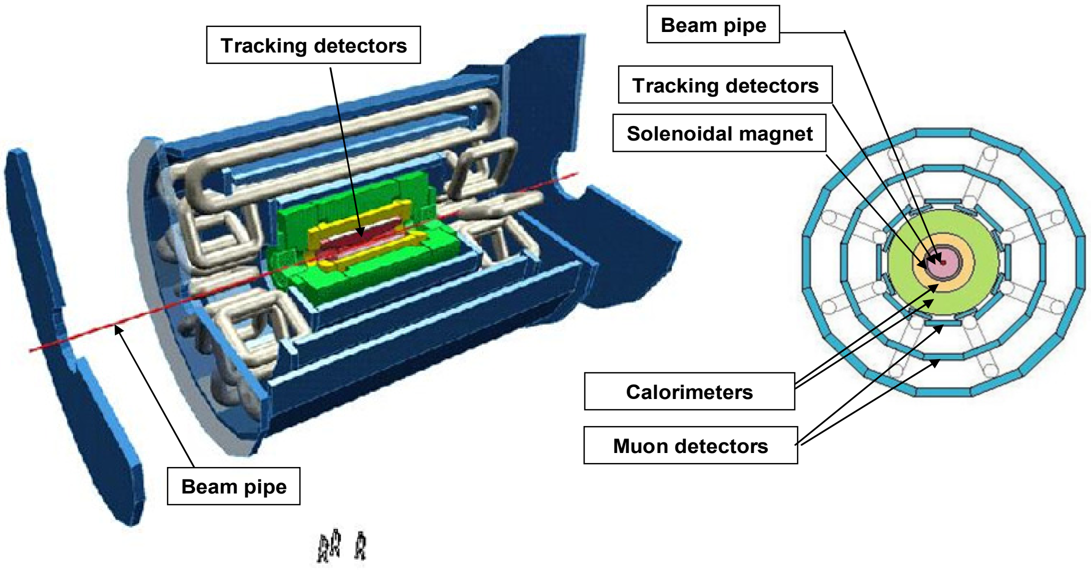

Figure 1. The ATLAS experiment. Left: Longitudinal cross section of the detector. 3 persons are represented on the bottom to illustrate the detector size. Right: Lateral cross section of the detector with the different sub-detectors [ATLAS].

In the LHC experiments, very high radiation levels will be attained, especially in the tracker which is located close to the interaction point (down to few centimeters). Requirements for the tracker sub-detectors are thus stringent and challenging. Large active areas with spatial resolutions down to few microns have to be used. A fast readout (less than 25 ns) associated to a resistance to the harsh radiation environment are some of the requirements for these detectors and their electronic readout. After 10 years of operation of the LHC, a maximum accumulated fluence equivalent to a fluence of 1 MeV neutrons of about 10^{15} cm^{-2} and a maximum dose of about 500 kGy (50 MRad) are expected in the tracker detectors (these maxima radiation levels will be attained in the pixel detectors of the ATLAS tracker, located at about 5 cm from the collision [Gro05]).

State-of-the-art silicon detectors are expected to be able to withstand such accumulated radiation levels [Gro05]. They also offer the high granularity and the excellent spatial resolution required and will thus be used in the trackers of the different experiments. Their active area is segmented into millions of diodes which are readout separately by Application Specific Integrated Circuits (ASICs) in order to obtain the spatial information about the trajectory of the detected particle. Sensing elements are in the form of pixels or strips, pixel detectors providing a direct two-dimensional pattern of the particle hit position [Wer05]. Each active area of a detector is connected to its electronic readout either through wire-bonding or through a metallic ball connection in a process called bump-bonding.

Although the LHC is not yet in function, future fixed target or collider experiments are already under study, asking for higher performance detectors. For example, studies on the physics potential and on the experimental challenges for an upgrade of the LHC to a ten times higher luminosity (Super-LHC or SLHC) have been performed [Gia05]. State-of-the art silicon detectors that will be used for the LHC will not be able to survive the harsh radiation environment of SLHC. Detectors of the trackers will have to resist to 10 times higher radiation levels than for LHC, i.e. to an accumulated fluence equivalent to a fluence of 1 MeV neutron of about 10^{16} cm^{-2} and to a maximum dose of about 5 MGy (500 MRad). A clear need of intensive research and development has thus been identified for the detectors in order to match the required radiation hardness and high spatial and timing resolutions of the detecting systems [Mol05]. The different strategies include material engineering and "new materials". Special emphasis is put on the development of more radiation tolerant silicon like high resistivity Czochralski (Cz), epitaxial (epi) silicon layers or other defect engineered silicon, while novel alternative solutions to silicon detector systems are explored and considered.

Due to this constant need for higher performance detectors, particle physics experiments have already proven over the years to be an important driving force in the development of detector technologies, many of which (as silicon detectors) have been commercialized and found applications in other areas of science and medicine [Wer05, MED]. An intensive research for radiation hard alternatives to actual silicon detectors for future High Energy Physics experiments can thus also permit the development and the characterization of novel technologies which might in turn present attractive features for other areas of science.

The work presented in this thesis has been carried out in this context in the Microelectronics group at CERN. This group provides expertise in the development and design of ASICs for High Energy Physics experiments, together with research activities in the development of semiconductor detectors and optimization of detection systems for applications in other areas of science. The thesis presents a novel solid state detector technology for ionizing radiation detection and the characterization of its performance and limitations. The work presented contributes to the research and exploration of alternative solutions to actual silicon detector systems and to the characterization of a novel technology which might present attractive features for other applications.

The technology studied in this thesis is based on the deposition of a hydrogenated amorphous silicon (a-Si:H) sensor directly on top of the readout integrated circuit and is called Thin-Film on ASIC (TFA). A TFA detector is represented in Figure 2. This thesis work has been motivated by the different advantages the technology potentially offers, originating both from the material used as sensing device and from the detector structure.

Hydrogenated amorphous silicon is used as sensing material and can be deposited at low costs and on large areas at temperatures below 250 °C, allowing the deposition on processed integrated circuits. Radiation hardness of this material has been studied in the context of testing solar cells for space applications. A good radiation hardness of the material in comparison to crystalline silicon has been shown [Sro98, Kis98, Kun03].

The Thin-Film on ASIC technology permits the vertical integration of a thin film sensor directly on top of the Application Specific Integrated Circuit (ASIC). The detector structure (presented in Figure 2) thus eliminates the need for bump-bonding or wire-bonding and enables a high level of integration between the sensor and the readout electronics. This results in a simpler detector construction which leads to an overall system cost reduction. The TFA concept thus provides similar advantages to monolithic detectors, while it also presents the advantages of the hybrid pixel approach. The sensing device and the electronic readout can be separately designed and optimized, the sensing device can be biased separately from the electronic readout and the pixel electronic shares the same die area with the photodiode array.

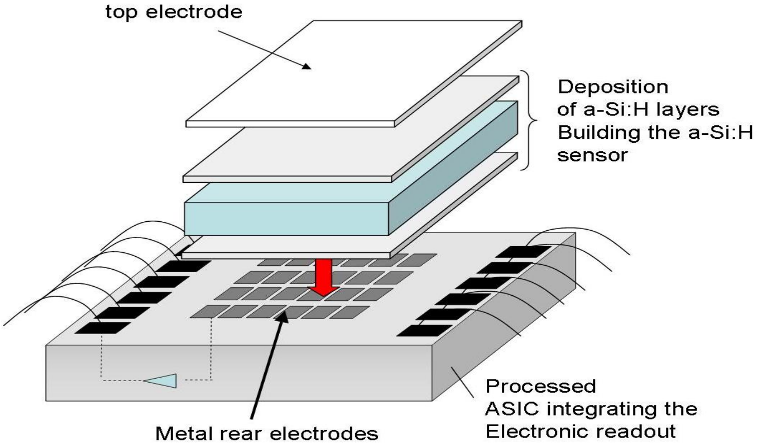

Figure 2. Schematic representation of a TFA detector. An a-Si:H sensor is deposited directly on top of an ASIC which integrates the electronic readout. Electrodes segmenting the detector are integrated in the ASIC.

The high level of integration of the detector and the properties of the sensing material render the presented technology very attractive for a radiation hard pixel detector and for other applications such as medical imaging devices. a-Si:H devices developed and commercialized so far are in the form of thin films of about 1 μm deposited on a glass substrate. Only recently such thin films have been deposited on ASICs to build image sensors [Sch99]. However, such thickness does not permit the creation of a sufficient signal from the track of a particle and thicker sensors are required for particle detection. The work that has been carried out thus presents a novel approach which consists in depositing a-Si:H sensors with a thickness up to about 30 μm on top of a processed ASIC to perform particle detection. Different novel characterizations are involved, from a-Si:H sensor study (sensors with a thickness up to about 32 μm have been little studied in the past) to device characterization (the deposition on the ASIC is very specific and involves different problems not studied yet).

The work carried out represents the first studies of the potential and limitations of the proposed novel particle detection technology. It involves a large field of investigation and comprises ASIC design, a-Si:H sensor characterization and TFA detector system study. In order to get sufficient signal over noise ratio from the passage of particles through the TFA detector, low-noise electronic readout has to be designed. Moreover, the deposition of the sensor is done directly on top of the ASIC, so that appropriate design of electrodes to segment the sensor has to be achieved at the ASIC level. I have thus developed integrated circuit dedicated to the TFA technology. The different characterizations done on the developed TFA detectors are presented, from detector leakage current and segmentation to signal induction and speed in an a-Si:H sensor. No pixel detector prototype has been built as TFA detectors have been developed and characterized in this work to first extract the potential and limitation of this novel technology, and to propose solutions for the design of a detector prototype.

The different integrated circuits, experimental results, models and conclusions I have obtained during this thesis work are presented in this manuscript. The presentation of the work carried out is organized in different chapters described in the following:

Chapter 1: The basic mechanisms leading to the creation of an electric signal from the passage of a particle through a semiconductor detector are presented. Some of the silicon detectors and their electronic readout used for LHC experiments are shown.

Chapter 2: The characteristics of a-Si:H are presented in order to understand the material specificities. The deposition techniques together with the different nowadays applications of this material are also presented. The Thin Film on ASIC technology is explained in detail and the different important challenges in the development of a TFA detector able to detect particles are introduced.

Chapter 3: The two different ASICs designed, integrating pre-amplifiers based on the active feedback pre-amplifier concept, are presented. A detailed study of the pre-amplifier architecture is done in this chapter. This systematic analytical study was performed in order to be able to extract from a measured output signal the input current, i.e. in the case of a TFA detector the a-Si:H sensor response. The first ASIC, called AFP, is introduced and experimental results of its characterization are presented. A second circuit, the aSiHtest circuit, has then been designed as a global test chip of the technology. The different characterization possibilities offered by this circuit together with the characterization of the speed and noise performance of the integrated pre-amplifiers are also presented.

Chapter 4: TFA detectors have been developed by depositing a-Si:H sensing devices on top of AFP and aSiHtest circuits. The different detectors studied during the thesis work are presented. A first crucial parameter of the sensing element is its leakage current. This parameter turned out to be a major limitation of TFA detectors. Leakage current has thus been studied in details, from intrinsic properties of the material (studied by measuring leakage currents at different temperatures) to the specific case of sensors deposited on ASICs. Results are presented.

Chapter 5: The charge transport and signal induction specificities of TFA detectors are presented. For High Energy Physics applications, the induced signal speed is a crucial parameter of the detector performance and has therefore been studied in detail. The measurement technique and the results obtained on the different TFA detectors developed are presented.

Chapter 6: Radiation detection efficiency of the developed TFA detectors has been studied on pixel or strip structures. The signal creation is explained and a measurement technique to estimate the a-Si:H sensor depletion is proposed and presented. Results obtained with different radioactive sources are detailed.

Chapter 7: A crucial parameter of a detector for future applications in High Energy Physics is its resistance to radiation. Detectors have been tested under 24 GeV/c protons and 26 keV electrons irradiations and results are presented in Chapter 7.

Conclusions: The main contributions of the thesis are presented, together with the final conclusions which can be drawn from this work.

1. Semiconductor Detectors for High Energy Physics

Semiconductors have been widely studied and commercialized all through the 20th century and are nowadays extensively used for the detection of ionizing radiation. The first semiconductor detector was made by van Heerden in the middle of the Second World War (1943) in Utrecht (Netherlands), in the form of an AgCl crystal [Hei03]. Since that, semiconductor detecting devices have become a well established detection technology, the most popular being silicon detectors. They are nowadays used for a broad field of applications from medical imaging, spectroscopy or instrumentation to detector systems for the future Large Hadron Collider (LHC) experiments at CERN. Solid state detectors offer a direct and efficient conversion of the radiation energy, permitting a high spatial resolution (down to few µm) and a high collection speed (collection times down to few ns) with a compact interacting medium in comparison to other detection technologies [Lut99].

Radiation detection will be briefly presented in section 1.1 in order to introduce the basic mechanisms involved in the creation of a signal by radiation in solid state detectors. The work presented in this thesis concerns the characterization of a solid state detection technology based on hydrogenated amorphous silicon (a-Si:H), so that each concept introduced in section 1.1 will serve as a basis for the understanding of the different chapters of the thesis.
Several types of silicon detectors are used for High Energy Physics experiments, and some of the detectors that will be used for tracking in the LHC experiments are briefly presented in section 1.2. Future High Energy experiments will impose more stringent and challenging requirements for detectors. These are briefly introduced in section 1.2 together with possible detection solutions, in order to present the basic context in which this thesis work is involved.

1.1. Semiconductor for radiation detection

The passage of ionizing radiation through a semiconductor detecting device induces an electrical current on the detector electrodes. Semiconductor detecting devices are generally built as p-n junctions [Lut99] so that an internal electric field can be built in the detector and permits the separation, drift and collection of the electron-hole pairs created by the incoming radiation. The detection process can thus be described by two mechanisms which are presented in this section:

- creation of electron-hole pairs in the detector via interactions of the incoming radiation in the detector material, presented in 1.1.1;
- induction of a signal on the detector electrodes by the motion of the generated free carriers in the detector internal electric field, presented in 1.1.2.

1.1.1. Generation of charge carriers

The first step in the detection process consists in the interaction of the incoming radiation with the detecting medium. The ionizing radiation loses all or a part of its energy generating free charge carriers in the detector (electrons being lifted from the valence band into the conduction band, thus creating free electrons and holes). Semiconductor detectors are built as junctions and reverse biased in order to obtain the separation, drift and collection of these free carriers.

Thermal agitation can also supply sufficient energy for the generation of free carriers. This generation directly depends on the material bandgap and has a detrimental effect in semiconductor radiation detectors because it leads to a noise superimposed onto the signal. The material bandgap has then to be big enough in comparison to the thermal energy kT to reduce the thermal generation and thus the detector leakage current. In silicon, the 1.12 eV bandgap leads to a low probability of direct excitation at room temperature ($kT \approx 26$ meV). Here the thermal excitation might principally occur in two steps through intermediate local states in the bandgap which are caused by imperfections (defects) and impurities. The thermal generation can become a crucial parameter for a detector material which presents a low bandgap (such as Germanium for which $E_G \approx 0.66$ eV) or (and) defect states in the bandgap. This mechanism has been studied for a-Si:H in the thesis work and is presented in detail in Chapter 4.

The manner radiation interacts with the detector material and the energy loss associated to the interaction depends on the type, the kinetic energy, the mass and the charge of the incident radiation, and on the density, atomic number Z and mass of the detector material. The ionizing radiation can be categorized according to the involved interaction mechanism into:

- Charged particles: they interact mainly through direct Coulomb interactions between the primary charged particle and orbital electrons of target atoms.
- Neutrons and photons: the interaction involves mainly a two-step process, where secondary charged particles are generated and can cause further ionizations. Electrons or positrons are created in the case of incident photons while heavy charged particles are almost always created in the case of neutrons, which interact with nuclei of the absorbing material. These secondary particles transfer energy to the medium via direct Coulomb interactions with orbital electrons.

1.1.1.1. Charged particles and Minimum Ionizing Particle

Energetic charged particles interact with matter principally via Coulomb interaction, transferring their energy to the atomic electrons at the vicinity of the track, either raising electrons to a higher lying shell of the atom (excitation) or removing completely electrons from the atom (ionization). The Coulomb interactions that a charged particle suffers in the absorbing medium are described by the so-called collision stopping power, which defines the differential energy loss for that particle within the differential path length of the material, $S = -(dE/dx)_{col}$. The linear stopping power is determined by the collision stopping power and is calculated using the Bethe-Bloch formula [Kno99, Lut99] which can be written as:

$$-\frac{dE}{dx} = \frac{N_A\,\rho}{A}\,\frac{2\pi e^4 z^2}{m_0 v^2}\,Z\left[\ln\left(\frac{2 m_0 v^2}{I}\right) - \ln\left(1-\frac{v^2}{c^2}\right) - \frac{v^2}{c^2}\right] \qquad (1.1);$$

where N_A is Avogadro's number and A and ρ the atomic mass and the density of the absorber, so that $N_A \times \rho / A$ defines the number of target atom per unit of volume. v and z×e are the velocity and charge of the primary particle, e being the electronic charge, m_0 is the electron rest mass and I represents the average excitation and ionization potential of the absorber. It must be noted that this energy transfer thus exhibits a statistical nature. An example of the variations of the mean mass stopping power $(dE/dx)/\rho$ in silicon as a function of the interacting particle energy is presented in Figure 1.1 left.

A minimum $(dE/dx)/\rho$ is reached for a given energy of a given particle, as it is illustrated for a proton in Figure 1.1 left. The energy of the particle for which the stopping power (or mean energy loss) is minimum varies according to the particle type [Alv04]. However, these minima are similar and particles with an energy corresponding to this minimum stopping power are referred to as Minimum Ionizing Particles (MIP).

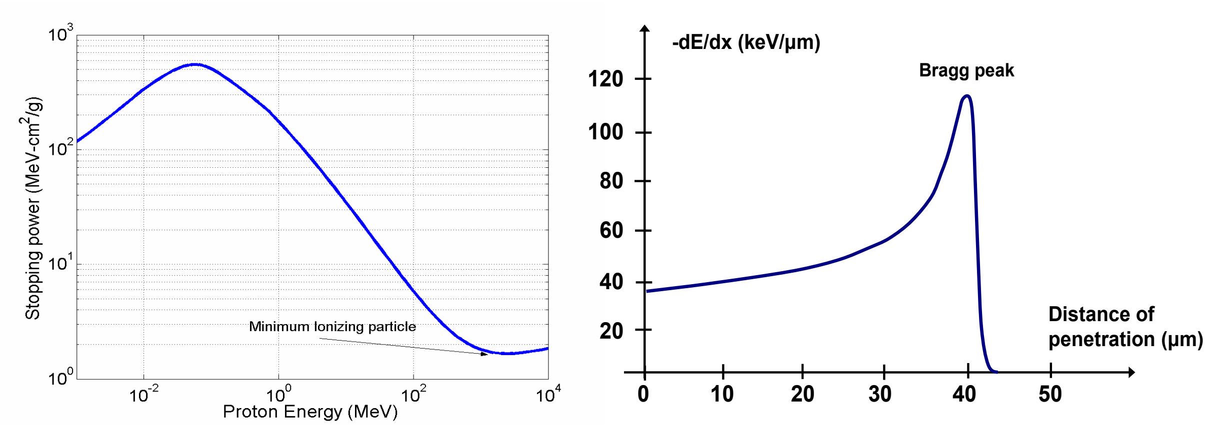

Figure 1.1. Left: Rate of energy loss due to ionization as a function of kinetic energy of a proton traversing silicon [STAR05]. Right: Bragg curve illustrating the energy loss of a 1.7 MeV proton in silicon as a function of penetrated depth [Cas98].

At any given time, a particle interacts with many electrons, so that the particle momentum decreases continuously until the particle is stopped. The collision stopping power in a material thus varies as the particle loses energy while it penetrates deeper into the material. The stopping power can be plotted as a function of the particle track length, resulting in the so-called Bragg curve presented in Figure 1.1 right, illustrating the variation of energy loss of the particle as it penetrates deeper the material.
Low energy particles have a high stopping power and are totally absorbed in a semiconductor detector. Their range (i.e. the total distance that the given particle can travel in the detector material before being stopped) is smaller than the detector thickness. Such particles will thus present a deposition of energy in a semiconductor detector similar to the presented Bragg curve. This will be the case for example for protons with energies lower than about 5 MeV in a 300 µm silicon detector. High energy particles will lose only part of their energy in the detector, so that the energy loss profile in the detector does not show the Bragg-peak. A MIP will lose a negligible part of its initial energy in the detector, so that the mean stopping power is nearly constant in the detection volume. A 2 GeV proton (MIP, see Figure 1.1 left) for example has a mean stopping power of 0.38 keV/µm in a silicon detector, so that it loses on average only about 116 keV of its initial energy in a 300 µm thick detector [STAR05].

The attenuation of electrons in matter is not described accurately by the Bethe-Bloch formula, since electrons are scattered more easily due to their smaller mass, resulting in very tortuous paths of electrons. More accurate expressions for the collision stopping power for electrons and positrons can be found in [Kno99, Lut99].

The number of free carriers generated by a charged particle in the detector depends on the energy lost by the particle causing ionization and on a fundamental parameter W which represents the mean energy needed to create an electron-hole pair. This average energy is 3.6 eV for silicon and depends on the material bandgap [Kle68] (Figure 1.2).

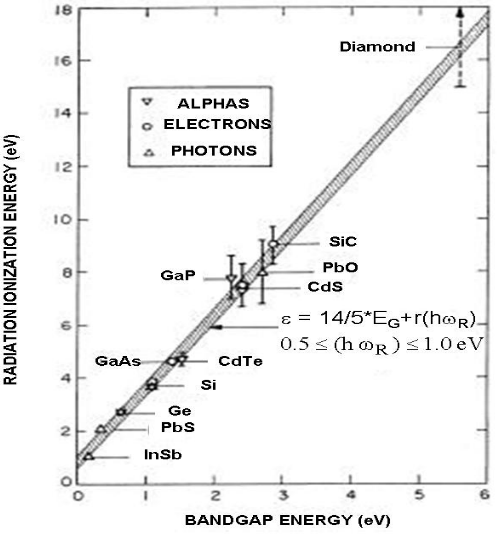

Figure 1.2. Mean pair creation energy versus material bandgap energy [Kle68].

The high stopping power of semiconductors permits the design of semiconductor detectors with thickness of few hundred of microns. Such detectors still allow the creation of enough electron-hole pairs to provide a significant signal corresponding to the track of a MIP in the detector. It can be noted that low bandgap of the material results in an interesting low W, but that it also results in increased leakage currents because of enhanced thermal generation.

1.1.1.2. Photon interactions

In contrast to charged particles which create electron-hole pairs continuously all along their path in the detector, photon interactions are localized. A photon will traverse a certain distance within a medium before depositing its energy. The probability η of interaction of a photon after traveling a distance d in the detector is given by:

$$\eta = 1 - \exp[-\mu(E, Z)\,d] \qquad (1.2);$$

where μ is the linear attenuation coefficient which depends on the photon energy E and on the atomic number Z of the detector. This dependency originates from the fact that a photon deposits locally its energy by either photo-electric absorption, Compton scattering or pair production, depending on the photon energy and on the absorber Z. The 3 different mechanisms are presented in the following:

Photo-electric effect: During photo-electric absorption the primary photon is completely absorbed in an interaction with a tightly bound inner shell electron. An electron is released with an energy given by the difference between the primary photon energy and the binding energy of the inner shell electron. The photo-electron subsequently loses its kinetic energy via excitation and ionization. For visible light photons, one electron-hole pair will be created by a photon as the photo-electron does not have sufficient energy for further ionizations. In the case of X-rays ($E > 1$ keV), the electron created by one photon will have a kinetic energy almost similar to the primary photon and will induce further ionizations in the detector. The number of electron-hole pairs created can be estimated using the incoming X-ray energy and the mean electron-hole pair creation energy W of the detector material. The significance of the photoelectric effect is greater for materials composed of elements with a high atomic number (Z), such as metals or other inorganic materials. However, this cross section drops off rapidly (i.e., the attenuation caused by the photoelectric effect becomes less relevant) with increasing x-ray energy (Figure 1.3).

Compton scattering: the incident photon ejects an electron from the atom and a photon of lower energy (longer wavelength) is scattered from the atom. The total energy of the incoming photon is thus divided in the photo-electron and in the re-emitted photon. Compton scattering is important for low atomic number materials as organic materials.

Pair production: The incident photon is completely annihilated and causes the creation of an electron-positron pair. This phenomenon can occur when the incident photon energy is greater than 1.024 MeV. Positrons are very short living and disappear (positron annihilation) with the formation of two photons of 0.51 MeV (Figure 1.3 left). Pair production is of particular importance when high-energy photons pass through materials of a high atomic number.

The 3 mechanisms are illustrated in Figure 1.3 left. The dominant effect determining the interaction of a photon with a medium depends on the photon energy and on the material atomic number Z, as it is presented in Figure 1.3 right. In silicon, the photo-electric effect will dominate for photons with energy up to about 60 keV.

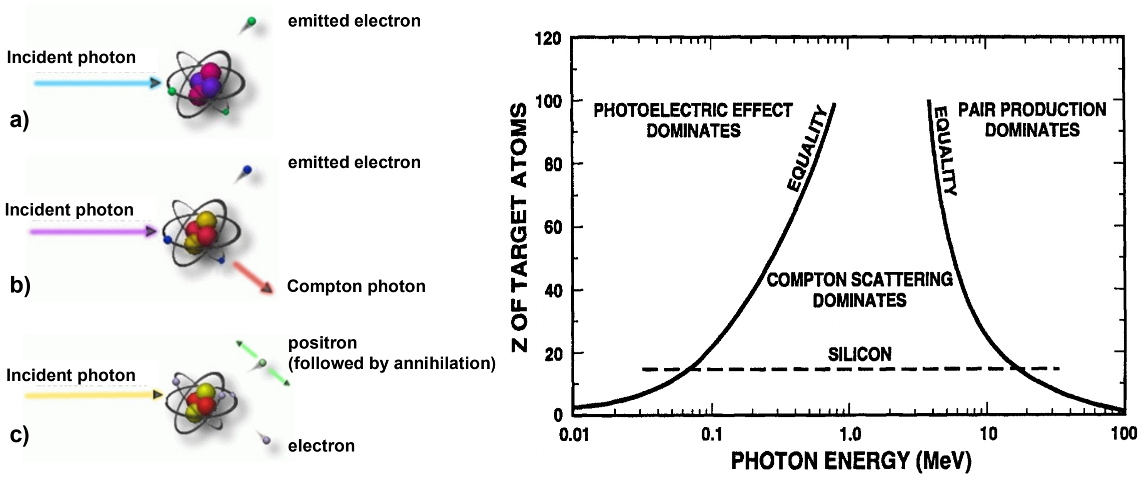

Figure 1.3. Left: Schematic representation of the 3 different processes through which photons can interact with matter: a) Photo-electric effect, b) Compton scattering, c) Pair production. Right: Dominant process of interaction as a function of photon energy and detector material Z [Sch94].

1.1.2. Signal formation and processing

A semiconductor detector device is usually designed as a p-n junction and reverse biased in order to obtain a space charge region and an electric field in the detector, as it is represented in Figure 1.4 left. Free electrons and holes generated by an incoming radiation in the space charge region of the detector are then separated by the internal electric field and drift with a velocity v_{drift} defined by:

$$\vec{v}_{drift} = \pm \mu \cdot \vec{E} \qquad (1.3);$$

where μ is the carrier mobility and $\vec{E}$ the electric field, the relation being positive for holes and negative for electrons. This relation is valid until charge carriers reach saturation velocity. For silicon, the drift velocity is defined by equation (1.3) up to the saturation velocity of 10^7 cm/s [Lut99] (the velocity starts to deviate from the linear relation for fields of about 10^4 V/cm).

Directly after their creation, the free charge carriers generated by the incoming radiation move under the electric field and their motion induces a current on the detector electrodes. Shockley and Ramo have first calculated the current and charge induced by the movement of free carriers in vacuum tubes on any electrode of the tubes [Sho38, Ram39]. Calculations are based on the laws of electrostatistics using the so-called "Ramo theorem" [Ram39] and show that the current I induced by a moving charge q·N can be expressed as:

$$I = \pm q \cdot N \cdot \vec{v}_{drift} \cdot \vec{E}_W \qquad (1.4).$$

E_W is the so-called weighting field (expressed in m^{-1}) and is a measure of the electrostatic coupling between the moving charge and the sensing electrode. The current induced thus depends on the total charge moving, on its speed and on the weighting field of the detector configuration. For an electric field directed from the bottom electrode to the top electrode (Figure 1.4), electrons (holes) drift to the bottom (top) electrode and a negative (positive) current is induced on the bottom (top) electrode.

The Ramo theorem has then been extended to the case of electrodes connected to resistive elements and for detectors with a space charge region, demonstrating that equation (1.4) is also valid for semiconductor detectors [Cav71].

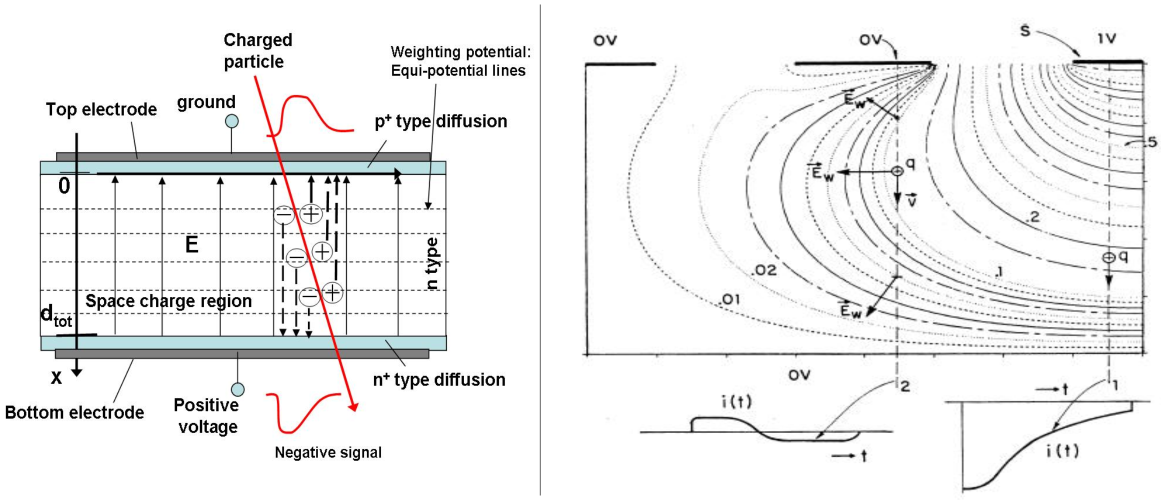

Figure 1.4. Left: Fully depleted semiconductor detector in a parallel plate configuration. Charge carriers are generated by an incoming particle, separated and accelerated by the internal electric field. At the moment of their creation and motion a signal starts to be induced on both electrodes. When all free carriers are collected the induced signal is at zero and all signal has been created. Right: Representation of weighting field for a multi electrode detector configuration represented as a plot of equi-potential lines [Rad88].

Two fields have thus to be considered in the calculation of the signal induced by free carriers, the physical electric field which drives the motion of charges and the weighting field which is purely defined by the detector geometry (it does not depend on the internal space charge). In the simple configuration of Figure 1.4 left of parallel plate diode electrodes separated by a distance d_{tot}, the weighting field is equal to $1/d_{tot}$ and is perpendicular to the electrodes. In the case of devices with more electrodes, as in microstrip detectors, the weighting field is more complicated and extends onto the electrode sides, as it is represented for 3 strips in Figure 1.4 right. It is determined by applying a unit potential on the sensing electrode of interest and zero potential on all other electrodes. All fixed charges are neglected and the resulting map of the weighting field is different to that of the electric field.

Signal induction theorems have also been recently extended by W. Riegler [Rie04] to the more general case of a detector which contains resistive elements, as it is the case in resistive plate chambers or underdepleted semiconductor detectors (Figure 1.5). The time dependence of the signals is in these cases not only given by the movement of the charges but also by the time-dependent reaction of the material, as once the charges reach the resistive part of the detector they are "compensated" by charges flowing in the layer with a time constant τ. This time constant is defined as $\tau = \varepsilon_0 \cdot \varepsilon_r / \sigma$, σ being the conductivity of the resistive layer (the non-depleted layer in the case of under-depleted semiconductor detector). The drift time of the generated free carriers is defined as T in the following, and depending on the difference between T and τ, the induced signal has different shapes, as it is shown in Figure 1.5 right.

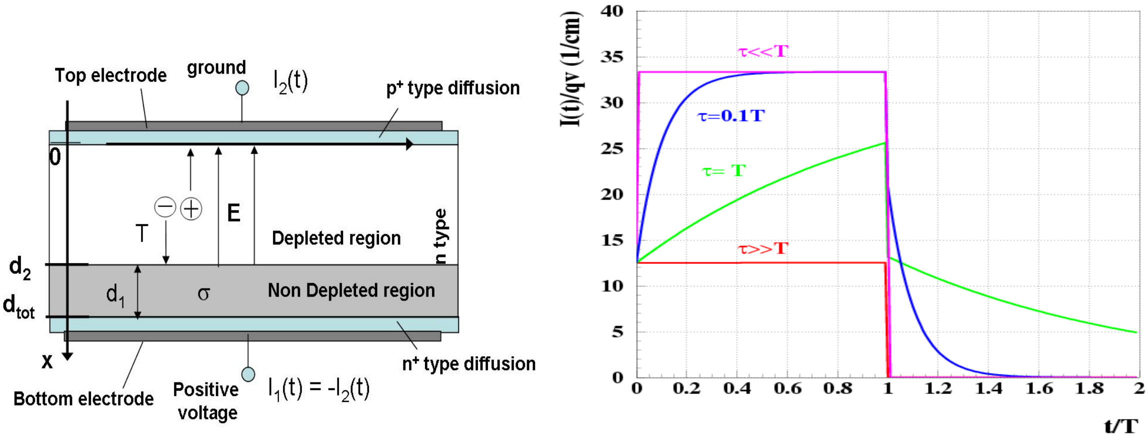

Figure 1.5. Left: Schematic representation of parallel plate configuration of an under-depleted silicon detector. Right: Induced current over charge and velocity of charge (i.e. weighting field) [Rie04].

For a high resistivity of the layer, $\tau >> T$, and a constant current is induced while the charge is moving. Once the charge hits the surface and is collected the current is zero (Figure 1.5 right). In case $\tau = T$, a current is also induced after the time T while charges reach the surface. For low resistivity layer ($\tau << T$), the layer acts as metal plate and the induced current is thus equal to the one created in a parallel plate geometry of plate separation d_2 (Figure 1.5). In the case of under-depleted silicon detector with doping concentration at about $N_A = 10^{12}$ cm^{-3}, the non-depleted layer volume resistivity is of

$1/\sigma \approx 5$ kΩ·cm, leading to a τ of about 0.5 ns, and therefore we will be usually in the case of $\tau \ll T$. The situation is different for a-Si:H and will be studied in detail in Chapter 5.
The signal created by a particle on a detector electrode is thus determined by the motion of the free carriers generated. The collection of these free carriers corresponds to the end of the created signal, so that the usually used expression of collection time refers to the duration of the created signal.

The signals induced by the motion of free carriers generated in the detector by the incoming radiation can be small. The charge created by a MIP is statistic, and in a 300 µm thick silicon sensor, the most probable charge created by a MIP is of about 22000 electrons [Alv04]. Amplification of the induced signal in a semiconductor detector is thus crucial to build a complete detecting system. Pre-amplification and shaping of the signal are necessary before any further signal treatment can be made. The signal generated from the detector is normally fed into either a charge sensitive amplifier or a current sensitive amplifier [Gat86]. A voltage pulse is created at the output of the pre-amplifier by the current (charge) induced on the detector electrode. The signal shape can be varied by using a further pre-amplification stage referred to as pulse shaping stage. At the output of this readout chain a voltage pulse V_{OUT} is thus created, the parameters of the pulse (height and width) depending on the charge or current induced on the detector electrodes. Final pulse processing and analysis electronics can then be performed.

Requirements for the electronic readout for High Energy Physics experiments are challenging. Low noise, low power, high speed, large dynamic range, high reliability, radiation hardness and low cost are usually required. However, the optimization of the readout electronics for one of the previously cited characteristic will always be detrimental to other of the cited characteristics of the circuit. Detail description of the pre-amplification stage and of technologies used in High Energy Physics will be presented in Chapter 3, illustrating the fact that a trade-off has to be defined between the different circuit characteristics. The detection chain is presented in Figure 1.6.

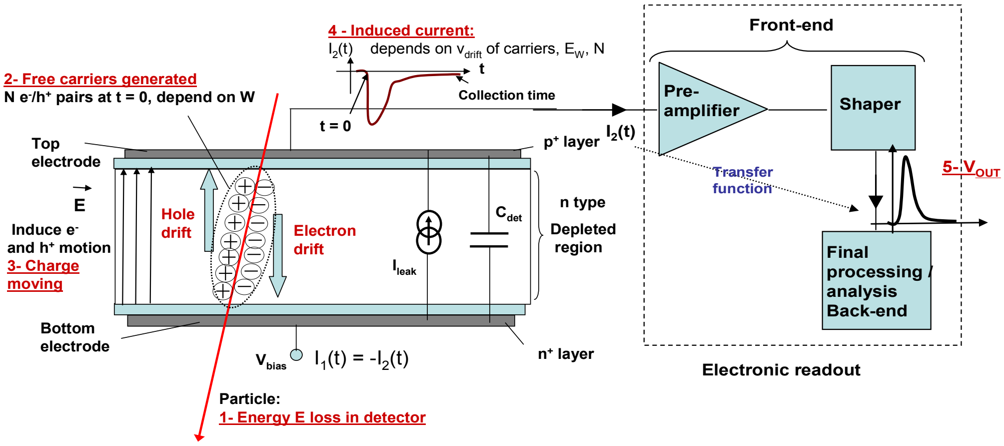

Figure 1.6. Diagram representing the relation from the energy deposited by an incoming radiation to the output signal V_{OUT} readout.

1.2. Semiconductor detecting devices for High Energy Physics

Different types of silicon detectors based on reverse biased p-n junctions will be used in the innermost regions of the LHC detectors for tracking, i.e. for measuring the position and time of passage of particles without disturbing their track. Two of the different detector types are presented in 1.2.1, silicon strip detectors and hybrid pixel detectors. The presentation is restricted to these two types as the detector technology presented in the thesis has been studied both for a pixel and for a strip segmentation of the detector. More recent detector technologies are then presented in 1.2.2.

1.2.1 Silicon strip detectors and hybrid pixel detectors

Silicon presents different advantages for tracking applications in high energy physics experiments. Its low bandgap of 1.12 eV leads to a low mean electron-hole pair creation energy of 3.6 eV. It permits a high conversion of the incident radiation energy into the creation of free carriers while the bandgap is still high enough to avoid a too high leakage current from thermal generation. Detectors have a thickness ranging from 100 to 500 µm and are operated with reverse voltages in the order of 100 V. High mobilities of electrons (μ_e = 1350 cm^2/(V·s)) and holes (μ_h =450 cm^2/(V·s)) lead to a fast charge collection (in a time < 10 ns). Silicon detectors also permit to achieve very good spatial resolution (as it will be presented for micro-strip detectors), and benefit from a high number of industrial technologies that have been developed by the microelectronics industry. Standard photolithographic processes allow the segmentation of the detecting area of one silicon crystal into millions of diodes. These diodes are readout separately in order to obtain the spatial information about the trajectory of the detected particle. Finally, state-of-the art detectors can survive 10 years of LHC operation at few centimeters from collision points, where an accumulated dose of about 500 kGy is expected [Wer05, Gro05].

The presentation of silicon detectors is restricted in this section to 2 types used in the tracking detectors at CERN, i.e. micro-strip and hybrid-pixel detectors.

A schematic of the structure of a Silicon Strip Detector (SSD) is presented in Figure 1.7. The detector is a thin (usually about 300 µm) silicon substrate with a resistivity of about 2 kΩ·cm and lightly n-doped ($N_D \approx 2\times10^{12}$ cm^{-3}). Thin and long p$^+$ strips are implanted to form the detecting diode structures. Each strip is connected to a dedicated channel on a readout integrated circuit through a wire bond connection. The detector strips can have a pitch from 50 µm to some hundreds of microns and a length up to several centimeters. This structure provides only one dimension tracking information so that several layers of tilted micro-strip detectors can be used to overcome this problem. Another technique is to use double sided strip detectors.

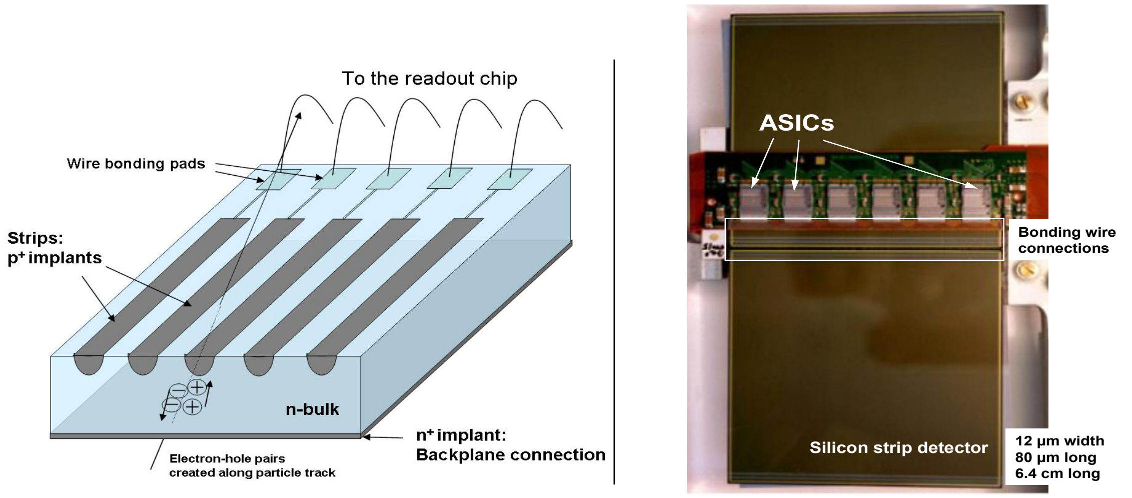

Figure 1.7. Left: Schematic representation of a single sided micro-strip silicon detector. Right: Picture of a Silicon Strip Detector module built for the ATLAS experiment at CERN (ATLAS SCT Barrel module) [Kap04].

A pixel particle detector consists in a matrix of contiguous particle sensing elements with dimensions between ~ 50 µm and ~ 500 µm, each sensing element being connected to an individual processing chain. The readout architecture permits to the user to obtain a bi-dimensional pattern of the particle hit position at each chosen timeframe, even at an interaction frequency in the MHz range.

Hybrid silicon pixel detectors will be used in the tracking detectors at LHC [Wer05]. This technology consists in the separate design of the silicon sensor (and sensing pixels) and of the readout chip. Each readout channel is then connected to its corresponding detecting element of the silicon sensor through a microscopic metallic ball, usually with a diameter of about 20 µm, as shown in Figure 1.8.

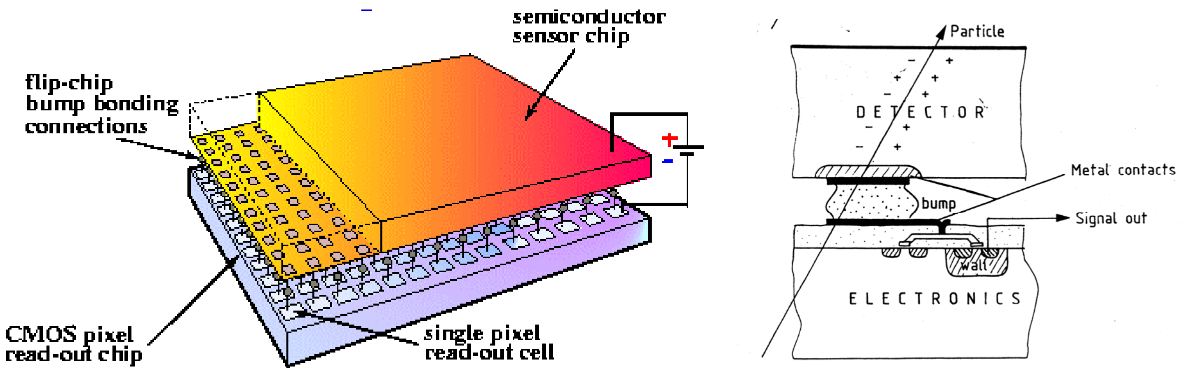

Figure 1.8. Left: Schematic three-dimensional representation of a hybrid pixel detector and of the bump-bonding process [MED]. Right: Schematic cross-section of a single pixel showing the connection through the bump-bond.

This process is called flip-chip bump-bonding and permits separate optimizations of the sensor and of the readout chip, and allows the connection to the readout chip of different sensors. All the electronics has to fit in an area similar to the area of the sensor pixel, and has to be replicated thousands of times, so that several major constraints have to be fulfilled by the designer in terms of complexity of the design and power consumption.

1.2.2. Recent detector technologies

Recently different alternatives to the standard silicon detectors have been presented and are currently under development [Wer05]. Two of them are presented here. Monolithic Active Pixel Sensor (MAPS) are described to illustrate the monolithic detector concept, in which the electronic readout and the radiation detecting sensor are one entity, i.e. integrated onto the same substrate. The 3D detector concept is also introduced as it appears as a promising novel silicon pixel detector technology.

Monolithic pixel detectors are thinner but more robust devices than hybrid pixel detectors. They also permit to avoid the bump-bonding process and leads to smaller parasitic capacitances at the pre-amplifier input, reducing the whole system noise (see Chapter 3). Monolithic Active Pixel Sensors (MAPS) have been developed using standard CMOS technologies and have been successfully tested for particle detection [Dep02, Gay05]. A pixel contains few MOS transistors and a photodiode (Figure 1.9). The active volume of the pixel is defined as the thin undepleted layer which lies underneath the electronic readout and the diode. Free charge carriers generated in this volume are collected, mainly through thermal diffusion, by the photodiode which forms a potential-well attracting electrons (Figure 1.9). Applications of these devices to eventual future LHC experiments are however restricted by the challenging speed requirements of the applications.

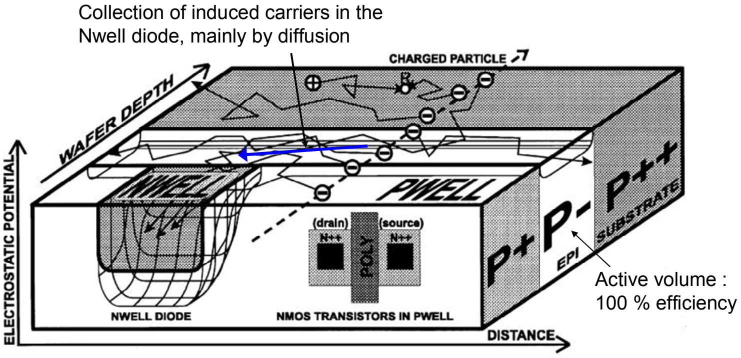
Collection of induced carriers in the Nwell diode, mainly by diffusion

Active volume : 100 % efficiency

Figure 1.9. Schematic representation of a pixel of a Monolithic Active Pixel Sensor for charged particle tracking. Electrons generated by the incoming radiation are connected in the n-well diode [Tur01].

A promising silicon detector device has been proposed and studied by Parker and collaborators [Par97]. The detecting device presents a unique geometry with n-doped and p-doped vertical columnar electrodes penetrating through the entire substrate. A further n-doped electrode can be built all around the detector allowing a so-called “active edge” of the detector. Small distances between the electrodes can be achieved with this technique, of about 50 to 100 µm. This results in very low full depletion voltage (about 15 V for a 50 µm pitch) and very short collection time. Full signal formation in a time of about 1 to 2 ns has been demonstrated [Kok05]. A drawback of the columnar electrodes is the dead regions they induce (at each electrode location, the detector will not be sensitive to ionizing radiation). However, a very interesting property of the presented geometry is the n^+ surrounding electrode which renders the detector "edgeless", i.e. that the detector does not present a dead area at its edges as it is the case in standard planar silicon geometries. The reduction of the distance between electrodes in comparison to standard planar technologies permits to lower the length generated carriers have to drift, resulting in a higher radiation resistance (the length carriers can travel before being trapped will be greater than the inter-electrode distance up to a higher radiation level than for standard silicon detectors). Moreover, this reduction leads to lower depletion voltage, so that even after irradiation full depletion is still possible with reasonable biasing voltages [DaV03].

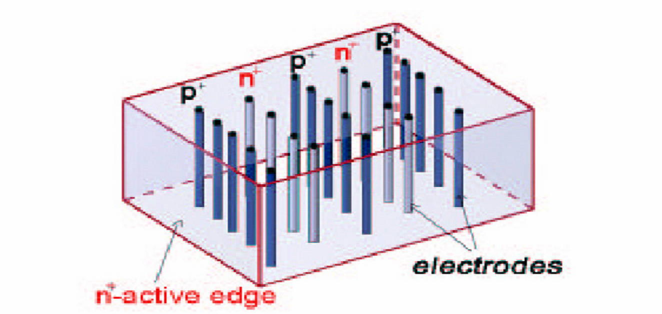

Figure 1.10. Structure of 3D detector with electrodes penetrating through the entire substrate with a surrounding n^+ electrode, allowing edgeless capability.

1.3. Conclusions

The different concepts and mechanisms describing radiation detection with semiconductor detectors have been presented in this chapter in order to provide the basis for further understanding of the characterizations presented in the thesis.

The thesis work performed on a novel detection technology follows the research on alternative solutions to silicon detectors. Although the LHC is not yet in function, studies on the physics potential and on the experimental challenges for an upgrade of the LHC to a ten times higher luminosity (Super-LHC or SLHC, proposed luminosity at about 10^{35} $cm^{-2}\cdot s^{-1}$) have been performed [Gia05]. A clear need of intensive research and development has been identified for the detectors in order to match the more stringent and challenging requirements of SLHC [Mol05]. State-of-the art silicon detectors that will be used for the LHC will not be able to survive the harsh radiation environment of S-LHC where a fluence of about 10^{16} hadrons/cm^2 is expected for the tracking detectors for a 5 years operation. Moreover, the necessary increased statistics will be obtained not only by increasing the luminosity but also by reducing the time between consecutive collisions to possibly half of the LHC one (down to about 12 ns). The CERN RD50 collaboration "development of radiation hard semiconductor devices for very high luminosity colliders" started in 2002 to study and develop detecting devices that will fulfill the required high spatial and timing resolution and radiation hardness of the S-LHC. The different strategies include material engineering with the development of defect engineered silicon with improved radiation hardness (such as Czochralski, epitaxial and oxygen-enriched silicon), different research on "new materials" (such as Silicon Carbide and Gallium Nitride), and development and production of 3D and semi-3D detectors.

The performance and limitations of detectors based on a novel technology which involves hydrogenated amorphous silicon detecting material have been studied during this thesis work in order to investigate the potential of the technology for future High Energy Physics experiments. The thesis work thus presents an important contribution to the research work started on "new materials" for radiation hard semiconductor detectors [Sel06]. This development is also of valuable interest for different other radiation detection applications.

2. Hydrogenated Amorphous Silicon and Thin Film on ASIC technology

In nature a small fraction of the inorganic solids can be found in the amorphous state, as obsidian and some other volcanic materials. However, since the time of the Babylonians and of the ancient Egyptians, man has extensively prepared and used amorphous solids such as glass. Most classes of materials can be prepared in the amorphous state and in the past decades amorphous semiconductors or amorphous metals have gained a lot of attention. Hydrogenated amorphous silicon (a-Si:H) is a tetrahedrally bonded amorphous semiconductor. It has been widely studied in the past 30 years, leading to a present coherent physical picture, with many novel aspects unique to the amorphous phase. However many controversial issues still abound. Section 2.1 gives an overview of the specific characteristics and properties of a-Si:H. Since its first application as a solar cell reported by Carlson and Wronski in 1976 [Car76], a-Si:H has been growing rapidly and is nowadays a widely used material for different applications, some of which are presented in section 2.2. Properties of the deposition techniques of a-Si:H render this material attractive and permit the development of novel techniques of detection. Recently, a novel detection technology based on the deposition of an a-Si:H sensor directly on top of an ASIC has gained a lot of attention. The work presented in this thesis focuses on the study of the potential of this novel technology for particle detection. The technology, called Thin Film on ASIC (TFA), is presented in section 2.3, together with some properties of an a-Si:H sensor for particle detection. Finally, advantages but also challenges involved with the development of a particle detector based on the TFA technology will be presented.

2.1. Hydrogenated amorphous silicon

Amorphous solids are non-crystalline solids: there is no long-range order in the arrangement of atoms, in contrast with the periodic array of atoms for crystalline solids. Still, the amorphous network holds a short range order when considering an atom and its first nearest neighbors. Amorphous semiconductors are classified into chalcogenide glasses (such as Selenium), and tetrahedrally-bonded amorphous semiconductors (such as Silicon and Germanium). Chalcogenides were first studied, in the 1950s, thanks to their early applications in xerography. Hydrogenated amorphous silicon (a-Si:H) thin films were first deposited by Chittick [Chi69] in the late 1960s followed by the report of the first substitutional n-type or p-type doping [Spe75] and the demonstration of the defect passivation by hydrogen [Fri77]. a-Si:H device research was started by Carlson and Wronski [Car76] with the development of photovoltaic devices, and led to considerable efforts in the study of the amorphous structure and of its unique properties. a-Si:H short range order and long range disorder are presented in 2.1.1. The electronic states and the existence of a mobility gap, of band tails, and of defect states are presented in 2.1.2. These states induce specific electronic transport properties, which are discussed in 2.1.3. Finally, the recombination processes and the optical absorption properties of a-Si:H are presented in 2.1.4 and 2.1.5.

2.1.1. Order in the disorder

Hydrogenated amorphous silicon is a tetrahedrally bonded amorphous semiconductor. While it does not show the regular and periodic structure of crystalline silicon, it is not totally random. Amorphous silicon presents covalent bonds between the silicon atoms that are much the same as its crystalline counterpart. The presence of short range order is best illustrated with X-ray, neutron, or electron diffraction measurements. A mathematical analysis of the diffraction patterns leads to the definition of the so-called Radial Distribution Function (RDF) [Laa99]. The RDF G(r) represents the number of atoms lying at a distance r from the center of a reference atom, and is expressed as $G(r) = 4 \pi r^2 g(r)$ [Laa99]. The function g(r) is called the atomic pair correlation function and gives the density of atoms lying at distances between r and r+dr of the reference atom. For a crystal, g(r) consists of sharp peaks (Figure 2.1 left) located respectively at the first-neighbor distance, second-neighbor distance and so on (a perfect crystal is completely ordered to large pair distances). In contrast, for amorphous silicon (Figure 2.1 right) the first few nearest neighbor distances are well separated but the peaks become broader and less distinct with increasing r.

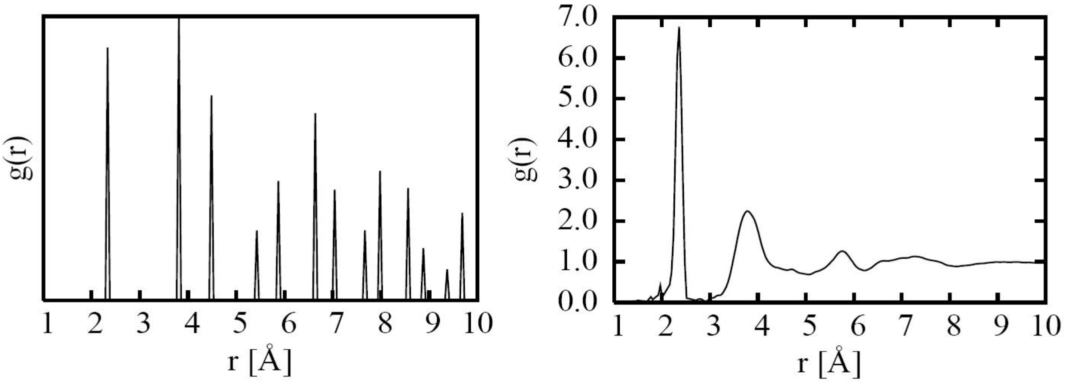

Figure 2.1. Atomic pair correlation function g(r) for crystalline silicon (left), obtained from a computer generated crystal structure and for amorphous silicon (right), obtained via X-ray diffraction [Laa99].

The positions of the first and second peaks are an estimate of the average first-neighbor and second-neighbor distances. From these distances and the width of the two first peaks it has been stated that the average Si-Si bond length in amorphous silicon is equal to that of crystalline silicon, i.e. 2.35 Å, and that the Si-Si-Si average angle equals 109°28’, with a mean variation of 8 to 10°. At larger distances, g(r) and the RDF tend to a constant value, indicating long range disorder.

Amorphous materials can however have order over length scales longer than those proposed by the X-ray, electron or neutron diffraction patterns, these methods being insensitive to the material "medium-range" order. Recently, measurements using a novel microscopy method, presented in [Gib97], have shown that the structure of amorphous semiconductors presents also a medium range order (MRO), linked with the correlation between atom positions in the range of one to a few nanometers [Das03]. Different models are nowadays developed to explain the MRO [Pop02] in the amorphous structure.

It is difficult to determine the structure of amorphous silicon through experiments only, because of the broadening of the diffraction patterns and because of the long range disorder. The modeling of amorphous networks by theorists thus provides an important basis to determine the structure. Comparison of RDF obtained experimentally and theoretically permits the estimation of accurate models. Zachariasen [Zac32] first proposed in 1932 a Continuous Random Network (CRN) to explain the atomic arrangement in an amorphous network. In this network, the atomic structure is determined by the bonds between the atoms, the coordination of an atom being defined as the number of atoms it is bonded to. The model introduces a homogeneous disorder which is on average the same for each atom. The random network has the property of easily incorporating atoms of different coordination, and elementary defects are defined as coordination defects, when an atom has too many or too few bonds. The Si-Si bonding distortion present in amorphous silicon induces bond strains which can result in broken Si-Si bonds, forming the so-called dangling bonds, and leaving the two silicon atoms with a coordination of 3. The dangling bonds are in high concentration in pure amorphous silicon, but they can almost all be passivated by hydrogen (Figure 2.2).

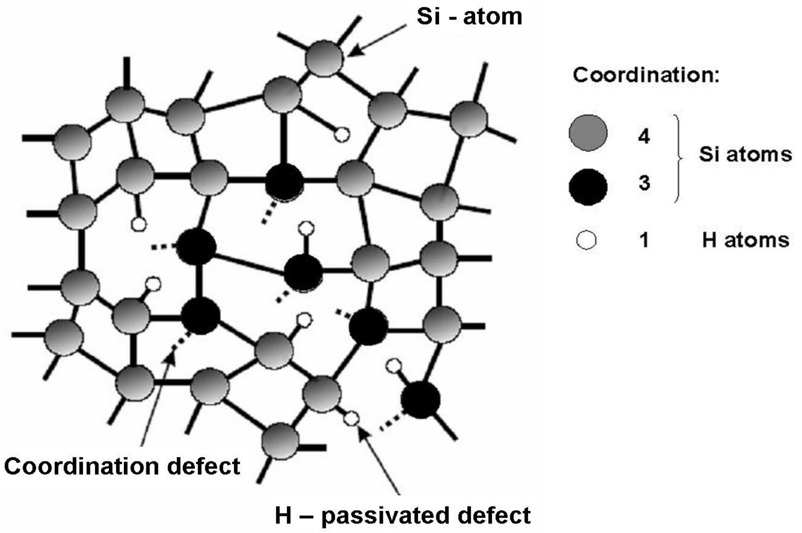

Figure 2.2. A Continuous Random Network (CRN) model of a-Si:H with silicon atoms 3-fold or 4-fold coordinated, dangling bonds (coordination defects) and hydrogen atoms.

Another feature of a-Si:H is that it is not a homogeneous material. Its structure consists of voids embedded in an amorphous matrix [Mos69, Van92]. The size and the density of voids depend on the deposition conditions. A poor-quality material can have a void fraction around 20 %, while a device quality a-Si:H has been shown to contain fewer voids, ~ 1 %, with a diameter of ~ 10 Å [Van92]. Surfaces of voids may partly be covered with hydrogen, and the influence of the voids on the defect density in a-Si:H is still a subject of much debate. The density of a-Si:H is then slightly lower than that of crystalline silicon, and for good quality a-Si:H it is ~ 2.15 g/cm^3.

Many computer generated amorphous networks have been developed, and the sizes of the networks that can be handled nowadays are simulation cells with a few tens of thousand of atoms. Different techniques are used to simulate amorphous silicon network. The most successful algorithm to perform simulations through a Monte Carlo technique is the www technique proposed by Wooten, Winer and Weaire [Woo85]. Challenges in the near future are the generation of realistic device size atomic networks, and simulations of an entire electronic device at the atomic level.

2.1.2. Electronic states

In crystalline silicon, the periodicity of the lattice greatly simplifies the theory for the electronic properties. The periodic potential energy arising from the atomic structure of ordered crystals leads to Bloch's solutions of the Schrödinger equation [Sze81]. Electrons and holes are described by wave functions extended through the entire crystal, with a well defined momentum k. The energy bands are then described by energy-momentum dispersion relations E(k). In amorphous silicon, the potential energy is not periodic. Bloch's solutions for the wave functions cannot be applied, and the potential fluctuations result in the strong scattering of electrons and in an uncertainty in k similar to its magnitude [Str91]. There is a need for a different theoretical approach to represent the electronic properties of amorphous silicon: the description is developed from the chemical bonding between the atoms and the energy bands are described by the density of states distribution N(E).

An isolated silicon atom presents the electronic configuration [1s^2 2s^2 2p^6 3s^2 3p^2]. Four valence electrons occupy the two 3s and the two 3p states. When the atoms combine to form a silicon network, the electron interaction splits these valence states into bonding and anti-bonding levels. Bonds between adjacent atoms are formed by the hybridization of an atom valence 3s orbital and an atom 3p orbital. The valence electrons of an atom are then located in 4 hybridized sp^3 orbitals, corresponding to the 4 bonds to the neighboring atoms (Figure 2.3). The band gap separating the occupied valence band from the empty conduction band states can be equivalently described by the splitting of the bonding and anti-bonding states of the covalent bond. The bonding states have the lowest energy and are usually occupied, while the anti-bonding states are empty. The band gap appears without considering the periodicity of the network, and holds even for amorphous semiconductors [Wea71], resulting in overall global similarities between the electronic properties of crystalline and amorphous silicon.

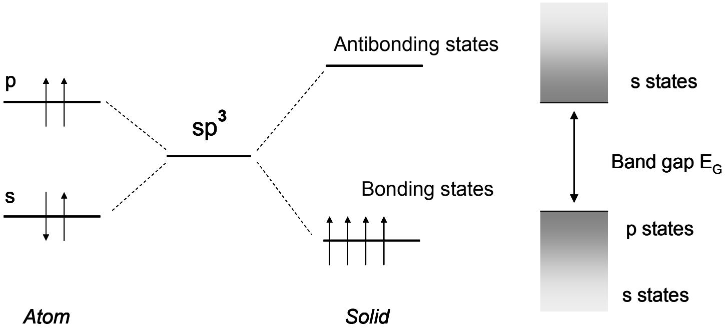

Figure 2.3. Schematic diagram of the energy levels of atomic orbitals, hybridized orbitals and bands for a tetrahedrally bonded semiconductor.

However, a feature of amorphous silicon bonding structure is the fluctuation in the bond length, in the bond angle and in the dihedral angle in Si-Si bonds. These spatial fluctuations create weak bonds, whose bonding energy is weaker than that of normal bonds. These bonds are also called stretched or strained bonds. The induced energy states are well separated in the lattice site, so that the tunneling probability between these sites becomes small and so that the associated states become localized. The spatial fluctuations thus induce localized energy states, for which no conduction is expected to occur when excited electrons occupy them. The extended states corresponding to the fully coordinated covalent bonds are delocalized, and transitions from one state to another are easy. The boundaries between the defined localized states and the extended states of the valence and conduction bands are called the mobility edges (E_C and E_V), and the region between these two energies defines the gap called the mobility gap. The localized states originating from spatial bonding fluctuations create so-called band tails in the mobility gap (Figure 2.4).

The mobility edges suggest an abrupt transition between localized states and delocalized states at the band edges E_C and E_V. However, the gradually decreasing densities of states from extended states to localized states suggest that localization of the electron wave function varies continuously as we move from extended states to states deep in the gap. The exact behavior of the properties of states near the mobility edges, and the localized to extended transition are still nowadays not fully understood and characterized, but for practical purposes, the conduction of a-Si:H films can well be described in terms of the mobility gap. The mobility gap of a-Si:H is different from its crystalline counterpart, and at 300 K, E_g =1.6 eV to 1.8 eV. The band tails in the density of state distribution can be approximated by exponential functions:

$$N(E) = N_0 \exp(-E/kT_v) \qquad (2.1).$$

The slope of the tail is described by the characteristic temperature T_V. For amorphous silicon, this temperature ranges from 220 K to 270 K ($kT_V \sim 25$ meV) for the conduction band tail and from 400 K to 450 K ($kT_V \sim 45$ meV) for the valence band tail [Str91]. There is no symmetry between the valence band tail and the conduction band tail. The conduction band edge is made up of s-like states which are less sensitive to the bond angle disorder than the p-like bonding states at the top of the valence band (Figure 2.3), so that the valence band tail has more states than the conduction band tail.

Some atoms in amorphous silicon also have deviations from their optimal coordination which result into coordination defects, and lead to electronic states deep within the band gap. These intrinsic defects and the induced localized states are presented in the following. The electronic structure of an amorphous semiconductor thus comprises the bands, the localized states in the band tails and the coordination defect states in the gap, as illustrated in Figure 2.4.

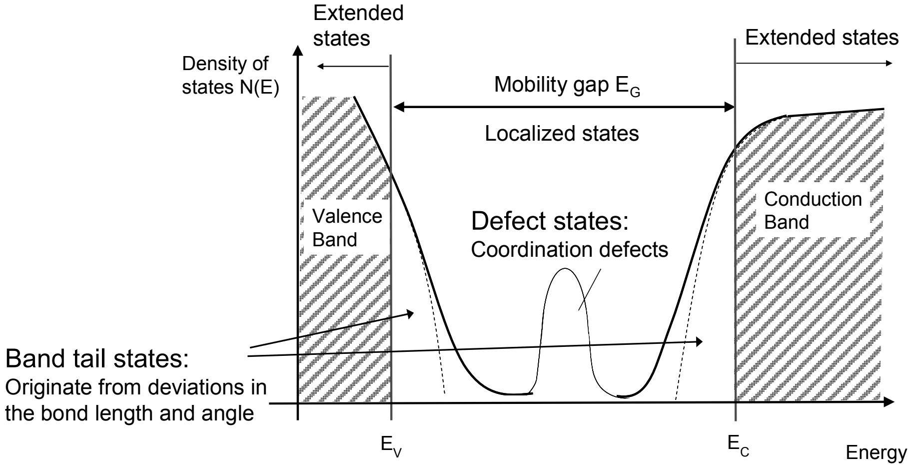

Figure 2.4. Schematic diagram of the density of states distribution for a-Si:H.

Intrinsic Defects

Some localized states are present in the middle of the mobility gap, attributed to defects in the a-Si:H structure. Contrary to crystalline silicon, any impurity in an amorphous semiconductor which is bonded with its optimum valency is expected to form a part of the continuous random network, and contributes only to the conduction and valence bands. Oxygen, nitrogen or carbon all behave in this way forming alloys with a-Si:H. For amorphous semiconductors, defects are coordination defects, when an atom has too many or too few bonds. There are few classes of defects in a-Si:H, but their energy levels are broadened out by the disorder. It is generally proposed that the most prominent intrinsic defect is the unsaturated bond, called the dangling bond or T_3 center. It corresponds to a 3-fold coordinated silicon atom and results from broken Si-Si strained bonds. Some works proved the importance of five fold coordinated defects, called the floating bond or T_5 center [Pan86, Kel88]. The dominant defect type is still a controversial issue but it has been stated that both T_3 and T_5 defects are present, that they induce states in the middle of the gap, and that they can be passivated by hydrogen [Per00]. The total defect density can be as large as 10^{19} cm^{-3} in amorphous silicon. A high reduction of the defect density is obtained by adding hydrogen (Figure 2.2), and for hydrogenated amorphous silicon with a hydrogen concentration C_H of 10 atomic %, the defect density can be about 10^{15} cm^{-3}.

The remaining dangling bond defects D have an amphoteric character: they can be neutral (D^0) with single electron occupancy, empty and positively charged (D^+), or negatively charged (D^-) with double electron occupancy. D^- defects have 2 electrons localized in a dangling bond. The two electrons repel each other with a Coulomb interaction, and hence the energy level of D^- states is raised by the energy U called the correlation energy (Figure 2.5). Hydrogenated amorphous silicon correlation energy U is assumed to be constant and between 0.2 and 0.4 eV [Str91]. Statistical considerations, similar to those made to derive the Fermi-Dirac function, permit to obtain the occupation functions of the 3 possible states of charge of the dangling bonds, namely f_{db}^+, f_{db}^0 and f_{db}^-, illustrated in Figure 2.5 [Vai86], where E_r corresponds to the D^0 dangling bond energy state.
All existing defect models assume a Gaussian energy distribution of deep defects, and the occupation of the 3 possible charge states of the dangling bond, so the central energy of the Gaussian, depends on the Fermi level E_F.

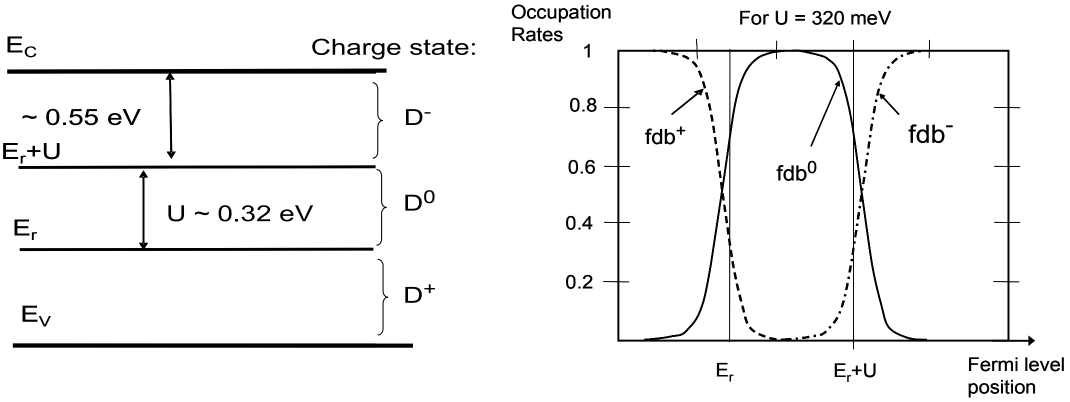

Figure 2.5. Left: Band diagram with energy levels of neutral, negatively and positively charged dangling bonds. Right: Dangling bond occupation functions [Vai86].

For a p-doped material, almost all dangling bonds are unoccupied (D^+). For a non doped material, the dangling bonds are in majority occupied by one electron (D^0). In both cases the density of state is a Gaussian distribution centered at E_r. For n-doped material, the dangling bonds are in majority occupied by two electrons. The density of state is a Gaussian distribution centered at E_r+U.

The dangling bond state occupancy depends on the position of the Fermi level, and on the doping type of a-Si:H. It has however been discussed before that impurity atoms can be incorporated in the continuous random network with their optimal coordination. This would lead to an impossibility of doping a-Si:H, as boron (B) or phosphorus (P) are 3-fold coordinated in their lowest energy configuration. However the 4-fold doping configuration of B or P, although of higher energy, may be low enough in energy to be present in reasonable concentrations. Part of the doping B or P atoms are integrated in the continuous random network in a 3-fold configuration, and part of the atoms are ionized and present as P^+ (n-type doping) or B^- (p-type doping) in a 4-fold doping configuration. One can consider a charged impurity: a positively charged phosphorus atom P_4^+ contains only four electrons instead of the usual five, and so its ideal bonding configuration is with a coordination of 4. We have to consider ionized donors, and compensating defects taking up the excess charge. This corresponds to the thermo-dynamical explanation [Str91] based on the equilibrium between Phosphorus ideally incorporated P_3 with 4-fold coordinated silicon Si_4 on one side, and active Phosphorus P_4^+ with a double occupied defect D^- on the other side (Figure 2.6). This creation of dangling bond tends to shift the Fermi level and to permit doping of a-Si:H. The doping efficiency (the rate between the concentration of active doping atoms and the total concentration of doping atoms) decreases with the square root of the total concentration of doping atoms, so that the Fermi level cannot be moved too close to the bands.

$$P_3 + Si_4 \leftrightarrow P_4^+ + Si_3 + D^- \qquad (2.2).$$

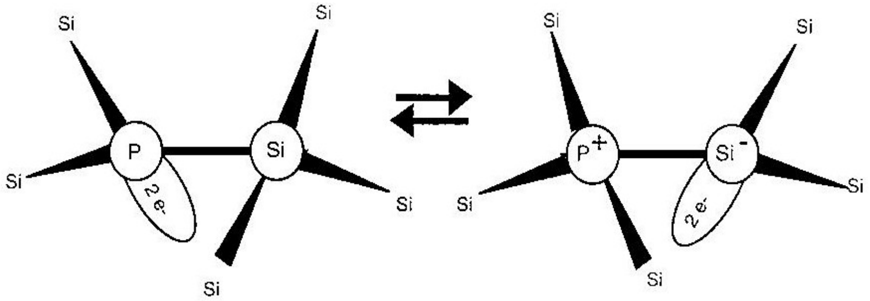

Figure 2.6. Thermodynamic equilibrium of Phosphorus incorporated in a-Si:H. Doping induces deep defects by the creation of a doubly occupied dangling bond [Sha95].

An important drawback of a-Si:H is its intrinsic metastability. Its density of defects is not fixed after the deposition, and different external perturbations can lead to a new equilibrium. Upon light exposure, the density of dangling bonds N_{db} increases, leading to a degradation of the electronic properties [Sta77]. The degradation of amorphous silicon upon light exposure is called the Staebler-Wronski effect (SWE). The induced defects are metastable as they can be removed by annealing the material at high temperatures for some hours. Despite the intensive study of light induced metastable changes in a-Si:H, a generally accepted microscopical model of the Staebler-Wronski effect has not been found yet. However, it is agreed that the hydrogen concentration, its bonding structure to the silicon network, and the disorder in the silicon network together affect the Staebler-Wronski effect. The amount of hydrogen bound to silicon in the dilute phase determines the saturated density of metastable defects. Branz recently proposed the hydrogen collision model [Bra98]: the defect-creating recombination takes place at a Si-H bond, and the recombination energy is used to lift the hydrogen to a mobile energy level. The mobile hydrogen atom diffuses interstitially through the material, and is represented by a mobile complex of a Si-H bond and a dangling bond. If two mobile hydrogen complexes collide, an immobile metastable two-hydrogen complex is formed. The net result is that two dangling bonds are created that are not spatially correlated to hydrogen atoms.

2.1.3. Electronic transport

The electronic transport in an amorphous semiconductor is a macroscopic quantity that represents an average property of the carriers as they move from site to site. The conductivity in semiconductors is the product of the carrier density n, the carrier mobility μ and the elementary charge e. The contributions to the conductivity can be summed over the density of states and:

$$\sigma = \int N(E)\, e\, \mu(E)\, f(E,T)\, dE \qquad (2.3);$$

where f(E,T) is the Fermi-Dirac distribution. If we consider the electron case, and if E_C is far above E_F, then non-degenerate Boltzmann statistics can be applied and:

$$\sigma = \frac{1}{kT} \int \sigma(E) \exp[-\frac{(E-E_F)}{kT}]\, dE \qquad (2.4);$$

where $$\sigma(E) = N(E)\, e\, \mu(E)\, k\, T \qquad (2.5).$$

The distinction between localized and extended electronic state properties is a fundamental concept in the study of the electronic transport in a-Si:H. The early model of conductivity in amorphous silicon considered that at 0 K the mobility of electrons and holes is nil in the localized states and that the conductivity takes place only in the extended states [Mot79]. Sharp mobility edges were considered, separating the localized states of the band tails from the de-localized states of the valence and conduction bands. The model proposes that the conductivity drops discontinuously to zero at the mobility edges. However, the "scaling" theory of localization [Abr79] proves that for disordered systems the transition from localization to de-localization, called the Anderson transition, is continuous at the mobility edge and that the conductivity goes continuously to zero at E_C. Inelastic scattering of the carriers and phonon-induced de-localization at the mobility edge [Fen85] are other mechanisms occurring around the mobility edge, which are not integrated nowadays into a global theory of conductivity.

Even though it is not a totally correct theory, the models still preferably rely on sharp mobility edges that separate extended states from localized states. The calculation of the conductivity in a-Si:H first involves the high band like conductivity in the extended states, called the standard transport model. The tunneling or hopping conductivity in the localized states has also to be taken into account. Finally, the transport is governed by multiple trapping processes occurring at the localized states, which lead to a dispersive transport.

Standard transport model

The standard transport model is based on the early theory of sharp mobility edges described by Mott. For this particular case and for activation energy E_A (which is E_C - E_F for the conduction band and E_F - E_V for the valence band), the conductivity can be calculated from equation (2.4) and exhibits an "activation-type" temperature dependence:

$$\sigma(T) = \sigma_0 \exp[-E_A/(k_B T)] \qquad (2.6).$$

The pre-exponential factor σ_0 correlates empirically with the activation energy as:

$$\ln(\sigma_0) = \ln(\sigma_{00}) + E_A/(k_B T_{MN}) \qquad (2.7).$$

This correlation equation (equation 2.7) may originate from statistical shifts of the Fermi energy [Ove89]. It is similar to the Meyer-Neldel Rule (MNR) known to be applicable to various activated phenomena [Mey37]. Recently, it has been shown that this Meyer-Neldel relation is expected to describe the conduction of materials which exhibit traps distributed exponentially in energy, as it is the case in a-Si:H (or organic semiconductors) [Sta05]. The factor σ_{00} is a constant value of about 0.1 $\Omega^{-1}\cdot cm^{-1}$, and $k_B T_{MN}$ is referred to as the Meyer-Neldel characteristic energy. The Meyer-Neldel temperature T_{MN}, also called isokinetic temperature [Sta05], equals about 450 K for electrons and 800 K for holes [Ham97]. Even if it is not a precise description, the standard transport model is an adequate model to describe the conductivity in a-Si:H at room temperature and above.

Hopping conduction

Anderson localization of electronic states leads to a non conductivity in the localized states at 0 K. However, above 0 K, some transitions between the localized states can occur and carriers can hop from one site to another by tunneling effect. This hopping conduction is more probable between two states that are close in energy and (or) position. The transition probability, p_{hop}, between two states separated by a distance R and an energy W is:

$$p_{hop} = \omega_0 \exp(-2R/R_0 - W/kT) \quad \text{for } W > 0 \qquad (2.8);$$

$$p_{hop} = \omega_0 \exp(-2R/R_0) \quad \text{for } W < 0 \qquad (2.9).$$

R_0 is the localization length, and the factor $\exp(-R/R_0)$ expresses the wave-function overlap of the two states. The hopping conduction can be described by two types of conduction, both illustrated in Figure 2.7. For the nearest neighbor hopping model, carriers hop from one site to its nearest neighbor, and the energy difference between the states is compensated by a phonon. Band tails hopping is of this type, as the localized states can be spatially close, but separated by an energy that can be overcome by electron-phonon coupling. As temperature decreases, the number of phonons will decrease and the probability of hopping in the band tails will also decrease. The conductivity σ_h is expressed in equation (2.10).

$$\sigma_h = \sigma_{ho} \exp(-W/kT) \qquad (2.10);$$

where the pre-factor σ_{h0} is directly proportional to the density of states N(E). For a N(E) of 10^{-19} cm^{-3}, σ_{h0} is in the order of 10^{-1}-10^{-2} Ω^{-1} cm^{-1}, and W is the average energy shift between states. In the variable range hopping model, carriers hop between localized states that are close to the same energy (small W), but spatially more distant than in the nearest neighbor model (higher R). It occurs in the localized states in the middle of the gap induced by the coordination defects. At low temperature, carriers more probably hop to a site which is not the closest, but which has a very close energy level. Mott has calculated the conductivity in this case, and:

$$\sigma_h = \sigma_{ho} \exp(-T_0/T^{1/4}) \qquad (2.11).$$

In amorphous silicon, this variable range hopping conduction has an important contribution to the global conductivity, because of the high defect density. However, in hydrogenated amorphous silicon, the saturation of almost all the dangling bonds leads to relatively small contributions of both hopping conductions, except at low temperatures.

The electron-phonon coupling, representing the interaction connecting the electronic and lattice systems, is responsible for the scattering of electrons. An excess carrier in a localized state polarizes its environment due to the electron-phonon coupling. In the case of a strong electron-phonon interaction, polarons are formed, i.e., electrons dressing phonon clouds, so that electrical conduction takes place by hopping of the polarons. Electron-phonon interaction is weak in amorphous silicon, but can be large around the band edges [Att04] and can affect the conduction at the band-edge [Fen85].

Dispersive transport

The band tail states in hydrogenated amorphous silicon have another fundamental role in the electronic transport. They lead to a dispersive transport, which can be described by a phenomenological trapping model [Tie80]. The conduction of excess carriers actually occurs by frequent trapping in the tail states, followed by thermal reemission into the conducting states. The cycle of trapping, emission, re-trapping, re-emission, etc, occurring during the transport of an excess carrier is termed “multiple trapping” (Figure 2.7). Trapped carriers are considered to be immobile, so that the effective (or “drift”) mobility of the carriers is determined by the mobility μ_0 in the extended states and by the fraction f_{trap} of carriers in the trap states:

$$\mu_d = \mu_0/(1+f_{trap}) \qquad (2.12);$$

$$f_{trap} = n_{trap}/n_c = \tau_{trap}/\tau_{free} \qquad (2.13).$$

n_c is the density of carriers above the transport edges, n_{trap} is the density of carriers trapped below the edges, τ_{trap} is the time spent in the traps and τ_{free} is the time spent in free states. The drift mobility reflects the release time of the trapped carriers.

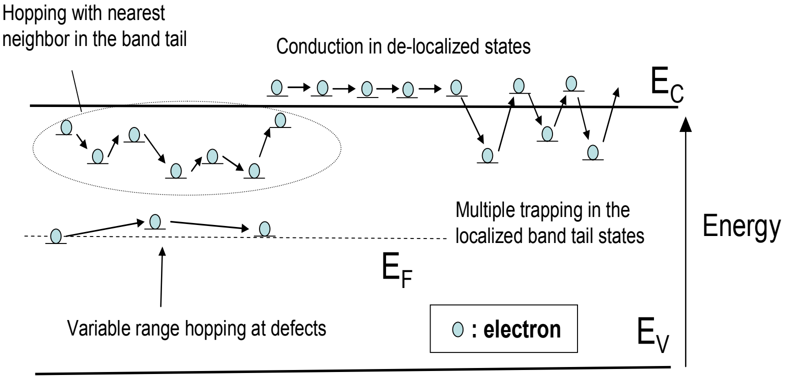

Figure 2.7. Electron conduction mechanism in a-Si:H: conduction in the de-localized states (standard transport model), hopping conduction in the localized states, multiple trapping of carriers in the localized states.

The emission of a carrier from a trap of energy E depends on the activation energy E_A of the trap (which is E_C-E for electrons and E-E_V for holes). The release rate of a carrier by thermal activation is defined by:

$$\tau_{rel}(T) = \omega_0^{-1} \exp[E_A/(k_B T)] \qquad (2.14);$$

where the pre-factor ω_0 is the "attempt-to escape" frequency. This pre-factor has also been shown to correlate with the activation energy E_A following a Meyer-Neldel rule [Bra94] and:

$$\omega_0 = \omega_{00} \exp[E_A/(k_B T_{MN})] \qquad (2.15);$$

The values of ω_{00} found in the literature are in the order of 10^9 s^{-1} for electrons and 10^{10} s^{-1} for holes [Ham97]. The attempt to escape frequency ω_0 thus varies depending on the trap energy, but is usually found in the range 10^{11}-10^{12} s^{-1} [Sch04]. The activation energy of traps might also be varied by the application of high electric fields (Poole-Frenkel effect [Fre38]). This has been observed in a-Si:H [Che94, Ham99] and will be presented and studied in detail in Chapters 4 and 5.

For an exponential distribution of trap energies N(E) (as in the band tails, see equation (2.1)), with a slope kT_V, the drift mobility reflects the average release time of the carriers given by:

$$\tau_{av} = \frac{1}{N_T} \int_0^{\infty} N(E)\, \omega_0^{-1} \exp(E/kT)\, dE = N_0\, \omega_0^{-1} \int_0^{\infty} \exp(-E/kT_V + E/kT)\, dE \qquad (2.16).$$

The resolution of equation (2.16) and the resulting drift mobilities depend on the temperature. At high temperatures, when $T > T_V$ (~ 250 K for electrons and ~ 450 K for holes) equation (2.16) can be solved. The band tail trapping is at elevated temperature a relatively weak effect and the drift mobilities have a modest residual temperature dependence that is fitted adequately by:

$$\mu_d = \mu_0\, (1 - T_V/T) \qquad (2.17).$$

This existing trapping model for high-temperatures is not totally exact as it does not incorporate the temperature dependence of the band tail width (and so T_V), and other theories have been recently proposed [Sch04]. Typical values of free electron mobility at high temperatures are in the range of 5-15 $cm^2\ V^{-1}\ s^{-1}$, and around 1 $cm^2\ V^{-1}\ s^{-1}$ for holes [Sch04]. At low temperatures, equation (2.16) cannot be solved, but T_V and the band tail width are “frozen in”, and a median energy E_m of the traps can be considered. A medium release time can be calculated from E_m using equation (2.14). At low temperatures, free carriers have a highly dispersive transport so that the mobility decreases with time, as the mean carrier distribution falls deeper into localized states through thermalization.

At room temperature, the conduction in a-Si:H is well described by the standard transport model and by the multiple trapping transport caused by the material exponential band tails. Holes are more subject than electrons to multiple trapping in the band tails, because of a higher density of localized states in the valence band tail than in the conduction band tail. The conduction from one extended state to another is also more difficult than in the case of crystalline silicon, and amorphous semiconductors in general do not exhibit as good carrier mobility as their crystalline forms. In a-Si:H and at room temperature, a constant drift mobility of $\underline{1\ \text{to}\ 10\ cm^2\ V^{-1}\ s^{-1}}$ is usually considered for the electrons, and a drift mobility varying in time down to ~ $\underline{0.1\ cm^2\ V^{-1}\ s^{-1}}$ is considered for holes.

2.1.4. Recombination

Radiation can generate excess carriers in a-Si:H, which then populate the conduction and the valence bands. The induced conductivity depends on the trapping in the band tail states, and on the recombination rate.

The carriers excited to the extended states or to the band tails lose energy by non-radiative thermalization process: they suffer small but frequent decrease in energy, the excitation energy being converted into phonons. Carriers in extended states lose energy by the emission of single phonons as they scatter from one state to another, and the thermalization process is very rapid. Between localized states of the band tails, thermalization occurs at low temperatures by direct tunneling, and becomes increasingly slow as the carriers move deeper into the band tail. At higher temperatures (above 200 K for holes and 50 K for electrons [Str91]), the multiple trapping mechanism of sequential excitation and trapping dominates tunneling. The two dominant recombination mechanisms in a-Si:H are radiative transitions between band tail states and non-radiative transitions from band edges to defect states. The different sequential steps of recombination processes are illustrated in Figure 2.8.

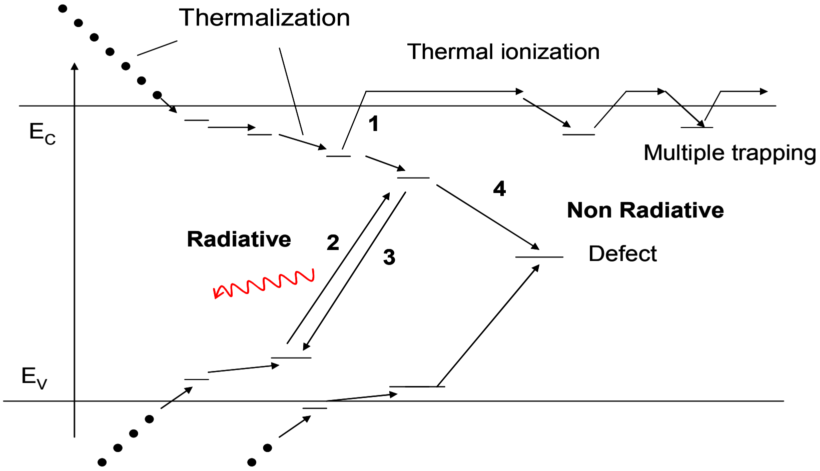

Figure 2.8. Illustration of the electron-hole recombination, showing thermalization of the carriers and different processes. 1: multiple trapping, 2 (3): radiative recombination in a conduction (valence) band tail state; 4: non radiative recombination at a defect state.

The radiative recombination in the tail states tends to dominate at low temperatures (< 100 K). Its transition rate is slow but there is a large density of band tail states at which recombination can occur. As the carrier thermalizes deeper into the band tail states, its probability to be emitted back into the conduction band by thermal excitation decreases, and its probability to capture an electron or a hole increases. An energy level E_{tn} can be defined as a quasi Fermi level for the trapped electrons: the states above this energy preferably act as traps (thermal emission of the electrons is higher), and states below this energy act as recombination centers (capture of a hole is higher) [Sha95]. The same concept can be applied for holes with the definition of E_{tp}.

The radiative tunneling transition rate is low, but there is a large density of band tail states that act as recombination centers at low temperature. The total recombination function in the band tails of the conduction band can be expressed as:

$$R_{btc} = \frac{n_f p_f}{n_f \tau_{pc} + p_f \tau_{nc}} \qquad (2.18);$$

$$1/\tau_{pc} = v_{th}\sigma_p \int_{E_{btc}}^{E_{tn}} N(E)dE \qquad \text{and} \qquad 1/\tau_{nc} = v_{th}\sigma_n \int_{E_{btc}}^{E_{tn}} N(E)dE \qquad (2.19);$$

where n_f (p_f) is the free electrons (holes) density, τ_{nc} (τ_{pc}) is the capture time of electrons (holes) in recombination centers located in the conduction band tail. v_{th} is the thermal speed of the electrons, σ_n (σ_p) the capture cross section of the electrons (holes), and E_{btc} the energy of the bottom of the conduction band tail. The same calculation can be made for electrons and holes captured in the recombination centers located above E_{tp}, leading to the recombination rate R_{btv}.

At temperatures higher than about 100 K, carriers diffuse rapidly from site to site, and the faster transition rate at the defect dominates the recombination. The defect recombination is predominantly non radiative, and strong electron-phonon interaction operates at the deep recombination center. There are four possible trapping transitions of electrons and holes into dangling bond defects. In undoped a-Si:H, the defects are neutral (D^0) and can capture either an electron (resulting in a D^- dangling bond state) or a hole (resulting in a D^+ dangling bond state). In doped a-Si:H, the defects are charged; the negative defect (dominant in n-doped material) can only capture holes, and the positive defect (dominant in p-doped material) can only capture electrons. The four different transitions are shown in Figure 2.9.

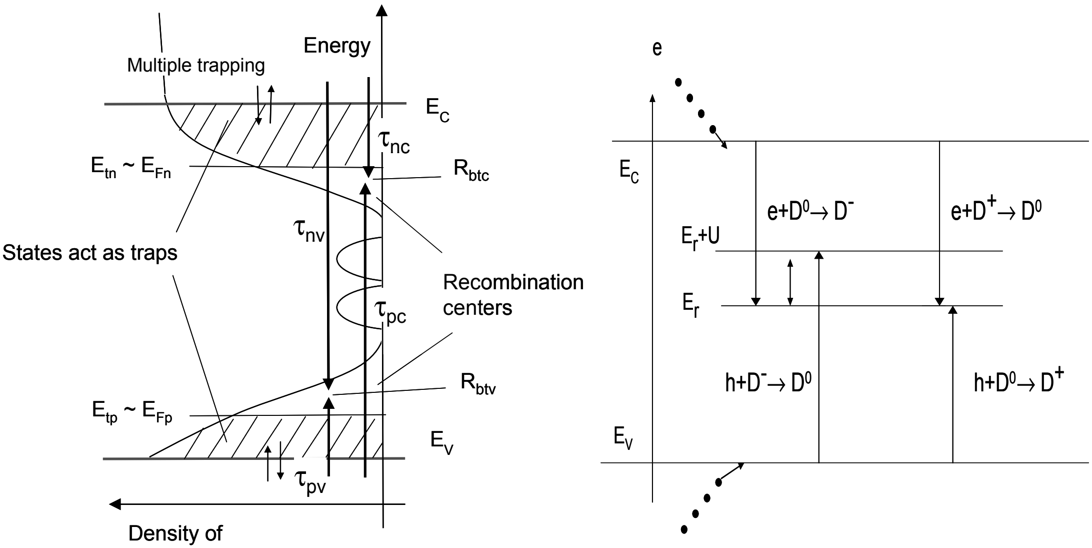

Figure 2.9. Left: Recombination in the band tails. Right: the four possible transitions for holes and electrons to a defect recombination center.

The recombination function can be calculated from the four "mean times to recombination" corresponding to the four possible transitions:

$$\tau_{eD0} = 1/(v_{th}\,\sigma_n^{\,0}\, n_f\, f_{db}^{\,0}\, N_{db}) \quad (2.20); \qquad \tau_{eD+} = 1/(v_{th}\,\sigma_n^{\,+}\, n_f\, f_{db}^{\,+}\, N_{db}) \quad (2.21);$$

$$\tau_{hD0} = 1/(v_{th}\,\sigma_p^{\,0}\, p_f\, f_{db}^{\,0}\, N_{db}) \quad (2.22); \qquad \tau_{hD-} = 1/(v_{th}\,\sigma_p^{\,-}\, p_f\, f_{db}^{\,-}\, N_{db}) \quad (2.23);$$

where σ refers to the capture cross-section of neutral (σ^0), positively (σ_n^+) or negatively (σ_p^-) charged dangling bonds for electrons (n_f) and holes (p_f), and f_{db} are the occupation functions of the 3 dangling bond states (see 2.1.3). In undoped a-Si:H, the recombination function can be simplified as in equation 2.24. For p-doped a-Si:H and n-doped a-Si:H, the recombination can be expressed as in equations 2.25 and 2.26.

$$R_{db} = \frac{n_f}{\tau_{eD0}} + \frac{p_f}{\tau_{pD0}} \quad (2.24); \qquad R_{db} = \frac{p_f}{\tau_{pD-}} \quad (2.25); \qquad R_{db} = \frac{n_f}{\tau_{eD+}} \quad (2.26);$$

2.1.5. Optical absorption

The optical properties of hydrogenated amorphous silicon are of considerable importance for its applications. In amorphous silicon, the disorder leads to an uncertainty in the momentum k that is similar to its magnitude, so that it is no longer a good quantum number and it is not conserved in optical transitions. Therefore, contrary to crystalline silicon, all optical transitions in a-Si:H can be considered as direct. The absorption coefficient for visible light is about an order of magnitude higher for a-Si:H compared to crystalline silicon. Consequently, the typical thickness (sub-µm) of an a-Si:H light sensor is only a fraction of that of a c-Si cell. The spectral sensitivity of a-Si:H matches the response of the human eye, with a peak in the green spectral range. In general, one can divide the absorption behavior in three ranges, as it is represented in Figure 2.10.

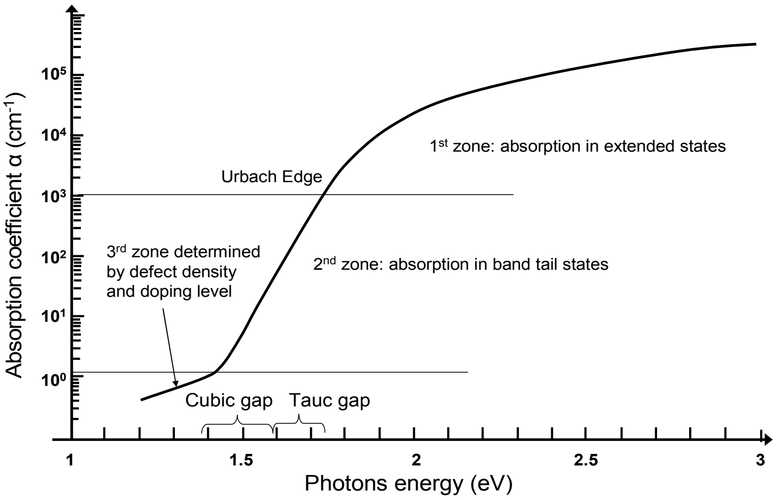

Figure 2.10. Typical example of a-Si:H optical absorption coefficient variations with the incoming photons energy [Sha95].

For a photon with an energy higher than the material "optical" bandgap E_g (of about 1.5 to 1.8 eV), the absorption coefficient is larger than 10^3 cm^{-1} and absorption takes place between extended states. It is described by [Tau72]:

$$\left(\alpha(E)\, n(E)\, E\right)^{1/(1+p+q)} = B\,(\hbar\upsilon - E_g) \qquad (2.27);$$

where $\alpha(E)$ is the energy dependent absorption coefficient, n(E) is the refractive index, p and q are constants related to the shape of the band edges, B is a proportionality constant, and ν is the frequency. Tauc has argued that the density of states near the band edges has a square root dependence on energy, as it is the case for crystalline semiconductors, resulting in p = q = ½ [Tau72]. Thus extrapolating equation (2.27) to $\alpha(E) = 0$ yields the so-called Tauc gap. Klazes [Kla82] has proposed linear band edges, so that p = q = 1. Evaluating the equation (2.27) now yields a so-called cubic gap, which is about 0.1 – 0.2 eV lower than the Tauc gap. This cubic plot is linear in a larger energy range than the Tauc gap, and fitting yields more accurate values. However, the Tauc gap is still widely used, and is for intrinsic a-Si:H typically of 1.7 eV.

For photons with energy smaller than the optical gap of the material, the absorption takes place between states in the band gap. Photons with energy of about 0.2 eV around the Tauc or cubic gap (i.e. from about 1.4 to 1.7 eV) have an absorption coefficient varying from 1-10 to 10^3 cm^{-1}, the absorption taking place between states in the band tails. An exponential dependence of α exists here [Tau72]:

$$\alpha = \alpha_0 \exp(E/E_0) \qquad (2.28);$$

where α_0 is a prefactor, and E_0 is the so-called Urbach energy, which depends both on temperature and on the disorder in the material. It is mainly determined by the slope of the valence band tail, and typically E_0 amounts to 50 meV.

Finally, at low energy ranges (i.e. photons with energy lower than 1.4 eV), the absorption takes place at the defect states. The absorption coefficient is inferior to 1-10 and depends on defect density, doping level, and details of the preparation process.

The optical properties of a-Si:H are influenced both by the hydrogen concentration and bonding in the film, and by the disorder in the a-Si:H network [Mal87].

2.2. a-Si:H device technology

The first practical device using hydrogenated amorphous silicon and demonstrating its interesting photovoltaic properties was the 2.4 % efficient solar cell reported by Carlson and Wronski [Car76] in 1976. Since then, interest in a-Si:H has been growing rapidly and a-Si:H is nowadays a widely used material for different applications. Despite its poor electronic properties compared to that of crystalline silicon, a-Si:H offers the important technical advantage of being deposited inexpensively and uniformely over large areas. Deposition techniques are presented in section 2.2.1. a-Si:H is mainly used in the form of light sensors and Thin Film Transistors (TFT), two structures that are presented in section 2.2.2. Hydrogenated amorphous silicon has already firmly established itself for many large-area electronic devices, such as displays and solar cells. New applications are presently emerging in the field of image sensors, pressure sensors or X-ray imaging detectors, and the deposition on large-areas and on flexible substrate of thin film silicon allows for many novel applications and novel inventions for the future. Different applications are presented in section 2.2.3.

2.2.1. Deposition techniques [Van02]

Amorphous silicon can be deposited from its gas phase, through chemical vapor deposition (CVD) techniques, using a chemical reaction occurring in the gas, and close to the substrate, so that the product of the reaction is deposited on the substrate. The chemical reaction energy can be supplied from thermal energy, optical energy or plasma processes. Nowadays the two dominant techniques for depositing hydrogenated amorphous silicon are the plasma enhanced CVD (PECVD) and the hot wire CVD (HWCVD) deposition techniques. A plasma is a partially ionized gas that consists of positive and negative charges, and not ionized neutral molecules. An external source of energy is needed to sustain the plasma for a sufficiently long time, and in PECVD technique, a RF electric discharge is used, with a typical frequency of 13.56 MHz. In a PECVD deposition, a silane gas (SiH_4) is admitted to a vacuum reactor chamber and excited by the RF plasma, which causes silane molecules to dissociate. The decomposition of silane yields radicals that reach the surface of the substrate giving rise to the growth of a-Si:H film (Figure 2.11).

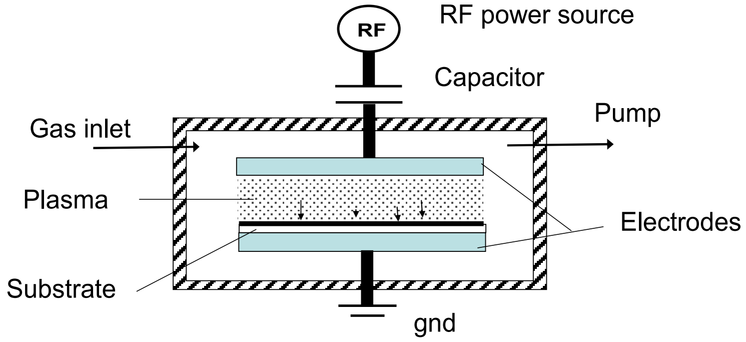

Figure 2.11. Schematic of a parallel plate RF PE-CVD deposition system

This deposition can be performed at relatively low temperatures (150 °C – 250 °C). Most research and industrial reactor systems consist of two parallel electrodes in a stainless steel chamber, allowing uniform deposition on large areas. Doping of the deposited film is done by adding phosphine or diborane to the gas. Several modifications to standard PECVD techniques have evolved. For example, the use of higher excitation frequencies of the plasma (50-100 MHz) permits an increase in the deposition rate by one order of magnitude with respect to a standard RF PECVD. This deposition technique is called Very High Frequency PECVD (VHF PECVD).

The Hot Wire CVD (HWCVD) is also used to produce thin films of a-Si:H. This method is based on the catalytic decomposition of silane at the surface of a heated tungsten filament, foil, or grid. The decomposition yields radicals that can reach the surface of the substrate to form either a polycrystalline or an amorphous silicon material depending on deposition conditions.

2.2.2. Light sensors and Thin Film Transistors

Light sensors based on a-Si:H can be divided into photoconductive (PC) and photovoltaic (PV) light sensors. In a photoconductive light sensor, two metal electrodes are placed on an intrinsic a-Si:H thin film (Figure 2.12). The contacts are ohmic, so that there is an injection of carriers in the semi conducting layer, which behaves as a resistor. The conductivity between the two ohmic contacts is changed during illumination: electron-hole pairs are created by the incident photons, increasing the free carrier density and the thin layer conductivity. This phenomenon is then utilized to detect the change of incident light intensity as the change in electric current when a constant voltage is applied between the electrodes.

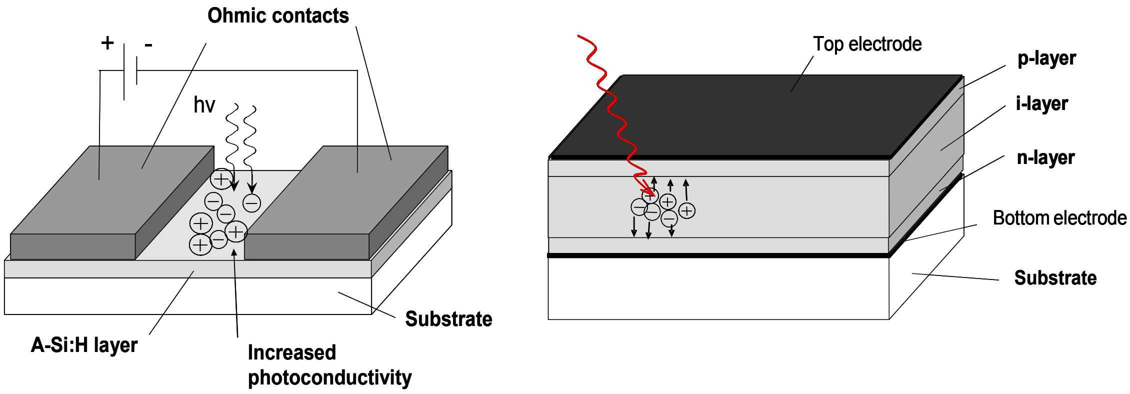

Figure 2.12. Schematic of photoconductive (left) and photovoltaic structure (right).

In a photovoltaic light sensor, the a-Si:H thin films are “sandwiched” between two electrodes that form blocking contacts, in contrast with the photoconductive sensors ohmic contacts. The energy of the incoming photons is converted into free charge carriers in the a-Si:H layer. Photo-generated electrons and holes must be spatially separated in order to contribute to the net current of the device, and the charge separation is done by an internal electric field. In crystalline semiconductors, this can be achieved by stacking a p-type doped material and an n-type doped material. In amorphous silicon, a simple p-n junction hardly shows photovoltaic action. Photo-generated charge carriers cannot diffuse over long distances, as the defect density in p- and n-type doped material is high in a-Si:H. Therefore an undoped (intrinsic) layer has to be introduced between p and n layers (Figure 2.12). The p and n layers provide the internal electric field, and do not contribute to the photo-generated current, therefore these layers are usually designed very thin (~ 10 nm). The incoming photons are absorbed into the i-layer. The predominant photovoltaic devices in a-Si:H are based on this p-i-n structure.

Shortly after the first a-Si:H p-i-n solar cells were made, the first Field Effect Transistor (FET) produced in a-Si:H was demonstrated [Sne81]. The Thin Film Transistor (TFT) is used as a switching element in many arrays applications. The TFT has three terminals, as a MOS transistor: gate, source and drain. The gate voltage controls the accumulation of electrons in the a-Si:H thin film, and the drain to source current of the TFT. The most common a-Si:H TFT structure is the so-called inverted staggered transistor structure shown in Figure 2.13. In this structure, the gate metal is deposited first on the glass substrate, followed by the silicon nitride used as gate, the intrinsic a-Si:H thin film, and the source and drain contacts.

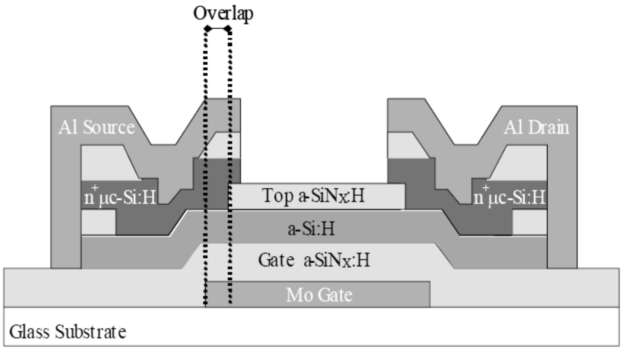

Figure 2.13. Inverted staggered a-Si:H Thin Film Transistor. [Moh01]

When a positive voltage V_G is applied to the gate, electrons are accumulated in the a-Si:H thin film. At small voltages, these electrons will be localized in the a-Si:H deep states. Above a certain threshold voltage V_{th}, a constant part of the electrons will be mobile, and the conductivity is increased linearly with $V_G - V_{th}$. The transistor switches on for $V_G > V_{th}$, and the current I_{ds} flows from source to drain:

$$I_{ds} = \mu_{FE}\, C_G \frac{W}{L}[(V_G - V_{th})\, V_{DS}] \qquad (2.29)$$

μ_{FE} is the effective carrier mobility, C_G the gate capacitance, V_{DS} the drain to source voltage and W and L the channel width and length, respectively.

Saturation occurs when $dI_{ds}/dV_D = 0$ and the saturation current is given by:

$$I_{ds} = \mu_{FE}\, C_G \frac{W}{2L}(V_G - V_{th})^2 \qquad (2.30).$$

The mobility is about 1 $cm^2\ V^{-1}\ s^{-1}$, the threshold voltage is ~ 1 V, and with standard transistor sizes of L from 4 to 20 μm and W around 10 μm, the maximum current in the "on-state" is about 10^{-4} A for $V_G \sim 25$ V, for a current of 10^{-11} A at $V_G = 0$ V [Str91]. There are interface states at the interface nitride-amorphous silicon, degrading the performance of the TFT. Problems are particularly severe when nitride is grown on top of a-Si:H, and for this reason all TFT designs use the inverted structure with the gate deposited first. TFTs are not perfectly stable, and a prolonged time of application of a gate voltage results in the creation of deep defects and in a shift of the threshold voltage. Fortunately, this effect is relatively low at room temperature, resulting in a shift of less than 0.1V, but the shifts become much more important as the temperature is increased. Another disadvantageous phenomenon in TFTs is the photoconductivity of a-Si:H, because a photocurrent reduces the on/off ratio of the TFT. A way of reducing this effect is to make the a-Si:H layer as thin as possible.

2.2.3. Applications

Solar cells

Hydrogenated amorphous silicon represents after crystalline silicon the second used material for photovoltaic devices. a-Si:H based solar cells are getting more and more developed and produced. They are made of p-i-n layers of a-Si:H. The front electrode consists of a Transparent Conductive Oxide (TCO), textured as a mean to reduce optical reflection, and the bottom contact is usually made of Indium Tin Oxide (ITO) or Zinc Oxide (ZnO). The high light absorption of a-Si:H allows the use of thin films (< 1 μm) and its low temperature deposition technique permits the deposition on cheap and flexible substrates. The material can be thin, flexible, and easy to manipulate, and can be used as a structural component. Its low weight and its enhanced resistance to radiation are key factors for space applications [Kun03]. It presents a reduced efficiency, of ~ 6-8 % for each solar panel [Goe03] and degradation after prolonged light exposure, namely the Staebler-Wronski effect (2.1.2), but its low price leads to an interesting price-performance ratio of about 3.2 Euros/W [Goe03].

Today, amorphous silicon is widely used in consumer applications, mainly for indoor use, as for example in calculators that do not require a battery. So far, a-Si:H has not played a very large role in the outdoor use of PhotoVoltaic (PV) modules for energy applications, but this is bound to change as the market increases rapidly and as PV industry will reach a scale in the next decades that can no more be maintained with mono or polycrystalline wafers alone.

The understanding and the reduction of the Staebler-Wronski effect are still nowadays adressed for a-Si:H. A way to reduce it is to design very thin solar cells operated with high electric fields. Nowadays research in the development of a-Si:H solar cells concerns the optimization of cell designs by introducing buffer layers, alloy and doping gradients, in order to increase the cell efficiency; and to the optimization of stacked cells and tandem devices [Sha05], to obtain higher stabilized efficiencies. The thinner is the cell, the less sensitive it will be to Staebler-Wronski effect. Effort is thus also done to find methods to increase the absorption of light and the light path in the cell in order to obtain high efficiency with thin cells [Ter04].

a-Si:H TFT to address active matrix displays

Active matrix arrays contain many pixels generally addressed or read out by a grid of interconnecting lines called gate and data lines (Figure 2.14). Thin Film Transistors (TFT) in amorphous silicon are widely used and dominant as switching elements. TFTs are used for example in flat screens (TFT LCD), for the active matrix addressing of liquid crystal displays (AMLCD). The light polarization of a liquid crystal between two glass plates is controlled by the voltage on the pixel electrode, which is controlled by the gate voltage of a TFT. If a voltage high enough is applied to the gate of the TFT, the TFT and so the pixel are "on", the liquid crystal cell is electrically activated, and the molecules in the liquid align in a single direction. This allows a polarization of the light so that it passes through unchanged. If the TFT and so the pixel are "off", the electric field is removed from the liquid. The LCD then polarizes the light so that it doesn’t pass through the pixel. This allows for high definition large area television displays and flat screen displays. Color displays are implemented by dividing each pixel in three sub-pixels each with a different filter, red, green or blue. Active matrix addressing can also be used in addressing a-Si:H photodiodes arrays.

Light sensors linear arrays

Linear arrays of a-Si:H photodiodes are widely used in optical page scanning such as fax machines, photocopying machines and document scanners. The large linear dimension of the array (page size) allows a much simpler design, for which no optics are needed for image-size reduction as it is required when a CCD camera is used as the detecting element. The matrix addressing is similar to that of an AMLCD technology. A pixel consists of a p-i-n photodiode connected to a TFT. During illumination of the pixel, charge created in the i-layer is transferred to the bottom electrode of the p-i-n structure, and accumulates when the TFT is off. When the TFT is switched on, the charge will flow out and can be read by an external electronic circuitry. In this way the sensor integrates the signal during the time it is not addressed (read out times are very short compared to accumulation times).

Large area X-ray detectors

High energy radiations can be imaged with large area a-Si:H linear arrays. The imaging can be performed directly or indirectly (Figure 2.14 right).
Direct imaging is achieved when the integrated sensors of the linear array directly converts X-rays into an electrical signal. Photoconductors such as amorphous selenium are used, one pixel being addressed through an a-Si:H TFT [Fis03]. The imaging can also be performed indirectly, i.e. via a scintillator. The intermediate scintillator layer such as Cesium Iodide (CsI) or phosphor [Fis03] is deposited on top of the active matrix array. X-rays are converted into visible light by means of the scintillator, and the visible light is

detected by a pixel made of a p-i-n a-Si:H photodiode addressed by an a-Si:H TFT, as illustrated in Figure 2.14.

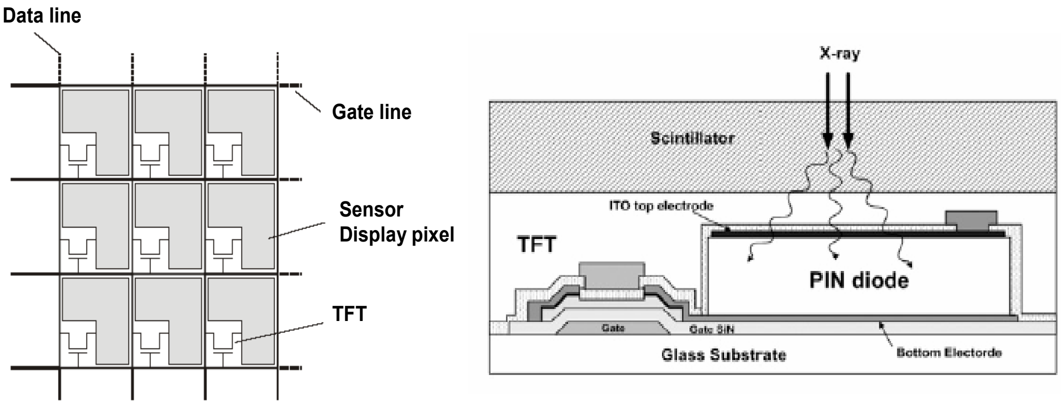

Figure 2.14. Left: Schematic of an Active Matrix Array comprising 9 pixels. In LCD screens, TFT control display pixels, while in light sensors linear arrays they control sensors. Right: individual pixel of X-ray indirect detector with scintillating layer, p-i-n a-Si:H photodiode and TFT addressing transistor [Kim03].

The development of a-Si:H large area X-ray detectors that started around 1985 has leaded to a large variety of different flat panel X-ray detectors, available for radiography, angiography, cardiology or mammography imaging, which started to penetrate the market in 2000.

<u>Other applications</u>

The a-Si:H photoconductors are also used as the light sensitive component in the electrophotographic or xerographic process [Shi81]. Compared to conventional materials, a-Si:H is non toxic and provides a hard surface. a-Si:H is also found as Thin Film Position Sensitive Detector (TFPSD), colour sensor (that consists of stacked p-i-n structure), infrared sensor, light emitting diode or as retention layer on the vibrating foils in loudspeakers. a-Si:H is nowadays widely used and industrialized, but novel technologies as novel applications of the material are being developed and will appear in the near future. For example the deposition on flexible substrate will certainly lead to novel applications. The Thin Film on ASIC technology is a novel technology based on a-Si:H that finds already applications as image sensors. The work presented in the thesis concerns the study of the applicability of this technology to the detection of charged particles, and this technology is presented in details in section 2.3.

2.3. Thin Film on ASIC technology

The Thin Film on ASIC technology represents an attractive alternative solution to build particle detectors for High Energy Physics (HEP) and for medical imaging applications. This section presents the technology concept, and the properties of a-Si:H detecting devices when developed for particle detection. The different advantages of using the TFA technology for particle detection together with the different challenges involved in the development of such detectors are discussed.

2.3.1. Thin Film on ASIC concept

Recent research in the field of sensors focuses on intelligent sensors, in which a part of the signal processing system is integrated together with the detecting device. Hydrogenated amorphous silicon is an excellent material for optical detectors. It presents a higher absorption coefficient for the visible spectrum compared with crystalline silicon, and its spectral response corresponds to the human eye response. Its deposition characteristics make it a very interesting material. However, its suitability for electronic circuits is very restricted. On the other hand, crystalline silicon, though providing poorer photoelectric properties, is very well known and largely produced for a wide range of highly developed technologies, as for example the fabrication of integrated circuits. By depositing an a-Si:H detector on top of an ASIC, it would be possible to combine the advantages of both materials. Hydrogenated amorphous silicon presents the technological advantage of being deposited at low temperatures on large areas and for reduced costs. Through Plasma Enhanced Chemical Vapor Deposition (PE-CVD), a-Si:H can be deposited at temperatures ranging from 150 °C to 250 °C. For crystalline silicon CMOS wafers with aluminium based interconnections, the maximum postprocessing temperature is generally considered to be slightly above 450 °C [Sed01], a temperature above which the aluminium connections start to melt. The deposition temperature of a-Si:H is then well below this limit. a-Si:H films can be deposited on top of post-processed CMOS wafers, and it is possible to integrate a detecting device in a-Si:H on top of the electronic readout. This is called the Thin Film on ASIC (TFA) or Thin Film on CMOS technology (TFC). It has an interesting potential for high-sensitivity, high dynamics imaging [Fis92, Sch99] and for both small-area pixel imagers [The02] and large-area imagers for X-ray medical applications [Str00]. The feasibility, the advantages and the challenges of a particle detector based on this technology are presented in this thesis.

The TFA technology consists in the deposition of an a-Si:H thin film detecting device direct on top of the ASIC. The detecting device can be realized in the form of n-i-p layers sequence or Shottky devices. In the case of an n-i-p structure (Figure 2.15), a Transparent Conductive Oxide (TCO) electrode is deposited on top of the p-layer to provide a common top electrode to all pixels.

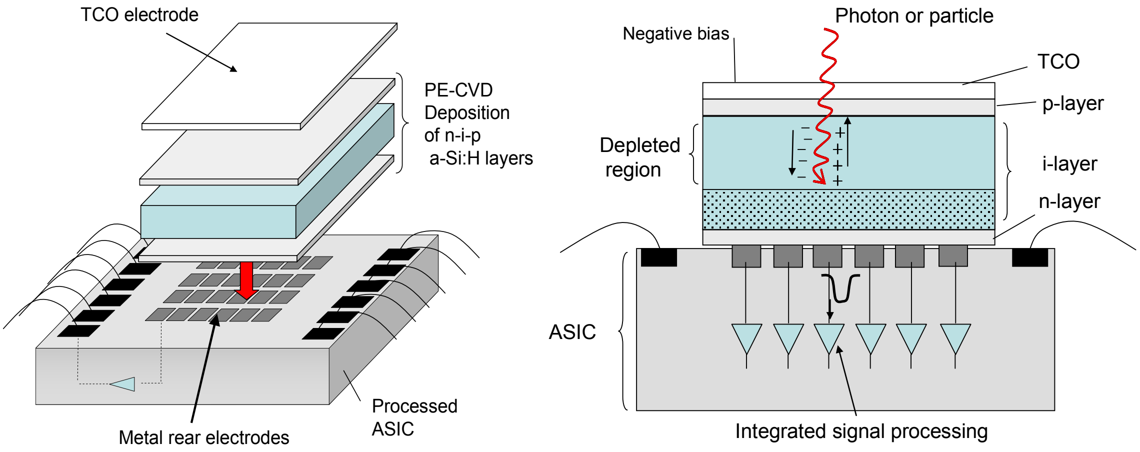

Figure 2.15. Left: Deposition of n-i-p a-Si:H layers on top of an ASIC to build a TFA detector. Right: Cross section of a detector: photogenerated carriers in the depleted i-layer region are separated and collected in the electrodes. Signal is readout with integrated readout electronics.

The bottom contact of each pixel is an individual metal rear electrode integrated in the ASIC, and connected to the pixel electronic readout. The reverse bias voltage applied through the electrodes to the two doped layers depletes the i-layer. Generated carriers by photons or particles in the i-layer depleted region are separated by the electric field and collected onto the electrodes. The corresponding induced signal is then processed by the integrated electronic readout.

The TFA technology offers a high integration level of the detecting device and of the readout electronics, resulting in an overall system cost reduction. It also allows for a geometrical fill-factor (ratio between the active area of the sensor and the total sensor area) close to 1: the pixel readout electronic shares the same die area with the photodiode array, the electronic readout being integrated below the active area of the detector. Another advantage of the technology is its flexibility: the detecting device and the electronic readout circuit can be separately designed and optimized.

The first detectors based on the TFA technology have been developed as image sensors [Fis92, Sch99]. The first company industrializing such imagers is Silicon Vision, which was formed in 1996 as a spin off of the University of Siegen in Germany. Typically, n-i-p structures are used as detecting devices for black and white imagers. Multilayers of a-Si:H as n-i-p-i-n or p-i-n-i-p structures, or n-i^x-p structures (subdivided i-layers), can be employed for multicolor recognition [Sch99]. Only thin active layers are required, thanks to the a-Si:H high optical absorption, and standard n-i-p structures have a 1 μm thickness (comparable with solar cells). Flexibility is one of the key advantages of the TFA technology, since identical ASICs can be supplied with different detector structures without compatibility problems. As different detector structures are possible, photoelectric properties like spectral sensitivity can be adapted to the specific requirements of an application, within a certain range even after finishing the ASIC fabrication. A standard Silicon Vision TFA image sensor pixel schematic is shown in Figure 2.16.

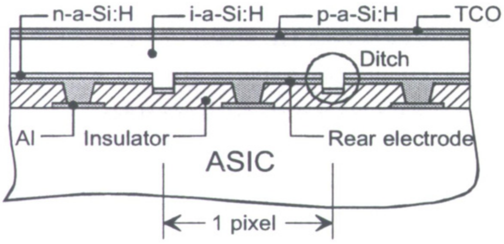

Figure 2.16. Self-structured thin film system [Sch99].

During the ASIC completion, a final metal layer is deposited in the passivation (insulator) openings, and rear electrodes are patterned. Prior to the thin film deposition, ditches can be etched into the insulator between the detector and the ASIC. During the deposition process the thin n-layer is disrupted on the edges of the ditches, so that lateral currents between the pixels are suppressed.

2.3.2. Particle detection in a-Si:H

Amorphous silicon has become an active research area in recent years for high energy radiation detection, because of its ability to be deposited for low costs on large areas. Several research groups have also demonstrated a higher radiation tolerance of a-Si:H compared to crystalline silicon [Sro98, Kis98, Kun03]. These studies were mainly performed with low energy protons to test a-Si:H solar cells for space applications. A high level of radiation hardness of particle detectors is nowadays a crucial issue in high energy physics experiments, so that further researches on the a-Si:H material are interesting for these applications. Conventional thin film a-Si:H devices with typical thickness of 1 µm are however not suited to high energy particles detection. High energy particles go easily through the entire a-Si:H layer with little energy loss, so that the signal induced by a single particle is too small to be readout. The TFA sensors or the a-Si:H active pixel arrays developed so far as imaging devices cannot be used for a direct particle detection. The detection of high energy particles with an a-Si:H device can be performed only by depositing thick devices or by using a scintillating layer.

A scintillating layer made of a high atomic number (Z) material can be deposited on top of a-Si:H photo sensors to perform particle detection. It converts the energy of the incoming particles into photons or particles that can be readout by the a-Si:H imaging device. X-ray detectors using a phosphor or a cesium iodide scintillating layer on top of an a-Si:H active pixel array [Fis03] have been developed and are nowadays commercialized by several companies. Neutron detectors based on an a-Si:H imager and a gadolinium scintillating material that converts neutrons into 70 keV electrons has been developed [Mir94]. A particle detector based on a thallium activated cesium iodide (CsI(Tl)) layer has also been proposed [Jin95]. The CsI(Tl) scintillator has a high conversion ratio, of about 40 000 visible light photons / MeV of deposited energy. The detection of a minimum ionizing particle (MIP) has been demonstrated with this detection concept with a 22 000 e^-/h pairs creation in the a-Si:H layer [Jin95]. However, this technology necessitates the addition of the scintillating layer, which can be as thick as 1000 µm, thus degrading the spatial resolution of the detector, and expensive.

The sensitivity of Shottky and p-i-n a-Si:H diodes to α particles were first demonstrated by Kaplan [Kap86], and in the last 20 years several research groups [Dub91, Fou01, Per87] have carried out a substantial work in trying to demonstrate that the hydrogenated amorphous silicon material can be used for reliable sensors in high-energy physics (HEP). A direct detection of a particle in an a-Si:H sensing device involves that the particle will create a sufficient electric signal above the system noise level. This noise depends on the detecting device noise, and on the readout electronic noise performance. The amplitude of the induced signal will depend on the thickness of the detecting device through which passes the particle: thick depleted a-Si:H layers (~ 50 µm) are needed to provide an adequate signal over noise ratio. In an n-i-p diode, the i-layer is the sensitive part and is depleted under appropriate reverse bias. The n-doped and p-doped layers can be kept thin (~ 20 nm) as they just provide the depletion of the i-layer. Generated carriers in these layers will not be collected because of a high recombination rate of the carriers, due to the high defect density of doped layers in a-Si:H. Generated carriers in the depleted i-layer are separated and accelerated by the internal field inducing a signal on the electrodes, but generated carriers in the non-depleted i-layer are not separated and do not participate to the signal (Figure 2.17).

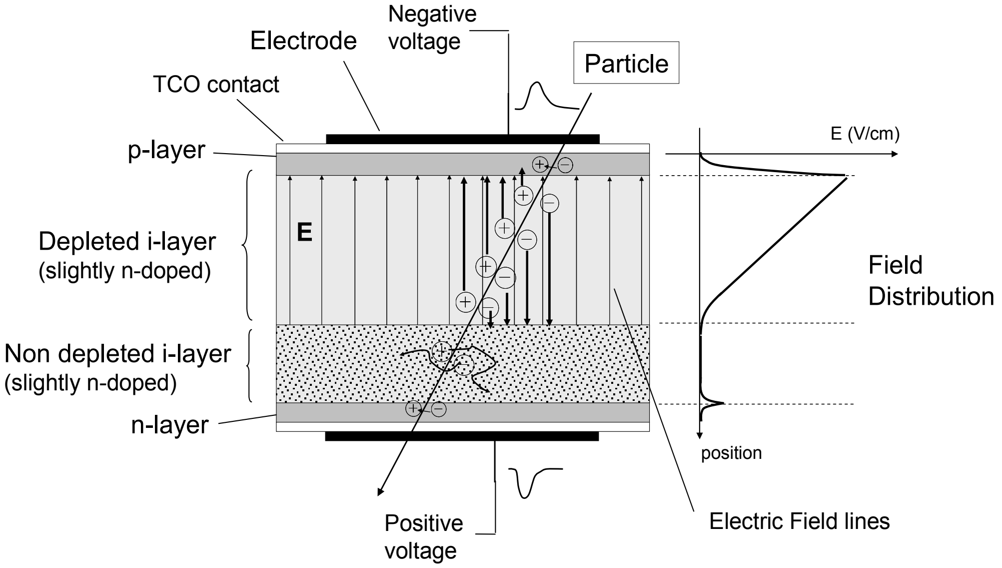

Figure 2.17. Schematic of an n-i-p thick diode. Charge carriers induced in the depleted i-layer are separated and accelerated by the internal electric field, contributing to the detector signal.

A thick i-layer and a full depletion of the layer are then required for an appropriate particle detection. However, depositing thick layers of a-Si:H is a technological challenge, as peeling of the layers due to a mechanical stress and to an insufficient adhesion to the substrate often becomes a problem [Cha96]. The concept of thick diodes as it will often be mentioned in the thesis is of course very relative. The deposition of a 50 µm thick a-Si:H layer of good quality is a technological challenge and is difficult to achieve, so that layers between 20 µm and 50 µm can be considered as thick in comparison to the 1 µm maximum thickness of standard a-Si:H devices. However, they can still be considered thin films in comparison with standard crystalline silicon detectors with thickness from 150 µm to 300 µm.

The thick a-Si:H layer has to be depleted to operate as a sensing device. The intrinsic i-layer of a-Si:H is actually slightly n-doped, so that part of the deep states of the amorphous semiconductor behave like donor states and are positively charged under inverse polarization conditions. As a consequence, the electric field is not constant but rather has a linear behavior in most of the depleted thickness of the i-layer (Figure 2.17). The electric field profile inside the i-layer is given by the Poisson equation [Hon95]:

$$\frac{d^2V}{dx^2} = \frac{-\rho}{\varepsilon_0\,\varepsilon_{aSi}} = -\frac{q\,N_{db}^{\,*}}{\varepsilon_0\,\varepsilon_{aSi}} \qquad (2.31);$$

where V is the electric potential, ρ is the electric charge density, ε_0 is the dielectric constant of vacuum, ε_{aSi} is the relative dielectric constant of a-Si:H, q is the electron charge, and N_{db}^{*} is the density of ionized defects. By considering a simple model in which the density of ionized defects is uniform within the depletion region, the necessary voltage V_f required to deplete an i-layer of thickness d is then given by:

$$V_f = \frac{q\,N_{db}^{\,*}\,d^2}{2\,\varepsilon_0\,\varepsilon_{aSi}} \qquad (2.32).$$

Therefore, the magnitude of the applied bias necessary for depleting the i-layer varies linearly with the ionized defect density N_{db}^{*} and is proportional to the square of the i-layer thickness. If we assume a dangling bond density of 2×10^{15} cm^{-3} for a state-of-the-art a-Si:H material, and that roughly 30 % of the dangling bonds are ionized [Hon95], a voltage V_f > 1100 V will be required to deplete a 50 µm thick a-Si:H diode. In any case, a maximum thickness of about 50 µm should be considered. For thicker devices, even if the deposition of a good quality a-Si:H is feasible, the high voltage required to deplete the p-i-n diode tends to induce either breakdown of the device or increased leakage currents, due to the presence of a very high electric field at the p-i interface. For a 100 µm thick diode a voltage of about 4.5 kV would be necessary to fully deplete the layer.

Several research groups have performed a substantial work of characterization of particle detection in a-Si:H. These works revealed the complexity of modeling the charge carrier collection process and the signal generation in a-Si:H detectors, since there is a continuous distribution of gap states, each acting as a trapping level with its own characteristic trapping and reemission times. N-i-p diodes with thickness ranging from 10 to 50 µm have been characterized by the different groups. Characterizations with 1 to 12 MeV protons and 2 to 18 MeV alpha particles demonstrated a fast electron collection (in less than 10 ns) and a slow hole collection (µs range) in fully depleted diodes (holes conductivity is rather dispersive at room temperature) [Dub91]. An absence of signal saturation was also observed even at very high collection fields (60 V/µm), and a mean energy required to produce an electron-hole pair in a-Si:H was measured and simulated between 3.6 and 6 eV [Dub91]. On average, a minimum ionizing particle has been measured to produce 770 electrons in a 21 µm thick n-i-p a-Si:H diode [Ale91], but the measurements were performed using a 1 µs shaping time amplifier, and the measured signal over noise ratio was ~ 2.5. Although these works have shown that charge particle detection is feasible, minimum ionizing particles detection turned out to be unrealistic for high energy physics applications. In the past years, the readout of a low signal as the signal induced by a minimum ionizing particle in a-Si:H n-i-p diodes turned out to be the major obstacle in using a-Si:H for particle detection. An integration of an a-Si:H sensor direct on top of the ASIC would decrease parasitic capacitances and allow for smaller pixels, thus permitting the design of high speed and low noise readout electronics. The Thin Film on ASIC technology then appears as an attractive solution for single particle detection.

2.3.3. TFA technology for particle detection

The TFA technology approach is especially attractive for radiation hard pixel detectors. It enables an integration level comparable to monolithic pixel detectors, while having the advantage of the hybrid pixel approach.

The detecting device is vertically integrated with the ASIC integrating the electronic readout, so that no bump bonding is needed as it is the case in hybrid detectors. The deposition process is very low cost, the price of a TFA detector being slightly more than the ASIC price itself. Together with this monolithic advantage, the TFA technology presents the same flexibility as hybrid pixel detectors: the detecting device and the electronics can be separately optimized, and the detector can be biased independently from the ASIC, and at high voltages. The integration is also vertical, so that the electronic and the sensing area do not share the same die area, and do not compete in the pixel area. Finally, a-Si:H is a material supposed to show a higher radiation resistance than crystalline silicon. These properties make this technology very attractive, but several important challenges have to be overcome at the same time. The first challenges in developing a TFA pixel detector are technological:

- the deposition of thick a-Si:H diodes on top of standard ASICs
- a low defect density to allow the full depletion of the a-Si:H sensing device
- the diodes have to exhibit a low leakage current

A particle creates a weak signal in the relatively thin a-Si:H layer compared to a standard crystalline silicon detector. A Minimum Ionizing Particle (MIP) creates a most probable peak charge of about 22 000 electrons in a 300 μm thick crystalline detector, which correspond to about 80 e^-/μm. A MIP creates a peak charge of about 770 electrons in a 21 μm thick a-Si:H detector [Ale91], which corresponds to about 37 e^-/μm. The difference observed in the average collected charge over the full detector thickness for crystalline and amorphous silicon can be attributed to a higher mean electron-hole pair energy creation in a-Si:H and to a partial collection of holes due to its dispersive transport in a-Si:H. The connection between the a-Si:H sensor (n-layer) and the integrated circuit (last metal layer defining detector bottom electrode) is also achieved during the deposition. The existence of a passivation layer on standard processed ASICs results in unevenness of the substrate and may lead to several problems. These characteristics lead to different challenges for the design of the integrated circuit:

- design of low noise pre-amplifiers able to readout the small signal induced by a single particle
- appropriate design of metal electrodes

Finally, the different mechanisms of radiation interaction, charge collection and signal induction in a-Si:H are rather complicated and not fully characterized nowadays. These mechanisms together with the evolution of a-Si:H properties after irradiations are not integrated nowadays in an accepted descriptive model. A substantial work on the signal creation in a-Si:H sensor and on the material radiation resistance has then to be performed in order to study the feasibility of a particle detector based on this material for high energy physics applications.

The work presented in this thesis focuses on the first investigations made on a particle detector based on the Thin Film on ASIC technology. The detector consists in thick n-i-p a-Si:H diodes deposited by very high frequency PE-CVD direct on top of ASICs designed in a deep submicron CMOS technology. Figure 2.18 displays a cross section of such a detector. In this example, the ASIC comprises three levels of metal, and it integrates part of the signal processing. A passivation layer covers the surface of the ASIC, and is opened on top of the electrodes made of the last metal layer. These openings and the last metal layer electrodes define pixel electrodes. A thick n-i-p a-Si:H diode is deposited on the uneven surface of the ASIC, and a Zinc Oxide (ZnO) or an Indium Tin Oxide (ITO) transparent electrode is deposited on top of the n-i-p structure, and serves as a global top electrode for all pixels. It is made transparent to permit the characterization of the sensor through laser techniques, as it will be presented in chapters 5 and 6. The movement of generated charges by a particle in the i-layer induces a signal on the last metal layer pixel electrode. This signal is directly processed by the integrated electronic circuit.

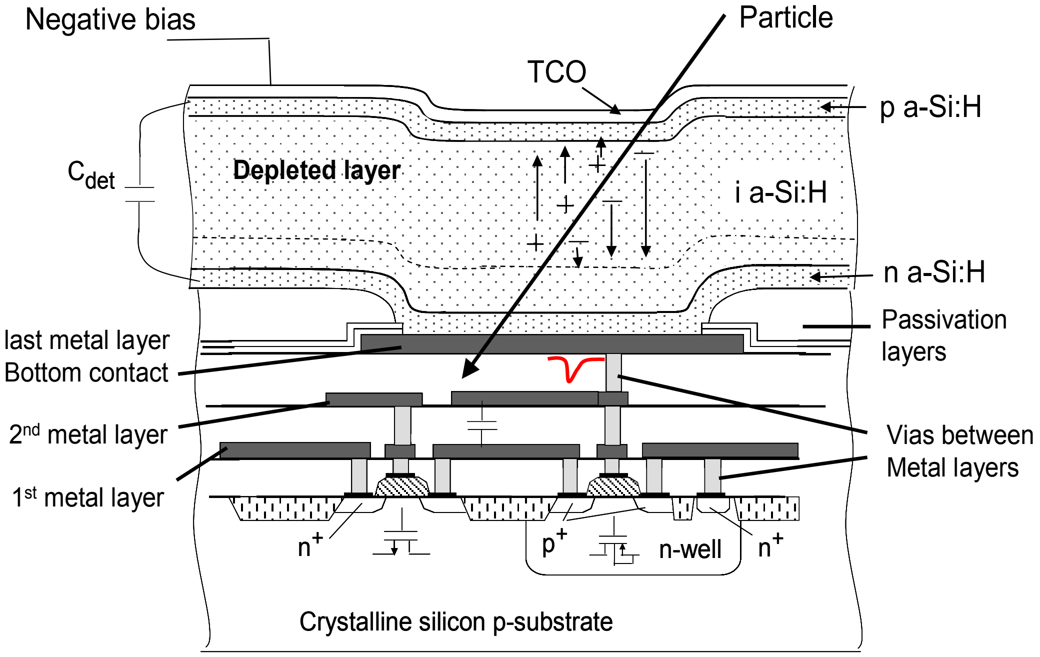

Figure 2.18. Cross-section of a TFA pixel detector. n-i-p layers are deposited on top of a three metal layer CMOS integrated circuit.

2.4. Conclusions

In the past 30 years, a lot of work has been carried out to investigate the specific properties of amorphous materials, and particularly that of hydrogenated amorphous silicon. A global coherent physical picture is nowadays admitted, involving many novel aspects unique to the amorphous phase. In table 2.1 different properties of a good quality amorphous thin film are summarized.

The a-Si:H disorder however leads to many controversial issues and to many uncertainties, so that research is still nowadays very active for this material. The possibility of depositing a-Si:H material on large areas, for low costs, and at low temperatures, together with a high optical absorption, has lead to the development of a wide range of devices based on a-Si:H, as displays or solar cells. Another important feature of this material is a supposed higher radiation hardness compared with crystalline silicon, and a possibility to be deposited on ASIC. A radiation hard pixel detector based on the TFA technology is then very attractive, but many challenges have to be overcome for its development. The work presented in this thesis concerns the first studies of the feasibility of a pixel detector based on this novel technology.

Property	Symbol	Value
Material Density	ρ	~ 2.15 g.cm^{-3}
Hydrogen content	C_H	10 – 20 %
Defect Density	N_{db}	~ 2×10^{15} cm^{-3}
Correlation energy	U	0.2 – 0.4 eV
Valence Band tail width	kT_V	45-50 meV
Conduction band tail width	kT_V	~ 25 meV
Mobility gap	E_G	1.7 - 1.8 eV
Tauc gap	E_{tauc}	1.6 – 1.7 eV
Cubic gap	E_{cubic}	1.4 – 1.6 eV
Urbach energy	E_0	50 meV
Dielectric constant	ε_{aSi}	~ 12
Ionized defect density of i-layer	N_{db}^*	~ 30 % × N_{db}
Depletion voltage of an intrinsic layer	V_f	~ 1100V for 50 μm
For a thickness d:		~ 0.45 V × (d in μm)^2
Absorption coefficient (600 nm)	α_{600}	4×10^4 cm^{-1}
Electron drift mobility	μ_e	1 – 10 cm^2 V^{-1} s^{-1}
Hole drift mobility	μ_h	0.01-1 cm^2 V^{-1} s^{-1}
Conductivity in intrinsic a-Si:H	σ_d	10^{-12}-10^{-10} S cm^{-1}
Pair creation energy	W	4 – 6 eV

Table 2.1. Selected Properties of a good quality a-Si:H thin film

3. Design of Integrated Circuits for the Thin Film on ASIC technology

The Thin Film on ASIC technology consists in the deposition of an a-Si:H detecting device direct on top of an ASIC that integrates part of the signal processing. The first step in the development and the study of pixel detectors based on the TFA technology is the design of integrated circuits adapted to this technology. As it has been presented in chapter 2, challenges in the design of these integrated circuits are principally the design of low noise preamplifiers able to readout the small signal induced by a particle, and an appropriate design of the metal pads defining the bottom electrodes. Moreover, high speed preamplifiers have to be designed. This is first to allow a fast readout of a particle signal, to ensure a reasonable time resolution for consecutive signals. Furthermore, the integrated circuits developed in this thesis are “test” circuits for the characterization of the a-Si:H sensor. In order to study the signal induction speed in the a-Si:H sensor, the electronic readout has thus to be fast to also shape as little as possible the signal originating from the sensor. The analog front-end preamplifier scheme chosen to perform the signal processing is a transimpedance amplifier using an active feedback [Jar96].

- In section 3.1, the active feedback transimpedance amplifier concept and architecture are presented, together with a detailed study of its transfer function, its stability, and its noise performance. The AFP (Active Feedback Preamplifier) chip [Ane03] is then presented. This chip has been designed in order to test different detectors and is not entirely dedicated to the study of the TFA technology.

- In section 3.2, the aSiHtest chip is presented. This Integrated Circuit is a test chip developed in order to characterize the Thin Film on ASIC technology. It comprises many different metal pads connected either to a current amplifier to perform leakage current characterization or to an active feedback preamplifier to perform particle detection measurements or to characterize the a-Si:H sensor speed. The different structures and the different electronic readout systems are presented.

3.1. The Active Feedback Pre-amplifier

In High Energy Physics applications, the commonly used front end pre-amplifier types to process signals from capacitive sensors are charge sensitive amplifiers, current sensitive amplifiers, or voltage sensitive amplifiers [Gat86]. CMOS technologies are usually chosen. They offer a high integration density, high speed, low power consumption, and permit the integration of analog and digital blocks on the same chip. The integrated circuits developed for the characterization of the TFA technology comprise Active Feedback Preamplifiers (amplifiers in a current sensitive configuration). The architecture of the amplifier and its implementation in a CMOS technology are presented in 3.1.1. Calculations of the amplifier frequency and transient responses have been performed. Different models have been developed and are presented in 3.1.2, together with calculations of the circuit stability. Finally, the circuit noise has been calculated. The dominant noise sources of the circuit are presented and their contributions to the output noise have been calculated and are presented in 3.1.3.

3.1.1. Architecture of an Active Feedback Pre-amplifier

The analog front end type chosen to readout signals from the a-Si:H capacitive detectors is presented in Figure 3.1. It is a transimpedance amplifier that uses an amplifier stage A, a transistor in the feedback path acting as a resistor, a feedback capacitance, and a buffer stage [Jar96].

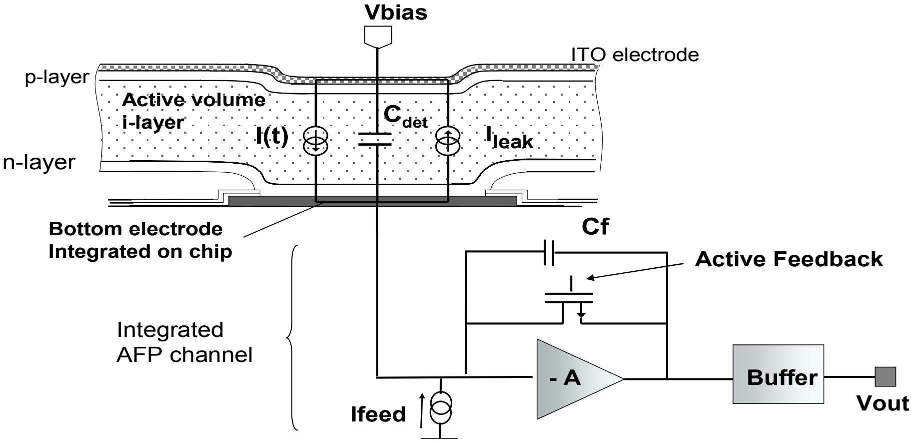

Figure 3.1. Schematic representation of a n-i-p a-Si:H diode connected through its bottom electrode to an Active Feedback Preamplifier. The electrode is integrated in the ASIC and fabricated using the topmost metal level available in the process.

A current pulse is created on the pixel bottom electrode when a particle goes through the a-Si:H detecting device. This signal charges the input capacitance C_{in} of the amplifier stage, the detector capacitance C_{det} and the feedback capacitance C_f, and induces a voltage step at the amplifier output. The NMOS transistor active feedback acts as a feedback resistance providing the decay of the voltage pulse at the preamplifier output node. The feedback capacitance is added to improve the stability of the system.

The different passive resistors offered in CMOS technologies present relatively low resistances, such as 210 Ω/square for a polysilicon resistor in the IBM 0.25 µm CMOS technology that we used for the design of the chips. Obtaining a resistance in the feedback path in the order of 100 kΩ by using passive resistors would lead to a loss of space and to parasitic capacitances with respect to the bulk, thus limiting the bandwidth. The use of a transistor allows for a much higher bandwidth (crucial for the gain and the speed) of the preamplifier stage than in case of a simple resistive feedback. Another advantage is the possibility to control the feedback transistor transimpedance, and therefore the feedback resistance, via an external current I_{feed}. This permits to adjust the circuit performance to the measurement requirements. Finally, this circuit can be easily integrated in a compact way in any digital CMOS process, which often does not offer integrated resistances. A practical implementation of the active feedback preamplifier is shown in Figure 3.2.

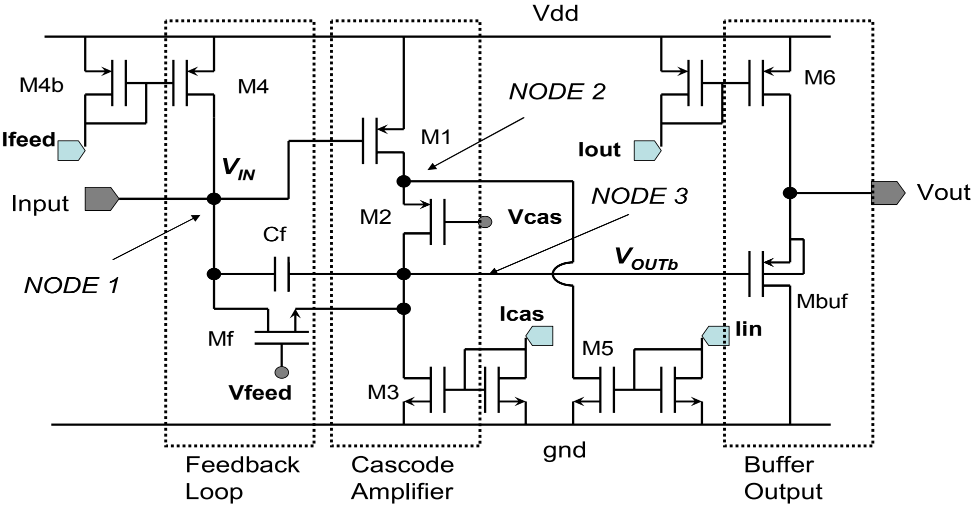

Figure 3.2. Circuit diagram of the AFP implemented in a CMOS technology.

It comprises a classical cascode amplifier structure, an NMOS feedback transistor M_f and a capacitance C_f in the feedback loop. The buffer stage is realized by a source follower using a PMOS transistor. The feedback transistor M_f is biased in weak inversion, so that its source transconductance gms_f varies linearly with the bias current I_{feed} fixed by the current mirror M4-M4b (equation 3.1). The transistor bulk is connected to ground, and the gate voltage is fixed, so that the source transconductance gms_f is the sum of the gate transconductance gm_f and of the bulk transconductance gmb_f:

$$gms_f = gm_f + gmb_f = \frac{\text{Ifeed}}{n\Phi_t} + (n-1)\frac{\text{Ifeed}}{n\Phi_t} = \frac{\text{Ifeed}}{\Phi_t} \qquad (3.1);$$

where $n = gms_f / gm_f$, and $\Phi_t = kT/q$ (~ 25 mV at 300 K).

The input transistor M1 is in common source configuration and amplifies the voltage variations of its gate. The gate to drain capacitance C_{gd1} of M1 loads the input node where it can be represented as an equivalent capacitance C_m to ground, which can be estimated by Miller’s theorem:

$$C_m = C_{gd1}(1 + gm_1 R_2) \qquad (3.2).$$

gm_1 is the input transistor gate transconductance and R_2 the resistance seen at the node 2. Adding a cascode transistor considerably lowers R_2 as it is then equivalent to the source transconductance of M2 (that can be made ~ 10^2 Ω), and therefore lowers C_m. The equivalent resistance R_{casc} of the cascode stage seen at the node 3 is given by equation 3.3. The gain of the cascode stage amplifier can then be estimated by equation 3.4 and is boosted by the cascode transistor M2 that increases the load resistance of the stage:

$$R_{casc} = r_{02} + [1 + (gm_2 + gmb_2)\, r_{02}]\, r_{01} \qquad (3.3);$$

$$A = \frac{V_{outb}}{V_{in}} = -gm_1 \,/\, (1/R_{casc} + 1/r_{03}) \qquad (3.4).$$

The resistance r_{03} corresponds to the output resistance of the current mirror transistor M3. Designing the transistor M3 with a long L permits to obtain a high r_{03} and a high gain.

The buffer output stage consists of a simple PMOS source follower. It provides an impedance adaptation. The preamplifier bandwidth strongly depends on the capacitive load C_L and on the resistive load of the cascode stage output (node 3 in Figure 3.2). The load capacitance at the preamplifier output node corresponds to the gate capacitance of the source follower, which can be made as small as 400 fF, in comparison with the standard load of 12 pF from an oscilloscope. It can be considered that no additional resistance is added in parallel to r_{03} and R_{casc}. The source follower then permits to readout the signal directly on an oscilloscope, without affecting too much the preamplifier bandwidth. The gain A_{buf} of the source follower stage is expressed, for an output load resistance R_{out}, as:

$$A_{buf} = \frac{gm_{buf}}{gm_{buf} + 1/R_{out} + 1/r_{0buf}} \qquad (3.5);$$

where gm_{buf} is the gate transconductance of M_{buf} and r_{0buf} its output resistance.

3.1.2. AFP Transfer Function

Different calculations of the frequency response and of the transient response of the Active Feedback Preamplifier presented in Figure 3.2 have been performed in this thesis work. The first studies have been carried out for the circuit frequency response calculated in the Laplace domain. A first simplified model of the AFP ("simple model") with 2 poles and a zero has been considered and is presented in 3.1.2.1. A model that considers each pole and zero of the circuit ("full model") has then been developed and is also presented in 3.1.2.1. The AFP circuit is linear in a limited range, and for high input signal its transient response cannot be precisely calculated from its frequency response calculated in the Laplace domain. Calculations have been carried out in the time domain to consider the non-linearity of the circuit, and results are presented in 3.1.2.2. Finally, the stability of the circuit has been studied by calculating the AFP loop gain frequency response and its phase margin. The calculations are presented in 3.1.2.3. The different calculations performed from the developed models have been compared with HSPICE simulations (done with the version BSIM3-v3).

3.1.2.1. Laplace domain simple and full model calculations

In the first study of the AFP transfer function, the internal poles and zeros of the cascode structure have been neglected. The cascode structure can be approximated with an input capacitance C_{in}, the transconductance gm_1 of M1 and an output impedance composed of the parallel combination of the total drain capacitance of M2 C_{dtot2} and the output resistance R_{casc} defined in equation 3.3. The AFP can then be represented and modeled as in Figure 3.3. The parameters of the transistors are referred by a subscript (1, 2, buf…) that corresponds to the transistor name given in Figure 3.2.

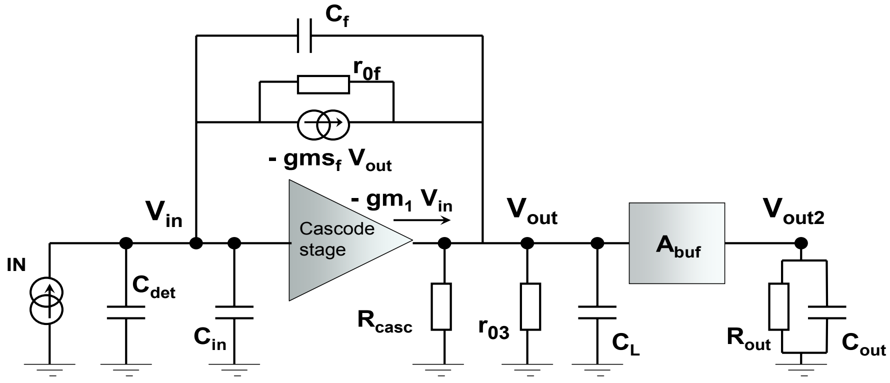

Figure 3.3. Schematic representation of the system with 2 poles and one zero.

The cascode stage equivalent input capacitance C_{in} and the capacitive load at the output node are defined as:

$$C_{in} = C_{gs1} + C_{gb1} + C_{gd1}\,(1 + \frac{gm_1}{gm_2 + gmb_2}) \qquad (3.6);$$

$$C_L = C_{gdbuf} + (C_{gsbuf} + C_{gbbuf})\,(1 - A_{buf}) + C_{dtot2} + C_{dtot3} \qquad (3.7);$$

where C_{gdbuf} (C_{gd1}), C_{gbbuf} (C_{gb1}), and C_{gsbuf} (C_{gs1}), are the capacitances at M_{buf} (M1) gate with respect to its drain, to the bulk and to its source.

To compute the transfer function, the currents are summed at the input and output nodes, and the following system of 2 equations is obtained:

$$IN = V_{in}\,(\frac{1}{r_{0f}} + s\,(C_{in} + C_{det} + C_f\,)) - V_{out}\,(gms_f + \frac{1}{r_{0f}} + s\,C_f\,) \qquad (3.8);$$

$$V_{out}\,(gms_f + \frac{1}{r_{0f}} + \frac{1}{r_{03}} + \frac{1}{R_{casc}} + s\,(C_L + C_f)) - V_{in}\,(-gm_1 + \frac{1}{r_{0f}} + s\,C_f\,) = 0 \qquad (3.9).$$

After a straightforward calculation of the system, using the assumptions that $1/R_L = 1/r_{03} + 1/R_{casc}$, that $1/r_{0f}$ is much smaller than gms_f, $1/R_{casc}$, $1/r_{03}$ or gm_1, and that $gm_1 >> 1/R_L$, the AFP transimpedance $H[s] = V_{out} / IN$ can be written as :

$$H[s] = \frac{-1}{gms_f} \times \frac{1 - s\, C_f/gm_1}{1 + s\,\frac{(C_f\, gm_1 + (C_{in} + C_{det})(1/R_L + gms_f))}{gm_1\, gms_f} + s^2\,\frac{(C_{in} + C_{det})(C_L + C_f)}{gm_1\, gms_f}} \quad (3.10).$$

The derived transfer function presents a dc gain equal to $-1/gms_f$, two poles and one zero z_1. Supposing that the two poles are real and that one of the two is dominant, the dominant and non dominant poles ω_d and ω_{nd} can be calculated and:

$$\omega_d = -\frac{gm_1}{C_f\,\frac{gm_1}{gms_f} + \left(C_{in} + C_{det}\right)\frac{gms_f + 1/R_L}{gms_f}} \quad (3.11);$$

$$\omega_{nd} = -\frac{C_f\,\frac{gm_1}{(C_{in} + C_{det})} + gms_f + 1/R_L}{(C_f + C_L)} \quad (3.12).$$

Supposing that $1/R_L << gms_f$, and that no feedback capacitance is added ($C_f = 0$), the 2 poles can be simply expressed as: $\omega_d = -\, gm_1/(C_{in}+C_{det})$ and $\omega_{nd} = -\, gms_f/C_L$.
These simplified equations show that the dominant pole of the circuit is controlled by the input transistor transconductance and by the capacitances of the detector and at the gate of the input transistor. These capacitances have to be kept low and the input transistor transconductance high to move the first pole to high frequencies and to increase the bandwidth. The second pole depends on the feedback transconductance and on the capacitive load at the cascode stage output. If the first pole is moved to high frequencies to optimize the circuit speed response, the second pole also has to be moved to higher frequencies to ensure the stability of the circuit. The load capacitance, which is mainly defined by the buffer load capacitance, has then to be kept small. The second pole can be further moved to higher frequencies by improving the transconductance of the feedback transistor. To optimize the speed response of the circuit, the capacitances at the circuit input and at the cascode output stage have thus to be kept as small as possible, and the input transistor and feedback transistor transconductances have to be high. However, increasing the feedback transistor transconductance also lowers the circuit gain, as the DC gain of the circuit frequency response is inversely proportional to gms_f (equation 3.10). A trade off between speed, gain and stability of the AFP circuit has to be defined.

Depending on the optimization and on the biasing conditions of the AFP, the two poles can become close and can also be found as complex conjugates. In these conditions, the natural resonant pulsation ω_0 and the damping ratio ξ of the system calculated from equation 3.10 are:

$$\omega_0 = \sqrt{\frac{gms_f\ gm_1}{(C_{in} + C_{det})(C_f + C_L)}} \qquad (3.13);$$

$$\xi = \frac{1}{2}\frac{(gm_1\ C_f + (C_{in} + C_{det})/R_L)}{\sqrt{gm_1\ gms_f\ (C_{in} + C_{det})(C_f + C_L)}} \qquad (3.14).$$

The buffer stage frequency response presents one pole ω_{buf} and one zero z_{buf}, with the DC gain A_{buf}:

$$H_{buf}[s] = V_{out2}/V_{out} = A_{buf}\frac{(1 + s\,C_{gsbuf}/gm_{buf})}{(1 + s\,(C_{gsbuf} + C_{sbbuf} + C_{out})/(1/R_{out} + gm_{buf}))} \qquad (3.15).$$

The buffer zero and pole are usually at higher frequencies than the two poles of the feedback preamplifier stage. The DC gain A_{buf} strongly depends on the resistance R_{out} (equation 3.5) that will load the AFP output. The source follower has to be designed with a minimum gate capacitance, which will load the cascode stage output, but at the same time with a high gm_{buf} in order to drive with a sufficient gain a low output resistance.

The AFP chip has been designed in a 0.25 µm CMOS technology and comprises 32 channels of a similar active feedback preamplifier [Ane03]. The optimization of each transistor sizes and biases are presented in section 3.1.4 but are used in all the present section to illustrate the different models. The nominal parameters are:

gm_1 = 16.5 mS	gms_f = 7.2 µS	gm_{buf} = 7.8 mS	R_L = 45 kΩ
C_{in} = 3.4 pF	C_f = 50 fF	C_L = 340 fF	

The two dominant poles calculated for these nominal parameters are complex conjugates, and: $\xi = 0.93$; $\omega_0 = 2.23\times10^8$ rad/s.

The AFP channel analog output can be directly readout on an oscilloscope using a decoupling series capacitance between the channel output and the 50 Ω load of the oscilloscope. Without this capacitance, the current set by the buffer current mirror would flow into the oscilloscope low resistance, switching off the buffer transistor. The resistive load of 50 Ω and the capacitive load of ~ 12 pF of the oscilloscope do not affect the preamplifier bandwidth thanks to the impedance adaptation provided by the source follower. However, the readout being performed on a low resistance, the buffer stage exhibits a low gain: the load conductance is of 20 mS, and for the AFP nominal parameters, gm_{buf} = 7.8 mS, so that a gain of 0.27 only is achieved. The pole and the zero associated to the buffer are: $\omega_{buf} = -2.24\times10^9$ rad/s; $z_{buf} = -3.22\times10^{10}$ rad/s.

The closed loop transfer function $H_{AFP}[s]$ of the AFP amplifier, and its frequency response $V_{out}[s]$ and time domain response $V_{out}[t]$ to an input pulse In[s] can be calculated:

$$H_{AFP}[s] = H[s] \times H_{buf}[s] \tag{3.16}$$

$$V_{out}[t] = L^{-1}[V_{out}[s]] = L^{-1}[H_{AFP}[s] \times In[s]] \tag{3.17}.$$

The buffer pole and zero can be neglected and the AFP transfer function can be considered in a simple model as $H[s] \times A_{buf}$. The transient response of the resulting second order feedback system is calculated in appendix 1. For a delta of Dirac input current pulse of charge Q, the output pulse rise time and gain can be analytically defined by:

$$t_{max} = \frac{1}{\omega_0} F_1[\xi] \quad (3.18); \qquad V_{outmax} = \frac{-\omega_0 \, Q \, A_{buf}}{gms_f} F_2[\xi] \quad (3.19).$$

$F_1[\xi]$ and $F_2[\xi]$ are decreasing functions of the damping ratio (appendix 1). For complex poles, i.e. for $\xi < 1$, the transient response overshoot and time to return to zero can also be calculated analytically (appendix 1).

The frequency and the transient responses of the AFP preamplifier have been calculated using the software Mathematica and the simple model defined before. The transient response of the AFP preamplifier to a 2 fC input signal obtained by a rectangular current pulse with 2 µA amplitude and 1 ns pulse width are presented for different parameters in Figures 3.4 and 3.5. It can be seen from equations 3.18, 3.19 and 3.13 that to get a fast peaking time of the circuit response, and high output signal amplitude, a high gm_1 is needed, together with a low cascode load capacitance and low input capacitances. This is illustrated in Figure 3.4.

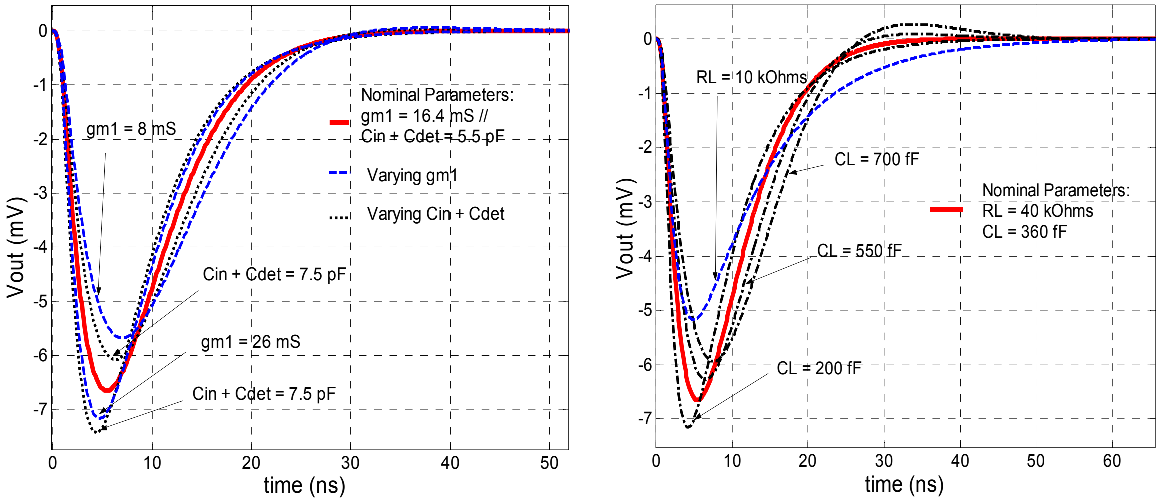

Figure 3.4. AFP response to a 2 fC input charge, for different values of R_L, gm_1, C_L and C_{in}, using the transfer function simple model.

The feedback transistor controls the gain and the speed response of the circuit: a low gms_f will lead to increased output pulse amplitude but at the same time to increased peaking time. The decay of the output pulse is ensured by the dynamic current derived in the feedback transistor. The lower is the feedback transconductance, the lower will be the current derived, and the pulse discharge will be slower. A low gms_f thus also leads to a longer time to return to zero. For high gms_f, the damping ratio (equation 3.14) becomes smaller and this might lead to instability of the circuit. A trade off between speed on one hand and gain and stability on the other hand has to be defined for the choice of gms_f (Figure 3.5).

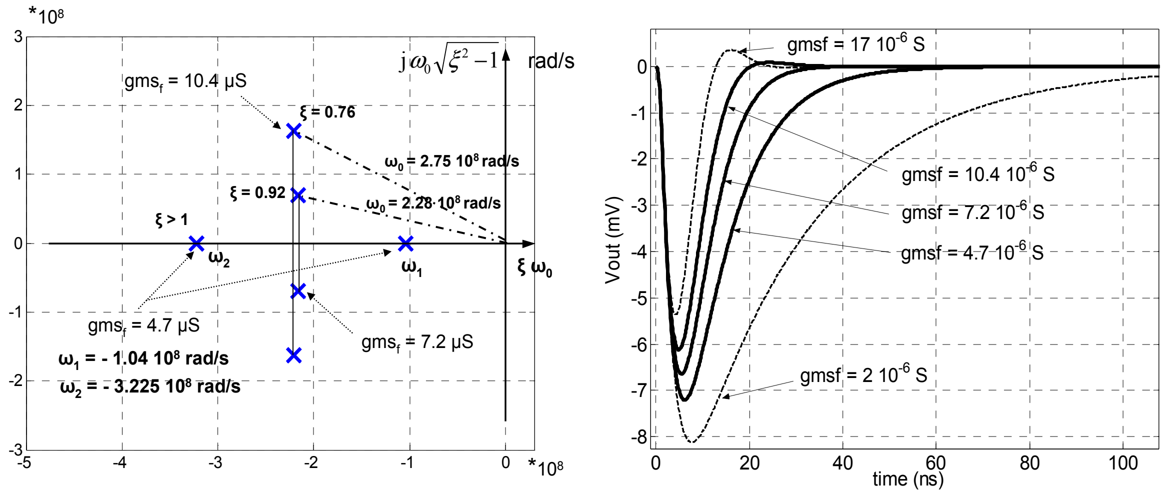

Figure 3.5. Poles location (left) and AFP response to a 2 fC input charge (right), for different gms_f, using the transfer function simple model.

For an accurate model of the AFP preamplifier, the inner structure of the cascode amplifier has to be included. The pole at the node 2 (Figure 3.2) can be estimated as:

$$\omega_{n2} = (gm_2 + gmb_2)/(C_{gd1} + C_{db1}) \tag{3.20}$$

The nominal parameters lead to $\omega_{n2} \sim 1.8\times10^9$ rad/s. A second analysis has been performed considering the whole AFP structure. Each parameter of each transistor has been accounted for in the model. By summing the currents at the 4 nodes of the circuit, a system of 4 equations has been established. The resolution of the 4 equation system leads to a "full model" of the AFP transfer function, $H_{AFPfull}[s]$. The AFP frequency response and transient response have been analytically calculated with Mathematica for the full model. The system of 4 equations and the analytical equations defining the frequency and the transient responses equations are not presented in the thesis as they are cumbersome equations. Only the frequency and transient responses calculated from the derived analytical equations using nominal biases of the AFP chip are presented in Figure 3.6. The results are compared with the simple model and HSPICE simulations of the circuit. The simple model frequency response fits the HSPICE simulation up to a frequency of 280 MHz, which corresponds to the frequency of the cascode structure internal pole. The full model responses are in a fairly good agreement with the HSPICE simulations (Figure 3.6). There is, however, a difference visible in Figure 3.6 right, between the full model calculations of the transient response and the HSPICE simulations. This is discussed in more details in the following section.

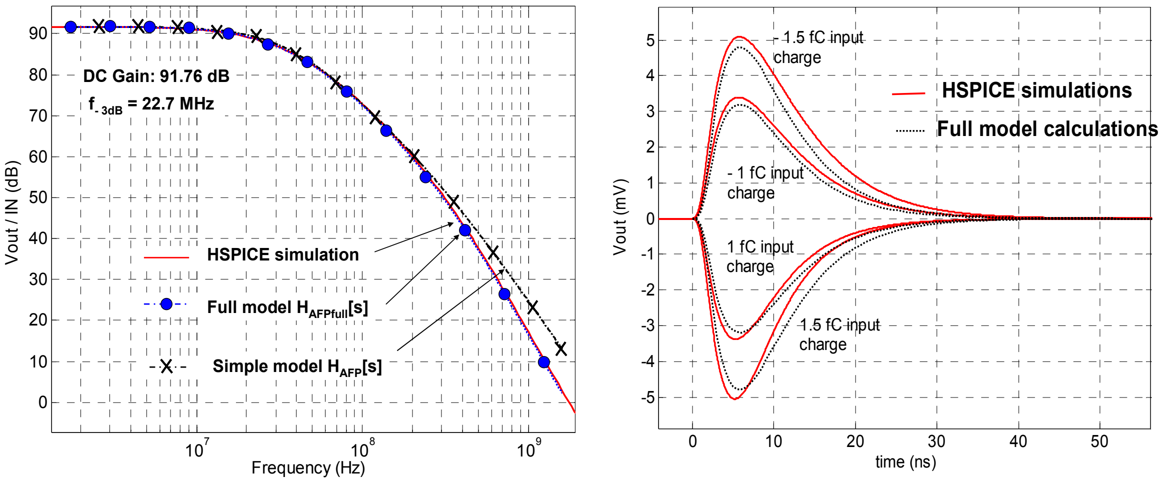

Figure 3.6. (Left): Frequency response of AFP for the full and simple models and obtained with HSPICE simulations. (Right): AFP output signal response to negative and positive input charges calculated with Full model and simulated with HSPICE.

3.1.2.2. Model Limitations: Dynamic variations of gms_f

The two models that I have defined are based onto the assumption of a linear amplifier response, and the calculations are based on a Laplace representation, using small signal equivalent circuits. However, it can be observed that the AFP transient response depends also on the input signal amplitude. Figure 3.7 represents the evolution of the AFP transient response simulated with HSPICE and calculated with the full model, while increasing the input charge.

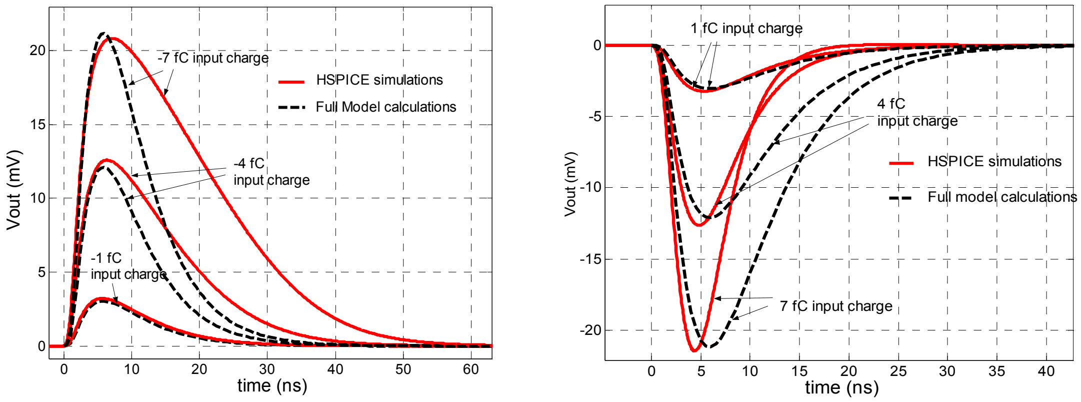

Figure 3.7. AFP transient response to positive and negative input charges of 1 fC, 4 fC and 7 fC, simulated with HSPICE and calculated.

As the input charge gets higher, the model becomes less and less accurate to represent the AFP time response. The variations between the model and the simulations are also non-symmetric for positive or negative input charges.

The feedback transistor is biased in weak inversion, with a DC current I_{feed}. When a current pulse is applied at the preamplifier input, the cascode stage output voltage is varied, V_{out} representing the variations of this voltage around its DC value. The feedback transistor V_{GS} is varied, and equals V_{GSdc} - V_{out} (V_{GSdc} being its static value that corresponds to I_{feed}). The feedback current then changes and provides the decay of the voltage step. The dynamic feedback current δI_{feed} corresponds to the difference between the total feedback current and I_{feed}. It can be calculated as:

$$I_{f\,eed} = I_0 \exp\left(\frac{V_{GSdc}}{n\,\Phi_T}\right) \tag{3.21}$$

$$\delta I_{feed} = I_0 \exp\left(\frac{V_{GSdc} - V_{out}}{n\,\Phi_T}\right) - I_0 \exp\left(\frac{V_{GSdc}}{n\,\Phi_T}\right) = I_{feed}\left[\exp\left(\frac{-V_{out}}{n\,\Phi_T}\right) - 1\right] \qquad (3.22).$$

When the voltage variations at the cascode output are small ($V_{out} << n\ \Phi_T$), simplifications of equation 3.22 lead to the small signal equivalent transconductance gms_f to describe the dynamic feedback current:

$$\delta I_{feed} = I_{feed}\left[\exp\left(\frac{-V_{out}}{n\,\Phi_T}\right) - 1\right] \cong I_{feed}\left[1 - \frac{V_{out}}{n\,\Phi_T} + 1\right] = -gms_f\ V_{out} \qquad (3.23).$$

The models that have been calculated from the circuit small signal analysis are thus based on the assumption of a small cascode output voltage. For higher input charges, the cascode output signal V_{out} has a higher magnitude and the current δI_{feed} cannot be approximated anymore as in equation 3.23, but has to be considered as in equation 3.22. Positive (respectively negative) input charges create negative (positive) output voltage variations V_{out}, and for high output voltage variations, the current δI_{feed} derived will be higher (lower) than gms_f V_{out}. The time to discharge the output node is then decreased (increased), as it can be seen in Figure 3.7. The system response is non-linear: its transfer function varies with the output signal amplitude, and for high input charges, the accurate output signal shape cannot be calculated using the models developed in the Laplace domain. It can be calculated through a direct calculation in the time domain.

A mathematical solution has been found using Mathematica, but is limited to the numerical solution of a non-linear system of second order differential equations. Calculations have then been performed considering only the two first poles represented in Figure 3.3. By summing the currents at the 2 nodes, the following system of differential equations is obtained:

$$IN - \frac{1}{r_{0f}} V_{in} + \left(C_{in} + C_f + C_{det}\right)\frac{dV_{in}}{dt} + \frac{1}{r_{0f}} V_{out} + C_f \frac{dV_{out}}{dt} - I_{feed}\left(\exp\left(\frac{-V_{out}}{n\Phi_T}\right) - 1\right) = 0 \quad (3.24)$$

$$\frac{1}{R_L} V_{out} + \left(C_L + C_f\right)\frac{dV_{out}}{dt} - I_{feed}\left(\exp\left(\frac{-V_{out}}{n\Phi_T}\right) - 1\right) + gm_1\, V_{in} - C_f \frac{dV_{in}}{dt} = 0 \quad (3.25).$$

The solution of these equations for an input current IN gives the transient response of the preamplifier before the buffer stage. The calculations have been done for nominal biases, and the results obtained are presented in Figures 3.8 and 3.9, in comparison with HSPICE simulations and calculations performed in the Laplace domain.

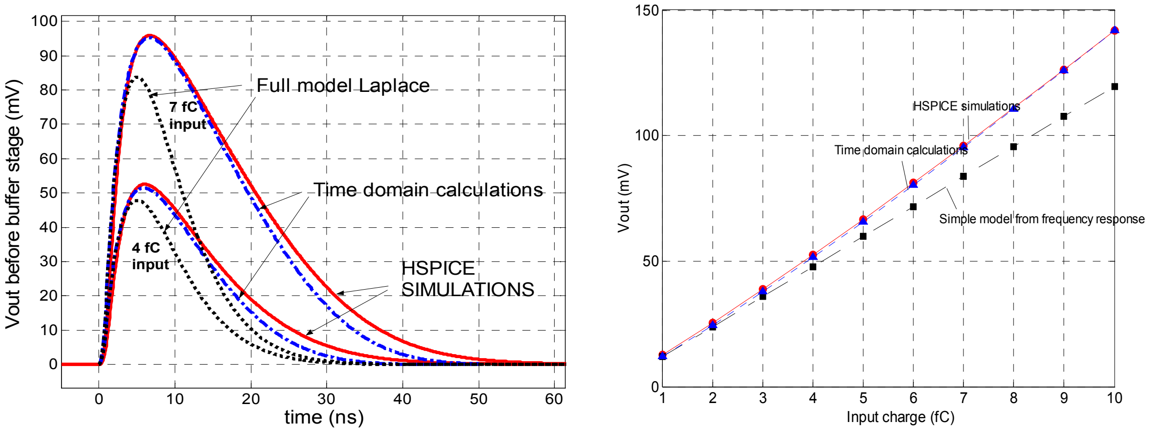

Figure 3.8. Transient pulse response before the buffer stage calculated with the linear model and the non-linear model, and simulated with HSPICE.

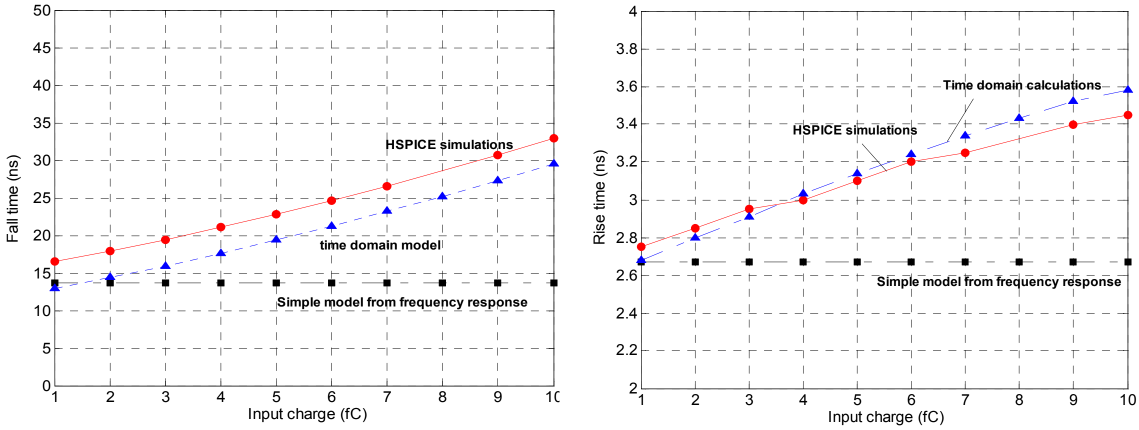

Figure 3.9. Transient pulse response, before the buffer stage, fall time (left) and rise time (right) calculated with the linear model and the non-linear model, and simulated with HSPICE.

The calculations are limited to a 2 pole system, so that the buffer pole and zero cannot be included. The results are presented for the response before the buffer stage for this reason, but the output signal can be approximated by multiplying the calculated signal by A_{buf}.

The model developed is well improved and does include the transfer function variations with the input signal amplitude. For charges above 4 fC, the output signal amplitude of the AFP channel is increased in comparison with the model calculated on a small-signal analysis. The rise time and fall time are also increased, and the model developed in the time domain does fit well the simulations. A difference in the fall time of the signals calculated in the time domain model and simulated is still observed (Figure 3.9 left). This difference does not vary with the input charge and has not been fully understood yet.
For high positive input charges, the exact opposite behavior occurs, as the effective dynamic feedback current becomes more important. As the input charge increases, the rise time, gain and fall time thus decrease.

3.1.2.3. Stability Considerations

A trade off has to be defined between the bandwidth, the gain, the stability and the noise performance. When increasing the bandwidth and so improving the speed response of the AFP preamplifier, the danger is to attain a non stability of the circuit, as the two first poles are then found as complex conjugates. The stability can be determined by examining the loop gain of the circuit as a function of the frequency. The AFP loop can be opened at the input transistor gate to calculate the loop gain. A voltage AC signal is applied as input on the input transistor gate, the output signal being the voltage variation at the node defined at the feedback transistor drain. The loop frequency response A[s] has been calculated by summing the currents at the 3 different nodes in the Laplace domain, and by solving the system obtained. A[s] shows a dc gain, 3 poles and one zero that can be estimated by:

$$A_{dc} \sim gm_1\, gms_f/(1/r_{03}(1/r_{0f}+1/r_{mf})+gms_f/r_{mf}) \quad (3.26); \qquad z_1 \cong gms_f/C_f \quad (3.27);$$

$$\omega_1 \cong \frac{1/r_{mf}+1/r_{0f}}{C_{in}+C_{det}} \quad (3.28); \qquad \omega_2 \cong \frac{1/R_L+gms_f}{C_L+C_f} \quad (3.29); \qquad \omega_3 \cong \frac{1/r_{01}+gm_2}{C_2+C_{gd1}} \quad (3.30).$$

The loop frequency response of the AFP preamplifier calculated and simulated for the nominal AFP parameters are represented by Bode plots in Figure 3.10 left. The phase margin is estimated to be 70 degrees for nominal biases. The stability of the circuit depends on the DC gain, and on the two first poles and the main zero locations. By increasing the gain, or shifting the poles to higher frequencies, the circuit becomes less stable. The feedback capacitance is added for compensation of the circuit and controls the added zero. Its effect on the AFP transient response to a Dirac input current pulse of 2 fC is presented in Figure 3.10 right. As it increases, the circuit becomes more stable. Decreasing the speed response of the circuit by increasing either the input transistor transconductance or the feedback transistor gms_f degrades the circuit phase margin. The load capacitance C_L has to be kept small for stability reasons, and the third pole has to be kept at much higher frequencies.

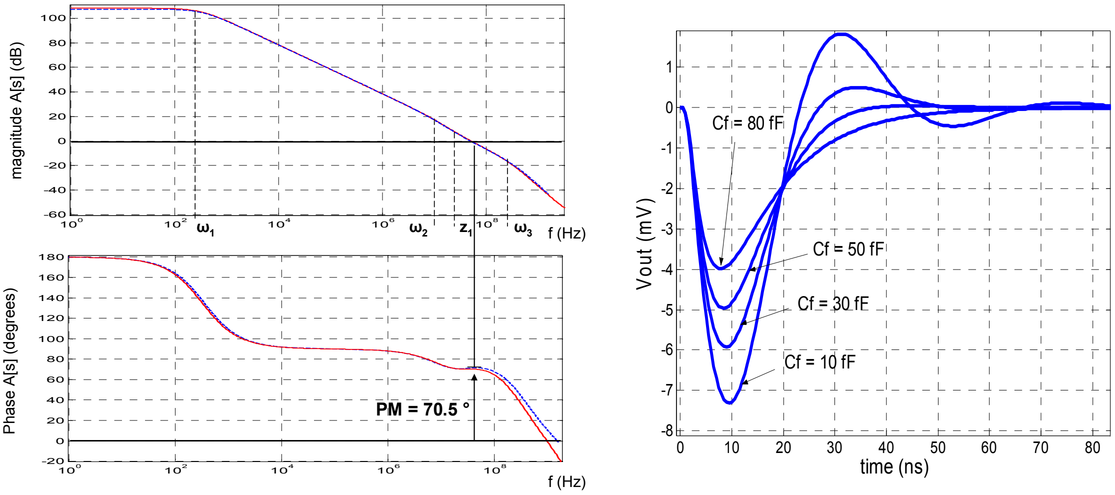

Figure 3.10. Left: Bode diagrams of the AFP loop A[s] gain and phase using nominal parameters, calculated with the loop model and simulated with HSPICE (BSIM3-v3). Right: Transient response to a 2 fC input charge, calculated with the full model for different feedback capacitance.

3.1.3. Evaluation of the AFP noise performance

The evaluation of the noise performance of the AFP circuit is presented in this section. The noise sources in MOS transistors are first presented in 3.1.3.1. The calculation of the propagation of the noise sources to the output noise, and the estimation of the dominant sources of noise of the circuit are presented in 3.1.3.2.

3.1.3.1. Noise sources in MOS transistors

The random motion of free carriers within the MOS channel generates thermal noise at the device terminals. A global variation of the drain current i_{nd} is generated at the drain electrodes, and its calculation for a MOS in saturation and in any regime is described in [Ane01], and can be expressed as:

$$\overline{i_{nd}^{\,2}} = 4\,k\,T\,n\,\gamma\,gm\,\Delta f \qquad (3.31);$$

where gm is the transistor gate transconductance. The bias dependent factor γ is determined by the excess noise factor Γ, which accounts for the excess noise observed in short channel devices, and by the region of operation of the transistor, calculated with the inversion coefficient IC. The factor γ varies from 1/2 Γ to 2/3 Γ from weak to strong inversion and can be calculated using the following formulae [Ane01]:

$$\gamma = \Gamma\left(\frac{1}{2}+\frac{2}{3}\,\frac{IC}{(\sqrt{4\,IC+1}+1)^2}\right) \quad (3.32); \qquad IC = \frac{I_{ds}}{(W/L)\,\mu\,C_{oxu}\,2\,n\,V_T^{\,2}} \quad (3.33);$$

where I_{ds} is the drain current, W and L are the effective channel width and length, μ the mobility of the carriers in the channel, and C_{oxu} the gate oxide capacitance per unit of area. Fluctuations of the channel charge will also induce a physical current in the gate, due to a capacitive coupling through the transistor gate capacitance. This gate induced current noise (GIC) varies with the square of the frequency, so that it is the dominating source of noise of a MOS device at very high frequencies. It was first modeled by Van der Ziel [Van86]. Its power spectral density can be estimated, for a non-ideal device working in any inversion condition, as [Van86]:

$$\frac{\overline{i_{ng}^{\;2}}}{\Delta f} = 8\,\gamma\,k\,T\,g_{gs} \qquad \text{where} \qquad g_{gs} = \frac{4}{45}\frac{\omega^2 (C_{oxu} WL)^2}{n\,gm} \tag{3.34}$$

To evaluate the thermal noise at high frequencies, one must also calculate the cross correlation between the channel thermal noise and the gate induced current noise, which can be described by [Van86, Kap04]:

$$\frac{\overline{i_{ng} . i_{nd}^{\;*}}}{\Delta f} = \frac{1}{9}\,j\,\omega\,(C_{oxu}\;W\,L)\,4\,k\,T\,\gamma \tag{3.35}$$

The third important source of noise in MOS transistors is the so-called 1/f or flicker noise, which dominates the MOS transistor noise at low frequencies. It is presented in details in [Cha91]. In the usual model, the flicker noise is accounted for by a current source generator between drain and source with power spectral density given by:

$$\frac{\overline{i_{nf}^{\;2}}}{\Delta f} = \frac{K_a}{f^{\alpha}}\,\frac{gm^2}{C_{oxu}^{\;2}\,W\,L} \tag{3.36}$$

where α is a parameter close to 1. The technology dependent parameter K_a expresses the noise characteristic of a given process, and should be constant for the devices of a given process with two different values for n-channel and p-channel transistors.

The other sources of noise found in a full description of MOS transistors are the noise associated to the gate resistance and to the bulk resistance. They are presented in details in [Cha91, Van86], and have been considered as negligible for the noise calculations carried out in this chapter. The calculations are based on the equivalent MOS model presented in Figure 3.11.

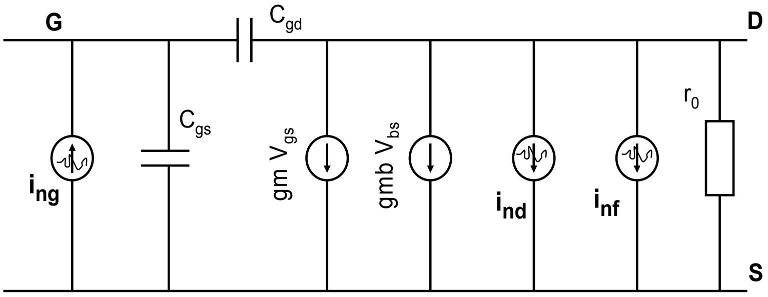

Figure 3.11. Simplified small signal circuit of a MOS with equivalent noise sources.

3.1.3.2. Calculation of Equivalent Noise Charge

The estimation of the noise performance of the Active Feedback Preamplifier first involves the calculation of the power spectral densities of the different sources of noise. They can be evaluated for each MOS transistor of the circuit if both the excess noise factor Γ and the flicker noise coefficient K_a are defined. For the IBM 0.25 µm CMOS technology, these factors can be found in [Ane01], and are listed in Table 3.1.

Symbol	**Parameter description**	**Value**	
Γ	Excess noise factor	1.3	PMOS in M.I[1] (M1)
		1.1	NMOS in M.I[1] (Mf)
K_a	Flicker noise coefficient	$0.6\times10^{-27}\ C^2/m^2$	PMOS
		$1\times10^{-27}\ C^2/m^2$	NMOS
$\mu\ C_{ox}$	Mobility × oxide capacitance	70 $\mu A/V^2$	PMOS
		300 $\mu A/V^2$	NMOS

Table 3.1 : Definition of some IBM 0.25 µm CMOS technology parameters used in the noise calculations.

The output noise of the preamplifier is calculated by evaluating the propagation of the noise sources to the preamplifier output. All contributions to the output noise can be calculated separately and then added quadratically. The method consists in calculating for each noise source its power spectral density $\overline{i_n^2}/\Delta f$ and its transfer function $H_{nout}[s]$ to the preamplifier output. The propagated noise at the output is then given by the rms output voltage v_n:

$$v_{n\,rms} = \left(\int_0^{\infty} \frac{\overline{i_n^2}}{\Delta f} (H_{nout}[j\times 2\pi f])^2 \, df \right)^{1/2} \qquad (3.37).$$

---

[1]: The excess noise factor increases for transistors operating in strong inversion (S.I): $\Gamma \sim 2.25$ for an NMOS transistor with L > 1 µm, as M3 and M5, and $\Gamma \sim 2$ for a PMOS with L = 360 nm (M2) [Ane01].

It is convenient to express the noise characteristics of the electronic readout in Equivalent Noise Charge (ENC). The output noise is expressed as an equivalent noise source at the circuit input. The referred input noise expressed by a charge (ENC) is calculated by estimating the output noise v_{nrms} and the maximum amplitude of the circuit output signal for an input charge of one e^-. By dividing the output noise by this maximum, one obtains the ENC in e^- rms. Calculations of the contributions to the output noise of the different noise sources of the different MOS transistors in the AFP circuit have been performed. The input transistor turns out to provide the dominant sources of noise. The propagation of the thermal noise is calculated by first extracting the transfer function V_{out} / i_{M1th}, where V_{out} is the AFP output voltage and i_{M1th} is a current source placed between the drain and the source of the input transistor. The transfer function can be simply evaluated as:

$$H_{M1th}[s] \cong \frac{Abuf}{r_{0f}\, gm_1\, gms_f} \cdot \frac{(1+ s\, r_{0f}\, (C_{in} + C_{det} + C_f))}{(1+2\, s\, \xi/\omega_0 + s^2/\omega_0{}^2)\,(1+ s/\omega_{n2})} \qquad (3.38);$$

where the two dominant poles are equivalent to the complex poles of the AFP transfer function, so that ω_0 and ξ are defined by equations 3.13 and 3.14, and where ω_{n2} is the internal pole of the cascode stage defined by equation 3.20.

These poles control the AFP frequency response, the system stability, and the noise propagation, so that increasing the bandwidth of the system irremediably increases the system output noise.

The noise contributions from the input transistor to the referred noise at the circuit input can then be expressed in equivalent noise charge as:

$$ENC_{M1} = \sqrt{ENC_{M1th}{}^2 + ENC_{M1GIC}{}^2 + ENC_{M1corr}{}^2 + ENC_{M1flicker}{}^2} \qquad (3.39);$$

$$ENC_{M1th} = \frac{1}{V_{max}} \sqrt{\frac{\overline{i_{M1th}{}^2}}{\Delta f}} \left(\int_0^\infty (H_{M1th}[j \times 2\,\pi\, f])^2\, df \right)^{1/2} \qquad (3.40);$$

$$ENC_{M1GIC} = \frac{1}{V_{max}} \left(\int_0^\infty \frac{\overline{i_{M1GIC}{}^2}}{\Delta f} (H_{AFPfull}[j \times 2\,\pi\, f])^2\, df \right)^{1/2} \qquad (3.41);$$

$$ENC_{M1corr} = \frac{1}{V_{max}} \left(\int_0^\infty \frac{\overline{i_{M1th} \times i_{M1GIC}}}{\Delta f} (H_{M1th}[j \times 2\,\pi\, f]) \times (H_{AFPfull}[j \times 2\,\pi\, f])\, df \right)^{1/2} \qquad (3.42);$$

$$ENC_{M1fl} = \frac{1}{V_{max}} \left(\int_0^\infty \frac{\overline{i_{M1flicker}{}^2}}{\Delta f} (H_{M1th}[j \times 2\,\pi\, f])^2\, df \right)^{1/2} \qquad (3.43).$$

V_{max} is the maximum of the output signal pulse, and can be approximated by the equation 3.19. The AFP circuit is a fast pre-amplifier, with a peaking time that can be set to less than 5 ns, and the gate of the input transistor is connected to the circuit input. The GIC noise has then to be carefully taken into account. This noise is represented by a current source at the input transistor gate. The contribution of the GIC noise to the output noise can then be expressed by equation 3.41, where $H_{AFPfull}[s]$ is the AFP transfer function calculated in 3.1.2. From the definitions of the thermal noise and of the GIC noise propagations, the correlation term can also be calculated by solving the equation 3.42. The flicker noise is dominant only at low frequencies, and presents very small contribution to the output noise in the AFP circuit. For nominal biases of an AFP channel integrated in the AFP chip, the following noise contributions have been calculated, for a 2 pF detector capacitance:

ENC_{M1th}	ENC_{M1GIC}	ENC_{M1corr}	ENC_{M1fl}	**ENC_{M1}**
338 e^- rms	68 e^- rms	142 e^- rms	7 e^- rms	**373 e^- rms**

The input transistor thermal noise contribution to the output noise dominates the noise performance and is usually referred to as the series white noise in Charge Sensistive Amplifiers (CSA) [Oco01]. This contribution, defined by equation 3.40, can be calculated analytically. It is equivalent in the time domain to:

$$ENC_{M1th} = \frac{1}{V_{max}} \sqrt{\frac{\overline{i_{M1th}^{2}}}{\Delta f}} \left(\frac{1}{2} \int_{0}^{\infty} \left| L^{-1}\left\{ H_{M1th}[-j \times 2\pi f] \right\} \right|^{2} dt \right)^{1/2} \qquad (3.44).$$

The integral can be calculated analytically by considering the transfer function $H_{M1th}[s]$ approximation defined in equation 3.38. Its Inverse Laplace transform has been calculated, squared, and integrated, and the following equation has been obtained:

$$\left(\frac{1}{2} \int_{0}^{\infty} \left| L^{-1}(H_{M1th}[-j.2\,\pi\pi f] \right|^{2} df \right) \cong \frac{A_{buf}^{2}}{(r_{0f}\ gm_{1}\ gms_{f})^{2}} \frac{\omega_{0}^{3}}{8 z_{1}^{2} \xi} \times \left(\frac{1}{(1+\omega_{0}^{2}/\omega_{n2}^{2})} \right) \qquad (3.45).$$

The third pole ω_{n2} is usually at much higher frequencies than the complex poles, so that the expression into brackets in equation 3.45 can be set to 1. By substituting equation 3.45 together with the equation 3.19 that defines the voltage pulse maximum into equation 3.40, the following ENC is obtained:

$$ENC_{M1th} = \left(\omega_{0} \frac{4\,k\,T\,n\,\gamma\,(C_{in} + C_{det} + C_{f})^{2}}{q^{2}\ gm_{1}} \frac{1}{F_{2}(\xi)^{2}\ 8\,\xi} \right)^{1/2} e^{-}{}_{rms} \qquad (3.46)$$

where q is the electron charge.

The equivalent noise charge contribution from the input thermal noise can finally be expressed with respect to the pre-amplifier peaking time t_{max}, given in equation 3.18, as:

$$ENC_{M1th} = \frac{(C_{in} + C_{det} + C_f)}{q} \left(\frac{4\,k\,T\,n\,\gamma}{gm_1\; t_{max}} \right)^{1/2} \times F_3(\xi) \qquad e^-_{\ rms} \qquad (3.47)$$

where

$$F_3(\xi) = F_1(\xi) / \left(8\,\xi\,F_2(\xi)^2\right) \qquad (3.48).$$

$F_1(\xi)$ and $F_2(\xi)$ are defined in appendix 1. The function $F_3(\xi)$ varies very little with ξ, and is comprised between 1 and 0.96 for a damping ratio varying between 0.5 and 2.

The analytical and general calculation of the ENC contribution from the input transistor thermal noise in a Charge Sensitive Amplifier (CSA) and in an AFP with a shaper can be respectively found in [Cha91] and in [Kap04]. The equation 3.47 that I have obtained is in agreement with the general expression, with a noise proportional to the total input capacitance of the circuit, and inversely proportional to the square root of the input transistor transconductance and of the circuit peaking time. However, in our equation, the shaping time t_{max} also varies with the input capacitance and the input transistor transconductance, as it is shown in equations 3.18, 3.13 and 3.14. The induced variations slightly change the noise variation with the input capacitance and the transconductance, but the noise optimization of the circuit still consists in minimizing the Cgs/gm ratio for the input transistor, as it is presented in [OCo01], and by keeping the transistor operating in weak inversion to minimize the excess noise factor. Variations of the ENC contribution from the input transistor thermal noise are shown in Figure 3.12 for different detector capacitances and for AFP nominal biases. The total input capacitance of the circuit is for the defined biases of 3.4 pF + C_{det}.

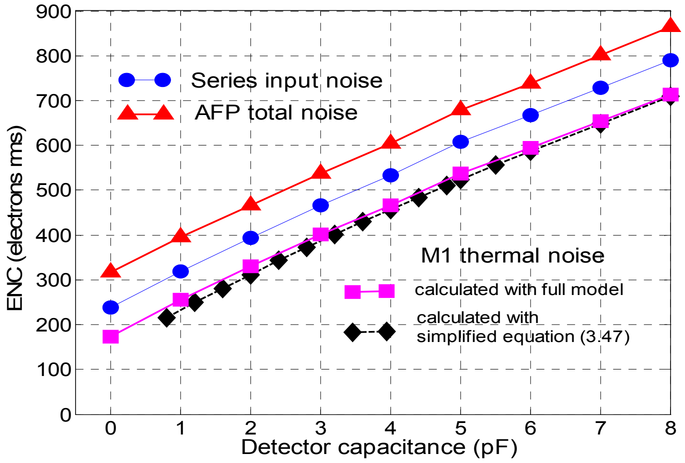

Figure 3.12. Left: Variations of the ENC noise induced by the input transistor thermal noise, by the noise sources of M1 and M5 (series input noise) and of the total ENC noise of the AFP circuit, for different detector capacitances and nominal biases.

Secondary noise sources have an important contribution to the global noise performance of the circuit. The different contributions for each transistor have been calculated, and the secondary noise sources are presented in Figure 3.13.

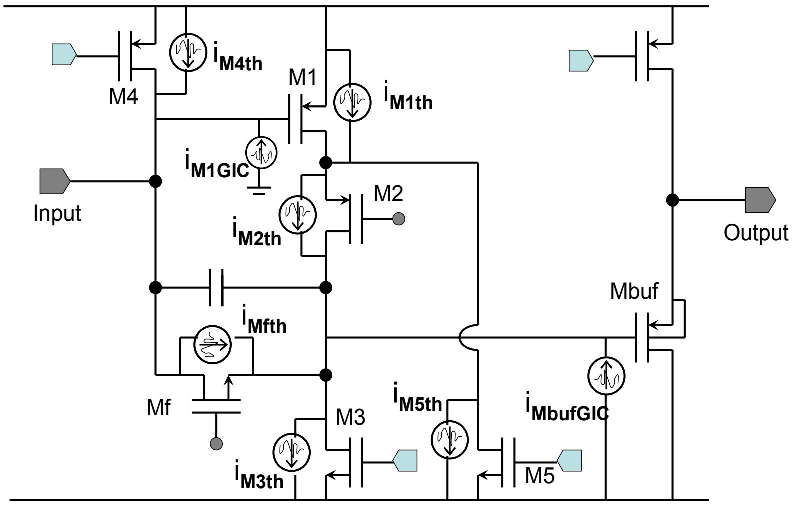

Figure 3.13. Schematic of an AFP channel with the added primary and secondary current noise sources.

The channel thermal noises of the feedback transistor and of the non-diode connected transistor M4 are important, as they are directly connected to the preamplifier input node. They are usually referred to as the circuit parallel noise. Their contributions to the circuit ENC (ENC_{Mth}) can be calculated analytically with the same method used to calculate the contributions of the input transistor thermal noise. The power spectral densities are referred to as $\overline{i_{Mth}^{2}}/\Delta f$. The transfer function that expresses the contribution of these noise sources to the output noise is the circuit transfer function. To perform an analytical calculation, the simple model presented in 3.1.2.1 is considered. The transfer function can be written as $H_{AFPsimp}[s] = H[s] \times A_{buf}$. H[s] is expressed in equation 3.10 and A_{buf} is the buffer stage gain. The calculation of the integral of the square of the transfer function has been performed in the time domain, so that the ENC contribution of either M4 thermal noise or Mf thermal noise can be expressed as:

$$ENC_{Mth} = \frac{1}{V_{max}} \sqrt{\frac{\overline{i_{Mth}^{2}}}{\Delta f}} \left(\frac{1}{2} \int_{0}^{\infty} \left| L^{-1}(H_{AFPsimp}[-j.2\pi f]) \right|^{2} dt \right)^{1/2} \cong \frac{1}{V_{max}} \sqrt{\frac{\overline{i_{Mth}^{2}}}{\Delta f}} \frac{A_{buf}}{gms_{f}} \sqrt{\frac{\omega_{0}}{8\xi}} \quad (3.49).$$

V_{max} is expressed in equation 3.19 and equation 3.49 can be equivalently written as a function of the circuit peaking time t_{max}:

$$ENC_{Mth} = \sqrt{\frac{\overline{i_{Mth}^{2}}}{\Delta f}} \frac{\sqrt{t_{max}}}{q F_{4}[\xi]} \quad (3.50); \qquad \text{where} \quad F_{4}[\xi] = F_{2}[\xi] \sqrt{8 \xi F_{1}[\xi]} \quad (3.51).$$

q is the electron charge, $F_1(\xi)$ and $F_2(\xi)$ are defined in appendix 1, and $F_4(\xi)$ varies from ~ 1.15 for $\xi = 0.6$ to ~ 0.9 for $\xi = 1.5$. The derived expression is in agreement with the general expression of the parallel ENC noise for CSA presented in [Cha91]. The parallel noise is then proportional to the transistor thermal noise and to the square root of the circuit peaking time. For the feedback transistor, the thermal noise power spectral density is proportional to the transconductance, while the peaking time is inversely proportional to the square root of gmsf, so that the feedback transistor contribution to the noise is proportional to $gms_f^{1/4}$. For any white noise source at the input of the circuit, its contribution to the equivalent noise charge of the circuit can be evaluated using equation 3.50. A shot noise is induced by the detector leakage current, and its contribution to the AFP output noise, referred to the input as ENC, can thus be calculated from the derived analytical expression.

The channel thermal noises of the cascode transistor, of the mirror transistor M3 and of the mirror transistor M5 have also important contributions to the output noise. The three transistors are biased in strong inversion, so that the excess noise factor becomes more important, and has been estimated at 2.5 for the calculations [Ane01]. The GIC noise of the buffer transistor is also considered as its gate loads the cascode stage output. The different noise contributions for an AFP circuit with the nominal biases and a 2 pF detector capacitance are listed to illustrate their relative importance:

M_{fth} = 105 e^- rms	M_{M4th} = 108 e^- rms	M_{M3th} = 145 e^- rms
M_{M2th} = 108 e^- rms	M_{M5th} = 125 e^- rms	$M_{GICMbuf}$ = 30 e^- rms

The total noise can be calculated by summing quadratically the different contributions and for the nominal biases, an equivalent noise charge of 460 e^- rms is calculated, for a 2 pF detector capacitance. This study shows that the secondary noise sources and the GIC noise of the input transistor have an important contribution to the final noise performance of the circuit, and have to be considered in the design phase.

3.1.4. The AFP chip designed in a 0.25 µm CMOS technology

The AFP chip [Ane03] comprises 32 channels of Active Feedback Preamplifier. The chip is presented together with the design optimization in 3.1.4.1. Electrical characterizations have been performed and are presented in 3.1.4.2 together with simulation results to present the circuit properties.

3.1.4.1. Presentation and design considerations of the AFP integrated circuit [Ane03]

The AFP chip has been designed first for applications in the NA60 experiment at CERN as analog electronic readout for a beam hodoscope: AFP chips were used in the experiment to process signals from silicon strip detectors placed in a heavy ion beam [Ane03]. The

AFP channel was thus optimized to readout detectors with a capacitance ranging from 2 pF to 5 pF, to obtain a pulse response with a 5 ns peaking time, and a low ENC of ~ 500 electrons. This circuit can be used to test different detectors and permit a fast analog amplification of current signals which can be directly readout on an oscilloscope.

The AFP chip is 2 mm × 4 mm and is represented in Figure 3.14. The chip contains two separate pad rings, and the 32 channels of AFP are integrated in one of the two rings, together with 2 extra test channels. The other pad ring contains 32+2 channels of a different version of the AFP chip, which will not be described in the thesis. The different currents biasing the circuit are set by current mirrors. The non diode-connected transistors of each current mirror are integrated into each channel, while the diode connected transistors are common for all the channels and grouped into a biasing circuit. The four currents I_{in}, I_{cas}, I_{feed} and I_{out}, together with the two gate voltages V_{feed} and V_{cas}, are set externally and can be adjusted from outside the chip. The AFP can thus be characterized in different working conditions, and can be adapted to the measurement requirements of the application. The pads at the top and at the bottom of the chip allow for the definition of all these biases and of the chip power supply voltage (2.5 V).

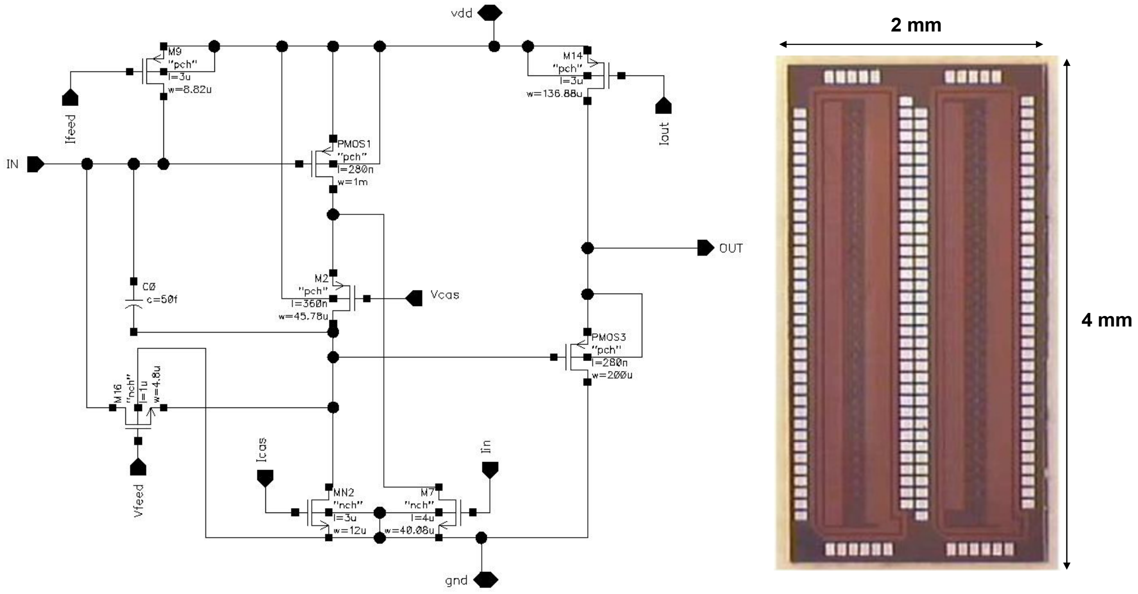

Figure 3.14. The AFP chip: schematic of one of the 32 integrated channels (left), photography of the chip (right).

The schematic of an AFP channel is presented in Figure 3.14 left, and some design choices that have been made for the most important devices of the circuit are first presented.

<u>Input transistor:</u>

The input PMOS transistor aspect ratio is W/L = 1000 µm / 0.28 µm. A gate length close to the minimum of the technology allows a compact design, a minimization of the C_{gs}/gm ratio, and shifts towards lower current values (i.e. lower power dissipation) the limit between weak and strong inversion. The transistor will be operated at this limit, thus maximizing the gm / I_D ratio, and lowering the thermal noise by limiting the excess noise Γ. Moreover, smaller drain-source voltages are then needed to operate the transistor in saturation. A PMOS transistor has been chosen as input transistor mainly because of the better noise performance of PMOS devices compared to NMOS in this technology, especially at short gate lengths [Ane01], and because of a lower output conductance. The width and the drain current of the input transistor have been chosen to obtain the desired trade off between bandwidth, power consumption and noise.

Feedback transistor:
The feedback transistor is a crucial element for the behavior of the circuit, as it has been discussed in details in the previous sections. The transistor is biased in weak inversion, in order to achieve low values of source transconductance as the desired transresistance gains are generally above 100 kΩ. The device is thus biased with currents smaller than 360 nA.

Source Follower:
The output buffer PMOS transistor is also of primary importance, as its gate capacitance affects the frequency response, and as its transconductance controls the buffer stage gain. A gate length of 280 nm has been chosen to maximize the transconductance and the buffer gain (equation 3.5). Increasing the width of the transistor increases the transconductance but increases also the transistor gate capacitance. This capacitance is the dominant capacitive load at the output of the cascode amplifier, and increasing the width of the transistor thus degrades the speed of the circuit. An optimum width has been calculated to be 200 μm, for drain currents of about 600 μA.

The layout of the AFP chip uses 3 levels of metal and the layout of a single channel is shown in Figure 3.15. The first large transistor on the left is the interdigited input PMOS, and the feedback capacitance C_f is obtained as a parasitic capacitance between two adjacent metal layers, so that no special analog features of the technology have to be used. The vertical lines shown in Figure 3.15 carry 7 DC signals to set the different biases.

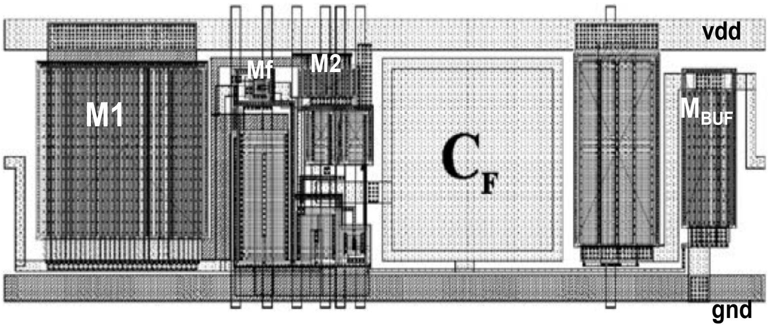

Figure 3.15. Layout of a single AFP channel, which measures 150 μm × 50 μm [Ane03].

3.1.4.2. Radiation tolerant layout approach [Ane01]

Circuits used in High Energy Physics experiments will have to be operated under a harsh radiation environment. A maximum accumulated dose of 100 to 300 kGy is for example expected for the integrated circuits at LHC after 10 years of operation [Sno00]. Radiation effects on a CMOS circuit are for the most ionization effects. Displacement damage caused by incoming radiation will have a much lower importance in a CMOS circuit. The ionization effects can be defined as Single Event Effects (SEE) or as Total Ionizing Dose (TID) effects. These effects are briefly introduced in the following, to understand the basic mechanisms involved.

Single event effects are caused by highly energetic particles passing through an integrated circuit, which will create an elevated number of electron-hole pairs along their path. These charges can induce a current at a sensitive node of the circuit and can generate an immediate malfunctioning of one or more transistors which can influence the entire circuit. These effects are of primary importance for digital circuits operated in high radiation environment. More details can be found in [Dod03].

Total ionizing dose effects are of primary importance for circuits and give origin to different variations of transistor properties. The most sensitive part of a MOS device to radiation is its gate oxide. Ionizing radiation induces electron-hole pairs in the oxide, and some of the generated will be trapped in the oxide. In a PMOS transistor for example, while electrons generated get collected at the gate or recombine, holes non recombined drift toward the oxide (SiO_2) – silicon interface where they are trapped. Moreover, irradiation leads to the creation of additional states at the SiO_2 – Si interface. The trapped holes induce a threshold voltage shift, negative for both NMOS and PMOS transistors. The radiation induced interface states will also give origin to a shift of the threshold voltage, positive for NMOS and negative for PMOS transistors. In addition to this voltage shift a parasitic conductive path from the source to the drain is created, which is due to an important radiation induced trapping of holes in the isolation structure and which leads to leakage currents. These currents only concern NMOS transistors. These different TID effects are detailed in [Old03].

An important work on the resistance to radiation of circuits has been carried out at CERN. The use of standard CMOS technologies in harsh radiation environment has been studied [Ane01], demonstrating the possibility to use standard technology up to radiation doses of more than 300 kGy by employing specific design rules and techniques. This approach has been used by designers of electronic circuits for the LHC. The circuits I have developed in this thesis use a similar approach which is only mentioned here, as this subject has been already widely presented [Sno00, Ane01, Gir00, Din04]. The scaling of CMOS technology reduces the thickness of the gate oxide, and the 0.25 µm technology utilized for the circuits of this thesis has a 5 nm thick oxide. This size reduction permits to reduce the importance of the radiation effects on the threshold voltage of the transistors, so that the leakage current only represents the limiting factor of this technology under irradiation. To tackle this problem, the circuit NMOS transistors can be designed with a specific geometry in order to avoid radiation induced leakage paths between source and drain, which could have a dramatic influence on the circuit response as the feedback transistor in the AFP architecture is an NMOS transistor. The specific layout technique consists in an annular design of the gate. The transistor source is inside this annular gate while the drain is designed outside, so that no parasitic path can be created between drain and source. These “Enclosed Layout Transistors” (ELT) permit to cancel leakage currents of NMOS transistors observed after irradiation [Ane99, Ane01]. All NMOS transistors of the developed active feedback pre-amplifiers in this thesis are laid out using such annular gate. This renders the electronic readout resistant to radiation and no variation of the circuit performance was observed for accumulated doses up to 300 kGy [Ane03].

3.1.4.3. Simulation and measurement results

The AFP chip is mounted on a dedicated printed circuit board (PCB), and connections from the PCB to the circuit pads are done via wire bonding. The 7 biases are set by different voltage generators. For the 4 currents, resistances are integrated on the PCB between the voltage supply and the chip, so that a direct readout of the applied currents can be performed on the PCB. The analog readout of an AFP channel can be performed on an oscilloscope using a 470 nF decoupling capacitance between the channel output and the 50 Ω load of the oscilloscope. Without this capacitance, the current set by the buffer current mirror would flow into the oscilloscope low resistance, switching off the buffer transistor. The AFP channel can be characterized by injecting current pulses at its input. This is realized by injecting a voltage step on a 1 pF SMD series capacitance integrated on the PCB (Figure 3.16). For a 4 mV voltage step, a 4 fC input charge is thus injected into the AFP channel under test. However, an important parasitic capacitance is added at the channel input, as the series injection capacitance is integrated on the PCB. The connection between this capacitance and one channel of the electronic readout is thus achieved through a metal line integrated on the PCB and a wire bond, which lead to an estimated 5.2 pF parasitic capacitance to ground (Figure 3.16).

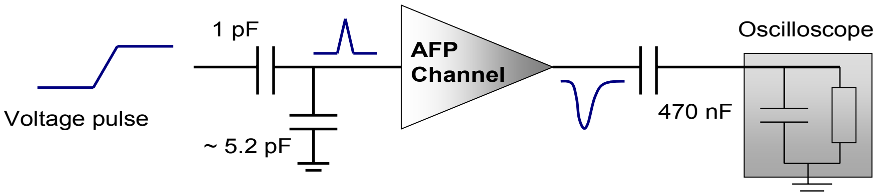

Figure 3.16. Measurement set up

The pulse generator used in the characterizations exhibits a 0.8 ns leading edge, thus very fast input current impulses are injected at the AFP channel input (Figure 3.17). The AFP response to 4 fC positive and 4 fC negative input signals are shown in Figure 3.17 (15000 signals are superimposed), for a channel biased with the nominal biases presented in 3.1.2.

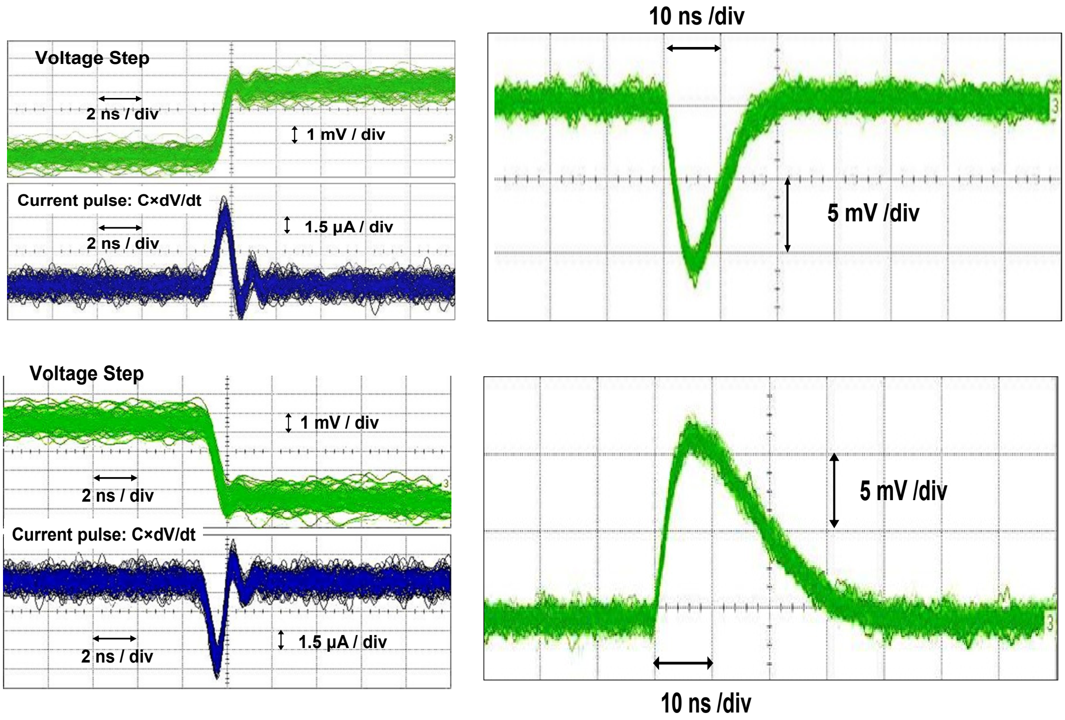

Figure 3.17. Left: 15000 positive and negative voltage steps applied to the 1 pF capacitance superposed, and corresponding positive and negative current impulses injected in the AFP channel. Right: superposed AFP response to the 15000 4 fC positive and negative input current pulses.

For a negative input charge, the output shows a fast rise time (10 % - 90 %) of 4.2 ns, a fall time (10 % - 90 %) of 20 ns, and an excursion of 11.8 mV. For a positive input charge, the results are slightly different, because of the non-linearity of the system with respect to the input charge (3.1.1.4). The response presents a fast rise time of 3.4 ns, a fall time of 9.6 ns, and an excursion of 10.8 mV (Figure 3.17). The characterization is performed with an input parasitic capacitance evaluated at about 5.2 pF. The pre-amplifier response varies with the input capacitance, and its bandwidth and gain are reduced for increasing input capacitances.

The input capacitance strongly affects the noise of the circuit (Figure 3.12), so that the pre-amplifier has an elevated noise in our test conditions. It can be estimated from the baseline of the signals in Figure 3.17 to be about 800 e$^-$ rms, which is close to calculations. For a 5.2 pF input capacitance, calculations lead to an ENC of about 720 e$^-$ rms, 800 e$^-$ rms corresponding to an input capacitance of about 6.8 pF.

The dc feedback current I_{FEED} flowing in the feedback transistor determines the transistor transconductance, and the AFP response, as presented in 3.1.2 and shown in Figure 3.18.

On the presented plots, the measurements are directly compared with HSPICE simulations of the AFP chip. The simulations were done by injecting the measured averaged input signal, and by considering the different parasitic capacitances inside the AFP chip and from the PCB. The measured output pulses are in good agreement with the HSPICE simulations.

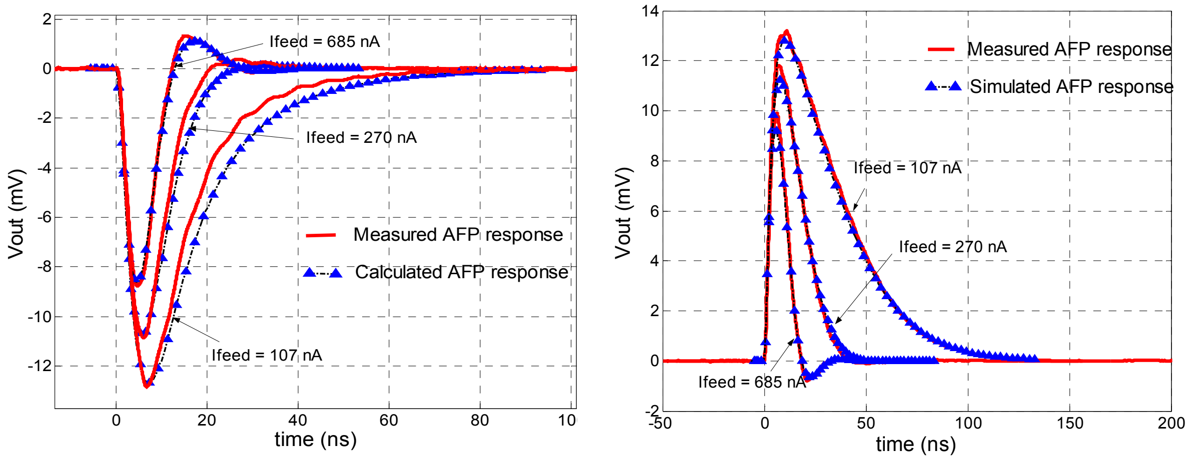

Figure 3.18. Averaged AFP response to a 4 fC input positive (left) and negative (right) charge, for 3 different feedback current.

As the feedback current decreases, the feedback transresistance increases, so that the AFP gain is increased (Figure 3.19) while the signal response gets slower (Figure 3.20). Similar variations of the feedback transresistance and of the time to return zero with respect to the feedback current are observed in Figures 3.19 and 3.20. This illustrates the fact that the time to return to zero depends on the dynamic feedback current that provides the pulse decay, which depends on the feedback transresistance.

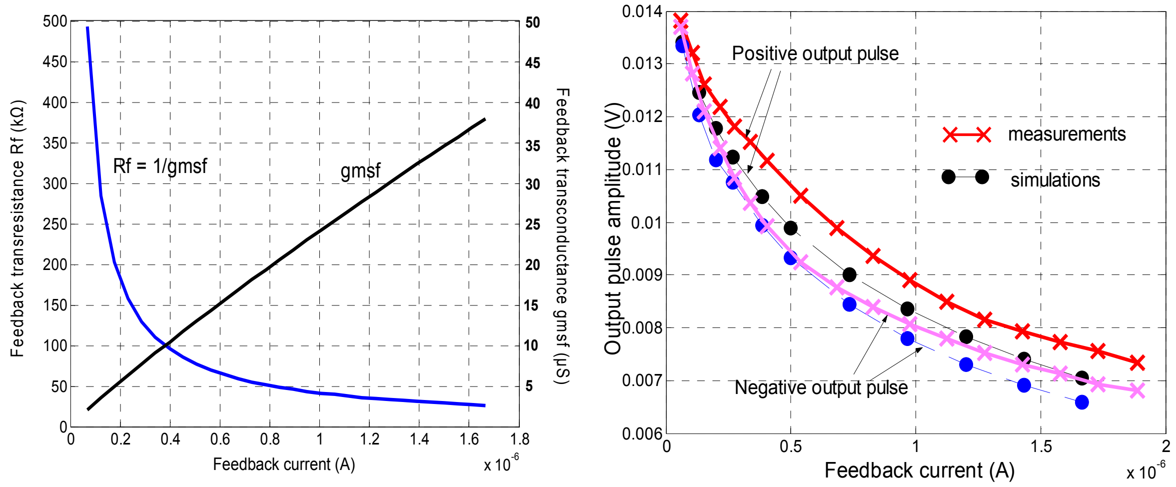

Figure 3.19 AFP amplifier output pulse amplitude for a 4 fC input charge and different feedback currents. Results from measurements and simulations are presented.

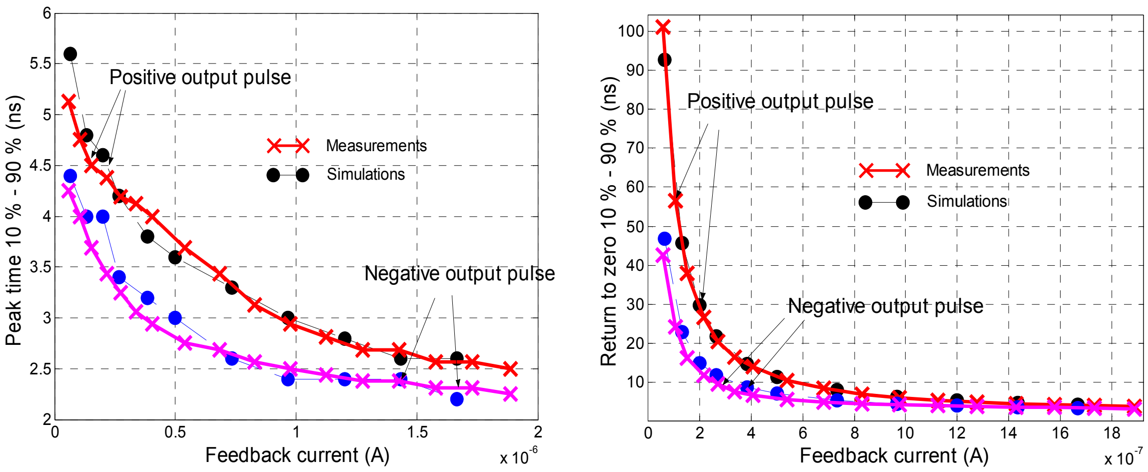

Figure 3.20 AFP amplifier speed response for a 4 fC input charge and different feedback currents. Results from measurements and simulations are presented.

The AFP transient response depends on the input signal charge, as presented in 3.1.2.2. Responses of the AFP channel to charges ranging from -11 fC to 11 fC are presented in Figures 3.21 and 3.22.

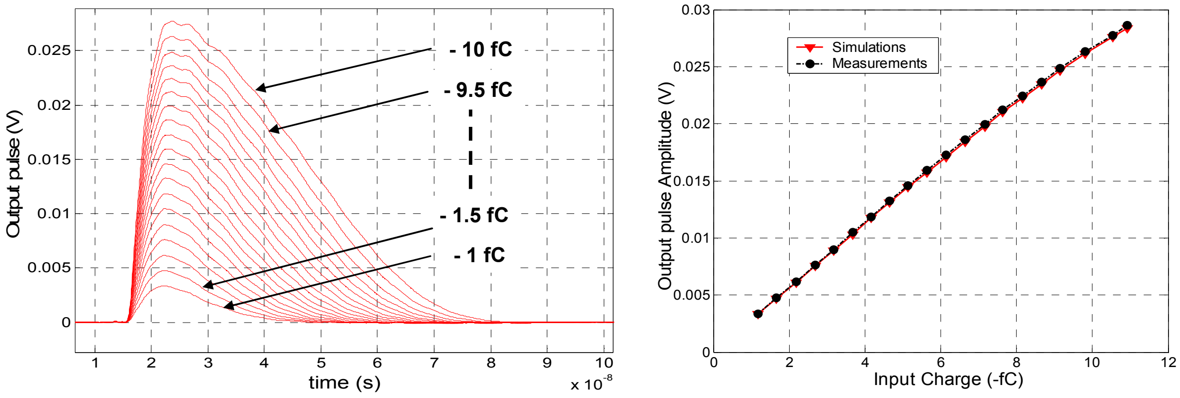

Figure 3.21 Averaged AFP pulse response for negative input charges.

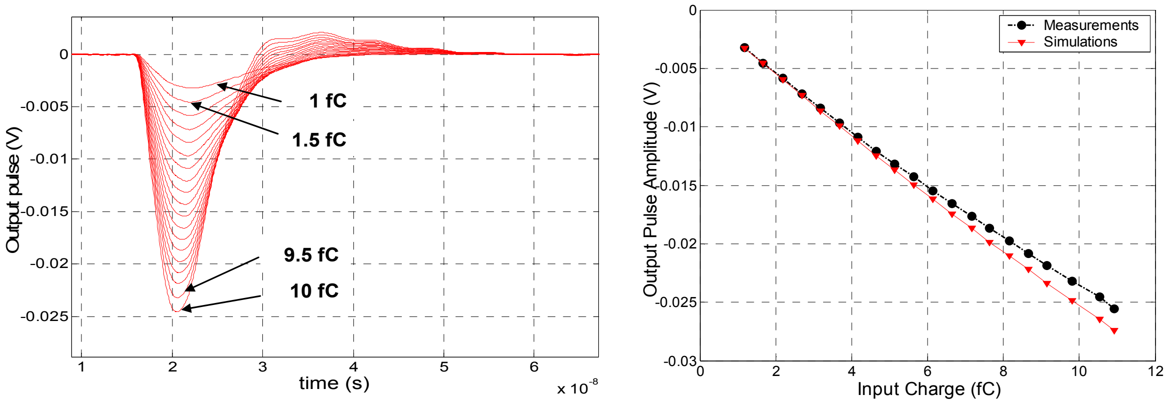

Figure 3.22 Averaged AFP pulse response to positive input charges.

A good linearity of the output pulse amplitude with respect to the total input charge is observed from -1 fC down to -8 fC, with a 2.77 mV/fC slope, and from 1 fC to 6 fC, with a 2.5 mV/fC slope. The pulse decay time is increased for negative input charges and decreased for positive input charges as the total input charge increases, as presented in 3.1.2.

The AFP chip has been chosen as the first chip on top of which we have deposited an a-Si:H detecting device. This choice was driven by the characteristics of the integrated pre-amplifiers which allow a fast readout. This is interesting in order to characterize the charge collection speed in a-Si:H detectors. The performances can also be shifted to get lower noise and to perform particle detection. Another advantage is the topology of the chip. The channel input pads are located at the center of the chip, facilitating the deposition of the a-Si:H detecting device. However, preliminary characterizations detailed in Chapter 4 have demonstrated high leakage currents linked to the TFA technology. I have thus designed a circuit entirely dedicated to the study of the technology, to permit characterizations of the interface a-Si:H sensor – integrated circuit and detailed explanation of the sensor properties.

3.2. The aSiHtest chip

I have designed in this thesis work the aSiHtest integrated circuit in order to characterize particle detectors based on the deposition of an a-Si:H detecting device on top of the ASIC (TFA detector). The chip is presented in 3.2.1. Some integrated structures and electronic readout permit the studies of the a-Si:H sensor leakage current and are presented in 3.2.2. Other structures permit the characterization of particle detection or signal induction speed in the TFA detector. Some Active Feedback Preamplifiers are integrated in the chip for these studies and are presented in 3.2.3.

3.2.1. A test chip for the characterization of detectors deposited on ASICs

The test chip has been designed in an IBM 0.25 µm CMOS technology using 3 levels of metal. The chip measures 4 mm × 4 mm and is represented in Figure 3.23. It comprises a 2.4 mm × 2 mm active area in the center of the chip where 35 metal structures made of the topmost metal layer of the technology are implemented. The detecting device can be deposited on top of this active area, the metal structures acting as bottom electrodes.
Different electronic readouts are integrated in the ASIC around the active area. Their inputs are connected to the metal pad structures integrated in the central active area, and their outputs are connected for external access to pads located at the periphery of the chip.

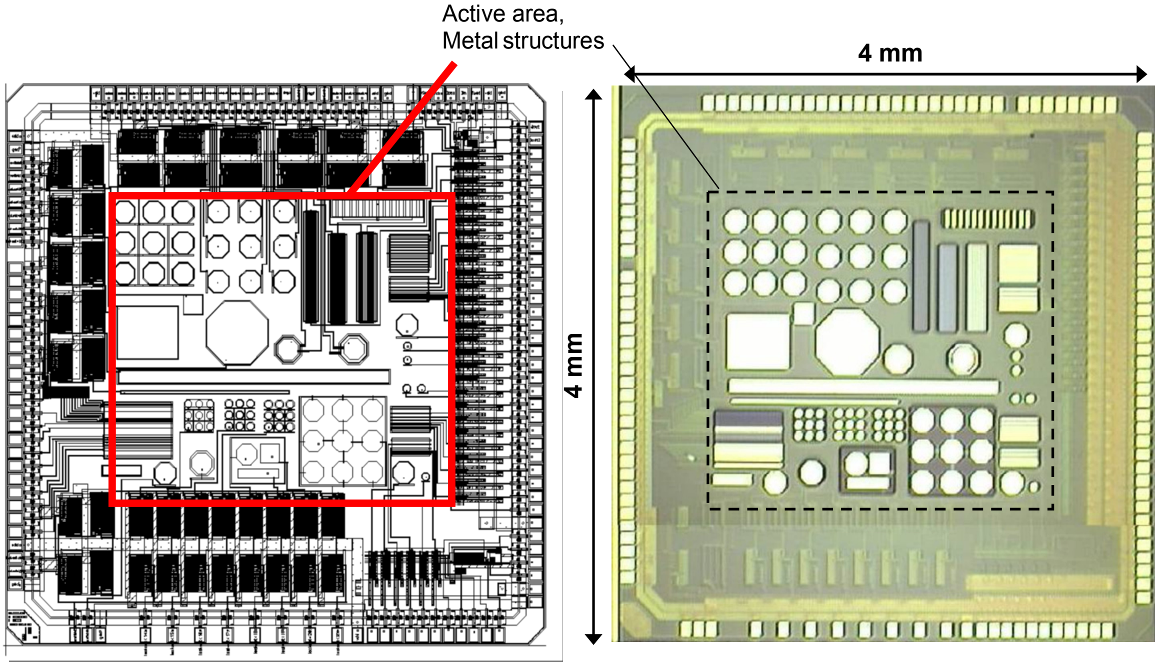

Figure 3.23 The aSiHtest chip: from layout to silicon

The aSiHtest integrated circuit has been designed for several objectives:

- A first challenge in the development of detectors based on the TFA technology is the design of appropriate metal pads in the ASIC, as they define the detecting device bottom electrodes. The aSiHtest chip has been developed to investigate the pixel segmentation of the a-Si:H sensor in TFA detectors. The effects of the interface ASIC/a-Si:H on the leakage current of the a-Si:H sensor can be first investigated. This study was motivated by the first results obtained on detectors based on the deposition of 32 µm thick a-Si:H diodes on top of the AFP chip. These first samples showed leakage currents that could be up to 3 orders of magnitude higher than the leakage current measured on the same diodes but deposited on a glass substrate. These results are detailed in Chapter 4. The measured discrepancies could originate from the TFA detector segmentation and from the uneven surface of the ASIC. 21 metal structures designed in the last metal layer are thus integrated in the test chip active area, with different sizes and different pixel segmentations. Each metal structure is connected to an integrated channel of a current amplifier, which allows measurements of currents down to few pA and up to few µA.

- Another major challenge in the development of TFA detectors is the development of low noise electronics able to readout with a reasonable timing resolution the low signals created by particles in a-Si:H. Several metal pads and thin strip structures integrated in the aSiHtest chip active area are connected to channels of 2 different Active Feedback Preamplifiers. The first AFP was optimized to have low ENC (~ 130 e^- rms) and fast pulse response (~ 5 ns peaking time), in order to characterize the detector speed or particle detection. The second AFP was optimized to have lower ENC (~ 70 e^- rms) and reasonable speed of the response (~ 25 ns peaking time). It is connected to thin strip structures to study the possibility of realizing high resolution strip detectors based on the TFA technology.

3.2.2. Electrical characterizations

The first objective of the aSiHtest chip is to investigate the leakage current of pixel or strip detectors based on the TFA technology. The a-Si:H n-i-p layers are deposited directly on top of processed ASICs. The ASIC process comprises several steps, the final steps being the deposition of insulating layers on top of the whole wafer surface. In the IBM 0.25 µm CMOS technology, layers of oxide, nitride and polyamide are deposited, with a total thickness of 4 to 6 µm (Figure 3.24). A final process step then consists in opening windows in these insulation layers on top of areas defined in the circuit layout. Windows opened on top of metal pads designed with the topmost metal layer of the technology enables an external access to the integrated circuit. In our applications, hydrogenated amorphous silicon films are deposited on top of the ASIC uneven surface. The detector bottom electrodes are thus defined by the metal structures designed in the topmost metal layer of the technology and by the windows opened in the passivation layer on top of these metal structures. The investigation of the leakage current characteristics of TFA detectors thus involves the study of the impact of the uneven ASIC surface and the study of the pixel size and segmentation.

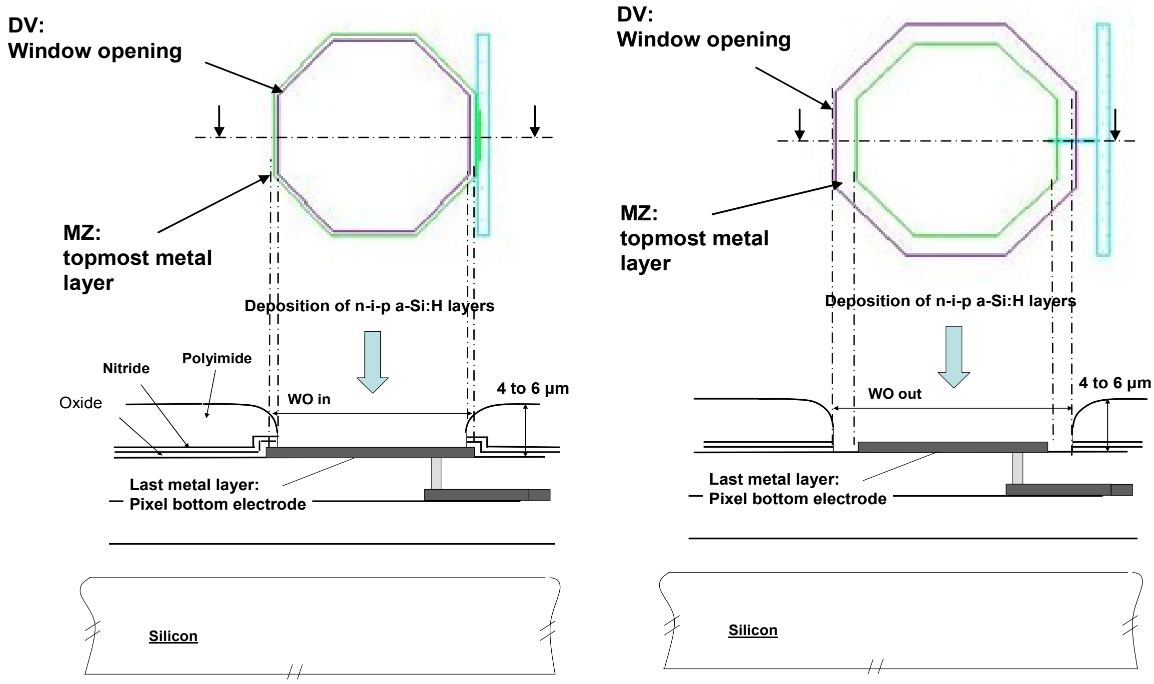

Figure 3.24 Illustration of the window opened in the insulation layers: octagonal pixel with window opened inside the metal pad, WO in (left) and outside the metal pad, WO out (right). Layout view of the pixels (top), and schematic cross-section (bottom).

In the technology, windows in the insulation layers are usually opened only on top of the last metal layer, so that the window is smaller than the metal pad itself. This is illustrated in Figure 3.24, and will be referred as *WO in* (window opening inside the metal pad). In that case, the pixel effective area is determined by the window edges. The opening can also be performed outside the metal, i.e. on top of the silicon dioxide layer that separates the metal structures (Figure 3.24). A window opened on top of the metal structure and all around the metal structure will be referred as *WO out* (window opening outside the metal structure). A single window can also be opened around several metal structures, so that no passivation layer is present between structures. This will be referred to as *WO overall* (window opening overall metal structures). In the 2 last cases, the effective pixel area is defined by the metal structure size. The openings in the passivation layer are defined in the ASIC layout by a "DV" layer which determines the edges of the windows to open, so that the passivation layer is removed on the surface delimited by the DV layer.

21 metal structures integrated in the aSiHtest chip active area are dedicated to the leakage current characterization, and are each connected to a current amplifier. 5 structures have an active area of 167747 μm^2, and 16 structures have an active area 9 times smaller, of 18638 μm^2. Octagonal pads, rectangular pads, long strips and groups of pads or strips are integrated. Some structures are integrated with a window opened in the passivation layer inside the metal structure (*WO in*). The DV layer is for that structures 4 µm inside the metal pad edges. Some structures are integrated with a *WO out* and a *WO overall*, and the distances between the DV layer and the metal pad edges are listed in the presentation of these structures.

Structures with an active area of 167747 μm^2:

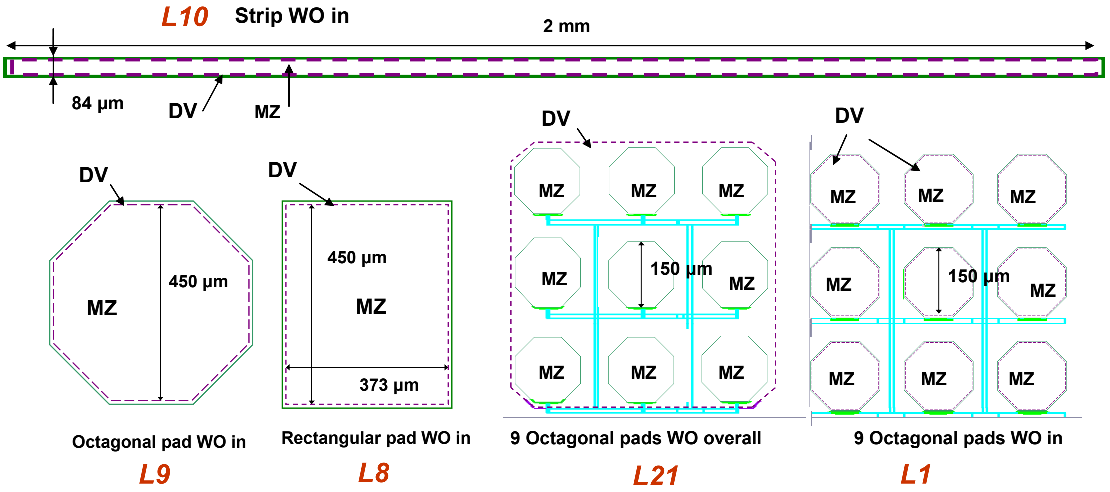

Figure 3.25. Layout of the implemented metal structures with an active area of 167747 μm^2.

These 5 structures comprise a square pad, an octagonal pad, a strip and a group of 9 octagonal pads connected together, all with a *WO in*. Each octagonal pad of the group of 9 pads has an active area of 18638 µm^2, so that an individual pad presents a similar area to that of the smaller structures presented later. Finally, a group of 9 octagonal pads connected together and with a global opening in the passivation is integrated.

Structures with an active area of 18638 µm^2:

Octagonal pads, square pads and rectangular pads with an active area of 18638 µm^2 are integrated with a WO inside the metal structure and a WO over 3 structures, to study both the shape and the passivation step influences (Figure 3.26). The integrated octagonal pads have the same active area as the individual pads of the groups of 9 pads which have a global active area of 167747 µm^2. Similar groups of 9 octagonal pads but with a global active area of 18638 µm^2 are also integrated. Each individual octagonal pad has thus a diameter of 50 µm and 3 groups are integrated. One has a window opened in the passivation inside each octagon, one outside each octagon, and the last one a global opening for the 9 octagons (Figure 3.27). These structures allow the study of the influence of the passivation layer, and also permit the characterization of smaller pads, given that each octagonal pad has an active area of 2071 µm^2.

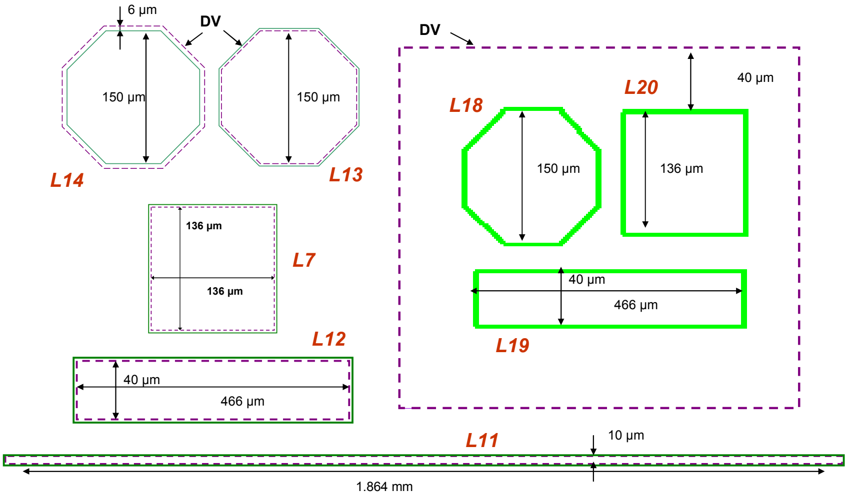

Figure 3.26. Layout of metal structures with an active area of 18648 µm^2.

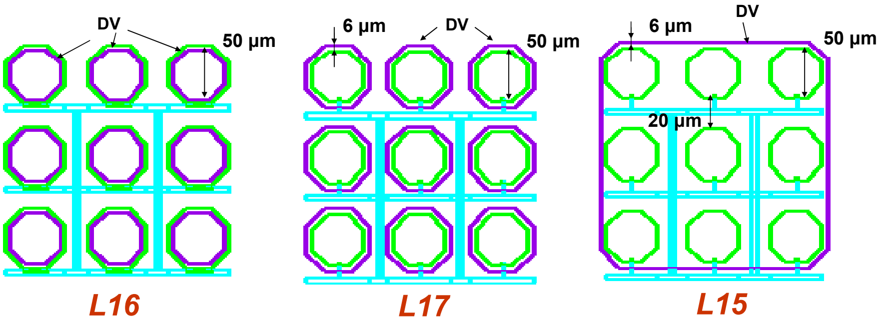

Figure 3.27. Layout of the 3 groups of 9 octagonal pads. Each pad has an active area of 2071 µm^2.

Several structures of metal strips connected together have also been implemented. Each of the 5 structures of strips has a total active area of 18638 µm^2, but the strips have different width, length and pitch, which are listed in table 3.2. These structures are implemented to study the feasibility of a high resolution strip structure. Each group has two additional dummy strips at both extremities and an additional strip at the group center which is connected to an AFP channel (Figure 3.28).

Metal structure name	Number of strips connected together:	Strip length:	Strip width:	Inter-strip distance:
L2	43	776.6 µm	0.6 µm	1.4 µm
L3	23	621.28 µm	1.5 µm	3.5 µm
L4	13	621.28 µm	3 µm	7 µm
L5	13	282.4 µm	6.6 µm	13.4 µm
L6	13	112.96 µm	16.5 µm	112.96 µm

Table 3.2. Dimensions of the 5 groups of strips structures implemented in the aSiH_test chip for I-V characterization. The total area of each group is 18648 µm^2.

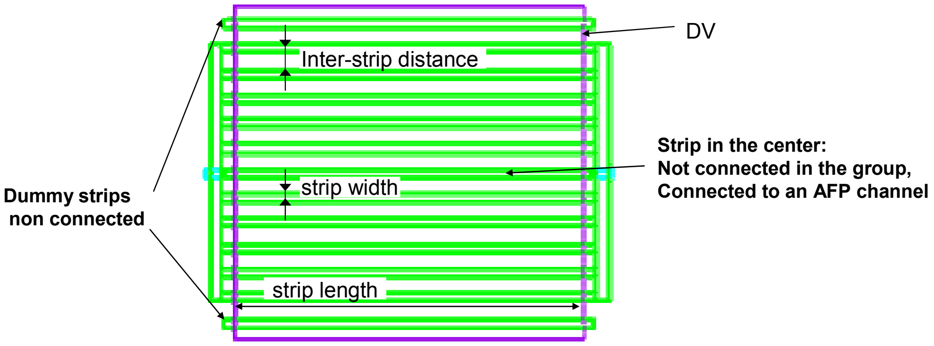

Figure 3.28. Illustration of a group of strips. Structure L6: 13 strips connected together and to a current amplifier for I-V characterization, and 1 strip at the center of the group connected to an AFP channel.

The 21 structures described and integrated in the aSiHtest chip are each connected to a channel of a current amplifier. The leakage current densities measured on 30 µm thick n-i-p a-Si:H diodes prior to the design of the aSiHtest chip were ranging from ~ 100 nA/cm^2 for a mean internal electric field of 10^5 V/cm for n-i-p diodes deposited on a glass substrate up to ~ 3 mA/cm^2 for a similar electric field and for n-i-p diodes deposited on ASICs (Chapter 4). The structures have an active area of respectively 167747 µm^2 and 18638 µm^2, thus the expected leakage current of 30 µm thick n-i-p diodes defined by the integrated metal structures would range respectively from ~ 200 pA to 5 µA and from ~ 20 pA to 560 nA, for a mean internal electric field of 10^5 V/cm. The amplifier has been optimized to readout currents from tens of pA to few µA, to have a dynamic range fitting with the wide range of the expected current values.

The current amplifier integrated consists in a simple combination of 3 stages of current mirrors. The first stage of the current amplifier is made of 101 similar PMOS transistors having common gates and common sources. One is diode-connected to the channel input, one has its drain directly connected to the second stage, the 99 others being connected to the second stage by a switch controlled by the voltage V_1 (Figure 3.29). The first stage allows the copy or the multiplication by 100 of the input current. The second stage consists also of a current mirror made by an NMOS input transistor diode-connected and 100 NMOS transistors that copy the input current. 10 of these transistors are directly connected to the input of the third stage, while the 90 others are connected through a second switch controlled by V_2. The second stage thus permits a multiplication of its input current by 10 or 100. Finally, the third stage is a simple current mirror comprising PMOS transistors, multiplying its input current by 10. The channel output, which corresponds to the drain of the 10 transistors of the 3rd stage, is connected to an external bond pad. It can be connected to a resistance outside the chip on a dedicated PCB, allowing a simple readout of the output current, by measuring the voltage difference at the resistance ends (Figure 3.29).

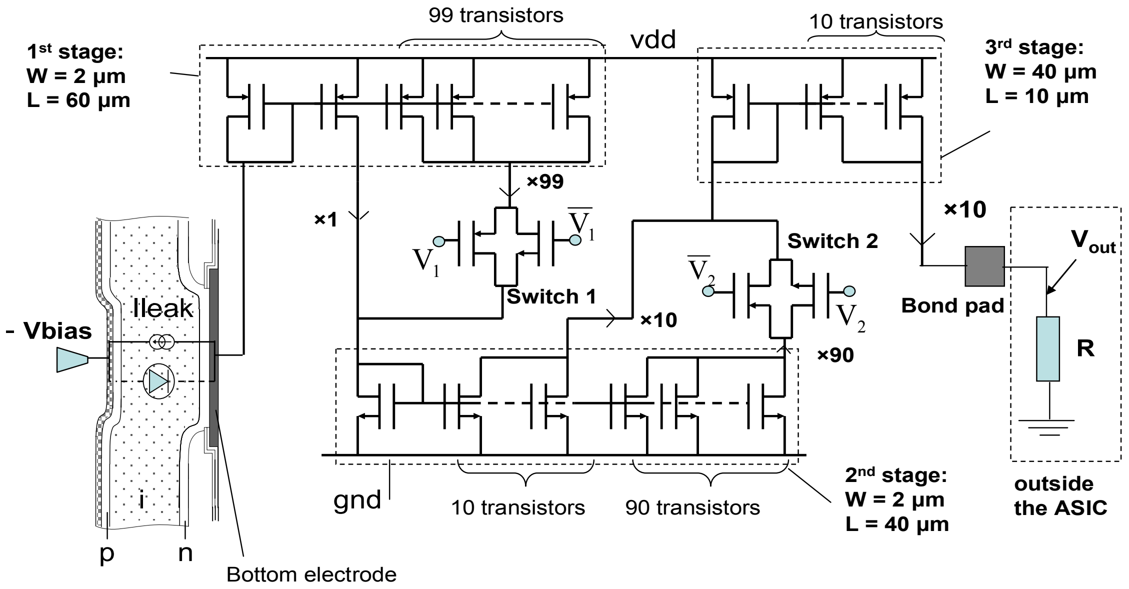

Figure 3.29. Schematic of a channel of the current amplifier implemented in the aSiHtest chip to readout the a-Si:H diodes leakage current.

The transistor sizes and biases have been first chosen to allow the readout of low currents with transistors operating in strong inversion and in saturation. Transistors with long channels have thus been designed. The sizes were also chosen to have an accurate multiplication, and to have 21 channels that can fit in the aSiHtest chip. The channel length and width of the transistors are annotated in Figure 3.29.

The two switches are designed as CMOS complementary switches, the transistors being designed with minimum length to obtain the desired W/L ratio for low W and to lower the junction leakage currents. Voltages V_1 and V_2 control the two switches, and integrated inverters permit the bias of the PMOS transistors with $\overline{V_1}$ and $\overline{V_2}$.

The current mirror multiplication accuracy will first depend on the differences induced by stochastic effects between the (supposed) identical transistors integrated for each current mirror stage. The mismatch between the transistors can be estimated by the difference in threshold voltage ΔV_T and by the difference in the transistor size parameter $\Delta\beta$. For a current mirror, the variation in the output current ΔI_{out} is calculated for transistors in saturation in [Raz01] and:

$$\frac{\Delta I_{out}}{I_{out}} = \frac{\Delta\beta}{\beta} + \frac{gm}{I_{out}} \Delta V_T \qquad (3.52);$$

where: $\beta = \mu\, C_{ox} \frac{W}{L}$ (3.53); $\frac{\Delta\beta}{\beta} = \frac{A_K}{\sqrt{WL}}$ (3.54); and $\Delta V_T = \frac{A_{VT}}{\sqrt{WL}}$ (3.55).

A_{VT} and A_K are proportionality factors. For the IBM 0.25 µm CMOS technology, the proportionality factors are found as $A_K \cong 1\text{-}3\,\%\cdot\mu m$ and $A_{VT} \cong 5.5\,mV\cdot\mu m$. The ratio gm/I_{out} is maximized for a transistor working in weak inversion, and the mismatch worst case can be calculated for transistors operating in that region and in saturation: in the 1st stage, transistors have a maximum $\Delta I_{out}/I_{out}$ of ~ 1.3 %, in the 2nd stage of ~ 1.6 %, and in the 3rd stage of ~ 0.7 %. The transistor wide W×L thus allows for a mismatch between transistors that would cause, in the worst case condition, incertitude of 1.45 % in the current multiplication.

The accuracy will also depend on a systematic current variation, induced by a difference in V_{ds} between the diode-connected transistor and the transistors copying the current. The relative difference for transistors in saturation is given by [Raz01]:

$$\frac{\Delta I_{DS}}{I_{DS}} = \lambda \cdot (V_{DS} - V_{GS}) \qquad (3.56)$$

where λ is the channel-length modulation coefficient. Maximizing the transistor length L lowers λ and then also minimizes the systematic current variation. Simulations performed with HSPICE show maximum $\Delta I_{ds}/I_{ds}$ of 0.1 % for transistors of the 1st stage and 2nd stage, and a maximum of ~ 1 % for transistors of the 3rd stage, for all transistors operating in saturation. The channel-modulation length has then a negligible effect in our current amplifier, when all transistors operate in saturation. The output resistance used to readout the output current has mainly to be chosen so that the non diode-connected transistors of the 3rd stage operate in saturation.

A final contribution to the multiplication variations comes from the 1st switch. For $V_1 = 0$ V, the switch is off, and the PMOS transistor still exhibits a current of about 20 pA.

This switch has to be off for currents higher than 40 nA (cf table 3.3), so that the induced error in the current copied is at a maximum of 0.5 %.

The integrated current amplifier then permits the readout of currents from tens of pA to ~ 2 μA. The gain can be shifted from 10^2 to 10^5 by varying the voltages V_1 and V_2, which control the 2 switches. The gain has to be adapted during the measurement as listed in table 3.3, so that all transistors of the amplifier operate in saturation.

Channel input current	V1 Stage 1	V2 Stage 2	Stage3	Output current	Channel gain
100 pA / 2 nA	2.5V (on) × 100	2.5V (on) × 100	× 10	10 μA / 200 μA	$\times 10^5$
2 nA / 40 nA	2.5V (on) × 100	0V (off) × 10	× 10	20 μA / 400 μA	$\times 10^4$
40 nA / 200 nA	0V (off) × 1	2.5V (on) × 100	× 10	40 μA / 200 μA	$\times 10^3$
200 nA / 1.5μA	0V (off) × 1	0V (off) × 10	× 10	20 μA / 150 μA	$\times 10^2$

Table 3.3. Gain adaptation of the current amplifier with the input current

3.2.3. Integrated Active Feedback Pre-amplifiers

The aSiHtest integrated circuit also includes several metal structures each connected to an active feedback pre-amplifier. The a-Si:H n-i-p sensor is deposited on top of the metal structures to build the TFA detector, so that the pre-amplifiers are connected to the n^+ layer through the bottom electrode (Figure 3.30). Free carriers created by radiation in the depleted i-layer will induce a negative signal at the pre-amplifier input. The a-Si:H dielectric constant can be assumed to be 12 [Str91]. The high resistivity of the non-depleted layer in an a-Si:H sensor leads to a constant sensor capacitance which only depends on the sensor thickness. The detector capacitance per active area for a 1 μm thick diode is thus of 1.06×10^{-16} F/μm^2, and for a 30 μm thick diode of 3.5×10^{-18} F/μm^2. For 30 μm thick diodes, the channel input capacitances will be dominated by the parasitic capacitance between the metal pad that defines the bottom electrode and the chip silicon substrate. In the IBM 0.25 μm CMOS technology with 3 levels of metal, the capacitance per active area between the last metal layer and the substrate is of 1.015×10^{-17} F/ μm^2. The global channel input capacitance load is then small and ranges from 30 fF to 250 fF for pixels with active areas from 2070 μm^2 to 18648 μm^2 and for 30 μm thick diodes. Active feedback pre-amplifiers can thus be designed with lower noise in comparison to pre-amplifiers integrated in the AFP circuit (which were designed for a 2 to 5 pF input capacitance).

Two different versions of active feedback pre-amplifiers have thus been optimized and implemented. 32 metal structures integrated in the aSiHtest chip active area are each connected to one of the pre-amplifiers. Octagonal pads with an active area of 18638 µm^2 or of 2070 µm^2 are integrated, and three similar structures each made of different metal strips have also been designed to investigate the feasibility of a high resolution strip detector. Each structure comprises 9 strips 6.6 µm wide and 282.4 µm long, with 4 different inter-strip distances of 4 µm, 6.6 µm, 13.4 µm and 23.4 µm (Figure 3.30).

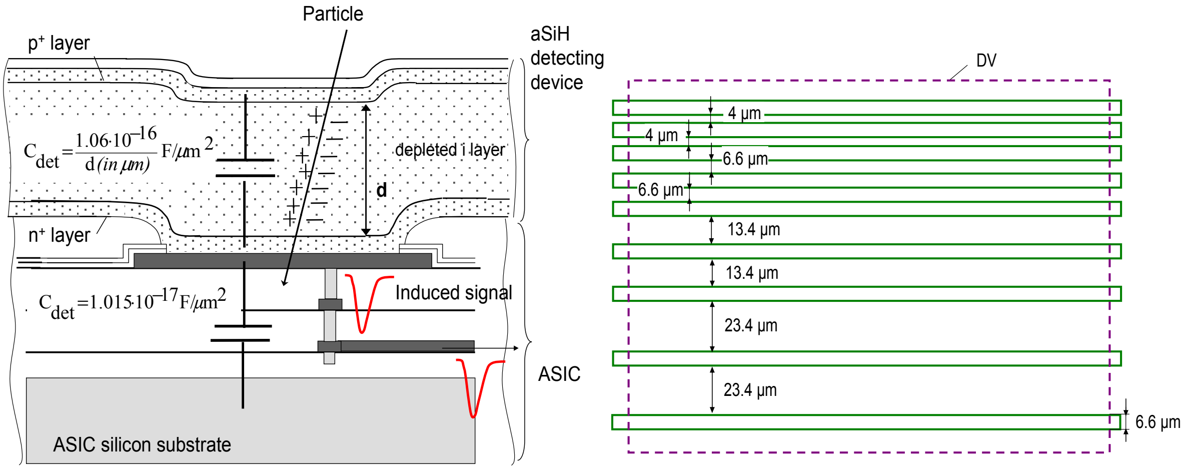

Figure 3.30. Left: Schematic cross section of a TFA electrode segmentation, with detector capacitance and parasitic capacitance. Right: Metal strips structure integrated in the aSiH_test active area. Each metal strip is connected to a channel of an active feedback pre-amplifier.

The MIBEDO active feedback preamplifier

The MIBEDO circuit is the 1st version of active feedback pre-amplifier implemented in the aSiHtest chip. MIBEDO stands for MIcroBEam DOsimetry, as the investigation of a high resolution strip sensor is of primary interest for dosimetry applications in a novel cancer therapy technique. This technique is called Microbeam Radiation Therapy (MRT) and uses X-ray microbeam radiation to treat tumors [Lai99]. This technique is under study at the European Synchrotron Radiation Facility in Grenoble [ESRF], and necessitates an online measurement of the microbeam doses, with a spatial resolution down to few µm, so that TFA detectors appear as an interesting technology for these applications.

The circuit has been optimized for negative input signals ranging from 0.2 fC to 4 fC, for an input capacitive load of about 200 fF, and to get a speed response similar to that of the AFP chip pre-amplifiers. Two different MIBEDO circuits are implemented. They only differ in their buffer stage: 7 channels are implemented with a PMOS source follower transistor as buffer stage (MIBEDO_LG), and 18 channels are implemented with a buffer stage that comprises two source followers, to improve the gain of the circuit (MIBEDO_HG).

The pre-amplifier stage is a standard AFP circuit designed as presented in Figure 3.2: it comprises a classical cascode amplifier structure with current sources loads, the input transistor being a PMOS transistor with a W/L ratio of 44 µm / 0.26 µm. It comprises a feedback path composed by an NMOS transistor and a 13 fF feedback capacitance. The feedback capacitance is realized as parasitic capacitance between same metal level, with an inter-digited structure.

The different currents are set by current mirrors. The non-diode connected transistors of each current mirror are integrated into each channel, while the diode-connected transistors are common for all the channels. The feedback current is set through a specific biasing circuit to inject feedback currents down to 20 nA, the ratio between the externally set current and the feedback current being of 50. The 5 biases I_{IN}, I_{CAS}, I_{FEED}, V_{CAS} and V_{FEED} are set externally. The nominal biases of the amplifier stage are listed in table 3.4, together with the corresponding most important parameters involved in the circuit transfer function:

Input Transistor:	I_{IN} = 400 µA	gm_1 = 2.5 mS	$C_{gs1}+C_{gb1}$ = 54 fF	C_{gd1} = 18 fF
Feedback transistor:	I_{FEED} = 90 nA V_{FEED} = 1.5 V	gms_f = 2.8 µS	**C_f = 13 fF**	
Cascode transistor:	I_{CAS} = 100 µA V_{CAS} = 1V	gm_2 = 1.06 mS	**Cascode Mirror:**	r_{0cascm} = 500 kΩ

Table 3.4 MIBEDO pre-amplifier stage nominal biases and parameters

In the MIBEDO_LG channels, the output stage is a PMOS source follower with a W/L ratio of 100 µm / 0.26 µm. The sizes are chosen to have the desired compromise between the gate capacitance Cg_{buf}, which will load the output node of the cascode amplifier, and the transconductance gm_{buf}, which controls the buffer gain and speed. With a nominal current I_{OUT} of 1.25 mA, the gate capacitance is estimated at 70 fF and the transconductance at 7 mS, thus leading to a buffer gain of 0.26 for readout on a 50 Ω resistance (equation 3.5).

Two octagonal pads with a window opening inside the metal pad and with an active area of 2070 µm^2 are integrated in the aSiHtest chip test structures and connected to 2 channels MIBEDO_LG. Seven strips of a first structure similar to the structure of Figure 3.30 right are also integrated and each strip is connected to a channel of MIBEDO_LG. Each of the 9 metal structures presents a parasitic capacitance of ~ 100 fF loading the channel input.

To allow the electrical characterization of the channels, some capacitances of 100 fF are integrated in the chip, and connected on one side to some channel inputs and on the other side to the same calibration external bond pad (Figure 3.31). The pre-amplifier channels can then be calibrated by applying a voltage step on this bond pad, independently from the metal structures of the active area, and avoiding the addition of parasitic capacitances at the channel input, as it was the case for the AFP chip.

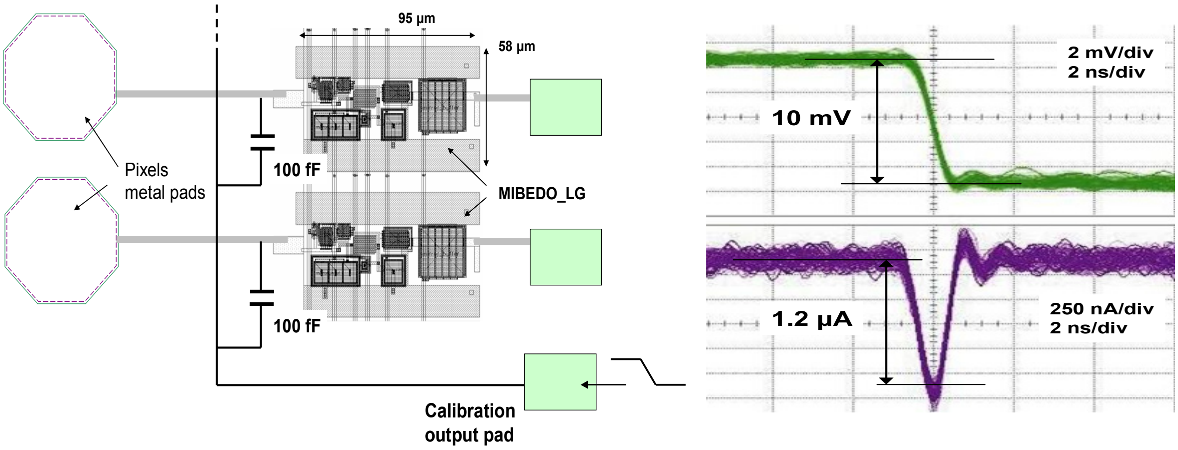

Figure 3.31. Left: Example of the 2 integrated octagonal pads connected to MIBEDO_LG channels. The channels can be electrically characterized by injecting a voltage step to the calibration output pad. Right: 10 mV voltage step injected during the tests (top), and corresponding current pulse (1 fC total charge) injected at the channel input (bottom).

An aSiHtest chip without any detecting device deposited on top of its active area has been mounted for electrical characterization on a dedicated printed circuit board. The characterization of the MIBEDO channels has been performed by injecting voltage steps to the external calibration bond pad. For a calibration voltage step of -10 mV, a negative charge of 1 fC is injected at the input of the test channels.

The output response of a channel of MIBEDO_LG is presented in Figure 3.32, in which 15000 signals superposed are presented so that the noise performance of the circuit is also illustrated. The average of the measured signals is compared with HSPICE simulations of the circuit taking into account the different parasitic capacitances and with theoretical calculations performed using the models developed in the Laplace domain and in the time domain in section 3.1.2. Time domain calculations and simulations are well fitting the measured signal, as it is represented in Figure 3.32. The output pulse exhibits a gain of 14.5 mV/fC for a 5 ns peaking time and for a 25 ns time to return to zero.

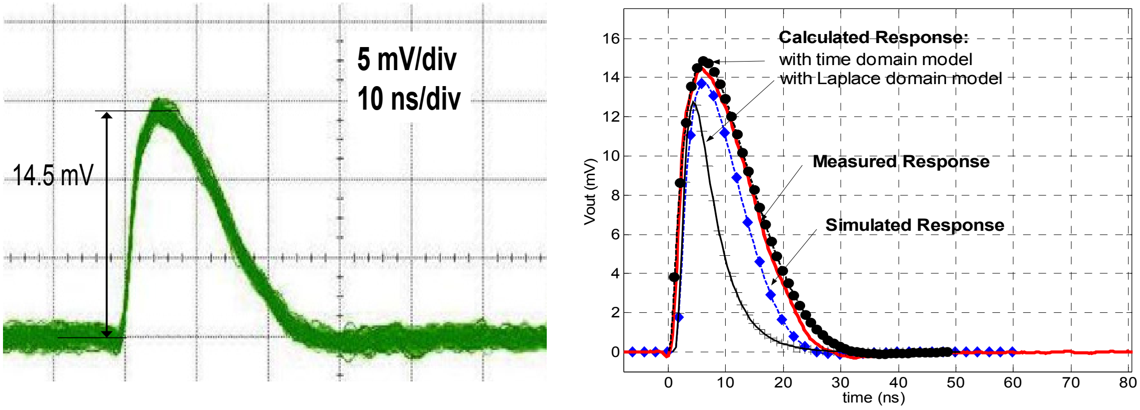

Figure 3.32. MIBEDO_LG transient response to -1 fC input charge. Left: superposition of 15000 measured output signals. Right: comparison of measurement (averaged signal) with theoretical calculations and HSPICE simulations.

The channel noise can be evaluated by measuring the channel output baseline distribution. A Gaussian distribution with a standard deviation of ~ 389 µV rms is measured (Figure 3.33), so that in the defined bias conditions, the MIBEDO_LG channel presents a noise of 166 e^- rms. The dynamic response of the channel presents a linear variation of the pulse amplitude with respect to the input charge up to ~ 3 fC (Figure 3.33). For charges above, the signal starts to saturate at the source follower output.

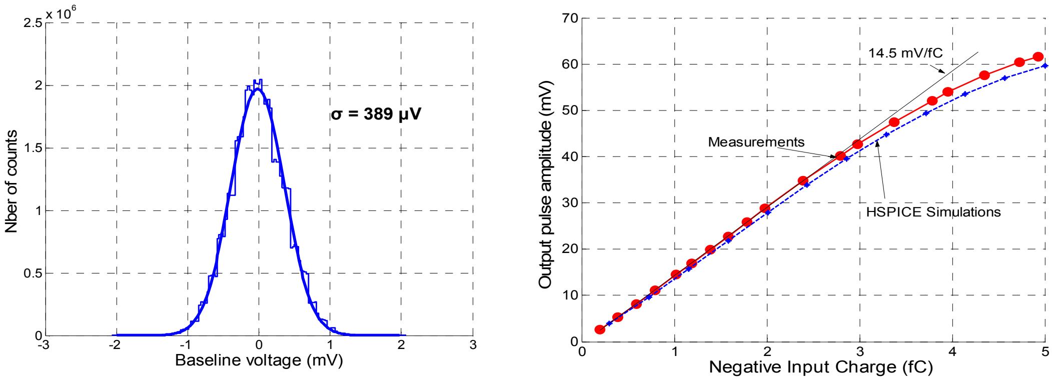

Figure 3.33. Left: Channel output baseline: Gaussian distribution with a standard deviation of 389 µV. Right: Dynamic of the channel response to negative input charges.

In order to improve the gain of the MIBEDO channel and to increase its dynamic range, the MIBEDO_HG AFP has been implemented. This version uses the same cascode and feedback stages as in the MIBEDO_LG, but a different buffer stage. The latter consists of a first PMOS source follower and of a second NMOS source follower added in series, as it is presented in Figure 3.34.

The first source follower can be optimized to load a minimum the cascode amplifier stage. The output resistance of the stage is not anymore determined by the 50 Ω oscilloscope resistance, but only by the parallel combination of the output conductances of the source follower and of the mirror providing the I_{OUT} current. The source follower transconductance can be made smaller than for MIBEDO_LG, but high enough to not change the speed of the response. Small currents can be used, so that the PMOS source follower output DC level is lowered compared with the MIBEDO_LG channel, and so that saturation will occur for higher input charges. The second buffer stage can be optimized to present a high transconductance. The nominal biases are the same as the nominal biases of the MIBEDO_LG for the cascode and the feedback stages (Table 3.4). The current in the PMOS source follower is set to about 30 µA, leading to an equivalent capacitance seen at its gate of 35 fF. The NMOS source follower has a W/L ratio of 300 µm / 0.44 µm. For an applied current of 1.5 mA, it presents a total transconductance of ~ 17.8 mS, thus leading to a gain of 0.46 for a 50 Ω output resistance.

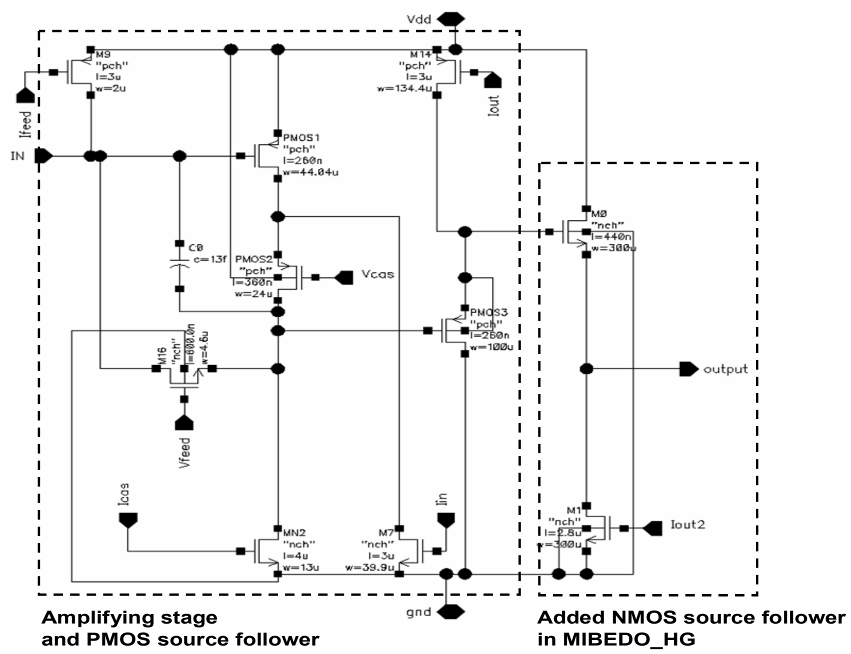

Figure 3.34. Schematic of a MIBEDO channel: the low gain version comprises the amplifying stage and the PMOS source follower, and the high gain version comprises an additional NMOS source follower.

17 different metal structures integrated in the aSiH_test chip active area are each connected to a channel of a MIBEDO_HG amplifier. 2 octagonal pads with an active area of 2070 µm^2 and 9 strips of a structure similar to the one presented in Figure 3.30 are integrated. They all present an input parasitic capacitance between 50 fF and 100 fF. The 5 central strips of the strip structures L2 to L6 presented in 3.2.2 are also connected to a MIBEDO_HG channel. These structures present an input capacitance ranging from 80 fF to 180 fF. Finally, an octagonal pad with an active area of 18648 µm^2 is integrated and connected to a MIBEDO_HG channel. This metal pad presents an input parasitic capacitance of about 200 fF. Some injection capacitances of 100 fF are integrated and connected on one side to some of the integrated MIBEDO_HG channels, and on the other side to a common external bond pad, as for the MIBEDO_LG channels (Figure 3.31). Electrical tests of the channels can be performed by injecting voltage pulses to the calibration pad.

The characterization of the MIBEDO_HG channels has been performed for the different structures, and results obtained with channels connected to the strips of the test structure (Figure 3.30) are presented in this section. The gain improvement obtained with the two buffer configuration is first illustrated in Figure 3.35. The output response of the MIBEDO_HG amplifier depends on the current I_{out2} set into the NMOS source follower, as this current determines the transistor transconductance and the buffer stage gain. An output shape close to the one obtained with the MIBEDO_LG channel is achieved for a current I_{out2} of 0.32 mA, while the current used in the MIBEDO_LG buffer was of 1.25 mA. A similar response is thus obtained for a reduced buffer current. For a current of

1 mA, the output signal presents a gain of 20.2 mV/fC, and the output noise of the channel is measured at 382 µV rms. The variations of the output noise, output signal amplitude for a -1 fC input charge, and ENC of the channel for different I_{out2} are presented in Figure 3.35. A stable ENC of 120 e$^-$ rms is observed for a current $I_{out2} > 1.2$ mA.

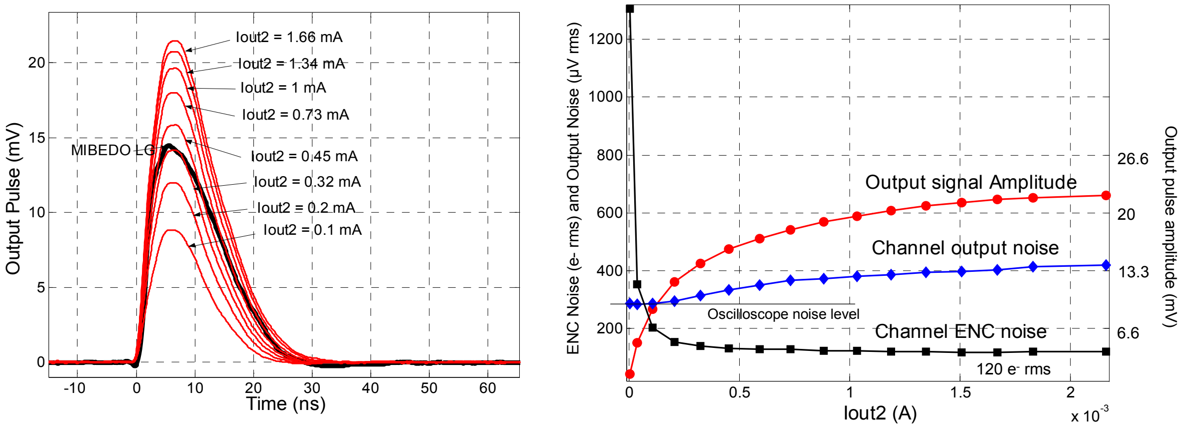

Figure 3.35. (left) MIBEDO_HG output response to a -1 fC input charge, with nominal biases and for different NMOS source follower currents, from 100 µA to 1.66 mA, compared with the MIBEDO_LG response.

The measured responses to a -1 fC input charge and for nominal biases are presented in Figure 3.35 with 15000 signals superposed, thus also illustrating the noise of the circuit. The HSPICE simulation of the output response is in agreement with the averaged measured signal (Figure 3.36), while the calculations performed using the time domain model presents a faster response. Calculations were performed by considering an ideal buffer stage with a gain of 0.46.

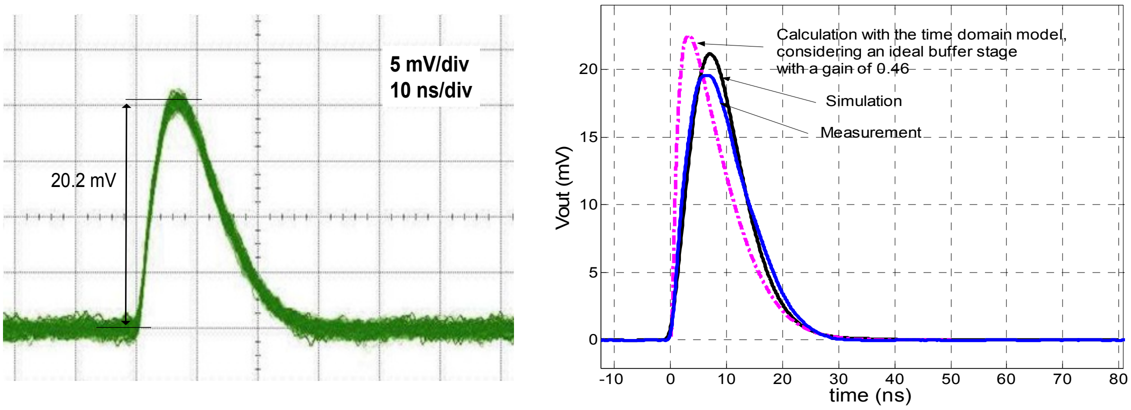

Figure 3.36. MIBEDO_HG transient response to a -1 fC input charge. Left: 15000 measured signals superimposed. Right: Averaged measurement compared with theoretical calculations and HSPICE simulations.

The transconductance of the PMOS source follower and the gate capacitance of the NMOS source follower still have to be considered. A pole is added at the AFP transfer function, at the NMOS source follower gate, and can be estimated as:

$$\omega_{buf2} = \frac{gm_{buf} + 1/r_{0buf} + 1/r_{0bufm}}{C_{GBUF2} + C_{dtbufm} + C_{stbuf1}} \tag{3.57}$$

where C_{GBUF2} is the total capacitance seen at the NMOS source follower gate, C_{stbuf1} and C_{dtbufm} are the total capacitances seen at the PMOS source follower source and at its mirror transistor drain. For nominal biases, gm_{buf} = 500 µS and C_{GBUF2} = 600 fF, so that the third pole is at a frequency of about 15 MHz that limits the output response. Higher speed response can be achieved by tuning up the I_{out} current and so gm_{buf}.

The circuit biases are set externally, as for the AFP chip, so that the circuit transfer function can be adapted to the measurement requirements. For example, a slower signal can be obtained by tuning down the currents I_{OUT}, I_{CAS} and I_{IN}. The output response shape can be shifted down to a signal peaking time of 50 ns, for a gain of 19.8 mV/fC (Figure 3.37).

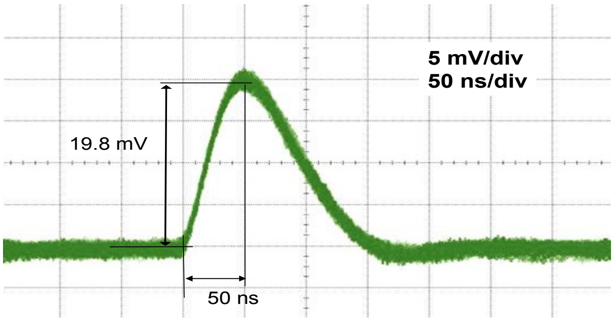

Figure 3.37. Biases adjustment to obtain a longer peaking time of the MIBEDO_HG response to a -1 fC input charge. 15000 signals are superimposed.

The feedback current controls the feedback transresistance and the circuit response (section 3.1). It can be adjusted externally and can be decreased to get a higher gain and a lower noise (Figure 3.38), or increased to get a faster response (Figure 3.39).

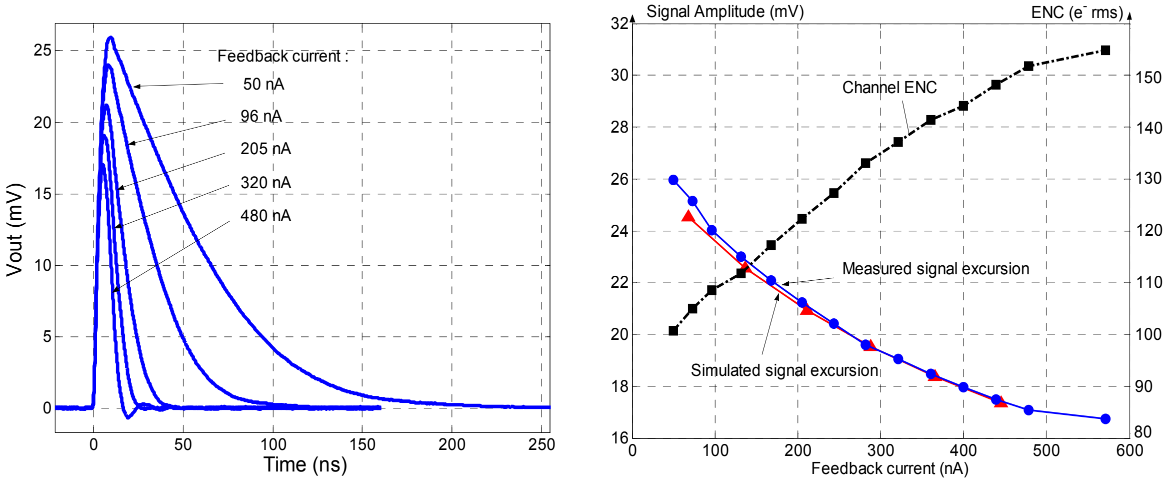

Figure 3.38. Variations of the MIBEDO_HG transient response to a -1fC input charge measured for different feedback current values. Evolution of its maximum excursion and ENC.

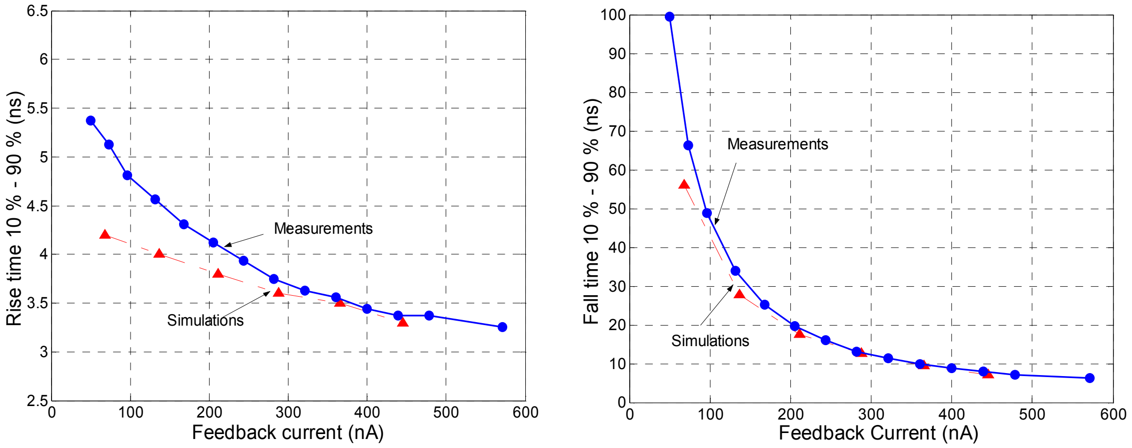

Figure 3.39. Evolution of the MIBEDO_HG speed response for a 1 fC input charge and for different feedback currents.

The MIBEDO_HG transfer function depends on the input signal amplitude. The output pulse amplitude varies linearly with the input charge, and for charges above 1.2 fC in the optimal biasing conditions, the excursion deviates more and more from the linear relation, as it has been presented in 3.1.2 and as it is represented in Figure 3.40.

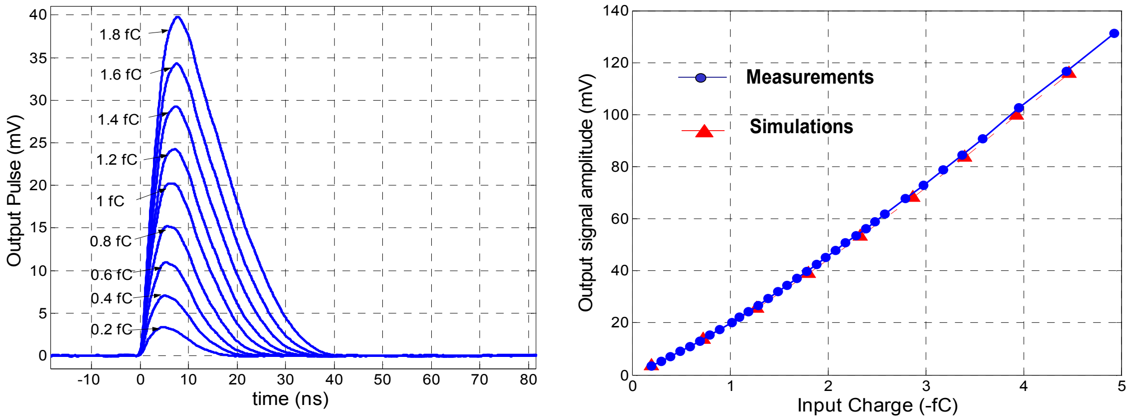

Figure 3.40. Dynamic variation of a MIBEDO_HG channel

Results have been presented for a channel connected to a strip of a structure similar to the one presented in Figure 3.30. The 9 integrated strips and the 2 octagonal pads with an area of 2070 µm^2 present the same equivalent input capacitance, which is around 100 fF. The 11 channels connected to these structures present equivalent characteristics compared with the presented results. The 5 other structures integrated present a higher parasitic input capacitance. This induces some differences in the channel performances: it slows down the response of the channel, reduces the gain, and increases the noise. The octagonal pad with an active area of 18648 µm^2 presents the higher capacitance, which has been estimated at about 250 fF. This results in a measured ENC of 170 e$^-$ rms for nominal biases. The signal output measured for nominal biases is represented in Figure 3.41. The output noise has been calculated for different input capacitances, and results are presented in Figure 3.41.

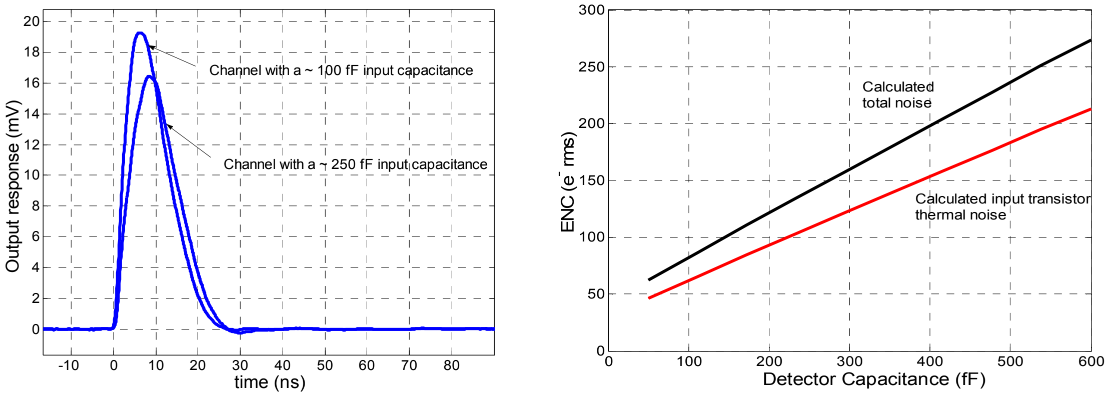

Figure 3.41. MIBEDO_HG variations with the input capacitance

The channel ENC strongly depends on its input capacitance. For n-i-p a-Si:H structures deposited with a thickness above 30 µm, the channel input capacitance is dominated by the chip internal parasitic capacitances, so that the response would be similar to the responses presented in this chapter. However, for thinner detectors, the detector capacitance can affect the channel response. For such cases, the channels can be calibrated thanks to the integrated injection capacitance, and the signal shape together with the rms output voltage can even lead to an estimation of the added detector capacitance.

The aSiScope active feedback pre-amplifier:

The noise performance of the MIBEDO_HG channels can be about 120 e^- rms for a reduced feedback current, as it can be observed in Figure 3.38. As it has been presented in Chapter 2, some studies have shown that a MIP could create only 700 electrons in a fully depleted 20 µm thick a-Si:H detector. A second version of active feedback pre-amplifier has then been designed to further improve the noise performance of the readout electronics, in order to obtain a better signal over noise ratio for the detection of particles down to the MIP. 6 channels of this transimpedance amplifier, so called aSiScope, have been integrated into the aSiHtest chip. 4 strips of the structure defined in the Figure 3.30, one octagonal pad with an area of 2070 μm^2 and one octagonal pad with an area of 18648 μm^2 are each connected to an aSiScope pre-amplifier.

The schematic of one channel is presented in Figure 3.42. The circuit is made of a standard cascode amplifier, together with the NMOS feedback transistor.

The input transistor presents a W/L ratio of 200 µm / 0.28 µm. The feedback transistor biasing circuit has been made especially to allow a biasing with low feedback currents. The feedback transistor operating in weak inversion, its transconductance is proportional to its drain to source current, so that reducing it will give a low transconductance, and a better ENC of the circuit (Figure 3.38). The biasing circuit is made of several current mirror stages controlled via 2 currents I_{f1} and I_{f2}, which are set externally. The current I_{f2} provides an additional current to the biasing circuit that will keep all transistors of the current mirror stages in saturation and in strong inversion. The current I_{f1} is used externally to shift the effective feedback current I_{FEED} in the circuit, and they are connected through the following relation: $I_{FEED} = (I_{f1} / 5 - I_{f2}) / 50$. Currents from 3 nA to 100 nA can be set into the feedback transistor.

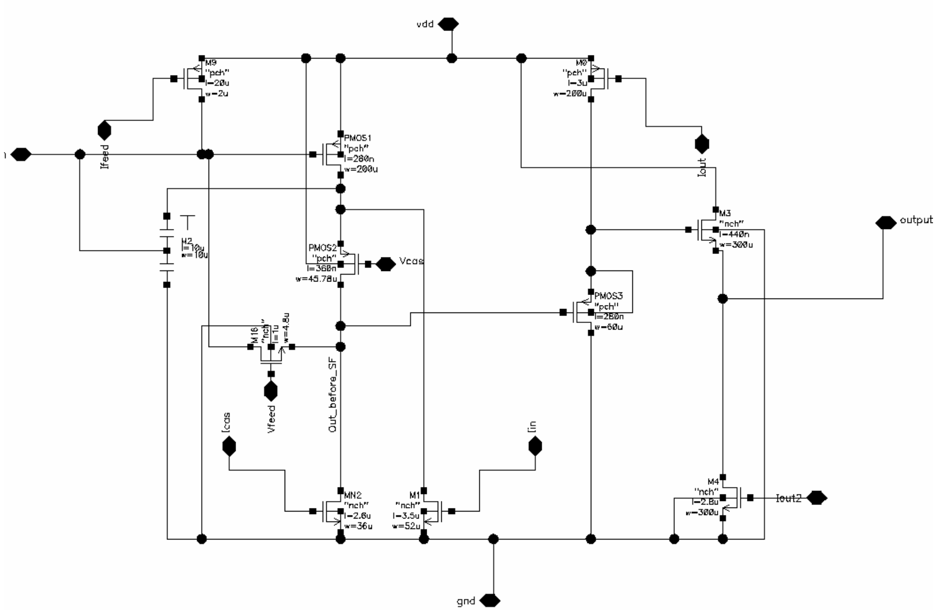

Figure 3.42. Schematic of a channel of an aSiScope pre-amplifier.

The speed response of the circuit has still been considered in the design optimization, so that the circuit has to present a peaking time of about 25 ns. The buffer stage comprises 2 source follower transistors in series, as in the MIBEDO_HG channels.

As for the MIBEDO channels, some 100 fF injection capacitances are integrated to allow the electrical characterization of the channels. Several results of the electrical characterization are presented in this section. Responses of the circuit to negative input charges of 1 fC and 0.2 fC, for a feedback current of 5 nA and biases for low noise, are presented in Figure 3.43.

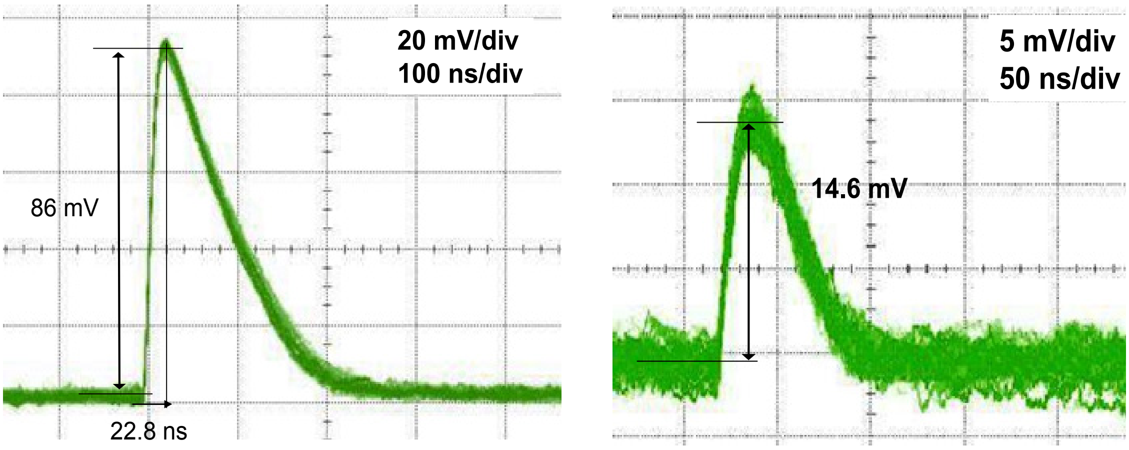

Figure 3.43. aSiScope channel response to a -1fC input charge (left) and to a -0.2 fC input charge (right). 15000 output signals are superposed.

The output signal shows a peaking time of about 23 ns and a peak amplitude of 14.6 mV for the 0.2 fC input charge. The output signal noise has been measured and exhibits a standard deviation of 810 µV rms.

The circuit biased with these “low noise” biases presents a minimum achievable ENC of 70 e^- rms, but a limited linearity in the dynamic range, as it is represented in Figure 3.44. As for the other Active Feedback Preamplifiers already presented in this chapter, the aSiScope circuit output pulse shape can be changed by varying the bias currents set externally. Another set of biases, defined as the nominal biases, permits a higher linear dynamic range, for a measured ENC of 80 e^- rms. The biases have thus to be chosen according to the measurement requirements concerning the input signal amplitude and the requested dynamic range of the measurement. For speed considerations, the circuit peaking time can be set between 20 ns and 50 ns, while the decay time can be varied, together with the circuit gain, by varying the feedback current, as it is presented with some measurements results in Figure 3.44.

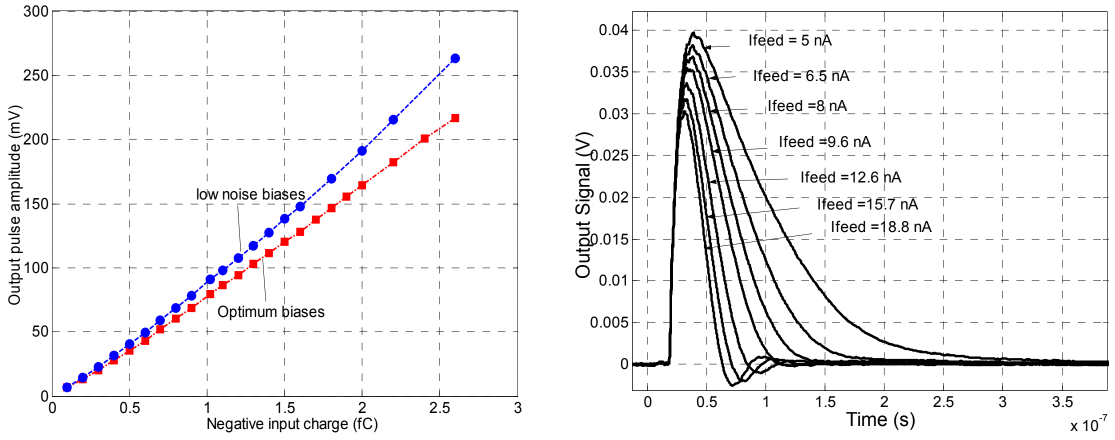

Figure 3.44. Measured dynamic variations of the output pulse amplitude (left). Signal shape measured for different feedback current (right).

The aSiScope circuit can readout low charge input signal thanks to a low ENC, the minimum achievable being of 70 e^- rms. This would allow a signal over noise ratio of 10 for a 700 electrons signal created by a MIP in the a-Si:H detecting device. The ENC, linearity of the pulse amplitude with the input charge, and speed can be slightly varied from their nominal values according to the measurement requirements.

3.3. Conclusions

The circuit scheme chosen to perform the electronic readout in the developed TFA detectors is the Active Feedback Pre-amplifier. The formation of a signal corresponding to the passage of an ionizing radiation in a TFA detector comprises the induction of an electric signal on the sensor electrodes and the readout of this signal performed by the pre-amplifier. A clear understanding of the front-end pre-amplifier transfer function and amplification is thus required to permit deeper analysis of the signal creation in TFA detectors. In the first section of the chapter, the theory of the active feedback pre-amplifier circuit and calculations of its frequency response, its transient response, its stability and its noise performance have been presented.

The AFP chip has then been presented in section 3.1. The 32 channels of Active feedback Pre-Amplifier integrated have been optimized to provide a fast output response. The design optimization has been presented together with results of simulations and of measurements. With nominal biases, the output pulse shows a 5 ns peaking time for a gain of 2.77 mV/fC and an ENC in the order of 450 e^- rms. These characteristics rendered the chip interesting in order to perform the first tests on a-Si:H diodes deposited on ASICs.
The aSiHtest chip has been presented in section 3.2. It has been designed as a global test chip and presents different structures and readout electronics, offering different possibilities of detector characterization. The central area of the chip integrates different metal pads on top of which will be deposited the a-Si:H detecting device. The designed metal structures present different sizes, different shapes, and different openings in the passivation, to study the TFA detector pixel segmentation. Leakage current characterizations of the defined pixels can be performed thanks to integrated current amplifiers which present a selectable gain from 10^2 to 10^5. The aSiHtest integrated circuit comprises fast preamplifier channels with a peaking time of 5 ns and an ENC of about 160 e^- rms connected to both thin strip structures and octagonal pads. Channels of a second version of active feedback pre-amplifiers are also integrated. They have a minimum ENC of 70 e^- rms for a peaking time of 25 ns. The different metal structures and electronic readout of the aSiHtest chip have been presented in details in the chapter.

The two presented chips and their different electronic readouts and integrated electrodes permit a large panel of test possibilities for the thin film on ASIC technology. Electrical characterization of the n-i-p a-Si:H structures can be performed, together with the study of the TFA detectors pixel segmentation. The 3 transimpedance pre-amplifiers developed present different properties of speed, noise, and dynamic range, which can be also slightly shifted thanks to an external setting of their biases. The different pre-amplifier can be chosen and tuned to meet the measurement requirements. The aSiHtest chip integrates fast pre-amplifiers with a minimum pulse peaking time of 5 ns in order to perform charge transport characterization in the a-Si:H detecting device. Pre-amplifiers with a minimum ENC of 70 e^- rms are also integrated to permit the study of particle detection efficiency with TFA detectors. Moreover, electrodes defining octagonal pixel or long strips with low inter-strip distances (down to 4 μm) are integrated to permit the characterization of the performance and limitations of both a pixel detector and a strip detector based on the TFA technology.

4. Electrical properties and pixel segmentation study of TFA detectors

The performance and limitations of a particle detector based on the TFA technology were studied by depositing a-Si:H sensors on top of the CMOS integrated circuits that have been developed for this work and which have been presented in detail in chapter 3. In the following, we will call:

- a-Si:H sensor: the a-Si:H sensing device based on a n-i-p configuration
- TFA detector: the detecting device made of the integrated circuit and of the a-Si:H sensor deposited on the integrated circuit.

The developed TFA detectors and the deposition technique are presented in section 4.1. The leakage current of the a-Si:H sensor is a crucial parameter for TFA detectors and its detailed study is the scope of this chapter. The results obtained on samples deposited on a glass substrate and on samples deposited on top of the AFP integrated circuit, together with the different mechanisms contributing to the a-Si:H detector dark current at high reverse voltages are presented in section 4.1. Discrepancies are observed between the test structures and the TFA detector which might originate from the electrode segmentation of the latter. These observations lead to the idea of scanning pixels of a TFA detector with an electron beam from a scanning electron microscope, in order to investigate the detector pixel segmentation. These tests and their results are presented in section 4.2. The impact of the detector bottom electrode shape and size and of the ASIC/a-Si:H interface on the leakage current of TFA detectors can be studied on detectors based on the aSiHtest chip (section 3.2). The different results obtained are presented in section 4.3.

4.1. Deposition of an a-Si:H sensor on integrated circuit and leakage current considerations

4.1.1. Vertically integrated amorphous silicon particle sensor

The depositions of the a-Si:H films for the different test structures and for the TFA detectors have been performed by the Institute of Micro-technology of Neuchâtel (IMT), at the Photovoltaics and Thin Film electronics laboratory [IMT]. This institute has a high degree of expertise in the deposition of a-Si:H thin films (< 1 μm) for photovoltaic applications. Moreover, a reactor is dedicated to the fabrication of thicker films (> 10 μm) for the research activities of the SIAM collaboration with CERN on the development of TFA detectors [SIAM]. The different a-Si:H devices used in the characterizations presented in this work were deposited by Very High Frequency Plasma Enhanced Chemical Vapour Deposition (VHF PE-CVD) at 70 MHz and 200 °C using an hydrogen dilution of silane [Wyr03]. This deposition technique is presented in section 2.2. It presents the advantage of using a plasma which results in a soft ion bombardment and in relatively low electric fields, so that no important voltage spikes can affect the integrated circuit during the growth of the TFA detector. Devices tested were deposited at a rate of 1.56 nm/s, thus allowing the deposition of a 30 μm thick device in less than 6 hours. A sequence of continuous, uninterrupted a-Si:H layers is deposited to form the diode structure, respectively n-doped, non doped and p-doped a-Si:H to form the n-i-p device. The n-doped and p-doped layers are deposited with a standard thickness of 30 to 60 nm, while the non doped layer thickness determines the diode thickness.

Test structures on glass were first developed and tested. N-i-p a-Si:H layers were evaporated on a Chromium (Cr) or Aluminium (Al) coated glass substrate. The pixel areas were then defined by a patterned Transparent Conductive Oxide (TCO) top electrode, either Zinc Oxide (ZnO) or Indium Tin Oxide (ITO). This transparent top contact permits to test the a-Si:H sensor with a laser, as it will be presented in Chapter 5. The patterning was done by a rubber stamping process followed by a wet etch of the TCO. A subsequent partial plasma etch of the a-Si:H layer was also carried out to better define the pixel area. A schematic cross section and a picture of a test structure are presented in Figure 4.1.

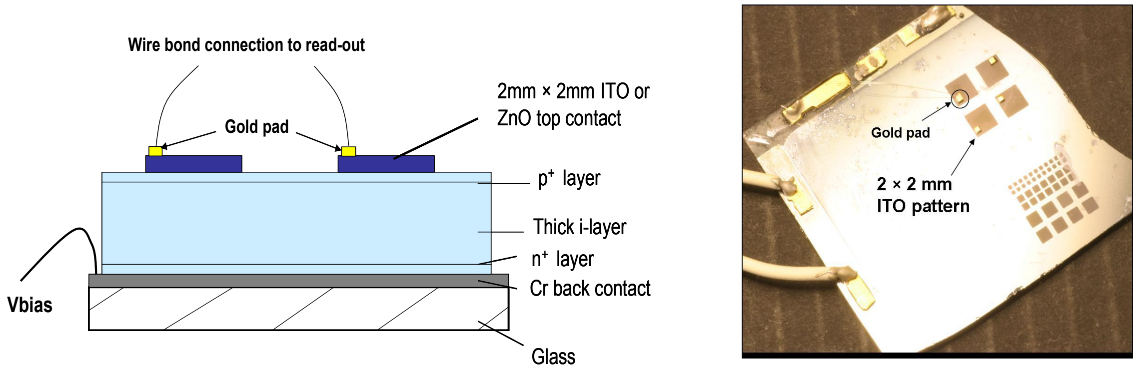

Figure 4.1. Left: Schematic cross section of a n-i-p a-Si:H diode test structure deposited on a glass substrate. Right: Picture of a test structure: the top square TCO electrode defines the active area which is here of 2 mm × 2 mm.

These test structures were in a first stage tested at the IMT to optimise the deposition conditions to obtain thick devices with low defect density, low internal stress, minimal powder formation in the reactor chamber and low leakage current [Cha96]. I have also characterized some optimised test in this thesis, to study the leakage current and also the radiation hardness of the material (Chapter 7).

The same process was then transferred for the fabrication of the TFA detectors. A first process step consists in plasma cleaning of the integrated circuit, and can be a critical step, since in this case the chip faces relatively dense plasma that could lead to the destruction of the circuit. Adapted plasma and Electro-Static Discharge (ESD) protections integrated in the chip for each metal pad prevent such deterioration. Successive depositions of a n-doped layer, a non doped layer and a p-doped layer of a-Si:H are then performed. Finally, a TCO layer defining the global top electrode contact is deposited. The TFA structure is presented in Chapter 2 (Figure 2.18). The different metal electrodes integrated in the chip which define the detector pixels are connected one to the other through the a-Si:H films. The n-doped layer is first deposited in a thin film of about 30 nm, and the i-layer presents a high resistivity (~ 10^{10}-10^{12} Ω·cm) in comparison to doped layers (~ 10^{3}-10^{5}Ω·cm). The resistivity between metal electrodes and the cross talk effects between pixels are then defined by the n-layer. A patterning of this layer can be performed to reduce the conductive path between pixels, but this process step could be avoided by the development of a specific low-conductivity n-layer (~ 10^{5}-10^{6} Ω·cm).

The a-Si:H sensors were deposited both on the AFP and on the aSiHtest integrated circuits I developed in this work and presented in detail in chapter 3. The obtained TFA detectors are presented in Figure 4.2.

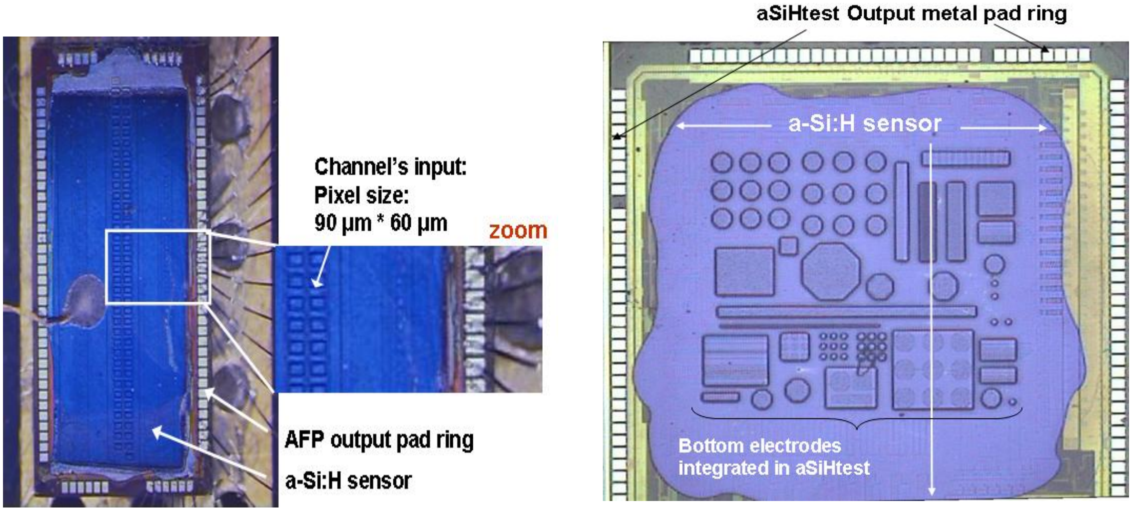

Figure 4.2. Pictures of 2 TFA detectors developed. The n-i-p a-Si:H layers and the TCO layer are deposited on an AFP chip (left) and on an aSiHtest chip (right). The deposited layers are removed by plasma etch above the metal pads of the circuit periphery to permit external access to the integrated biasing circuits and pre-amplifiers outputs.

The top electrode is transparent, so that tests as the laser tests presented in chapter 5 could be performed. The different tests carried out have thus been done with specific care to ensure dark conditions on the diode, as a-Si:H is a good photo-detector. The measured leakage currents are thus often referred to as dark currents. Different tests have been made at CERN to connect the top electrode using micro wave wire bonding, but with no success, because of the uneven surface of the TCO layer. The connection was performed by gluing with conductive glue a small gold pad on the conductive layer from which wire bonding could be performed or by directly gluing the bond wire on the TCO layer (Figure 4.2). The different experimental results I have obtained with these 2 different kind of TFA detectors are presented in this thesis.

4.1.2. High reverse bias current in n-i-p diodes deposited on glass or on ASIC

The leakage current of a detector is a crucial parameter for particle detection applications. Low dark reverse bias currents of the a-Si:H n-i-p structures are needed for a good operation of the device, mainly for noise reasons. A shot noise source is associated to the n-i-p diode leakage current I_{leak} and its power spectral density is defined as $2 \cdot q \cdot I_{leak}$. A particle will create a low amplitude signal in the a-Si:H sensor, so that the leakage current has to be low enough to ensure a noise lower than the expected signals. The different noise sources and the calculations of the Equivalent Noise Charge (ENC) of the Active Feedback Preamplifier have been presented in detail in section 3.1. The contribution from the noise source associated to the leakage current of the a-Si:H sensor (Figure 4.3) to the pre-amplifier output noise can be calculated using the equation 3.50 established in section 3.1, referred to as equivalent noise at the pre-amplifier input (ENC).

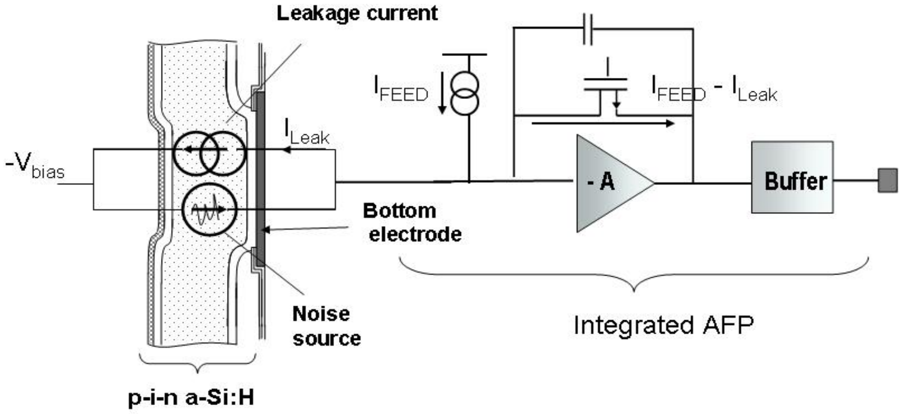

Figure 4.3. Schematic representation of a single pixel. The n-i-p layers are deposited on top of the AFP, each bottom electrode integrated in the AFP defines the pixel active area and is directly connected to the readout pre-amplifier. The pixel leakage current induces additional noise to the circuit and varies the feedback current of the pre-amplifier.

The current mirror structure which delivers the biasing current I_{FEED} flowing through the active feedback of an AFP is also connected to the input node, as it is represented in Figure 4.3. A high leakage current I_{leak} originating from the diode will then strongly impact the pre-amplifier transfer function, as the real current that will flow in the active feedback will not be I_{FEED} but $I_{FEED} - I_{leak}$. The leakage current has to be negligible in

comparison with the feedback currents used in the pre-amplifiers. To obtain low noise AFP, the feedback current has to be low, and a feedback current of few nA is used in the aSiScope readout electronics integrated in the aSiHtest chip (section 3.2).
The n-i-p a-Si:H diodes also require high voltages to be fully depleted, as it is presented in section 2.3, and high voltage breakdown of the diodes are also needed to optimise the a-Si:H sensor, requiring low leakage current for high reverse biases on the sensor.
It is therefore crucial to understand the origin of a-Si:H sensor dark currents for high reverse biases and the mechanisms influencing it in a TFA detector configuration.

The dark reverse bias current in thin n-i-p a-Si:H diodes (< 1 µm), such as solar cells and photo-detectors, has been analyzed by many authors. The experimental results are compatible with perfectly blocking electrodes and the reverse current is determined by the thermal generation of charges in the intrinsic layer [Str90, Mei04]. The thermal generation current I_{th} arises from the excitation of electrons from the valence band to the empty defect states in the gap, and from the filled defect states to the conduction band. The current density thermally generated J_{th} depends on the defect density N_{db} and on the bandgap of the semiconductor material [Mei04]:

$$J_{th} = q\, d\, N_{db} \frac{1}{\tau_{gen}} \exp\left(-(E_C - E_{FD})/kT\right) \qquad (4.1);$$

where d is the intrinsic layer thickness, τ_{gen} the time constant governing the thermal generation, and E_C-E_{FD} the energy between the conduction band and the traps involved in the generation. This latter energy is usually $E_G/2$ as the dangling bond traps are located around the mid-gap. Low values of J_{th} in the range of 1 to 10 pA/cm^2 were measured at the IMT for 1 µm thick diodes [Wyr03]. However, for the development of TFA detectors, thicker diodes had to be deposited, resulting in higher applied reverse voltages on the detector and in high internal electric fields (10^4 to 10^5 V/cm). Previous studies on thick n-i-p diodes (up to 20 µm) have already demonstrated sharp increases of the dark current for high reverse biases [Che94, Poc96]. This effect has also been observed on some measurements we have performed on the test structures evaporated on a glass substrate. The results I have obtained for a 32.6 µm thick and a 25 µm thick n-i-p diode are presented in Figure 4.4. The diodes under test had an active area of 4 mm^2, and the 25 µm thick sample incorporates an additional layer called “buffer” layer at the p-i interface, deposited under higher hydrogen dilution of silane than used for the rest of the intrinsic layer. The incorporation and effect of this buffer layer will be explained later.
The measured current densities are much higher than those measured on 1 µm thick diodes. The higher sensor thickness results in a higher total number of defects and in a higher thermal generation current in the i-layer, which is moreover enhanced by the elevated internal electric field of the diode for high reverse biases, by a Poole-Frenkel mechanism presented later on. The increase of the leakage current with the device

thickness has been characterized at the IMT on test structures and results are reported in [Wyr04], indicating a contribution to I_{leak} from defects in the bulk of the i-layer. This is also observed on the measurements we have carried out on the test structures: at low reverse voltages on Figure 4.4, the 25 µm thick diode exhibits lower leakage current than the 32.6 µm, while the high reverse voltages differences are explained by other mechanisms.

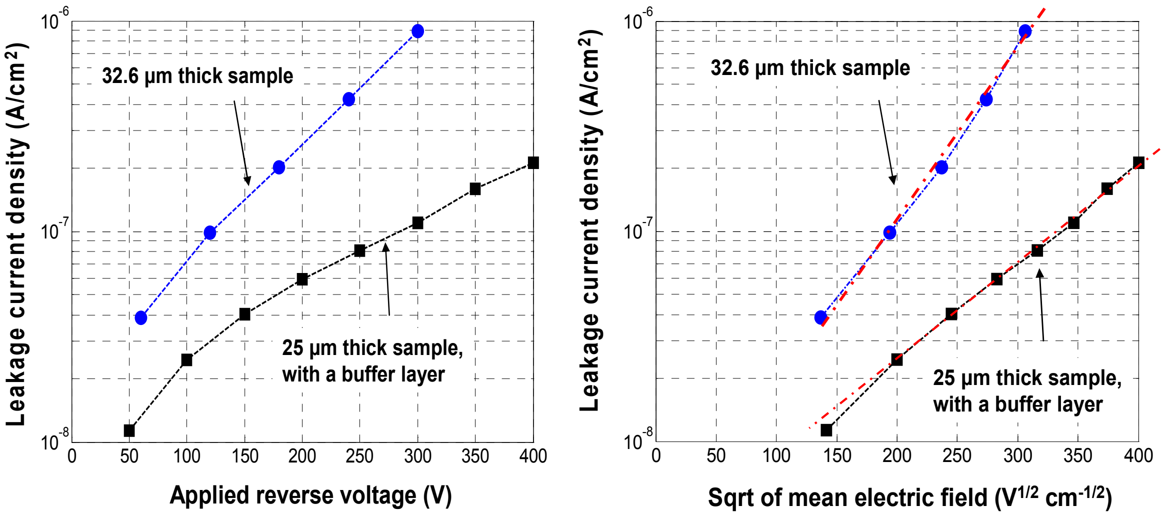

Figure 4.4. Leakage current densities measured on 32.6 µm and 25 µm thick diodes with an area of 0.04 cm^2 and deposited on glass. Left: Variations with the applied voltage. Right: Variations with the square root of the mean electric field ($\sqrt{V/d}$).

The measured currents sharply increase with the applied reverse bias voltage, and for both samples the currents at 300 V are about an order of magnitude higher than the currents at 100 V. This rapid increase indicates that other mechanisms are involved. Three different leakage mechanisms have been considered by some authors: tunnelling conduction by variable range hopping through the p-layer defects, field enhanced generation current at the p-i interface by a Poole-Frenkel mechanism, and injection from the metal electrodes [Che94]. The p-i interface is a high field region, as the electric field extends from this interface (section 2.3), and it also contains high defect density. The interface field enhanced generation can thus be the dominating process at room temperature.

In the presence of an electric field E, the effective activation energy of the ionisable defects decreases with the field and is lowered by the amount $W = q \cdot \gamma \cdot E^{1/2}$ (Poole-Frenkel mechanism), so that the reverse bias current can be expressed as [Che94]:

$$I \approx I_0 \exp\left(-(E_0 - \gamma\sqrt{E})/kT\right) \qquad (4.2); \qquad \gamma = \sqrt{\frac{q}{\pi \varepsilon_0 \varepsilon_{aSi}}} \qquad (4.3).$$

E_0 is the energy between the trap and the conduction band, and γ is the Poole-Frenkel constant with a theoretical value of ~ 2.25×10^{-4} eV·V$^{-1/2}$·cm$^{1/2}$. Combined effects of the field enhancement of the thermal generation (equivalently seen as a decrease of the activation energy) and of stronger generation and injection at the p-i interface can explain the sharp increase of dark current with increasing reverse biases.

The measured currents presented in Figure 4.4 are in agreement with a field enhanced generation, as for both samples the current I_{leak} seems to vary exponentially with the square root of the estimated electric field, simply defined here as the applied voltage V over the i-layer thickness (Figure 4.4 right). The two observed slopes are however different, and this can be attributed to the additional buffer layer added in the 25 µm thick sample, which permits to lower the dark current at high fields by reducing the contributions to the dark current originating from the p-i interface. Optimisation performed at the IMT proved that an important leakage source was originating from this p-i interface: different n-layer configurations were not inducing variations of the current, an increase of the p-layer thickness didn't improve the diode performance, but the introduction of a thin buffer layer deposited under much higher hydrogen dilution of silane than used for the rest of the intrinsic layer resulted in a sharp reduction of the current at high reverse bias voltages. These results are presented in [Wyr04] and illustrated with the currents we have measured on structures with and without buffer layer (Figure 4.4). They demonstrate a strong field dependent dark current for high reverse voltages. The main contributions to the dark current are different for thin layers used in solar cells and photo-detectors than for thick layers used for particle detection, for which high reverse voltages and high internal electric fields are needed. The resulting optimisations and "recipe" to build the diodes are then different for the two cases, and specific care has to be taken with the p-i interface for thick diodes. The measurements presented in Figure 4.4 show a reasonable current density of about 10^{-7} A/cm^2 at high fields, so that the obtained leakage current of a 100 µm ×100 µm pixel would be at maximum in the range of 10 pA.

The first depositions of a-Si:H n-i-p films on top of an ASIC were performed on top of an AFP integrated circuit. The developed detector is represented in Figure 4.2. 32 metal pads, each having an active area of about 60 µm × 90 µm, are located in the centre of the circuit and are connected to the inputs of AFP integrated pre-amplifiers presented in section 3.1. The n^+ layer is directly connected through the bottom electrode to the pre-amplifier input, which is at a fixed voltage of about 1.7 V. The reverse biasing of the detector is achieved by applying a high negative voltage on the p^+ layer via a wire bond connected to the top electrode of the detector. A first characterization of the detector consisted in studying the high reverse voltage currents. These currents have been measured using two different techniques. First, the global leakage current of the whole structure can be readout on the Keithley voltage generator used during the tests to bias the detector.

Moreover, a solution was found to measure the individual pixel leakage current and is illustrated in Figure 4.5.

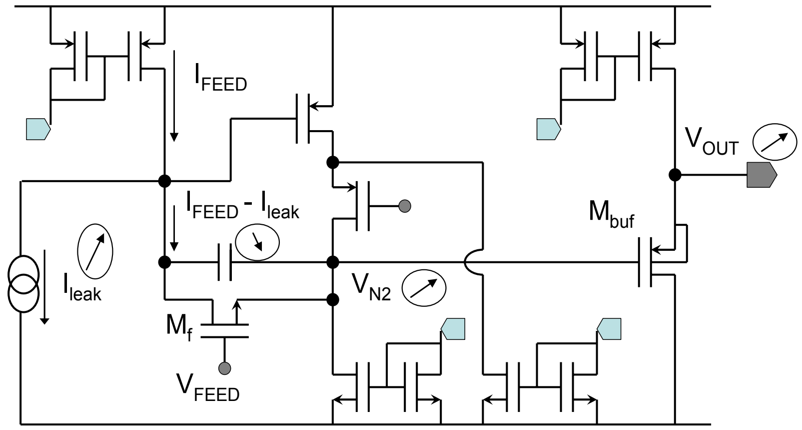

Figure 4.5. Schematic of an Active Feedback Pre-amplifier with the n-i-p diode current source connected at its input.

The pre-amplifier output DC level V_{OUT} is fixed by the gate to source voltage V_{gs} and drain to source current I_{ds} of the buffer transistor (M_{buf}). The current I_{ds} is fixed and V_{OUT} equals V_s, so that a variation of the M_{buf} gate voltage (V_{N2}) will induce a similar variation of the output DC level. This voltage V_{N2} is moreover fixed by the feedback transistor. Its gate voltage V_{FEED} is fixed, and its source voltage which fixes V_{N2} will then depend on the current flowing through M_f. This current equals I_{FEED} for no leakage current originating from the detector. A current I_{leak} will lower the effective current flowing through M_f and will then result in a decrease of M_f V_{gs}, and in an increase of V_{N2} and of the DC output voltage.

The individual pixel leakage current was thus measured by first measuring the DC output voltage for no bias applied on the detector, so that it corresponds to I_{FEED}. For applied reverse voltages, the output DC level was observed to increase, and the current I_{leak} was extracted by increasing I_{FEED} to obtain the same DC output level as measured for no leakage, the current increment being equal to a pixel I_{leak}. The individual pixel leakage currents have been measured on a 32.6 µm thick a-Si:H detector deposited on an AFP chip, for the 12 connected channels and results are presented in Figure 4.6. These results together with the global leakage current corresponding to 32 pixels are presented as current density versus the applied voltage over the detector thickness in Figure 4.6 right, and compared with the results obtained on the 32.6 µm thick detector deposited on a glass substrate.

A sharp increase of the detector current is measured for increasing reverse voltages, and high currents of about 60 nA for a reverse voltage of 260 V are measured per pixel. The resulting current densities measured are very high in comparison to the ones measured on the glass sample. The difference increases as the reverse voltage increases, and for a detector bias of 260 V (equivalent to an applied bias of ~ 8×10^4 V/cm), the currents measured on the TFA detector are 3 orders of magnitude higher than on the test structure. A difference of 2 orders of magnitude is measured between 3×10^4 V/cm and 8×10^4 V/cm.

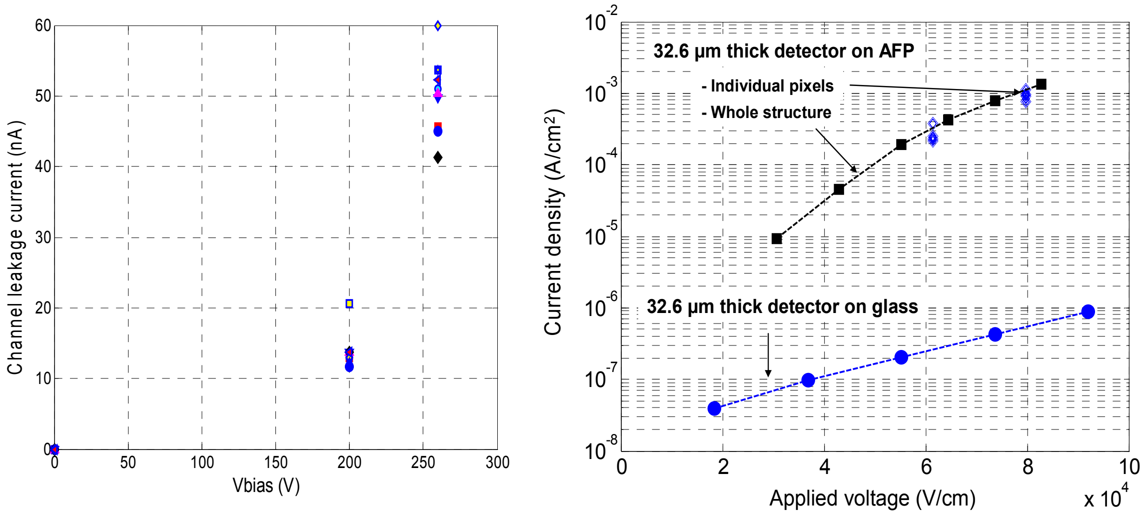

Figure 4.6. Left: Individual pixel dark current for different detector reverse biases on the TFA detector with 32.6 µm thick sensor and AFP chip. Right: Comparison between measured current densities on 32.6 µm thick detector deposited on glass and on ASIC.

This strong reverse bias dependent current measured for the TFA detector indicates that the additional currents are for the most created by field enhanced generation. These current discrepancies between n-i-p diodes deposited on a glass substrate and on integrated circuit have been confirmed by measurements performed on a TFA detector based on a chip called MACROPAD also developed at CERN, and the results are presented in [Mor04]. The measured TFA detector dark currents are too high to get reasonable operating conditions of the detecting device. The understanding of the mechanisms creating these high currents and the reduction of these currents are then of primary importance for the development of TFA detectors.

4.2. TFA detector electrode segmentation characterized with a Scanning Electron Microscope

As it has been presented in section 4.1, the dark current of n-i-p a-Si:H diodes for high applied reverse biases can be attributed to a field enhanced thermal generation. The high currents measured on a TFA detector could then be caused by high local electric fields in the TFA detector pixels. The n-i-p layers are directly deposited on processed integrated circuits and the passivation layers of the chip create an unevenness of its surface, as it has been presented in sections 2.3 and 3.3. The n-i-p a-Si:H layers then have the same profile as the circuit surface, as it is schematically represented in Figure 4.7.

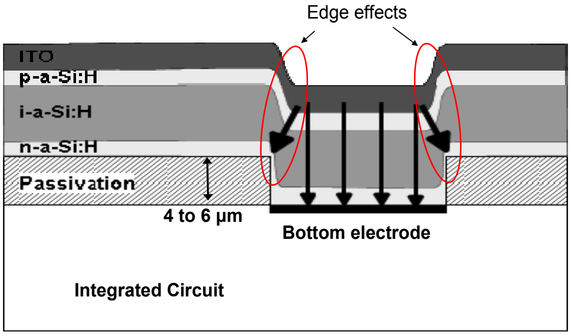

Figure 4.7. Schematic cross-section of a TFA detector. The passivation layers of the integrated circuit induce an unevenness of the deposition substrate profile, and result in complex geometry of the detector that might induce high fields at the edges of a pixel.

The obtained complex diode geometries might cause edge effects at the pixel periphery where higher fields could be induced because of the passivation step (Figure 4.7) and that could explain the high dark currents. In order to study in detail the topology of the TFA detector surface and the internal field distributions, we have proposed and used a measurement technique based on a Scanning Electron Microscope (SEM). The measurement set up is presented in 4.2.1, together with the first results obtained on test structures. The results obtained on the TFA detector based on the AFP circuit are presented in 4.2.2.

4.2.1. Electron Beam Induced Current technique for a-Si:H detectors

The technique we used to characterize the pixel segmentation of a TFA detector and to study possible edge effects is based on a scan of the active area of a pixel with the electron beam of a SEM. The electron beam allows the injection of keV electrons into the detector with a precision of few nanometers. The keV electrons will create electron-hole pairs in the depleted region of the a-Si:H sensor, and a corresponding signal will be induced on the electrodes defining the pixel active area. The induced signal amplitude depends on the effective depleted thickness, on the diode geometry that defines the weighting potential, and on the drifting carrier number and speed, so that variations of the internal electric field of the active area result in different induced signals. A detailed study of the induction of signal by drifting electrons and holes in a-Si:H sensors has been done and theory and results are discussed in more detail in Chapter 5.

This Electron Beam Induced Current technique, referred to as EBIC, is a well known powerful semiconductor analysis technique [Lea82, Zhu03]. The signals induced on the detector electrodes by the scan of the electron beam on a defined surface can be directly readout on an oscilloscope or can also be amplified and fed back to the SEM operating system as “EBIC” signal, in such a way that a picture can be constructed from this signal (Figure 4.8).

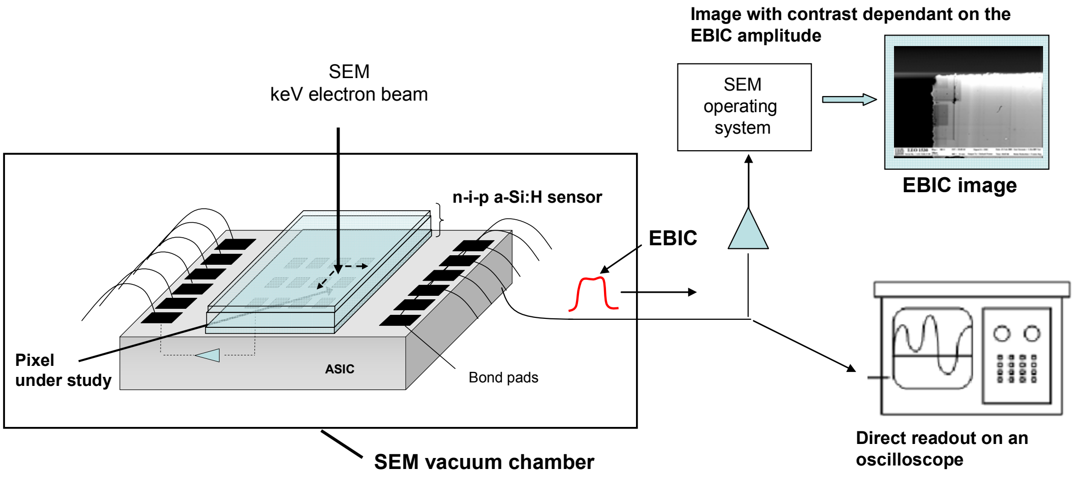

Figure 4.8. Schematic of the EBIC measurement technique. The Electron Beam Induced Current in the detector is amplified by the ASIC pre-amplifiers and the output signals can be directly readout on a scope or used to build an EBIC image which displays varying contrast for varying induced current.

Variations of the signal are then displayed as variations of contrast in the EBIC image. This technique is thus very interesting for the characterization of TFA detectors, as mono-energetic electrons can be injected in a very precise zone, and a scan of the pixel active area gives a direct insight into the internal field properties, which can even be directly imaged thanks to the EBIC mode of SEM.

Tests were carried out with a 300 V reverse bias applied on the diodes and with a 20 keV electron beam. When the electron beam scans the active area, the current induced on the detector top electrode is then amplified by an Active Feedback Pre-amplifier, and a corresponding output voltage can be readout. The AFP output signal was directly fed back to the SEM operating system to build the EBIC image. Any change in the generation, drift or recombination of the generated carriers in the detector is then displayed as variations of contrast in the EBIC image. An illustration of the measurement technique is presented in Figure 4.9. The electron beam scans the selected area by doing 768 horizontal line scans from the top to the bottom of the selected area, one line scan being performed from left to right. On the SEM picture of one of the diodes (Figure 4.9 center), one can see the ITO pattern defining the pixel area, a gold pad glued on top of the ITO electrode and a wire bond connected to another diode passing above the tested diode active area. An EBIC image of the same diode is presented in Figure 4.9 right. When the electron beam is above the active area, a corresponding signal is created in the detector so that the diode active area appears in white. However, when the electron beam is above the "crossing wire-bond" and the gold pad, electrons are absorbed before reaching the detector, so that no signal is created, and so that these regions appear dark in the EBIC image. The slight contrast differences observed in the active area are due to a degradation of a part of the diode with the electron beam. Degradation of the a-Si:H material under keV electron beam has been characterized during this work and will be presented in detail in Chapter 7.

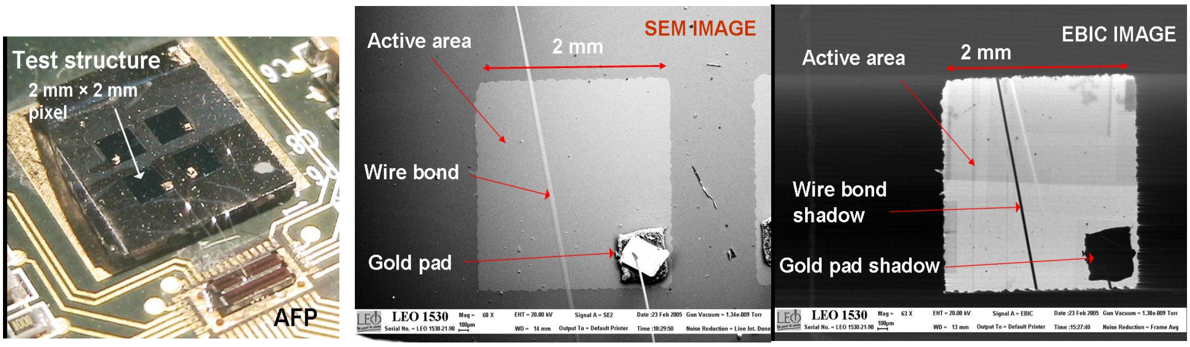

Figure 4.9. Left: Picture of the test structure with 4 diodes wire bonded to 4 AFP inputs. Center: SEM image of one diode. Right: EBIC image using the signal induced by the electron beam in the diode as contrast.

The EBIC technique is a very interesting tool to characterize an a-Si:H sensor. The homogeneity and edge behaviour of one diode of the test structure can be characterized and directly imaged. Some results obtained on the test structure are presented in Figure 4.10. The full diode EBIC image shows a good homogeneity of the signal response (uniform contrast in the active area) and no edge effects are observed on this image. The SEM picture and EBIC image of a diode edge show clear similarities between the geometrical ITO electrode and the diode active area, and no edge effect is observed on this structure. This measurement then demonstrates that no significant variations of the electric field profile are present at the edges, so that the active area of the diode is well defined by the geometry of the ITO electrode. No significant additional currents from edges are then expected to contribute to the dark current measured for high reverse voltages on the test structures.

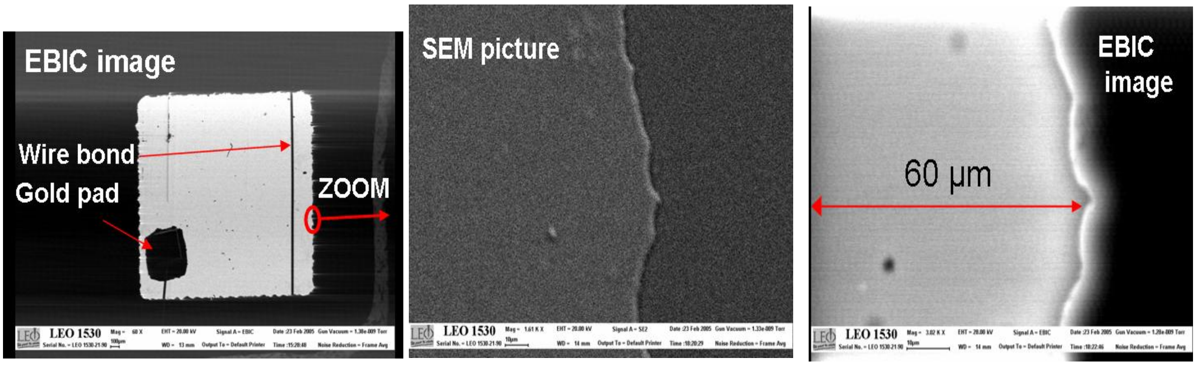

Figure 4.10. Left: EBIC image of one diode. Center: SEM picture of the diode edge. Right: EBIC image of the diode edge.

4.2.2. EBIC study of a TFA detector

The EBIC technique was used on the TFA detector made of a 32.6 µm thick a-Si:H diode and of an AFP circuit (Figure 4.2 left) to study the pixel segmentation of the detector and to look for high field regions that could induce the high measured dark currents. The AFP circuit metal pads located in the centre of the chip define the detector pixels (Figure 4.2). These metal pads are designed in the last metal layer of the technology (Aluminium) and have a surface of 102 µm × 76 µm. Passivation layers, respectively nitride, oxide and polyimide, are deposited on the integrated circuit in a final process step, covering the whole chip surface. Windows are opened in these passivation layers on top of and inside each metal pad, so that a 94 µm × 68 µm metal pad is seen at the chip surface. All around this zone 8 µm of the metal pad is covered by the passivation layers (Figure 4.11 left). The deposition of the a-Si:H n-i-p layers on top of the uneven surface of the AFP chip results in an uneven detector topology, which is illustrated by a cross section picture in Figure 4.11 right, for a TFA detector made of an AFP and of a 6.5 µm thick a-Si:H diode. The windows opened in the passivation layers do not have a sharp profile, and the passivation falling edges decrease with an inclination of ~ 55 ° (Figure 4.11 right). The a-Si:H layers follow the same topology at the pixel edges. The polyimide passivation layer presents an uneven surface, and this can induce some defects at the passivation/a-Si:H interface which can cause additional dark currents. A silicon nitride passivation would result in a flatter and more controlled layer and therefore in a better interface with the a-Si:H n-i-p diode.

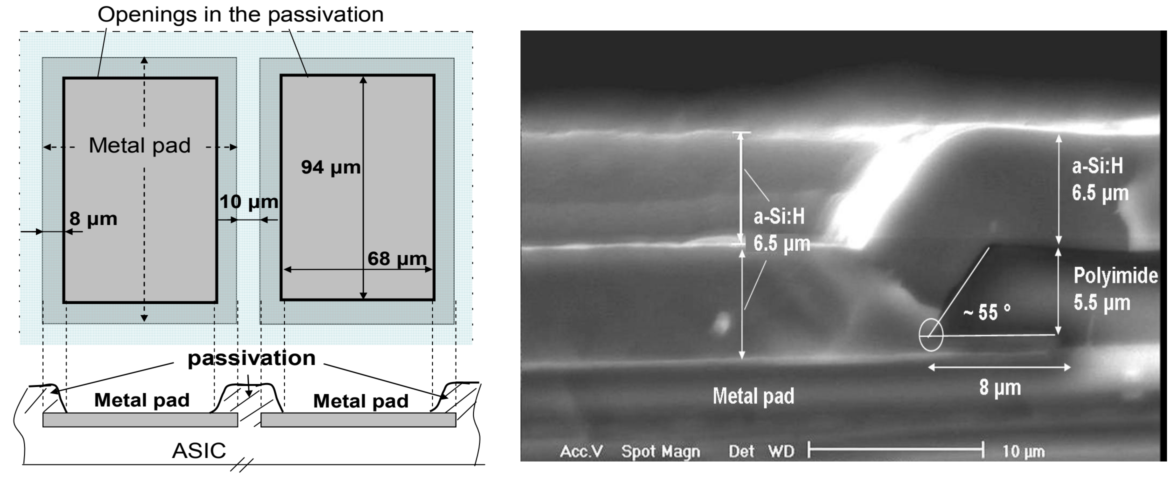

Figure 4.11. Left: Schematic representation of 2 metal pads of the AFP chip, viewed from the top (top) and as a cross section (bottom). Right: Picture taken with a SEM of a cross section of a TFA detector with a 6.5 µm thick a-Si:H diode. The passivation layers present a falling edge with a 55 ° inclination down to the metal pad, and the deposited a-Si:H layers present the same topology.

The TFA detector used in the EBIC characterization has first been studied with standard SEM pictures, presented in Figure 4.12, to observe the pixel topology. The shape of the a-Si:H layers on top of the metal pads is consistent with Figure 4.11 right. At the passivation layer edges, the a-Si:H layers fall onto the metal pad. In a first time, three edges can be defined (Figure 4.12): the first edge corresponds to the beginning of the passivation (and thus a-Si:H) falling edge, the second edge corresponds to the end of the passivation falling edge (thus corresponding to the opening in the passivation) and the third edge corresponds to the end of the a-Si:H falling edge.

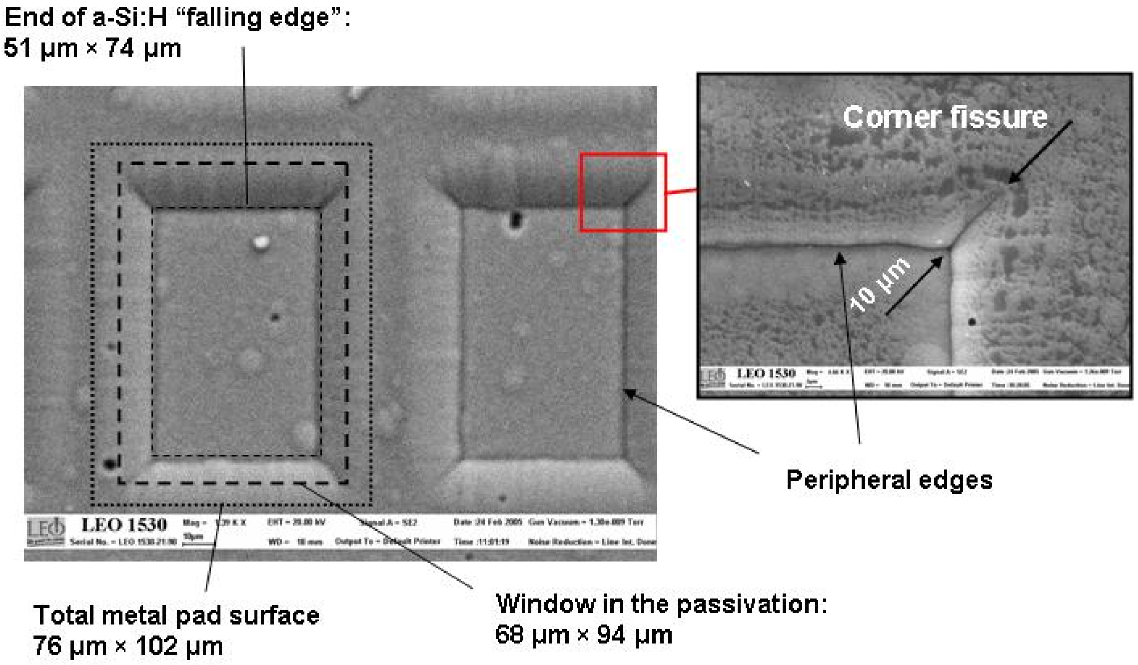

Figure 4.12. SEM picture of two pixels of the TFA detector under study. Peripheral edges are observed together with fissures in the corners, as seen in the zoom (right).

A strong geometrical effect is already observed with the SEM pictures at the third edge. A peripheral edge inside the metal pad is observed. This corresponds to the junction between the a-Si:H layers which were grown on the falling passivation layers and on the flat metal pad. Moreover, another important geometrical effect is observed at the pixel corners, at the junction between the a-Si:H layers grown on the flat metal pad and on two falling passivation layers with perpendicular orientations. This results in a ~ 10 µm long fissure displayed in Figure 4.12. These first observations already give a clear visual indication of a peripheral edge effect and of a corner effect in the TFA detector, caused by the passivation layer step.

The TFA detector was then characterized using the EBIC mode of the SEM and results are presented in Figure 4.13. The EBIC images presented in Figure 4.13 were obtained using a 20 keV electron beam and a 270 V reverse bias applied to the detector. The two pixels first studied with a SEM picture (Figure 4.12) were readout by simply connecting together their pre-amplifier output to the SEM. The electron beam scan results in the EBIC image seen in Figure 4.13 left.

Figures 4.12 and 4.13 left then present the geometrical characteristics and the internal field properties of the same two pixels. An EBIC image of a single pixel connected to the SEM is also displayed in Figure 4.13 right.

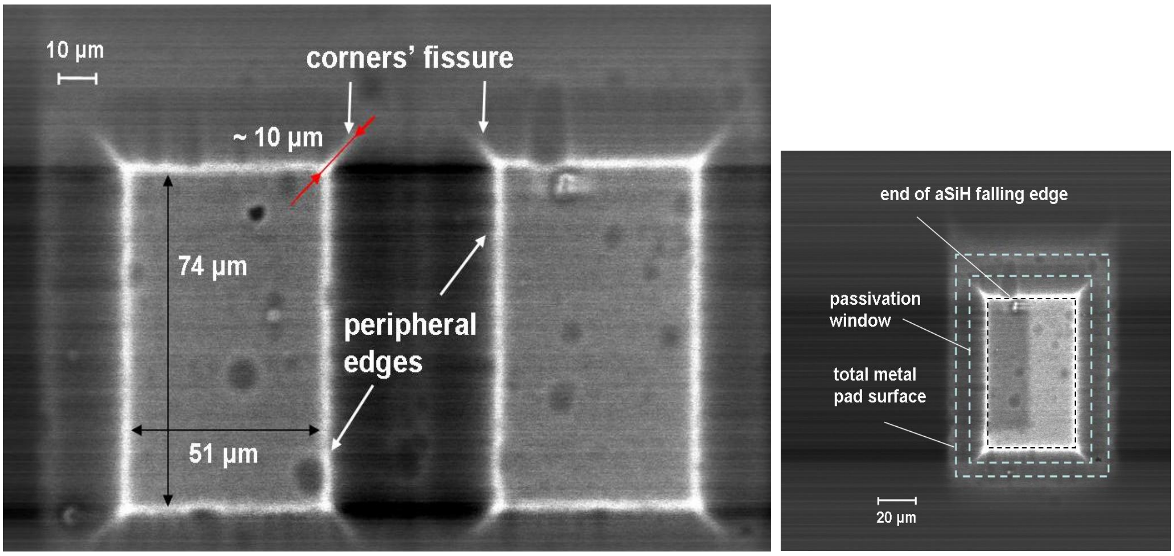

Figure 4.13. Left: EBIC image of 2 pixels with their AFP outputs connected together to the SEM. Clear peripheral edges and corner fissures are observed. Right: EBIC image of a single pixel with its AFP output connected to the SEM.

The contrast images presented in Figure 4.13 are function of the amplitude of the signal induced in each zone of the scanned area. The clearest zones correspond to the higher signal amplitude. These EBIC images clearly show the effect of the particular geometries observed on the SEM pictures on the detector electric field: higher EBIC currents (white zones) are observed at the peripheral edges and at the corner fissures and the defined pattern of the EBIC image is very similar to that of the SEM picture. These higher induced currents then indicate distorted and higher field zones at the pixel edges and corners.

The surface inside the end of the a-Si:H falling edges (or inside the peripheral edges) corresponds to a flat a-Si:H deposited on the metal electrode, and a globally constant contrast is observed in that region. It is interesting to see that any imperfection in this region observed in the SEM image has a particular contrast in the EBIC image. A dust particle is observed on top of the left pixel and also shows itself as a dark spot in the EBIC image. Some circles can be observed in the SEM picture, for the a-Si:H layers either on top of the metal layer or on top of the polyimide. The aluminium metal surface is not perfectly flat and some micrometric small spheres can be found on ASIC metal pads. The same effect has been observed at polyimide surface. The observed circles are however much larger but could originate from the observed metal and polyimide smaller surface non linearity. Successive deposition of material on a micrometric sphere enhances the dimensions of the sphere when looking to it from the last deposited layer. The 30 µm thick a-Si:H layer might enhance the micrometric spheres present at the surface of the metal pad and result in the observed circles. These zones are also seen in the EBIC images with darker contrast and indicate a lower charge collection in these regions. By increasing the energy of the electron beam in EBIC mode, it is also possible to study sub-surface damages that are not visible with any other technique (for example three grey spots are visible on the EBIC image and do not appear in the SEM picture).

Around the peripheral edges, the induced currents are lower (dark contrast). The lowest signals are observed in a zone that corresponds to the falling step of the passivation layers and of the a-Si:H layers. Finally, a slightly higher signal is observed when the electron beam scans the region where the a-Si:H detector is flat and deposited on the passivation layers covering the metal pad, and no signal is induced on the pixel electrode for an electron beam scanning further away.

To study the Electron Beam Induced Currents and the different zones presented above and seen in the EBIC images, the electron beam was set in a line scan mode. In this mode, the beam does scan horizontally the delimited surface always at the same position, as it is illustrated in Figure 4.14 top. A line scan study has been performed using a 20 keV electron beam with an intensity of 386 pA and for different detector reverse biases. One AFP output was connected to an oscilloscope, so that the induced signal in the corresponding pixel was amplified and the output voltage was directly readout and recorded with an oscilloscope. This study was performed on one corner of a pixel. The combined EBIC image, pixel segmentation profile and output voltage permit a detailed analysis of the geometry and of the induced electric field profiles (Figure 4.14). The output voltage of the AFP corresponds to the induced currents in the pixel under study, and therefore to the electric field profile in the region where the keV electrons are injected. Four different regions are recognized in the output voltage of Figure 4.14, which correspond to the different regions observed in the EBIC images. They are presented in Figure 4.14 and the different characteristics of each zone are presented.

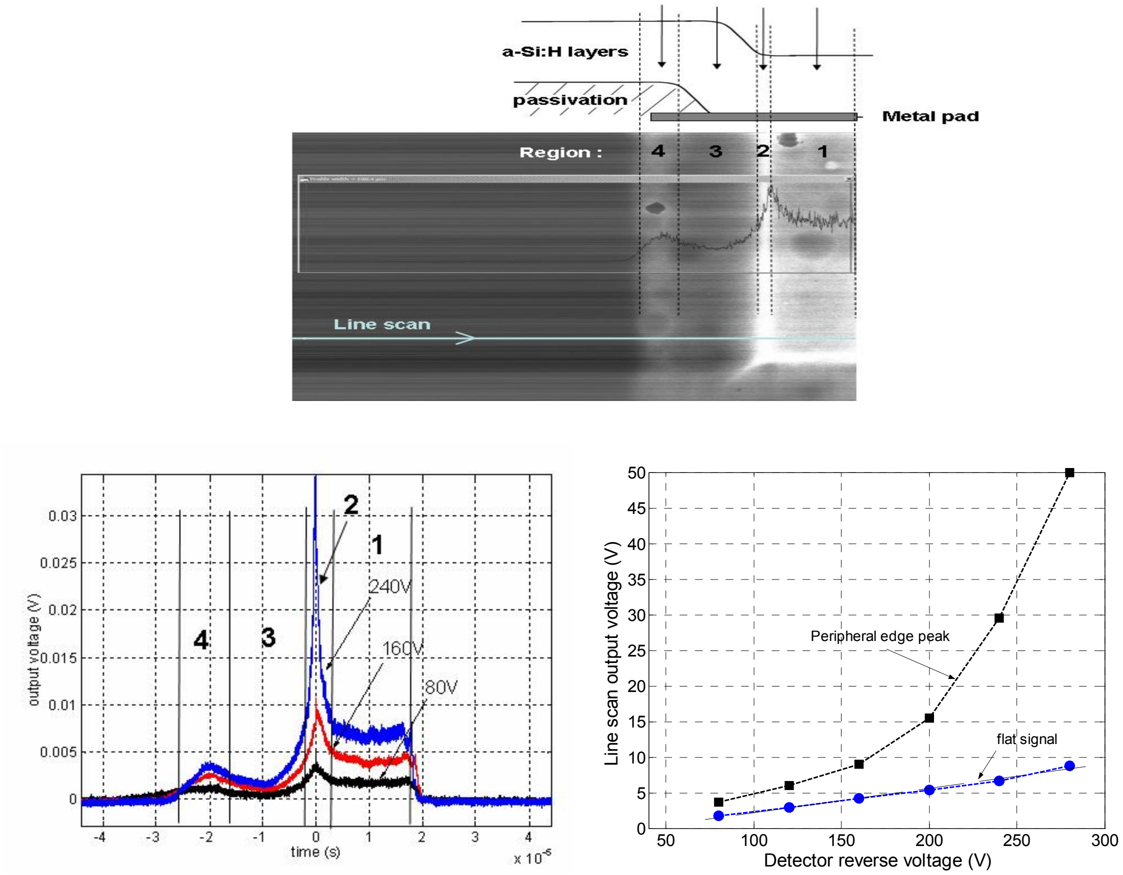

Figure 4.14. Top: EBIC image of a pixel corner, line scan representation and schematic cross section of the sample at the line scan level. Bottom, left: EBIC signal of a line scan for 3 different detector reverse biases (80 V, 160 V and 240 V). Bottom, right: Peripheral edge induced current and current induced in the a-SiH sensor in region 1. Evolutions with the detector bias.

The four different regions can be defined as:

1. The pixel linear region: a flat signal is observed in the region where the a-Si:H layers are flat and above the metal pad. A linear relation between the induced signal and the applied voltage is observed (Figure 4.14), which is reasonable as the electric field profile and depletion width vary as the square root of the voltage and as the number of created electron-hole pairs varies with the depletion width.
2. Edges and corners: a large peak in the signal is observed at the beginning of the rising slope of the top layer (p^+ a-Si:H layer) and above the metal pad, and at the pixel corners. These high currents indicate that higher fields are present in these regions. Moreover, the peak amplitude varies sharply with the applied voltage, as it is represented in Figure 4.14, showing that this region of the diode presents specific electric field and weighting field profiles.
3. Passivation and a-Si:H layers step: in the rising slope above the metal pad the signal is decreased very fast. In this region the electric field and the weigthing

potential present distorted and complicated profiles. An exact explanation of the low induced current is difficult to perform. The low induced currents might originate from the distorted drift of charges in the depleted region and from a higher non-depleted thickness seen between the electrode and the location of the charge creation drift leading to a lower signal (as explained in chapters 5 and 6).

4. a-Si:H layer flat above passivation and metal pad: in this region also the electric field and weighting potential profiles might have distorted and complicated profiles. By passing from the end of rising slope, the electric field could have a distorted profile that will push the electrons toward the rear metal contact, which increases the amplitude of the EBIC signal. A signal could also be induced on the metal pad through the passivation layers when charges are created in a region above the passivation layer and the metal pad. Finally in the regions far enough, for which the lateral electric field is decreased, the EBIC signal completely disappears. Because of a complex profile of the electric field in that last region, it is still possible that EBIC signals are detected.

The EBIC characterization of TFA detector turned out to be a successful technique to observe edge effects and to study the pixel segmentation and homogeneity. The currents induced by the electron beam are similar when the electron beam creates charges in the zone corresponding to flat a-Si:H layers on top of the metal pad. However, at the pixel edges, geometrical effects caused by the unevenness of the ASIC surface and by the passivation layer 5 μm step induce peripheral edges and fissures at the four corners of the pixel, as observed in the SEM pictures. These topological properties result in distorted and high fields at the pixels edges demonstrated by the EBIC measurements. No such effect has been observed on the n-i-p diodes deposited on a glass substrate, which exhibit homogeneous contrast in the EBIC images. As the dark reverse bias currents are mainly attributed to a field enhanced thermal generation, the observed high fields of the TFA detector pixel edges explain the high dark currents measured. In order to reduce the dark currents for TFA detectors, adapted metal pads and passivation opening have to be done during the process of the integrated circuit. The aSiHtest chip has been designed with different metal pad structures and passivation opening, and the results obtained on dark currents are presented in section 4.3.

The EBIC measurement technique is also a very interesting tool to observe material defects and homogeneity in the signal creation, and turned out to be a good technique to characterize the radiation hardness of a TFA detector as degradation of the EBIC signals were observed after a prolonged time of irradiation of a pixel with a high intensity electron beam. These results and studies are presented and discussed in Chapter 7.

4.3. Characterization of TFA detector dark current and back electrode configuration with aSiHtest integrated circuit

The EBIC measurements performed on a TFA detector suggest that the leakage current of the detecting device comprises 3 components: a first current scaling with the pixel surface, a second current associated to the peripheral edge high fields scaling with the back electrode perimeter, and a third current caused by the high fields at the observed fissures at the corners of a pixel, not scaling with the dimensions of the pads. Each of these currents is most probably a combination of field enhanced thermal generation and injection at the p-i interface. The two first contributions have been identified in previous works done on a-Si:H diodes deposited on a glass substrate [Sch96], and the third current was even mentioned in these works but turned out to be negligible. In TFA detectors, the observed high field regions at the edges and corners caused by the integrated circuit unevenness suggest that the two associated currents might have a strong contribution, thus strongly limiting a TFA detector performance. The aSiHtest chip integrates several metal structures in the centre of the circuit that can be used to characterize the impact on the dark current of the back electrode shape, size and opening in the passivation, and to study the existence of the 3 components in the leakage current. The different metal structures are presented in detail in section 3.2, together with the integrated current amplifiers used to readout the leakage currents. The current amplifiers present a gain that can be tuned from 10^2 to 10^5, so that a wide range of currents can be readout (from tens of pA to few μA).
The dark currents of TFA detectors based on the aSiHtest chip have been characterized and results are presented in this section. The measurement set up is first presented in 4.3.1. The influences on the dark current density of the back electrode shape and size, and of the location of the opening in the passivation layers are presented in 4.3.2. Measurements presented in 4.3.2 were performed at room temperature, and some tests have also been carried out at different temperatures. Results are presented in 4.3.3.

4.3.1. Measurement set up

The 21 metal structures integrated in the aSiHtest chip and connected to current amplifiers are presented in detail in section 3.2, and numbered from L1 to L21. These different structures and their associated number are summarized in Figure 4.15. Different TFA detectors have been built using the aSiHtest chip. The depositions of the a-Si:H detecting device have been performed at the IMT in a different reactor than the one dedicated to the characterizations of TFA detectors. This is due to the replacement of the reactor by a new reactor with a larger chamber and able to perform depositions at a higher rate. During the period of installation and optimisation of this new reactor the depositions were performed on another reactor with lower deposition rate (~ 4 Å/s). Samples with a 1 μm, 10 μm and 20 μm thick a-Si:H diode on aSiHtest chips have been produced. Each sample was then mounted on a dedicated Printed Circuit Board (PCB) specially designed to perform the different tests with the aSiHtest chip. A picture of the PCB with a sample mounted on is presented in Figure 4.15.

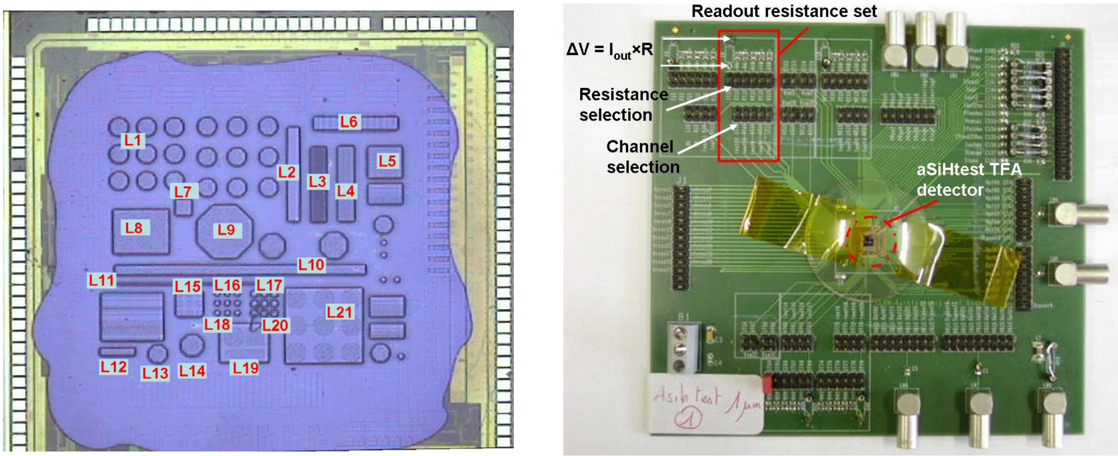

Figure 4.15. Left: TFA detector based on an aSiHtest chip. The 21 metal structures numbered from L1 to L21 in the centre of the detector are connected to current amplifiers for dark current measurements. Right: aSiHtest PCB. The TFA detector is glued in the centre of the PCB. 5 resistance sets are available on the PCB to readout the currents.

The 21 outputs of the current amplifiers connected to the 21 metal structures integrated for I-V characterization are wire bonded to the PCB and connected to readout systems integrated on the PCB. The readout of the output current of a structure is simply performed by connecting the channel output to a resistance connected to ground, and by reading out the voltage difference at the resistance terminals. The different channel outputs are organized into 5 groups on the PCB (4 groups of 4 structures and 1 group of 5 structures). For each group of structures, a set of resistances is available on the PCB for readout. A first stage allows the selection of one of the channel of the group via a jumper, and the second stage permits to choose a readout resistance between 5 different resistances, from 2.4 kΩ to 100 kΩ (Figure 4.15). Depending on the output current amplitude, the resistance is chosen to ensure a sufficient voltage for readout and a maximum voltage difference of 1.8 V, as this voltage determines the drain to source voltage of the transistors connected to the output stage of the current amplifier (section 3.2). By doing so, the current mirror of the output stage is kept in saturation.

When a reverse bias is applied across a thick n-i-p a-Si:H junction, the ionization of defects lying close to the Fermi level is a slow process. Deep defects are thermally ionized and the excited electrons are swept out by the field, leaving behind positive space charges. The positive space charge in the depleted layer is then increasing with time from zero up to a stabilized maximum value $q{\cdot}N_{db}^{*}$. The electric field profile inside the depleted layer can be calculated from the Poisson equation (section 2.2). During the stabilization time of the ionization of dangling bonds, the internal electric field profile varies from a constant value after the application of the reverse voltage to a linear profile with a maximum at the p-i interface after stabilization (the electric field profile is calculated and presented in

Chapter 5). A resulting time-dependent leakage current is observed during this stabilization after the application of a reverse bias, in times that may range from seconds to hours, depending on the applied biases [Dub91]. This effect has been observed in our studies and long stabilization times of the dark current were measured. The TFA detector aims to be used under DC biasing, so that the dark currents were measured in their steady state value for a given reverse bias.

Due to the long stabilization times, a specific data acquisition system was developed. A Keithley voltage generator was used to bias the detector and an Agilent 34970A multi-channel multi-meter was used to readout the voltage drop of the resistances on the PCB (to measure the leakage current). The two devices were controlled by a custom developed Labview program via GPIB connections to a computer. The maximum reverse bias is first applied on the detector, and a time t_1 is chosen for the first stabilization. After this time, several measurements of the voltage drop on the resistances are performed and the reverse bias is then tuned down. Similar sequences are then performed, one sequence consisting in varying the reverse voltage, waiting stabilization time t_2 and acquiring several voltages drop on the resistance. When the reverse bias reaches the minimum bias set, similar sequences are performed with a bias going back up to the maximum reverse voltage by equal voltage steps. The measurement protocol is presented in Figure 4.16, with currents readout during the stabilization times, where t_1 = 1h and t_2 = 10 mn. This measurement has been performed on a 20 µm thick a-Si:H n-i-p diode deposited on top of the aSiHtest chip, and the presented results correspond to the dark current of the structure L21 which consists of 9 octagonal structures, with a global active area of 167747 μm^2. Similar shapes and transients were observed for the different structures.

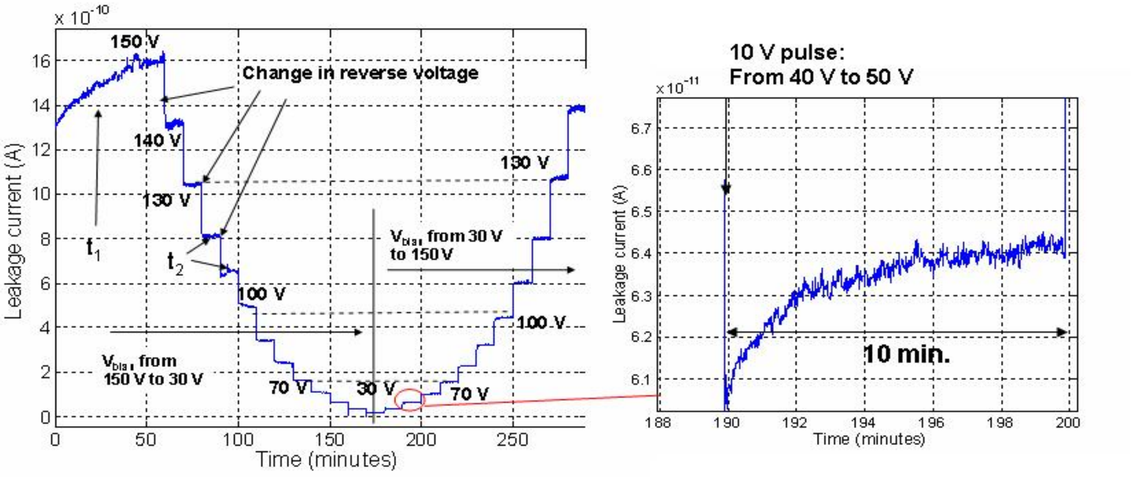

Figure 4.16. I-V measurement sequence on an aSiHtest TFA detector represented as current vs time. 150 V is first applied, after t_1 the bias is switched down to 140 V and then changed of 10 V every 10 minutes, down to 30 V (at this bias voltage and below, leakage currents are too low to be readout) and then up again to 150 V. Stabilization behaviour of the dark current is represented on right, after a 10 V variation (from 40 V to 50 V of reverse bias).

After the application of a positive reverse bias step on the detector, the current rises sharply and then decreases very fast with time. This first transient behaviour can be attributed to the time-dependent field enhanced generation current in the bulk, originating from the varying electric field profile [Kim02], and from the ionization of the dangling bonds. However, the dark current is then observed to slowly increase until stabilization, as it can be observed in Figure 4.16 right. The varying density of ionized dangling bonds and varying electric field are responsible of the transient behaviour of the current, and the electric field at the p-i interface increases with time until stabilization. Enhanced thermal generation or injection [Kim02] at the interface are increased until stabilization and can explain the observed transient.

This transient behaviour of the dark current after a voltage step is already an indication of contributions from bulk thermal generation and enhanced generation or injection at the p-i interface to the dark current in the TFA detector.

4.3.2. Influence of size, shape and passivation layers on the leakage current components

The different structures integrated in the aSiHtest chip have been characterized by using the measurement procedure defined in 4.3.1. A repeatability study has been performed on different structures showing close results for the different measurements, but due to the stabilization time and to the sensitivity of the dark current to the operating conditions, the measurements present an uncertainty that can be estimated at ~ 30 %. Moreover, the currents measured on the different samples present similar global tendencies presented in this section, but some observed deviations between samples suggest a high sensitivity of the dark current to the deposition process.

The results obtained at room temperature on structures with an opening in the passivation layers inside the metal structure and with electrodes presenting different shapes and sizes are first presented. The dark currents of the structures L7, L8, L9, L10, L11, L12 and L13 were measured for varying detector biases. The tested structure shape and number are presented in Figure 4.17 left.

The currents measured on a 20 µm thick sample are first presented in Figure 4.17 right. The measured dark currents present a sharp increase with the detector reverse bias and the structures with an area of 167747 µm^2 present currents from 700 pA to 1.6 nA at 150 V while the smaller structures with an area of 18638 µm^2 have lower currents from 400 pA to 900 pA. The two long rectangles (L10 and L11) present the higher currents. The structure L13 could not be characterized on this 20 µm thick sample (because of an alteration at its surface), but has been studied on the different other samples.

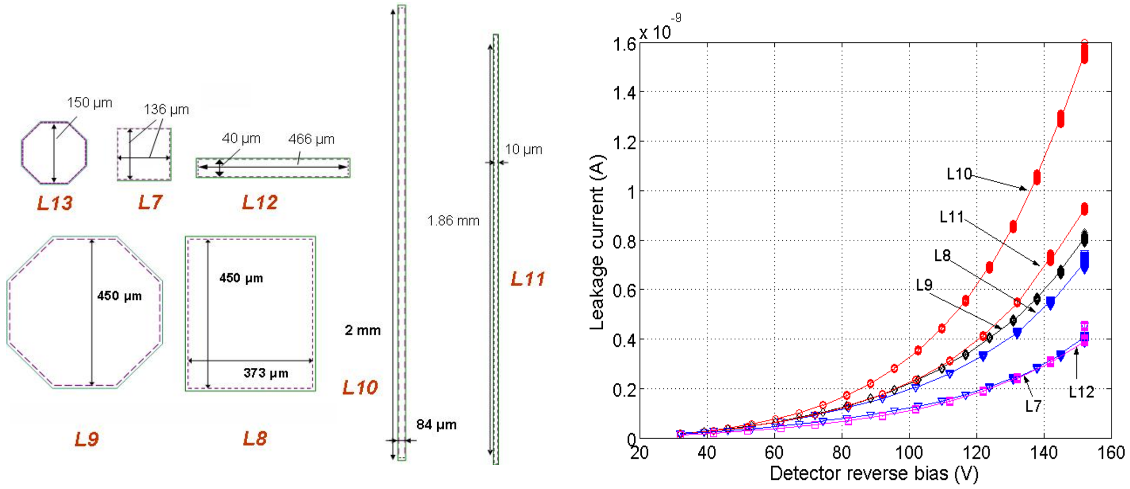

Figure 4.17. Left: Structures under test: L8, L9 and L10 have an active area of 167747 µm^2 and L7, L11, L12 and L13 of 18638 µm^2. Right: Dark currents measured at room temperature on a 20 µm thick sample.

The currents measured can also be displayed as current density in order to study the effect of the electrode size, and with respect to the square root of the applied voltage. In the following, the results are presented with a logarithmic scale for the current density and a linear scale for the square root of the voltage.

The internal field for non-fully depleted diodes varies with the square root of the applied voltage, so that in the case of Poole-Frenkel field enhanced thermal generation, the current should vary exponentially with $V^{1/4}$ (equation 4.2) but the variations with the applied voltage of the attempt to escape frequency presented in equation 4.1 are not precisely defined and other contributions may be involved in the current. Exponential rise of the dark currents with respect to either the square root of the applied reverse voltage V or to $V^{1/4}$ have been observed in the different measurements presented in this section. The chosen representation simply permits the observation of the exponential rise of the current density with the square root of the applied bias while keeping the x-axis easily readable.

Currents measured on the first 20 µm thick sample and on a 1 µm thick sample are first presented in Figure 4.18. The 1 µm thick sample is interesting in order to study the influences of the passivation layer steps and of the induced edges and corners high field effects on the dark current, as the deposited thickness is smaller in comparison to the 5 to 6 µm thickness of the passivation layers. The side effects are then expected to be more important for this sample. Moreover, it has been tested with reverse biases up to 2.5 V that ensure a full depletion of the intrinsic layer.

Similar tendencies are observed for the 2 samples. A clear dependence of the current density is observed with the bottom electrode size, and the bigger structures L8, L9 and L10 have a lower current density in comparison to L7, L11, L12 and L13. This first difference can be explained by the currents originating from the electrode periphery and corners. As the electrode gets smaller, the ratio perimeter over area of the electrode becomes higher. The perimeter of a square is equal to 4×$(\text{area})^{1/2}$, the perimeter of an octagon can be defined as 3.64×$(\text{area})^{1/2}$, and the relation for a rectangle depends on the respective lengths of the sides but the ratio perimeter over area also increases as the area decreases. Moreover, a contribution from electrode corners should not vary much with the area, as the corners fissures observed in the EBIC study depend on the gathering a-Si:H falling edges and not on the electrode area.

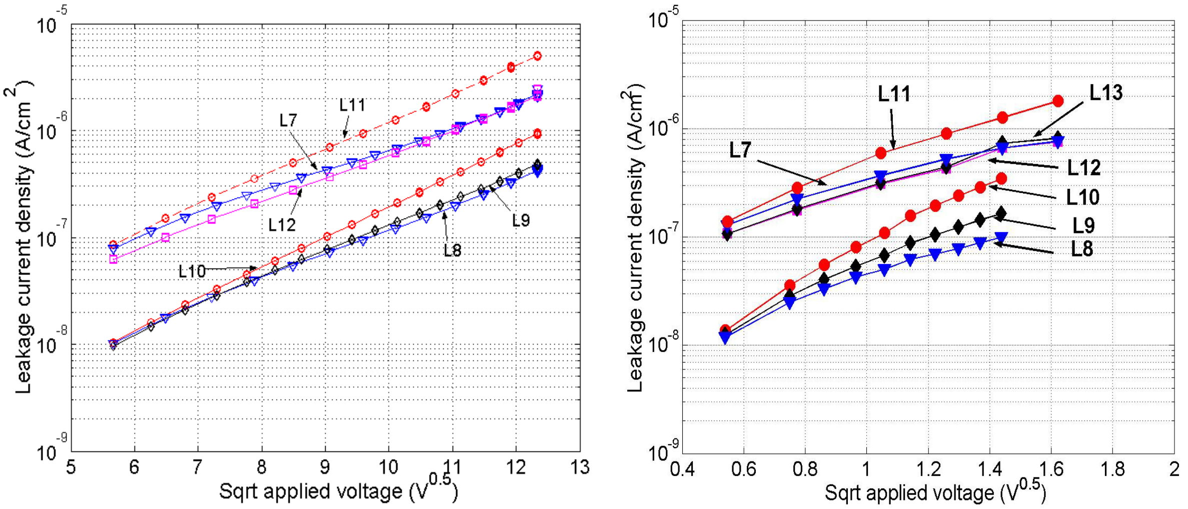

Figure 4.18. Current density measured for varying applied reverse biases on the detecting device. Left: Results obtained on a first 20 µm thick sample. Right: results obtained on a 1 µm thick sample.

By considering this model of three components contributing to the dark current, respectively bulk (J_1), periphery (J_2) and corners (J_3) current densities, one can express the measured current density J_{leak} as a function of the area A of the bottom electrode:

$$J_{leak} = J_1 + J_2 + J_3 = J_1 + \frac{K_2}{\sqrt{A}} + \frac{K_3}{A} \qquad (4.4).$$

The terms J_1, K_2 and K_3 do not depend on the electrode dimension, though K_3 depends on the shape of electrode, and J_1, J_2 and J_3 can all be attributed to thermal generation or interface injection. Decreasing areas then lead to increasing dark current density. The active areas of the tested structures differ by a factor 9 so that the contribution from J_2 and J_3 are expected to be 3 times and 9 times higher for the smaller structures (equation 4.4). A factor 5 to 7 is observed in the currents presented in Figure 4.18, which is consistent with the model and indicating a strong contribution from J_2 and J_3 to the total dark current.

The shape of the bottom electrode can influence the total current density in different ways. The first important point is that the additional currents arise from geometrical effects so that the deposition of a-Si:H layers on top of electrodes with different shape might create different diode geometry at the edges. The second important point is the ratio perimeter over area of the electrode. This second parameter becomes important when considering strips, as the ratio perimeter over area of a rectangle increases when increasing the difference between the side lengths. Considering this second parameter, an octagon and then a square should present the smaller dark currents for equivalent areas, but in our case the first cited point might vary the relation. For both samples presented in Figure 4.18, the current densities of the structures L10 and L11 which are long strips are a factor 3 higher than the currents densities of other structures with similar areas but different shapes, thus confirming the perimeter contribution to J_{leak}. The other structures present close currents densities so that no tendency can be extracted.

Same measurements have also been performed on a second 20 µm thick sample and on a 10 µm thick sample. The results are presented in Figure 4.19.

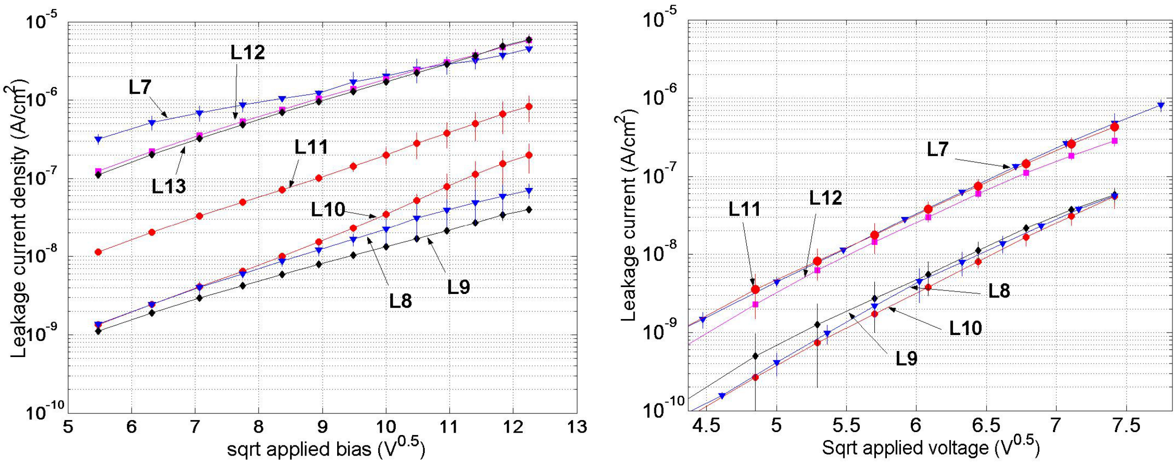

Figure 4.19. Current density measured for varying applied reverse biases on the detecting device. Left: Results obtained on a second 20 µm thick sample. Right: results obtained on a 10 µm thick sample.

Similar differences in current density are observed for electrodes with different areas. However, no significant differences are observed for the 10 µm thick sample for the different shapes of electrodes. This difference is observed for the 20 µm thick sample only on the big structures, so that L10 has a current density with a factor 4 higher than L8 and L9. However the structure L11 shows a low current density in comparison with the other structures with similar areas, themselves showing very high currents in comparison with the smaller structures. The discrepancies observed in these samples first confirm for some structures the tendencies extracted from the measurements of Figure 4.18, but also show that the current density is strongly linked to the deposition process parameters and uniformity, as different behaviours were observed on these samples.

These first results are consistent with the assumptions of additional currents from the periphery and corners of the bottom electrode and with the model of three components defining the dark current. The measurements demonstrate that the two additional components have a high contribution to the total current, so that the leakage current density increases decreasing the back electrode area. More statistics is however needed for a detailed study of the influence of shape on the dark current, but the measurements already show that long strips will induce higher currents.

Additional currents have then been identified arising from edges and corners caused by the passivation layers step. The openings in the passivation layers to access the last metal level of a CMOS technology are usually done on top of the metal pad. One way to reduce the high dark currents would be to perform larger openings. For the aSiHtest chip, some specific violations to the design rules have been accepted by the foundry so that some openings were performed around the metal pads. The openings in the passivation layers and the specific metal structures integrated in the aSiHtest chip are presented in detail in section 3.2. The effect of the opening location has been studied by measuring the dark currents of the integrated structures presented and numbered in Figure 4.20.

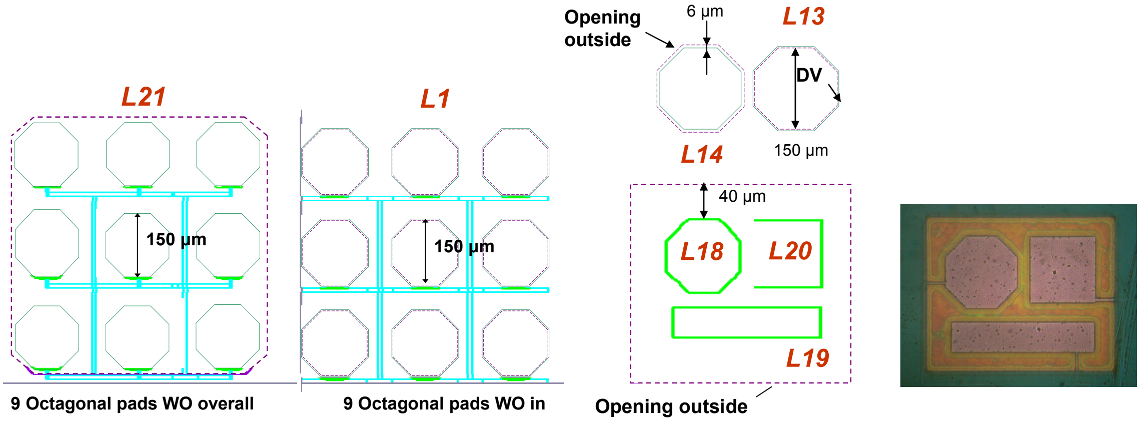

Figure 4.20. Structures with openings in the passivation inside the metal pad (L1 and L13) and outside the metal pad (L14, L18, L19, L20 and L21). Bottom right: Picture of structures L18, L19 and L20 taken with a microscope on the 1 µm thick sample. The different colours are due to the different zones (metal pad, SiO_2, passivation layers), and give an idea of the structure topology.

The structures L7, L12, L13 and L1 present openings inside the metal pad. The structure L14 presents an opening at 6 µm around the metal pad and the structures L18, L19 and L20 have an opening at 40 µm around the metal pad. Finally the structure L21 comprises 9 octagonal pads with a similar global opening located at 6 µm around the octagons of the structure periphery.

Measurements have been performed on the 1 µm thick sample and on the two 20 µm thick samples. Results obtained on the 1st 20 µm thick sample are presented in Figure 4.21. The currents measured on the structures L13, L14 and L18 show that when the windows in the passivation layers are opened around the metal pad, the leakage current is reduced, and that the reduction scales with the distance of the opening location to the metal pad. For a reverse bias of 150 V, an opening at 6 µm around the metal pad reduces by a factor 3 (from 750 pA to 250 pA) the current, and an opening at 40 µm reduces by a factor 10 the current (down to 70 pA), as it is shown in Figure 4.21.

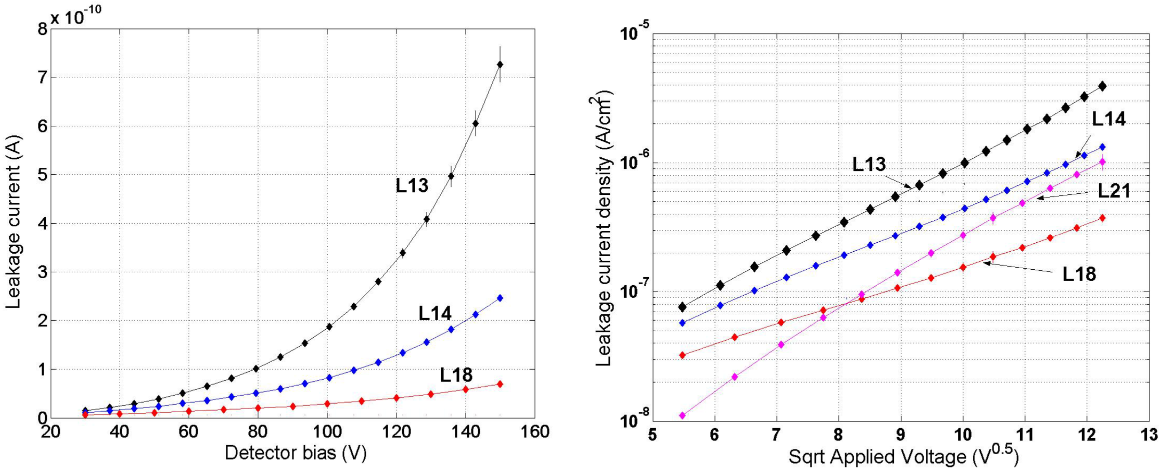

Figure 4.21. Passivation openings impact on dark current: currents measured on the first 20 µm thick sample on structures L13 (openings inside metal pad) L14 (opening at 6 µm around the metal pad), L18 (opening at 40 µm around the metal pad) and L21.

Openings outside the metal pad lead to a reduction of the current by reducing the additional peripheral and corner current densities defined as J_2 and J_3 in equation 4.4. This effect is illustrated in Figure 4.22.

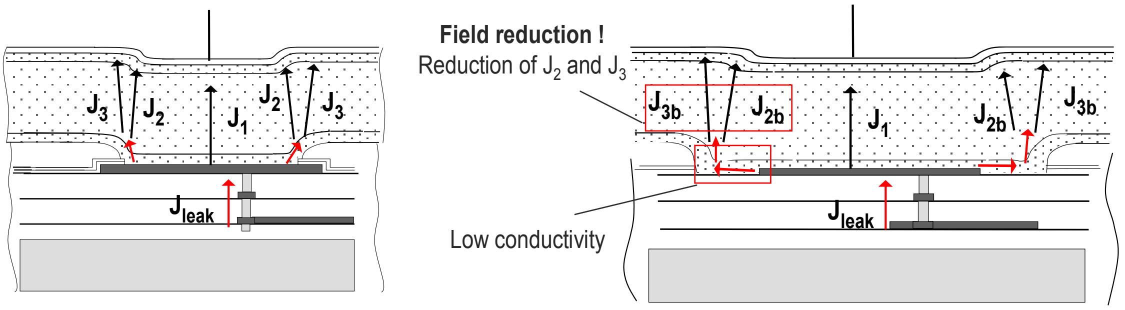

Figure 4.22. Reduction of current density J_2 and J_3 contribution to J_{leak} by opening passivation layers outside the metal pad. The component J_1 is not changed but J_2 and J_3 are reduced because of lowered electric fields at the falling edges, and because they contribute to J_{leak} only after conduction through low conductivity n-layer.

For an opening inside the metal pad, the additional current densities J_2 and J_3 caused by high internal electric fields directly contribute to the total leakage current density. For large openings, the fissures due to the corners and the peripheral edges are away from the metal pad, so that the electric field at these edges may be reduced causing a decrease of the current densities J_2 and J_3. Moreover, the lowered additional current densities contribute to J_{leak} only by conduction from their creation location to the metal pad through the low conductivity n^+-layer. Both effects can thus explain the fact that larger openings lead to a higher reduction of these currents.

Edge effects might still be present at the metal pad periphery, as the metal pad and the surrounding SiO_2 layers do not show a flat transition from one to the other, and a reverse (metal pad higher than the surrounding layers) and thin (< 500 nm) step is expected at the edges. However, the measured currents show that these effects are negligible in comparison to the edge and corner effects created by an opening inside the metal pad.
The current reduction is confirmed by the currents measured on the same sample on structures L12 and L19, and L7 and L20 (Figure 4.23 left). For similar structures, lower currents are measured for an opening outside the metal pads (L18, L19 and L20). Similar reductions of the currents are observed on the second 20 µm thick sample when varying the passivation layer openings, and results are presented in Figure 4.23 right. Similar variations between L13, L14 and L18 are observed, and structures L19 and L20 present lower currents than L12 and L7.

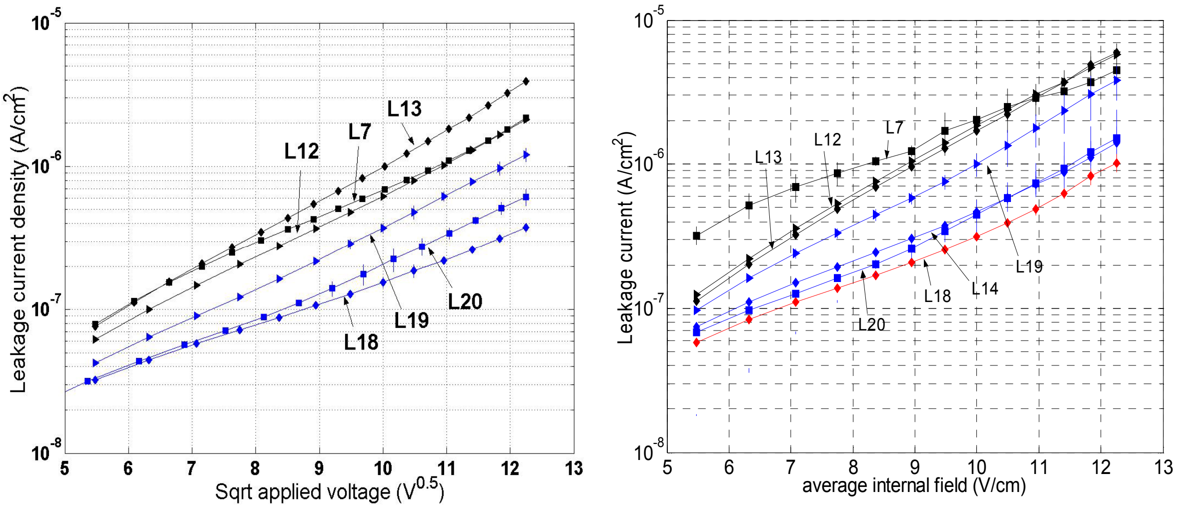

Figure 4.23. Leakage current density for structures with openings inside the metal pad (L7, L12 and L13) and outside the metal pad (L14, L18, L19 and L20). Left: measured on the 1st 20 µm thick sample. Right: measured on the 2nd 20 µm thick sample.

Finally, the influence of the passivation layer opening has been studied on the 1 µm thick sample, and results are presented in Figure 4.24. For this TFA detector, the deposited thickness is smaller than the 5 to 6 µm thickness of the passivation layers, so that edge and corner effects should be more pronounced for this sample, as the geometrical effects are more pronounced and as the bulk current is reduced due to a thin a-Si:H layer.

The pronounced geometrical effects are seen in the currents measured on structures L13, L14 and L18, and on structures L1 and L21 (Figure 4.24 left). For a 5 V reverse bias voltage applied to the detector, the structure L13 has a current of 75 pA, while the structure L14 has a current an order of magnitude lower of about 7 pA. The currents measured for the structure L18 are even smaller, and reach the resolution limit of the integrated current amplifier, so that a current of ~ 2 pA is readout but even smaller values can be expected. The high differences measured then confirm the pronounced edge and corner effects for this sample and confirm that an efficient way to reduce the dark current is to perform larger openings: currents of an order of magnitude lower are measured for structures L18, L19, L20 and L21 in comparison to L13, L12, L7 and L1 (Figure 4.24).

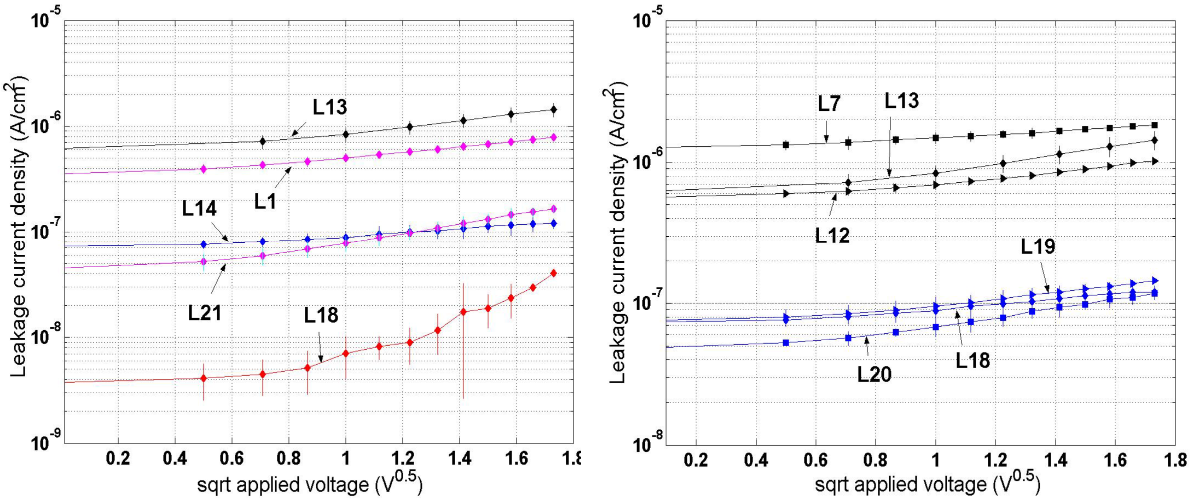

Figure 4.24. Leakage current density for structures with openings inside the metal pads (L1, L7, L12 and L13) and outside the metal pad (L14, L18, L19, L20 and L21) measured on the 1 µm thick sample. Left: Octagonal structures (L13, L14 and L18) and group of 9 identical octagonal structures (L1 and L21). Right: Octagons (L13, L18), Squares (L7, L20) and rectangles (L12, L19).

The different measurements show that the dark current of TFA detectors is a sum of three currents originating from the bulk and p-i interface. One current corresponds to the region where the a-Si:H layers are flat and above the metal electrode, a second one to the electrode periphery and a third one to the electrode corners. The two last currents have high contributions for electrodes designed with an opening in the passivation layers inside the metal pads. These currents can be reduced by opening the passivation layers outside the metal pads and for such structures the first component can be considered as dominating the dark current. This can be observed on structures L18, L19, L20 and L21 which present currents in the order of 10-20 pA for the maximum reverse bias of 5 V on the 1 µm thick sample and currents in the order of 70 to 350 pA for maximum reverse bias of 150 V on the 20 µm thick sample. The current also scales with the diode thickness, as a thicker diode leads to a higher bulk thermal generation current, and as higher reverse biases are applied. Higher electric fields are then induced in the depleted region and at the p-i interface, enhancing both the thermal generation by Poole-Frenkel mechanisms and the current generated and injected at the p-i interface. During the design of integrated circuits for applications as electronic readout of TFA detectors, the metal pads that will define the bottom electrodes have thus to be designed with openings in the passivation layers outside the metal pads in order to reduce the dark current. Further reduction necessitates a linearization of the integrated circuit and an optimisation of the deposited a-Si:H detecting device.

4.3.3. Temperature and field dependent leakage current

The dark currents in thick n-i-p a-Si:H diodes have been shown to be strongly field dependent in 4.1.2 and 4.3.2. An efficient method to study the mechanisms responsible of this field dependent dark current is to study the evolution of the dark current for varying temperatures, as both thermal generation and injection by tunnelling at the p-i interface vary with the temperature. The thermal generation variations with the temperature are presented in equations 4.1 and 4.2, and the dark current scales exponentially with the inverse of the temperature. In case of injection, the conduction is due to variable range hopping through the traps, and the current scales exponentially with $T^{-1/4}$ (section 2.1, equation 2.15). The temperature dependence of the dark current of different structures has been measured on a third 20 µm thick sample, for temperatures varying from 25 °C to 95 °C, and for detector reverse biases ranging from 80 V to 160 V.

First characterizations have been done on the structures L13 and L18, and results are presented in Figure 4.25 left. It can first be noted that strong differences are also observed on this sample between the currents of structures with the opening in the passivation layers inside (L13) and outside (L18) the metal pad. The passivation opening outside the metal pad leads to a reduction of the leakage current by a factor 7 for the different applied biases (Figure 4.25 left). The currents sharply increase with temperature for both structures, and similar exponential variations are observed. At 95 °C the leakage current density is more than an order of magnitude higher than the current density at room temperature for both structures. For the different temperatures, the leakage current densities show the same variations with the reverse voltage (the slope of the plots is always the same in Figure 4.25 left and right for the different temperatures).

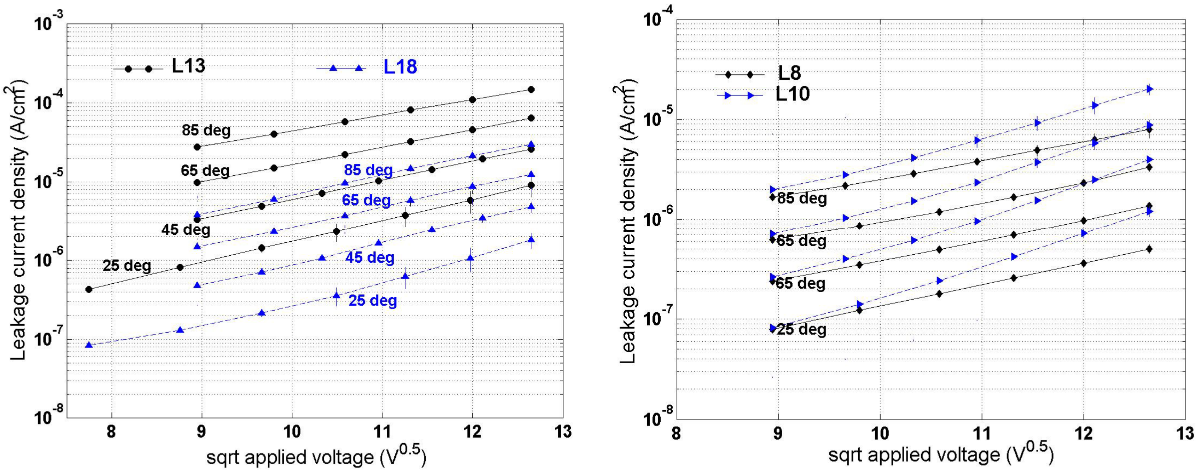

Figure 4.25. Leakage current density variations with reverse applied voltage and temperature. Left: Current density measured on structures L13 and L18. Right: Current density measured on structures L8 and L10.

A similar exponential increase of the leakage current density is observed on structures L8 and L10 (Figure 4.25 right). For this sample the long strip structure L10 also presents a higher dark current than the octagonal structure L8. The currents measured at 85 °C are more than an order of magnitude higher than the currents measured at room temperature on these structures. The currents presented in Figure 4.25 present both the strong field dependence and the strong temperature dependence of the mechanisms responsible of the dark current in n-i-p a-Si:H diodes.

The measured currents are plotted as leakage current density versus the temperature in Figure 4.26 left. An exponential rise with the temperature is observed, and the dark current is multiplied by a factor 1.5 every 10 degrees. Similar variations are observed between the 2 structures L13 and L18 and for the reverse voltages of 96 V, 128 V and 160 V.

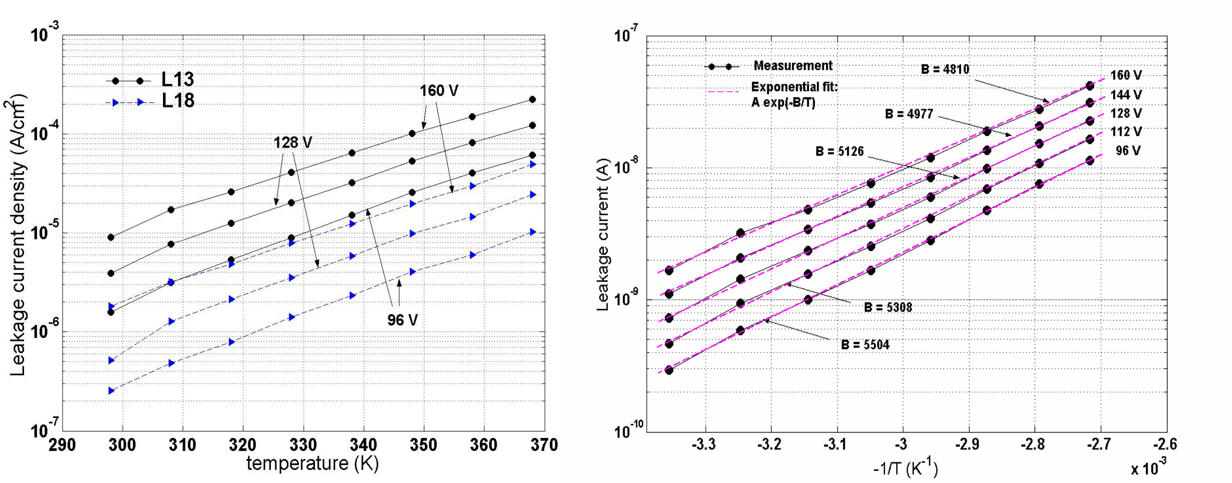

Figure 4.26. Leakage current variations with temperature. Left: Leakage current density vs temperature for structures L13 and L18 and for 96 V, 128 V and 160 V. Right: Leakage current variations with -1/T and fits obtained for reverse voltages from 96 V to 160 V.

The exponential rise with the temperature can be attributed to a dark current induced by field enhanced thermal generation. Leakage currents determined by this enhanced generation can be defined as:

$$I \approx I_0 \exp\left(-E_A / kT\right) \qquad (4.5); \qquad\qquad E_A = \left(E_G/2 - \gamma\sqrt{E}\right) \qquad (4.6).$$

E_A is the activation energy, i.e the energy needed to activate ionisable defects, and γ is the Poole-Frenkel constant presented in equation 4.2. The enhanced generation can then be studied by plotting the measured currents as leakage current versus -1/T. The curves obtained for the structure L13 are displayed in Figure 4.26 right. The leakage current variations can be well fitted by curves defined by the equation A×exp(-B/T). The fitting results are presented in Figure 4.26 right. These results and the good fitting demonstrate that the dark currents are principally caused by field enhanced thermal generation, and can arise from the p-i interface and from the bulk.

The Poole-Frenkel mechanism reflects the lowering of the energy needed to activate ionisable defects for increasing electric fields. At low-fields, the activation energy E_A is defined as $E_G/2$ (E_G being the bandgap energy), but decreases for high-fields as a function of the square root of the electric field (equation 4.6). Some previous works [Che94] reported activation energies of 0.9 eV for low fields ($E_G/2$) and down to 0.4 eV for a field of 1.5×10^5 V/cm.

The good fitting of the experimental data presented in Figure 4.26 right permits to extract the activation energies from the extracted factor B of the exponentials as $B = q\times E_A/k$. Activation energies for different applied reverse voltages and for the structures L13, L18, L8 and L10 have been extracted from the measurements, and results are presented in Figure 4.27.

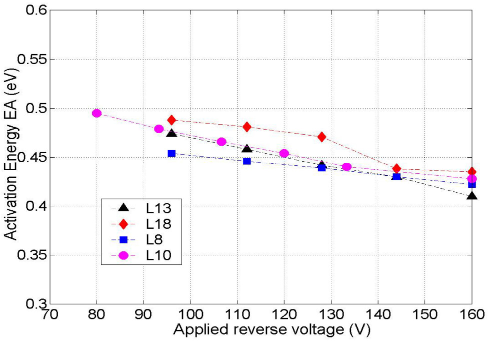

Figure 4.27. Extracted reverse current activation energy vs applied reverse bias for structures L8, L10, L13 and L18.

Activation energies in the range of 0.4 - 0.5 eV have been extracted for the different structures and different reverse biases. The activation energy is well observed to decrease as the reverse voltage is increased, and activation energies of about 0.49 eV for 80 V and about 0.42 eV for 160 V have been extracted. The electric field profile in the depleted zone of the diode can be calculated from the Poisson equation presented in section 2.3 (equation 2.34). The calculations are presented in detail in Chapter 5 and lead for a 80 V and 160 V reverse bias to a maximum expected field of about 1.2×10^5 V/cm and 1.7×10^5 V/cm at the p-i interface. The constant γ defined in equation 4.3 can then be estimated from the extracted activation energy and estimated electric fields, and a constant value of 1.1×10^{-3} $eV\cdot V^{-1/2}\cdot cm^{-1/2}$ is found. The values found are larger but not too far from the theoretical value of 2.25×10^{-4} $eV\cdot V^{-1/2}\cdot cm^{-1/2}$, and the calculated value is in agreement with the value extracted by Chevrier and Equer in [Che94] of 1×10^{-3} $eV\cdot V^{-1/2}\cdot cm^{-1/2}$.

The measurements performed on this sample are first in agreement with the results presented in 4.3.2. The smaller structures present higher current densities because of the additional currents originating from the peripheral edges and from the corners of a pixel. A long strip also presents a higher current density than an octagonal electrode because of a longer perimeter for the same area, so that the peripheral edge additional current is increased. The additional currents are reduced by opening the passivation layers outside the metal pads. The variations of the measured dark current densities with the temperature are similar for the different structures, showing that the mechanisms responsible of the dark current density components J_1, J_2 and J_3 (equation 4.4) are the same. The exponential rise of the currents with -1/T shows that these currents can be attributed to a thermal generation enhanced by the electric field by Poole-Frenkel mechanisms. The activation energy defining the currents decreases increasing the reverse bias voltage and is about 0.42 eV for a maximum reverse bias of 160 V applied on the 20 μm thick diode.

4.4. Conclusions

Different detectors have been used to study the performance and limitation of the TFA technology. An important limitation of the first developed TFA detectors performance was found to originate from elevated dark currents of the a-Si:H sensor. Current densities up to 10^{-3} A/cm^2 have been measured on a TFA detector with a 32 μm thick a-Si:H sensor for a maximum applicable reverse voltage of 300 V. These currents are 3 orders of magnitude higher than currents measured on test structures and strongly field dependent, and the maximum applied voltage of 300 V is low in comparison to the needed voltage of about 460 V needed to fully deplete 32 μm of a-Si:H. These elevated currents induce:

- elevated noise
- voltage breakdown lower than the expected reverse voltage needed to fully deplete the a-Si:H detector

The understanding and the reduction of these elevated dark currents for high reverse bias voltages are then of primary importance for the development of TFA detectors. The work that has been done on TFA detectors and the different results presented in this chapter have permitted to make significant progress in the understanding of the mechanisms governing the dark currents, and in the solutions to reduce them.

The different measurements performed on the TFA detectors based on the AFP and on the aSiHtest integrated circuits have demonstrated a strong variation of the leakage current with the applied reverse biases. The currents can be attributed for the most to thermal generation, and the induced leakage current density is:

- enhanced by the electric field by Poole-Frenkel mechanisms
- dependent on dangling bond density and so detector thickness
- enhanced at the p-i interface (higher electric fields and higher defect density)
- dependent on temperature

Elevated internal electric fields are needed in the a-Si:H detector to deplete the non doped layer and to permit a fast collection of charges induced by radiation or particles (chapter 5). However, high electric fields also have the effect of enhancing the current thermally generated by lowering the activation energy of the traps. The temperature measurements have confirmed that the dark currents are mainly due to field enhanced thermal generation, which is an intrinsic property of the material, and activation energies of about 0.42 eV have been extracted for a 20 µm thick reverse biased at 160 V.

For TFA detectors, 2 additional currents have been identified by scanning a detector with a SEM. These studies showed pronounced geometrical effects and induced higher electric fields at the peripheral edges and at the corners of a pixel, created by the unevenness due to the passivation layer opening. The EBIC study of a detector also turned out to be a very interesting characterization technique for TFA detectors (pixel segmentation study, particle detection, radiation hardness…). The different measurements performed on the aSiHtest TFA detectors demonstrate the existence of the additional currents:

- dark current density decreases for increasing bottom electrode area and the additional currents explain this as the ratio perimeter over area increases for decreasing areas and as the corner effects do not scale with the electrode area.
- Long strips have higher leakage current density (factor ~ 2 to 3) than square or octagonal electrodes as its perimeter is higher for the same area, and as the peripheral edge currents gets higher.
- Structures with an opening in the passivation layers outside the metal pad present a factor 3 to 10 current density lower than structures with opening inside the metal pad (the current reduction scales with the distance from the metal pad to the opening location).
- Additional current contributions scale with the detector thickness.

A first way to reduce the dark current of the a-Si:H sensor consists thus in opening large windows in the passivation layers on top of the metal structures that will act as bottom electrodes. Low dark current densities of 4×10^{-7} to 1×10^{-6} A/cm^2 have been obtained on structures with an area of 18638 µm^2 and for a 160 V reverse bias on the 20 µm thick detecting device for such structures.

The reduction of the dark current of the detecting device has then to be taken into account already during the design phase of the integrated circuit of the TFA detector. Large openings in the passivation layers around the metal pads have to be performed. A further improvement could be achieved by a linearization process of the integrated circuit surface. The detecting device sequence can also be changed in order to reduce the additional currents, and metal-i-p configurations have been proposed at the IMT to reduce the currents as currents induced around the metal pad would not be collected because of the removal of the n$^+$ conductive layer. Specific care and optimisation of the p-i interface have also to be performed in order to reduce the currents and the adjunction of a buffer layer might be an interesting solution.

5. Signal induction and speed in TFA detectors

Charge carriers generated by ionizing radiation incident on an a-Si:H sensor induce a current on the electrodes directly after their creation. This induced signal depends on the movement of the generated carriers, and the expression "signal efficiency and speed" is used rather than "charge collection efficiency and speed". In high energy physics experiments, the induced signal speed is a crucial parameter of the detector performance and is therefore studied in detail in this chapter. The charge transport and signal induction specificities of TFA detectors are presented in section 5.1, together with the measurement technique we have used to characterize the induced signal speed. The results obtained for TFA detectors developed using an AFP Integrated Circuit are presented in section 5.2. A TFA detector using an aSiHtest chip has also been characterized with the same measurement technique and the results are presented in section 5.3.

5.1. Charge transport in a-Si:H

The electronic transport of charge carriers in a-Si:H and the multiple trapping model have been presented in section 2.3.1. The non-dispersive transport of electrons and the dispersive transport of holes at room temperature are presented in more detail in 5.1.1, together with the carrier lifetime and the internal electric field profile in n-i-p a-Si:H diodes. The measurement technique we used to characterize the charge collection speed in the TFA detectors is presented in 5.1.2.

5.1.1. Carrier mobility and internal field in thick a-Si:H diodes

At room temperature, the carrier mobility in a-Si:H is explained by the multiple trapping model. The conduction of the free carriers occurs in the extended states, and carriers are consecutively trapped into localized states below the band edges where they are immobile, and reemitted into the conduction bands. The release time of a carrier from a trap is a crucial parameter for the conduction. It depends on the trap level energy, on the temperature and on the material "attempt-to-escape" frequency ω, as defined in section 2.1 (equation 2.14). A broad distribution of localized states in the band tails then leads to a broad distribution of carrier release time. The localized states are located in exponentially shaped band tails with a slope $(kT_V)^{-1}$. For temperatures above T_V, the transport is considered non-dispersive and is defined by constant drift mobility. For temperatures below T_V, the transport is dispersive and the drift mobility varies in time. In that case, the average drift mobility is usually defined as power-law time dependent [Zho94]:

$$\mu_d(t) = \alpha(1-\alpha)\mu_0(\omega t)^{(\alpha-1)} \quad (5.1).$$

μ_0 is the ohmic mobility defining the conduction in the extended states. The parameter α is defined as the dispersion parameter and is equal to the ratio T/T_V ($0 < \alpha < 1$).
At room temperature, electrons and holes transport have a different transport:

- The conduction band tail has a slope determined by $T_V \sim 270\text{-}300$ K, so that at room temperature $\alpha \sim 1$ and the electron transport is considered to be non-dispersive. For temperatures close to or above T_V electron multiple trapping processes take place mainly in shallow states. The thermal de-trapping is a fast process for these states and can be well described by a single trapping time. The electron mobility is thus defined by the conduction in the extended states (which determines the electron mobility μ_0) and by the time spent in the shallow state traps determined by a single release time constant. This is equivalent to an apparent reduction of electron mobility μ_0, defining the constant drift mobility μ_{de} [Equ89]. Electron drift mobility in thick n-i-p a-Si:H diodes has been measured by different groups and a value of $\mu_{de} \sim 1\text{-}5\ \mathrm{cm^2\,V^{-1}\,s^{-1}}$ has been found [Bei90, Dub91, Hon95].

- The valence band tail has T_V equal to about 450 K. At room temperature $\alpha \sim 0.65$ and hole transport is considered to be dispersive, as the broad distribution of traps induces a broad distribution of release times. Hole mobility then decreases with time as the mean carrier distribution falls deeper into localized states (equation 5.1). Different characterizations of the dispersive hole transport have been performed and a low mean drift mobility of $\sim 0.01\ \mathrm{cm^2\,V^{-1}\,s^{-1}}$ has been found [Bei90, Dub91, Hon95].

In comparison, crystalline silicon drift mobility is of the order of $1350\ \mathrm{cm^2\,V^{-1}\,s^{-1}}$ for electrons and $480\ \mathrm{cm^2\,V^{-1}\,s^{-1}}$ for holes [Sze81].

Charge carrier lifetime τ corresponds to the average time needed for an electron or a hole to be recombined or trapped in a deep localized state. The carrier drift velocity v_{drift} and lifetime define the carrier drift length L_{drift}, which represents the distance on which the carrier can drift before being deeply trapped or recombined:

$$v_{drift} = \mu_d \times E \quad (5.2); \qquad L_{drift} = v_{drift} \times \tau \quad (5.3);$$

The carrier lifetime for both carrier types is usually found equal to about 10^{-6} s in intrinsic a-Si:H, in comparison to a τ of about $10^{-5}\text{-}10^{-3}$ s in crystalline silicon depending on the bulk doping concentration [Sze81].

The $\mu\tau$ products for an hydrogenated amorphous silicon sensor are much lower than for crystalline silicon, and will evidently play an important role in the formation of the signal in detectors based on the TFA technology. The detectors need to be operated with a high reverse bias in order to provide high internal electric field to overcome the low mobility and to present sufficient drift lengths and low drift time of the carriers.

When a reverse bias is applied across a thick p-i-n a-Si:H junction, a slow thermal ionization of the deep defects leads to the slow formation of a stable electric field profile, in a time that may range from 10 s to 600 s [Dub91]. The deep defect excited electrons are swept out by the field, leaving behind the positive space charge, so that part of the deep states behaves like donor states. In a first approximation, the depleted i-layer space charge is determined only by the density of ionized dangling bonds N_{db}^*. The steady-state electric field profile can be calculated from the Poisson equation presented in section 2.3.2 (equation 2.30). The detector reverse bias voltage V is linked to the corresponding depletion width d by the equation 2.31. At high potentials, N_{db}^* is supposed to be constant, so that the electric field decreases linearly with the distance x to the p-i interface (Figure 5.1).

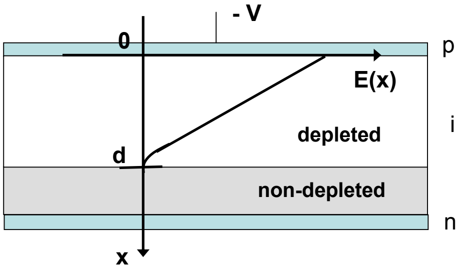

Figure 5.1. a-Si:H n-i-p structure and electric field E(x) along the depleted width d.

For a non-fully depleted diode, the electric field is nil at the distance d from the p-i interface and it can then be simply expressed as a square function of the applied reverse voltage:

$$E(x) = \frac{-q\, N_{db}^*}{\varepsilon_0\, \varepsilon_{aSi}}\, x + \sqrt{\frac{2\, q\, N_{db}^*}{\varepsilon_0\, \varepsilon_{aSi}}}\, \sqrt{V} \qquad (5.4).$$

Below full depletion and at low potential regions, i.e. for distances x close to d, N_{db}^* has been shown to vary linearly with the electric field, resulting in an exponentially dropping off electric field [Qur89a]. This first model of the electric field profile is represented in Figure 5.2 left, taken from calculations of Qureshi [Qur89a] on a 27 µm thick p-i-n a-Si:H diode. More recently, Fischer [Fis94] presented detailed simulations of the electric field profile. The model is based on a density of charge defined by the concentration of ionized dangling bonds, and by the density of free and trapped electrons and holes. The electric field profile is calculated from the Poisson equation and from the basic equations governing the transport properties of semiconductor devices under steady state conditions, namely the current density equations and the continuity equations [Fis94, Sze81]. The results are consistent with a linear field for high voltages and an exponential behavior in low potential regions (Figure 5.2 right).

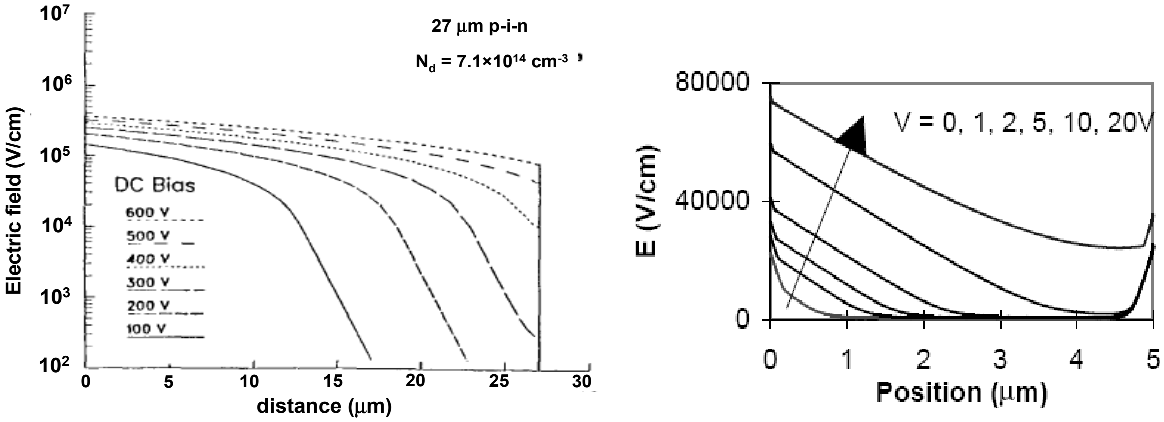

Figure 5.2. Left: Electric field profiles in 27 μm p-i-n diodes at various bias voltages, calculated by Qureshi et al. [Qur89a]. Right: Electric field profiles in 5 μm p-i-n diodes, calculated using the model developed by Fischer [Fis94] and presented in [Cha96]. Position and distance are referred to as the distance from the p-i interface.

A "mean" electric field in the depleted region can be defined as E(x = 0)/2. It simply corresponds to the ratio V/d (equation 5.4). A mean field of 10^5 V/cm, which corresponds to an applied voltage of 200 V on a 20 μm thick sample, leads to an average electron drift length higher than 1 mm, and to a low hole drift length of about 10 μm. The electron and hole drift times can be roughly estimated by dividing the detector thickness by the carrier mobility and the mean electric field. From the values defined before and a 20 μm thick diode, one can expect an electron drift time of 20 ns, and a hole drift time of ~ 2 μs.

Even though charge carriers have low mobilities in a-Si:H, the high reverse bias that can be applied, which results in a high internal electric field, together with a reduced detector thickness compared to crystalline silicon may lead to reasonable carrier drift time. Due to the high electric fields (of about 10^5 V/cm) and to low carrier mobility, diffusion of the carriers will have a negligible effect in an a-Si:H sensor. For the LHC experiments, the time between bunch crossings will be only 25 ns. The upgrade of the LHC would even lead to an assumed bunch crossing interval of 12.5 ns [Gia05]. The measurement of the detector signal speed is then of primary importance for the characterization of the performance and limitation of TFA detectors for HEP applications.

5.1.2. Charge transport measurement technique and set up

Carrier drift time in TFA detectors can be measured by stimulating the detector with a pulsed laser, thus photo-generating in a short time electron-hole pairs in the depleted zone of the detector. The photon energy of the laser light source can be chosen so that the emitted photons will be absorbed in a few microns in a-Si:H. By illuminating the detector either on the front implant (p-layer) or on the rear implant (n-layer), equal number of electrons and holes are created close to either the p-i interface or the i-n interface. For an illumination on the p-layer (n-layer), holes (electrons) will be absorbed by the nearest implant, while electrons (holes) will drift across the entire depleted region of the detector. This technique, called Time Of Flight (TOF), is used to measure the mobility in a-Si:H diodes, by applying a pulsed reverse bias on the detector shortly before the laser pulse [Str83]. The pulsing of the detector bias is achieved to ensure a constant electric field profile inside the depleted zone, as the ionization of the dangling bonds that leads to the establishment of a positive space charge in the depleted region and to a linear electric field profile is a slow process (section 4.3.1). However, in our tests the detector was operated under DC biasing in order to characterize the signal speed in standard operating conditions of the detector. The technique we used is similar to the Transient Current Technique (TCT) used to determine the effective trapping times in irradiated silicon detectors [Kra00].

In our tests, electron-hole pairs were created by a 660 nm laser pulse. The diodes are built on the ASICs by first depositing the n^+ layer, then the i-layer, the p^+ layer and the top semi-transparent electrode. The tests could thus only be performed by illuminating the diodes on the p^+ layer. The absorption in a-Si:H of photons with an energy of 1.88 eV (corresponding to a wavelength of 660 nm) takes place in extended states and is defined by the absorption coefficient α_{ab}. This coefficient can be extracted from the models presented in section 2.1.5 and in Figure 2.10, and $\alpha_{ab,1.88eV} \sim 10^4$ cm^{-1}. The 660 nm laser pulse light thus presents a mean free path in a-Si:H of about 1 μm, so that the majority of the electron-hole pairs are created in the close proximity of the detector p-i interface. Under the influence of the internal electric field, which is at its maximum at the p-i interface, electrons and holes are separated. Holes drift to the top electrode, while electrons drift to the bottom electrode through the whole depleted thickness. An illustration of the measurement technique is presented in Figure 5.3.

As it has been presented in chapter 1, a charge moving between 2 electrodes induces on both electrodes a signal which is proportional to the charge, the velocity of the charge, and the weighting field which depends on the detector geometry. In case the detector contains resistive elements, as for an under-depleted n-i-p a-Si:H diode, the time dependence of the signals is not only given by the movement of the charges but also by the time-dependent reaction of the detector material [Rie04]. Intrinsic a-Si:H has a low conductivity ($\sigma < 10^{-10}$ S·cm^{-1}), so that its characteristic time constant $\tau = \varepsilon_0 / \sigma$ is > 800 μs. The high resistivity of a-Si:H non depleted i-layer then leads to $\tau >> T$, T being the drift time of carriers. We can conclude from [Rie04] calculations (presented in section 1.2) that a current is induced while the charge packet is moving, and that once the charges reach the non depleted zone the current is zero. The carrier drift then induces a negative signal on the bottom electrode integrated in the ASIC.

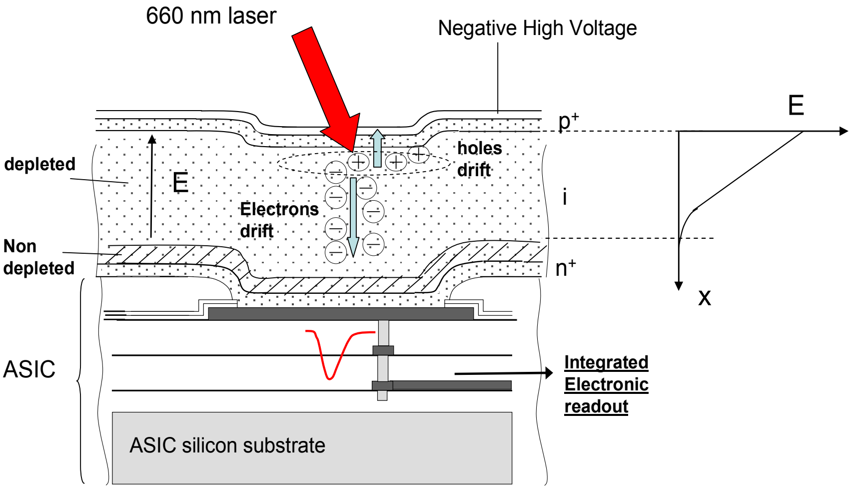

Figure 5.3. Schematic view of the measurement principle. A 660 nm laser pulse illuminates the p^+ side of the diode. Generated carriers are separated and accelerated by the field, electrons travel through the entire depleted region. Photo-generated carrier motion induces a negative signal on the bottom electrode integrated into the ASIC.

The charge drift is usually measured by integration of the induced signal. In our studies, the n-i-p diodes were deposited on the AFP and aSiHtest ASICs which integrate fast trans-impedance amplifiers, with a peaking time of about 5 ns (Chapter 3). The current induced can then be readout, and the pre-amplifier output signals correspond to the drift of the generated carriers.

Measurements of charge transport have been performed on different samples. TFA detectors made of n-i-p a-Si:H diodes deposited on an AFP integrated circuit or on an aSiHtest integrated circuit have been tested. The results obtained with a 13 µm thick and a 32.6 µm thick a-Si:H detector deposited on an AFP circuit are presented in section 5.2. 20 µm thick diodes deposited on an aSiHtest circuit have also been characterized and results are presented in section 5.3. The experimental set up is presented in Figure 5.4.

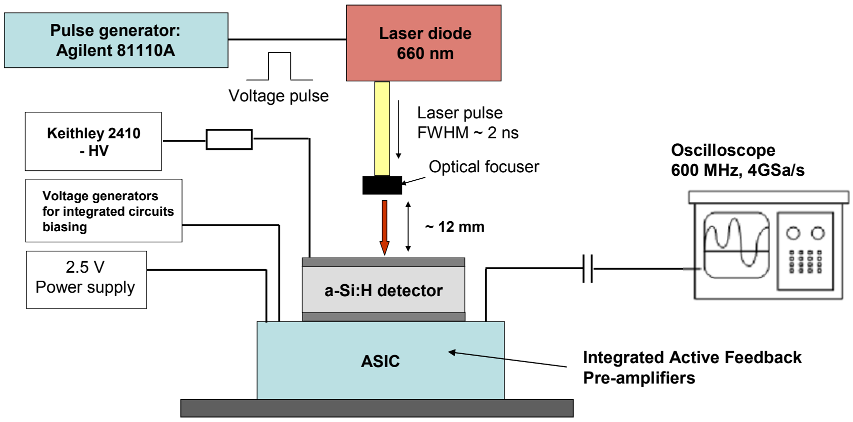

Figure 5.4. Schematic diagram of the constructed set up for charge transport measurement.

An Agilent 81110A pulse generator was used to drive the 660 nm red laser diode. With a voltage pulse width of ~ 3 ns, a laser light pulse with a FWHM ~ 2 ns is obtained. The laser light passes through an optical fiber and an optical focuser so that light spot sizes of < 100 μm can be achieved at the detector surface. The TFA detector is mounted on a dedicated PCB. The different biases of the integrated circuit are brought using different voltage generators, and the high voltage reverse bias applied to the p^+ layer of the detector is provided via a Keithley 2410. The pre-amplifier output signals are readout on an oscilloscope through a decoupling capacitor.

The PCB is fixed on a x-y-z micro-positioner. The detector can then be moved with ~ 50 μm precision in the 3 directions of space to align the structures to test with the laser light spot. Part of the set-up is placed in a dark box to avoid any additional light source on the detector. A picture of the set-up inside the dark box is presented in Figure 5.5. An aSiHtest sample is mounted on its PCB and fixed to the manual micro-positioner.

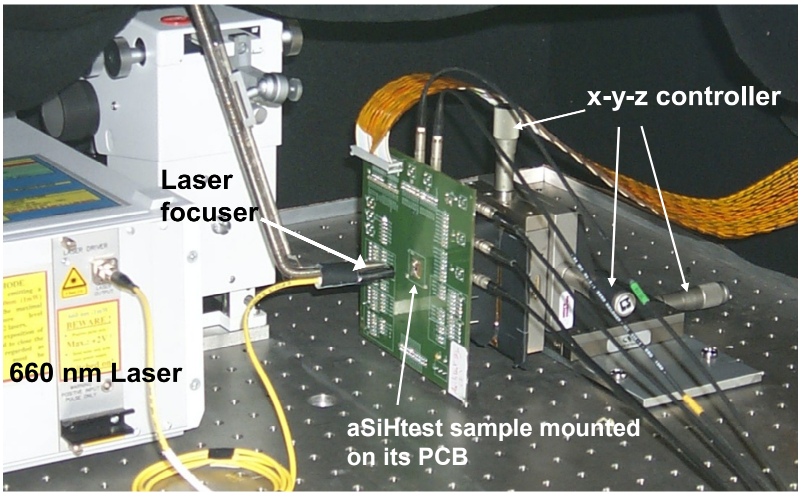

Figure 5.5. Picture of the measurement set-up for an aSiHtest sample characterization. TFA detector on its PCB biased through the flat cable. Coaxial cables are connected to some channel outputs. The manual micro-positionner permits a precise alignment of the detector with the laser light spot.

5.2. Characterization of n-i-p diodes on the AFP Integrated Circuit

Charge transport and charge collection speed in TFA detectors have first been studied on samples made of n-i-p a-Si:H diodes and AFP integrated circuits. These detectors are presented in 4.1 and illustrated in Figure 5.6, while the AFP chip is presented in detail in section 3.1.4. The effective pixel active area is about 60 μm × 80 μm, as it is shown by the EBIC measurements presented in 4.2. The results obtained on two different samples [Des03] are presented in 5.2.1, and models of the signals induced by the drift of the created electrons and holes are presented in 5.2.2.

5.2.1. Measurements of the signals induced by the laser pulse

The n-i-p a-Si:H diode is 13 µm thick in the first sample, and 32.6 µm thick in the second sample. The DC feedback current flowing into the feedback transistor of each active feedback pre-amplifier is equal to the difference between the applied I_{FEED} through the specific current mirror and the pixel diode leakage current, as it has been presented in section 4.1 and represented in Figure 4.3. High leakage currents then prevent a correct biasing of the circuit and precise measurements. These high leakage currents presented in section 4.1 together with a risk of breakdown of the detector at high voltages only permitted a characterization of the first sample up to 80 V and of the second sample up to 280 V. Below these voltages, each individual pixel leakage current is sufficiently small compared to the AFP feedback current of about 1 µA used during the tests, and does not induce variations in the amplifier transfer function. The detector capacitance is small for each sample (< 60 fF) and negligible for tests with the AFP circuit.

The 2 samples have been tested using the measurement technique and set up presented in 5.1.2. For these preliminary tests, the laser light pulse amplitude was not measured during the tests. It was set to obtain sufficient output signals amplitude for the different detector biases, while keeping the AFP pre-amplifier in a linear dynamic region. The light pulse presents a FWHM of about 2 ns. These first investigations were focused on the measurement of the signal response speed.

Charges are generated during the whole laser pulse duration, and the induced signal rises during this time as the number of drifting carriers increase. At the end of the laser pulse, it can be considered that a constant packet of electrons moves away from the p-i interface under the effect of the electric field, and that a packet of holes moves to the p^+ layer where it is collected. The drift of the electrons induces a decaying signal which corresponds to carrier decreasing speed in the linearly decreasing field until the electrons reach the non-depleted region. A negative signal with a shape represented in Figure 5.6 should be induced on the bottom electrode connected to the pre-amplifier.

Diffusion coefficients D cannot be calculated very accurately using Einstein's relation $D = (kT/q)\cdot\mu$ in amorphous silicon [Gu96] because of the material structural disorder. However, the relation still permits an estimation and detailed study presented in [Gu96] shows a diffusion coefficient for holes a factor 2 higher than obtained with Einstein's relation and closer values for electrons. Diffusion of the carriers can thus be considered negligible as carriers drift in a high field region (~ 10^4 V/cm) and present low mobility so low diffusion coefficient (in the order of 10^{-2}-10^{-3} cm^2/s for electrons and 10^{-4}-10^{-3} cm^2/s for holes). The induced signal is thus determined only by the carrier drift.

The response of the first sample to a laser light pulse and for a reverse bias of 80 V applied to the n-i-p diode is presented in Figure 5.6. The AFP pre-amplifier is inverting, so that the output signal response corresponds to a negative signal induced by the detector on the bottom electrode. The output signal peaking time is close to the laser light pulse duration, but the AFP pre-amplifier still shapes the signal induced by the detector. It can however be considered that the output pulse maximum and decay correspond to the electrons drift in the depleted zone, and is an image of the diode internal electric field. The signal shape is consistent with the model of a positive space charge and of electrons drifting under an electric field decreasing with the distance from the p-i interface. A long tail is also observed in the signal response. Holes have a very low mobility compared to electrons in a-Si:H, so that holes created are not directly collected at the p^+ electrode and their slow drift can still contribute to the output signal shape with a long and low amplitude signal. For an electric field of 10^5 V/cm at the interface, electrons would move at a drift velocity of about 10^5-10^6 cm/s and holes at about 10^3 cm/s, corresponding to respective drift times of ~ 1 to 0.1 ns/µm and ~ 100 ns/µm. Different mechanisms as a long contribution from slow holes drift to the p^+ layer may create this tail and will be discussed later.

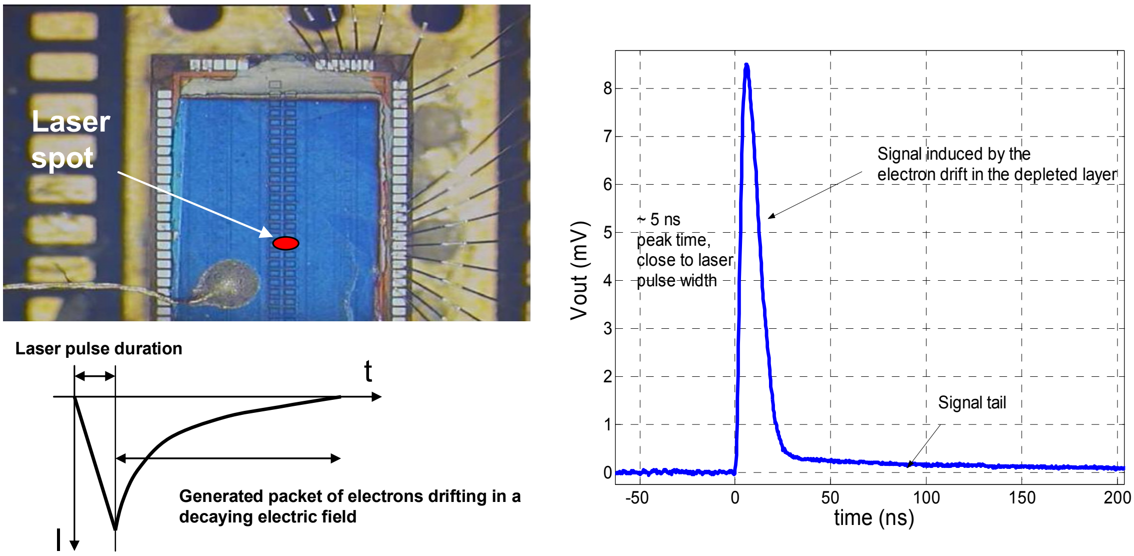

Figure 5.6. Left-top: Picture of a 13 µm thick a-Si:H diode deposited on an AFP integrated circuit. Channel outputs are wire bonded to the PCB. Left-bottom: Expected shape of the signal induced on the bottom electrode. Right: Response of the 13 µm thick TFA sample to a 2 ns FWHM 660 nm laser light pulse, for a 80 V detector bias.

The detector response to the laser pulse has been measured for different applied biases. The results obtained on both samples are presented in Figures 5.7 and 5.8. The signal rising time is about 5 ns for both samples and corresponds to the AFP peaking time. The output signal maximum amplitude can be approximated as an average of the signal induced by the motion of the electron packet at the p-i interface, where the maximum electric field is present. By increasing the reverse bias of the detector, the electric field is increased, and so is the output signal maximum amplitude, as it can be observed in Figures 5.7 and 5.8. The pulse decay has a fast component attributed to the drift of the electrons in the decreasing electric field along the whole depleted thickness. The pulse fast decay has a measured falling time of 16 ns (for the 32.6 µm thick sample) to 20 ns (for the 13 µm thick sample), constant while varying the detector bias. This constant fast decay for different reverse voltages applied on the detector will be discussed later. Finally, the slow component is also observed in the signals response (with a falling time > 600 ns). Its time constant decreases increasing the bias voltage.

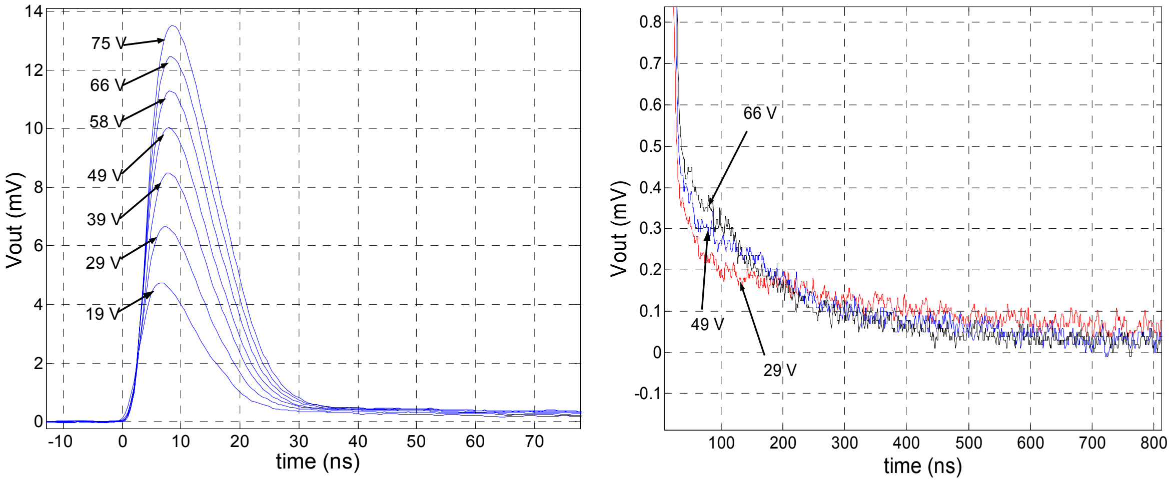

Figure 5.7. Output responses to a laser light pulse, for the 13 μm thick sample, for different detector bias voltages. Left: fast component, Right: slow component.

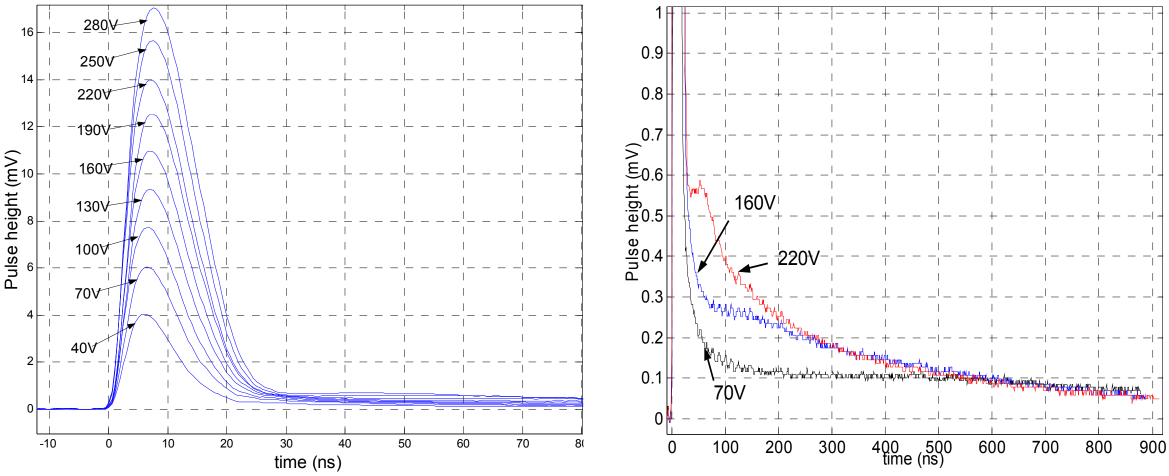

Figure 5.8. Output responses to a laser light pulse, for the 32.6 μm thick sample, for different detector bias voltages. Left: fast component, Right: slow component.

5.2.2. Models for the currents induced by the created electrons and holes

The electron drift and induced signal have been first studied by considering a simple one dimension model developed on the assumption of a linear electric field profile inside the depleted zone (equation 5.4). The depletion width d is defined in equation 2.31. The electric field and the electron drift velocity can be written as:

$$E(x) = \frac{q\, N_{db}^{*}}{\varepsilon_0\, \varepsilon_{aSi}} (d - x) \qquad (5.5); \qquad v_{drift}(x) = -\mu_d\, E(x) \qquad (5.6).$$

Electron transport at room temperature can be considered as non-dispersive. However, the carrier drift mobility in a-Si:H depends on the temperature and also on the electric field. Enhanced drift mobility has been measured for high electric fields [Gu95]. High reverse voltages are applied on the TFA detector resulting in high internal electric fields. A maximum electric field can be considered at the p-i interface. It can be estimated from (5.4) and for the 32.6 μm thick sample biased at – 280 V $E(0) = 2.2\times10^5$ V/cm. The increase of drift mobility for increased electric field has been attributed to a modification with the field of the "attempt-to-escape" frequency parameter ω which determines the release time of trapped carriers. The electric field lowers the activation energy of the traps through Poole-Frenkel mechanisms (as it has been reported in section 4.3 to explain the leakage current field dependence). Increased field thus leads to a decrease of the time spent by carriers in traps. This phenomenon can be accounted for by the following relation which has been proposed in [Gu95]:

$$\omega = \omega_0 \exp(-E/E_0) \qquad (5.7).$$

E is the electric field and E_0 is a constant parameter ($E_0 \sim 5.7\ 10^4$ V/cm). The mobility dependence on the attempt-to-escape frequency is defined in equation 5.1. This high field effect can thus be explained by a simple field assisted ionization of traps, equivalent to a field-dependent mobility edge [Gu95]. The release time from traps varies with field, so that the field effect will be important for a dispersive transport, but at the same time modest and negligible for a non-dispersive transport [Sch04]. At room temperature, the dispersion parameter α for electrons is close to 1, thus leading to small variations of the mobility with the field (equation 5.1). For α = 0.95, the factor $\exp(-E/E_0)^{(\alpha\ -1)}$ varies from 1.2 to 1.05 from the p-i interface to the limit of the depleted zone when considering the 2nd sample biased with 280 V. Little variation of mobility is expected for electrons at room temperature and has been observed, and no saturation of drift velocity has been observed for measurements up to ~ 10^6 cm/s [Gu95]. In the presented model, mean constant electron mobility has been considered. However, the field effect can be important for holes transport. In the laser measurements, holes drift on a maximum length of 1 μm, for which the electric field can be assumed constant, so that the field effect will not have an important impact. However, this effect can be important in particle detection, as particles create electron-hole pairs all along their path.

For the simplified model of a constant mean electron mobility μ_d and a linear electric field, the time required for an electron originating at the position x_0 to reach a point at the position x can be defined by:

$$t(x) = \int_{x0}^{x} \frac{1}{\mu_d\, E(x)}\, dx = \frac{\varepsilon_0\, \varepsilon_{aSi}}{q\, \mu_d\, N_{db}^{\ *}} \int_{x0}^{x} \frac{1}{(d-x)}\, dx = -\frac{\varepsilon_0\, \varepsilon_{aSi}}{q\, \mu_d\, N_{db}^{\ *}} \ln\left(\frac{d-x}{d-x_0}\right) \qquad (5.8).$$

From this model, the transient or collection time constant τ_c that defines the electron motion is:

$$\tau_c = \frac{\varepsilon_0 \, \varepsilon_{aSi}}{q \, \mu_d \, N_{db}^{*}} \tag{5.9}$$

For electrons originating at the proximity of the p-i interface ($x_0 \sim 0$), their position in time in the depleted region of the diode can then be defined using the simplified model and:

$$x(t) = d \left[1 - \exp(-t/\tau_c)\right] \tag{5.10}$$

The electrons collection time is then determined by the drift mobility μ_d and by the density of ionized dangling bonds N_{db}^{*}, and should not vary with the applied reverse bias. This is explained by the fact that the electric field and so the electron speed increase proportionally with the square root of the applied voltage, and that the drift distance of the charges also increases proportionally with the square root of the voltage. It results in a globally constant total drift time, assuming constant drift mobilities and constant density of ionized dangling bonds under different fields. This result is confirmed by the measurements presented in Figures 5.7 and 5.8: the output signal fast component shows a relatively constant decay time while varying the detector bias, for the 2 samples tested.

The signal induced on the bottom electrode connected to the AFP pre-amplifier can be calculated by using the Schokley-Ramo theorem extended to the case of electrodes connected to resistive elements [Rie04]. The induced current can be expressed as:

$$I(t) = -q \, N(t) \, v_{drift}(t) \, E_w \tag{5.11}$$

N(t) is the number of drifting carriers with the elementary charge q and E_w (in cm^{-1}) is the structure weighting field. As it has been presented in 5.1.1, the high resistivity of the non-depleted a-Si:H layer results in the induction of a current only when charges are moving under the electric field, as it is represented in Figure 5.9. The weighting field of the bottom electrode can be calculated by considering a simple parallel plate detector configuration.
The detector can be represented with 2 zones corresponding to the depleted and non-depleted regions, with respective width d and d_2 and respective relative permittivity ε_{r1} and ε_{r2} (Figure 5.9). The calculations have been performed using the model presented in [Rie04], and lead to:

$$E_W = \frac{\varepsilon_{r2}}{\varepsilon_{r2} \, d + \varepsilon_{r1} \, d_2} \tag{5.12}$$

The relative permittivity of depleted and non-depleted intrinsic a-Si:H are both taken equal to 12, so that the weighting potential is simply defined as $1/(d+d_2)$, i.e. the inverse of the i-layer thickness.

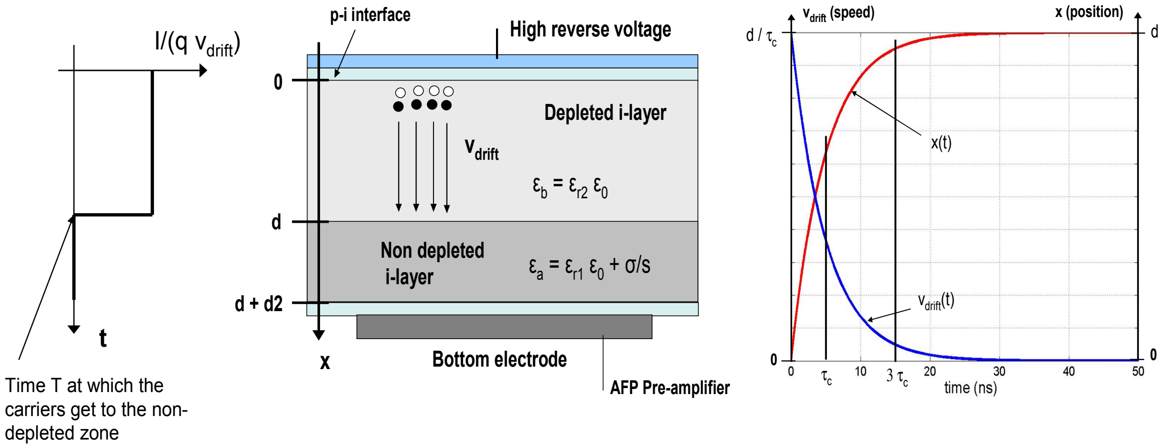

Figure 5.9. From left to right: induced currents for high resistivity non-depleted layer; a geometry representing the under-depleted amorphous silicon detector; electron position and speed variations with time for a τ_c = 5ns and using equation 5.10 and its derivative.

The drift velocity is obtained by derivation of equation 5.10 and a simple formula describing the current induced by the electrons has been obtained:

$$I(t) = \frac{-q\,N(t)}{(d+d_2)}\,\frac{d}{\tau_c}\exp\left(-\frac{t}{\tau_c}\right) = \frac{-q\,N(t)}{(d+d_2)}\,\mu_d\sqrt{\frac{2\,q\,N_{db}^{*}}{\varepsilon_0\,\varepsilon_{aSi}}}\,\sqrt{V}\,\exp\left(-\frac{t}{\tau_c}\right) \qquad (5.13).$$

The number of drifting electrons N(t) increases linearly with time during the laser light pulse duration t_1 ~ 3 ns and can then be considered as constant until the end of drift, as the electron lifetime is usually considered to be around 1 µs. The AFP pre-amplifier shapes the current signal, and during the time period t_2 corresponding to the pre-amplifier peaking time, a total charge defined by Q_{peak} is created by the drifting electrons. The output pulse peak amplitude corresponds to this charge. The charge Q_{peak} can be calculated by integrating equation 5.13 from $t = 0$ to $t = t_1$ using $N(t) = (N \cdot t)/t_1$, and by integrating equation 5.13 from t_1 to t_2 using $N(t) = N$, where N is the total number of drifting electrons. The equivalent charge created by the electron drift during the pre-amplifier shaping time t_2 can then be defined as (for $t_1 < t_2$):

$$Q_{peak} = \frac{-q\,N}{(d+d_2)}\,\mu_d\sqrt{\frac{2\,q\,N_{db}^{*}}{\varepsilon_0\,\varepsilon_{aSi}}}\,\sqrt{V}\,\tau_c\left(\frac{\tau_c}{t_1}\left[\exp\left(\frac{-t_1}{\tau_c}\right)-1\right]+\exp\left(\frac{-t_2}{\tau_c}\right)\right) \qquad (5.14).$$

The output signal peak amplitude depends on this charge Q_{peak}, so that the maximum amplitude of the signal varies with the pre-amplifier peaking time t_2, with the laser light pulse duration t_1, with the total number of electrons created N, with the electron drift time constant τ_c and with the square root of the reverse bias applied to the detector.

The peak amplitudes of the different measured signals versus the square root of the applied voltages are presented for both samples in Figure 5.10. The first sample response shows a linear relation, while for the second sample at higher fields the signal peak amplitude starts to deviate from the linear relation. This can be attributed to a different shape of the electric field at the p-i interface in the case of high fields, or to the induced current from hole drift which can have a significant contribution at high fields to the signal, or to a combination of the 2 effects.

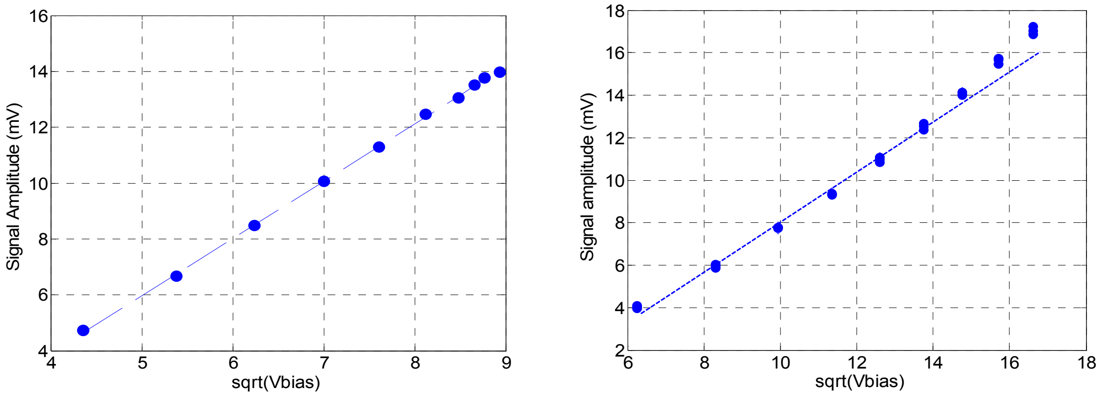

Figure 5.10. Evolution of the output signal peak amplitude with respect to the square root of the reverse bias applied to the detector (left: 13 μm thick sample, right: 32.6 μm thick sample).

The decay of the pulse directly corresponds to the induced current defined as in equation 5.11, for N(t) = N. The AFP pre-amplifier still shapes the signal and some simulations have been performed in order to verify the developed theory of signal induced by the electron drift.

In this study, the current induced by the charge motion was considered as a negative input current rising during the 3 ns corresponding to t_1, and then decreasing with 2 exponential components defining the decay. The first exponential has a fast time constant to fit the electron drift, and the second exponential has a slow time constant to try to fit the long tail observed in the signals. Simulations were then performed with HSPICE using this equivalent detector signal as input of the Active Feedback Pre-amplifier integrated in the AFP chip. The amplitude and time constant of the two decaying exponentials defining the equivalent input current signal were then adjusted to obtain a simulated output signal fitting the measured output signal from the laser tests. The signal extraction technique is illustrated in Figure 5.11. The induced current estimations obtained from simulations are presented in Figure 5.12, for the 2 samples, and for different biases of the detector. The output pulse rise and fast decay component are similar between the measured signals and the signals simulated by considering an input current rising for ~ 3 ns and then exponentially decreasing with time.

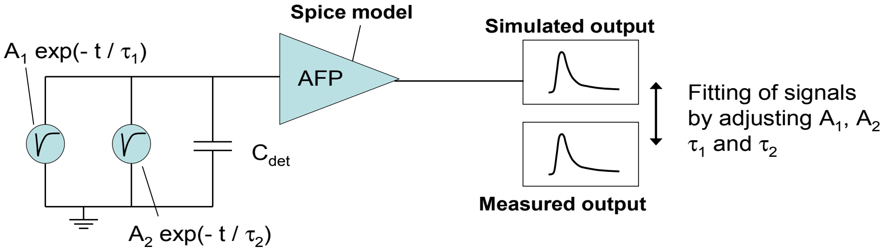

Figure 5.11. Schematic of the simulations performed to estimate the signal induced on the bottom electrode by the carriers drift.

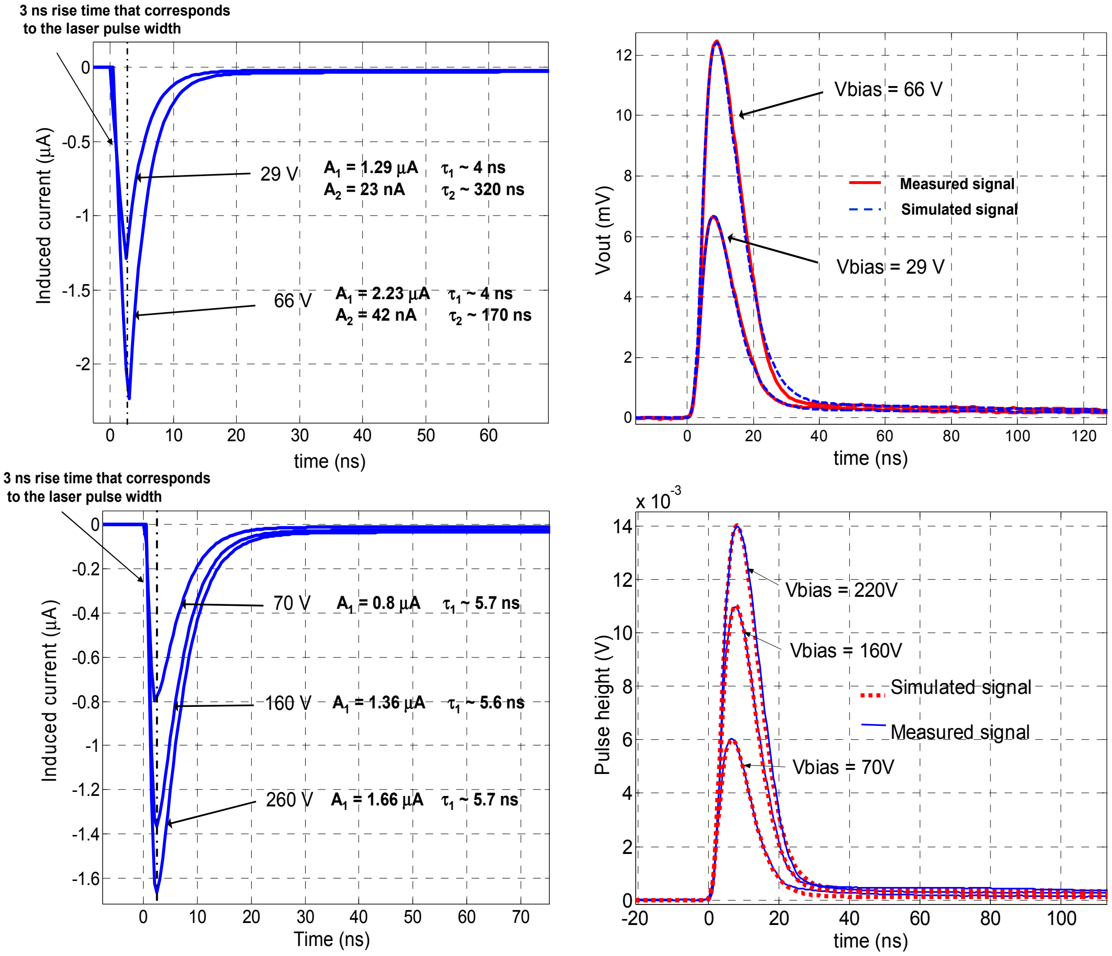

Figure 5.12. Left: Current signals with 3 ns rising time corresponding to the laser light pulse width, and with two exponentials representing the carriers drift in the depleted region. Right: Comparison of the simulated AFP responses for input currents presented on left and measured signals. TOP: results for the 13 μm thick sample. BOTTOM: results for the 32.6 μm thick sample.

These results show that the simple model of equation 5.13 is valid and explains the signal shape obtained during the laser tests. The long tail is approximated with a second exponential component to estimate the decay time constant. The simulated and measured signals show close tails but a more complex model is needed to perform a good fitting in that region of the signal response.

From the simulations presented in Figure 5.12, the electron collection time constant τ_c has been extracted. After a time $t_{coll,e} = 3\ \tau_c$, 95 % of the signal created by the electrons is achieved. The $\mu_d \cdot N_{db}^*$ product can also be extracted from these measurements. The extracted values of these different parameters are listed in Table 5.1. The dangling bond density is estimated to be about 2×10^{15} cm^{-3} (data from IMT Neuchatel), and usually 30 % are considered to be ionized [Qur89b]. This results in a measured electron drift mobility in the first sample and second sample of ~ 2.7 cm$^2\cdot$V$^{-1}\cdot$s^{-1} and ~ 2 cm$^2\cdot$V$^{-1}\cdot$s^{-1}, which is in agreement with the expected range 1-5 cm$^2\cdot$V$^{-1}\cdot$s^{-1}.

Sample	τ_c	$t_{coll,e}$	$\mu_d \cdot N_{db}^*$	μ_d
13 μm thick	4 ns	12 ns	1.65×10^{15} cm^{-1} V^{-1} s^{-1}	2.7 cm^2 V^{-1} s^{-1}
32.6 μm thick	5.6 ns	16.8 ns	1.18×10^{15} cm^{-1} V^{-1} s^{-1}	2 cm^2 V^{-1} s^{-1}

Table 5.1. Extracted parameters from laser measurements on AFP TFA detectors.

The measurements then confirm the assumptions of a linear internal electric field profile in most of the depleted region of the detector and the model developed for the signal induced by the electrons drift. This leads for under-depleted a-Si:H to a constant electron induced signal time for varying detector biases of 12 ns to 16.8 ns. Faster collection could be achieved by over-depleting the i-layer. In that case, the electric field would still increase with increasing the detector bias (as it is shown by the simulations of Figure 5.2), while the depletion and so the drift length would remain constant. The electrons collection time would then be decreased and faster signal from the electrons could be achieved.

Photons with an energy of 1.88 eV are expected to be totally absorbed in about 3 μm of a-Si:H, so that a similar number of charges are expected to be created in the 13 μm and in the 32.6 μm thick TFA detector. By using the measured parameters presented in table 5.1 and the equivalent current signals extracted, it is possible to estimate the number of electrons that are drifting thanks to the equation 5.13. Calculations lead in our case to N ~ 68 000 e$^-$ for the tests carried out on the 32.6 μm thick sample and N ~ 66 000 e$^-$ for the 13 μm thick sample. This information can also directly be extracted from the measurements by using equation 5.14 that links the number of electrons created to the charge that corresponds to the output signal peak. Similar number of electrons created by the laser pulse is then measured, which is consistent with the expected charges created by a 1.88 eV laser pulse.

A "long" component is also observed in the signal response. This has been estimated as a current collected in a time varying with increasing applied voltage from 1.5 μs to 200 ns. Different mechanisms can cause this long tail. It can be attributed to the slow movement

of the induced holes in the vicinity of the p-i interface or (and) to a non-linear electric field profile between the depleted and non-depleted regions.
Holes are created by the laser pulse in a 1 μm thick zone. Due to their low mobility (about 100 times lower than for electrons), they will not be directly absorbed in the p^+ layer and their movement will induce a signal I(t) as defined by equation 5.11. The electric field can be considered constant in the small drifting region of the holes. However, as it has been presented in equation 5.1, hole transport is dispersive, so that their mobility varies in time as $t^{(\alpha-1)}$. Moreover, the number of drifting holes will increase during the laser pulse duration, but will then decrease as the holes reaching the p^+ layer do not participate anymore to the induced signal. The signal ends when all holes will have reached the p^+ layer or will have been recombined. The hole induced current can thus be written as:

$$I(t) \approx -q\, N(t)\, \mu_{d,h}(t)\, E(x=0)\, E_w \qquad (5.15).$$

The electron-hole pairs are generated close to the p-i interface and their exact position follows the exponential decrease of the radiation intensity I_0 in the i-layer. The spatial distribution of the generated holes is exponentially decaying with the constant $\alpha_{ab} \sim 10^4$ cm^{-1}, and the number of drifting holes N corresponds to the integral of this distribution (Figure 5.13). When holes get to the p^+ layer they do not participate anymore to the signal, and N(t) can be equivalently calculated by considering a time varying starting point x_0 of the distribution integral (Figure 5.13):

$$N(x_0) \propto \int_{x_0}^{\infty} I_0 \exp(-\alpha_{ab}\, x)\, dx = \frac{I_0}{\alpha_{ab}} \exp(-\alpha_{ab}\, x_0) \qquad (5.16);$$

$$x_0(t) = \mu(t)\, t\, E = \alpha\,(1-\alpha)\, \mu_0\, \omega^{\alpha-1}\, t^{\alpha}\, E \qquad (5.17);$$

$$N(t) \propto \frac{I_0}{\alpha_{ab}} \exp\left(-\alpha_{ab}\, \alpha\,(1-\alpha)\, \mu_0\, \omega^{\alpha-1}\, t^{\alpha}\, E\right) \qquad (5.18).$$

The combined effects of a decreasing number of holes participating to the signal induction (equation 5.18) together with a low and decreasing drift mobility with time (equation 5.1) lead to a variation of the induced signal with time such that:

$$I(t) \propto A\, t^{(\alpha-1)} \exp\left(-B\, t^{\alpha}\right) \qquad (5.19)$$

$$B = \alpha_{ab} \cdot \alpha \cdot (1-\alpha) \cdot \mu_0 \cdot \nu(E)^{(\alpha-1)} \cdot E \qquad (5.20); \qquad A = B\left(\frac{q\, I_0}{(d+d_2)\, \alpha_{ab}^{\;2}}\right) \qquad (5.21).$$

The attempt to escape frequency varies with the electric field which lowers the activation energy of traps so that A and B are variables increasing with the electric field. The induced signal shapes for different electric fields and thus for different values of parameter B are presented in Figure 5.13.

The derived induced signal shape is consistent with the image of a low amplitude and long signal induced by the holes that could explain the long tail observed. Increasing the detector bias voltage also increases the signal speed and the signal amplitude, as it has been observed in the measurements.

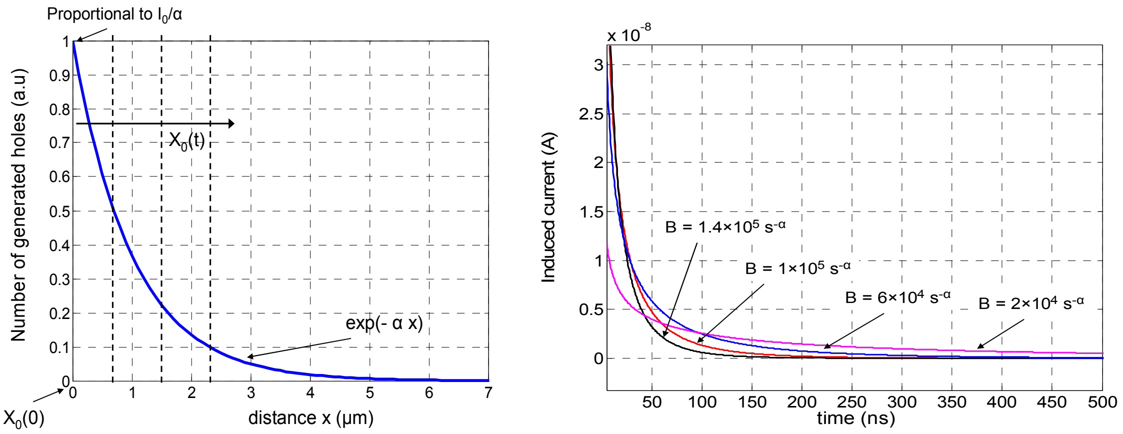

Figure 5.13. Left: Distribution of holes created by the 660 nm laser pulse. Their motion in time leads in a new distribution that can be estimated as a movement of the barrier x0. Right: Qualitative evolution of the holes induced signal with increasing fields (increasing B).

However, the different phenomena involved in the formation of the signal as the dispersive hole mobility and the field dependent attempt-to-escape frequency render the analysis complicated, as variations of parameters as μ_0, ω or E_0 lead to important variations of the signal. The observed low amplitude of the induced signal covered by the electron induced signal also renders the exact analysis of this induced signal complicated. The model however represents a good possible qualitative explanation of the observed tail of the signals, and gives an image of the variation of signal shape induced by the holes for different electric fields. In particle detection holes are created in the whole depleted thickness in regions with different electric field strength. The model presented here then shows the complexity of estimating the total signal originating from the holes.

The internal electric field in the a-Si:H sensor depends on the density of ionized dangling bonds, as it is presented in the simplified equation 5.5. However, the electric field acts on the activation energy of the traps and so on the density of ionized dangling bonds. The density N_{db}^* and the electric field thus depend on each other. For low electric field regions, as it is the case in the region between the depleted and the non depleted zones, a lower N_{db}^* can be expected. A non-linear electric field profile is thus most probably present at the vicinity of the non-depleted region, with a low field slowly decaying. Electrons drifting in this region could thus also be responsible of the low and slowly decaying tails observed in the signals.

5.3. Characterization of n-i-p diodes on the aSiHtest Integrated Circuit.

The speed and the induction of signal in TFA detectors have also been characterized on detectors made of a n-i-p a-Si:H diode on an aSiHtest integrated circuit. The aSiHtest chip integrates different metal structures grouped in the center of the circuit, on top of which is deposited the a-Si:H detector. The metal structures are connected to different electronic readouts, as it has been presented in Chapter 3. Some of the structures are connected to fast pre-amplifiers MIBEDO_HG presented in 3.2.3. The standard biases of these channels ensure a peaking time of the signal response of 5 to 8 ns for a minimum equivalent noise charge of ~ 150 electrons rms, and thus permit a characterization of the speed of the induced signal in TFA detectors as it has been performed on the samples deposited on the AFP circuit. A sample with a 20 µm thick n-i-p a-Si:H diode deposited on top of the group of metal structures has been tested and results are presented in this section.

The measurements have been performed on diodes defined by octagonal pads with an active area of 2070 μm^2 and of 18648 μm^2, and on different structures of strips, using the measurement technique and set up presented in section 5.1. Because of high leakage currents and risk of breakdown of the diode at high fields, a maximum reverse bias of 200 V was applied on the 20 µm thick diode during the tests. An interesting characteristic of the aSiHtest chip in comparison with the AFP chip is that the integrated pre-amplifiers can be electrically tested even when the detector is deposited: the pre-amplifier inputs are each connected to a metal pad defining the pixel or strip diode, and at the same time to an integrated injection capacitor which permits the electrical characterization (3.2.3).

The MIBEDO pre-amplifier transfer function can be varied in case of high leakage current originating from the a-Si:H detector. The pre-amplifier response is also very sensitive to any change in the input capacitance, as it has been presented in section 3.2, where a structure with an input capacitance of 100 fF and a structure with an input capacitance of 250 fF exhibit different impulse response at the pre-amplifier outputs (Figure 3.41). The response to a 1 fC charge of the pre-amplifiers integrated in the aSiHtest TFA detector have been measured by applying a 10 mV voltage step on the 100 fF integrated capacitor, and for detector reverse biases varying from 0 V to 200 V. No variations in the output signal shapes were measured, thus showing in a first time that the leakage current originating from the detector is negligible in this range of reverse biases. Moreover, this result shows another important aspect of the a-Si:H n-i-p detector. The similar output shapes for varying reverse biases indicate no variation of the detector capacitance. Contrary to crystalline silicon, the non-depleted i-layer in a-Si:H has a high resistivity, so that the n-i-p configuration capacitance is only determined by the i-layer thickness, as even if the depleted and non-depleted thicknesses are varied, the dielectric thickness remains the same. Similar impulse responses are thus seen for varying detector biases. The depletion of an a-Si:H n-i-p detector cannot be determined as it is usually done for crystalline silicon detectors by measuring the variations of the detector capacitance with the applied voltage. An alternative method based on the laser pulse measurements is proposed later in this section to study the depletion and will be used in Chapter 6.

The different structures have been tested with 660 nm laser light pulses with a ~ 3 ns FWHM. The results obtained on a small octagonal pixel of 2070 µm^2 are presented in this section. The laser light amplitude was set to lower amplitudes than for the tests performed with the AFP circuit, as the aSiHtest integrated pre-amplifiers have a lower noise. The laser pulse frequency was set to about 1 kHz. The superposition of 10 000 signals response to the laser pulses illuminating the small pixel are presented in Figure 5.14, for a 200 V reverse bias applied on the detector. The shape of the signals observed is in agreement with the different measurements performed on the AFP circuit and with the developed model of the electron drift. The pre-amplifier peaking time is here of ~ 7 ns. The maximum amplitude corresponds to the charge Q_{peak} presented in equation (5.4) and the pulse decay corresponds to the drift of the electrons in the decreasing electric field, and a signal falling time of ~ 20 ns is measured. It can be noted that at this high reverse bias voltage, no significant signal tail is observed.

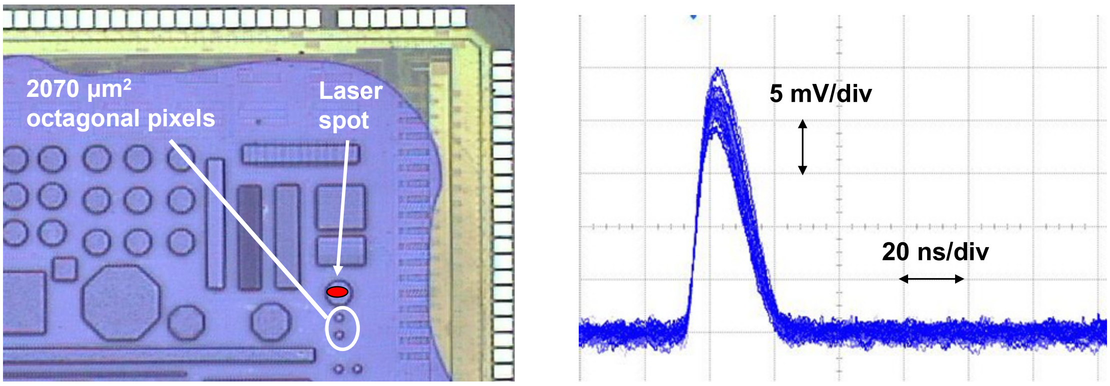

Figure 5.14. Left: Picture of the top-right corner of the TFA detector. The laser spot is aligned on one of the structures by moving the detector with the x-y-z positioner. Right: Output response of a pre-amplifier connected to a 2070 µm^2 octagonal pixel for a 3 ns 660 nm laser light pulse, and for a 200 V reverse bias applied on the diode.

The detector response to the laser pulse has been measured for different detector reverse biases. The pre-amplifier transfer function can be varied from the outside, and the tests were performed with 2 different feedback currents, respectively I_{FEED} = 100 nA and I_{FEED} = 280 nA. The results are presented in Figure 5.15 as an average of 560 measured signals for each detector bias. The pre-amplifier shapes the signal induced by the detector on the octagonal pixel bottom electrode, so that faster output signals are obtained with the higher I_{FEED}. For both set of data, the peak amplitude varies with the detector bias, as expected from the model developed in 5.2, and the output signal has a fast decay component and a long decay component.

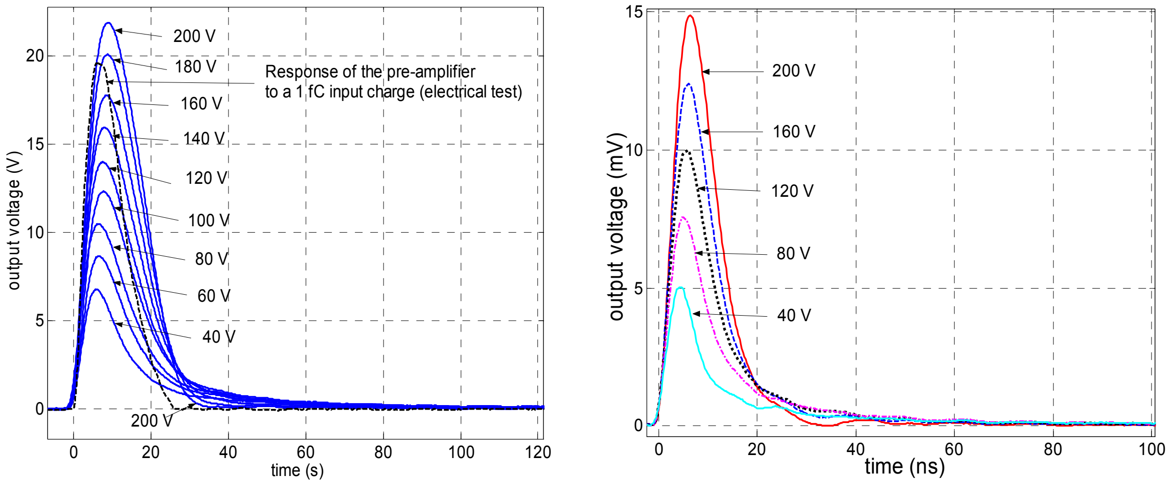

Figure 5.15. Output signals for a 660 nm laser pulse on the detector, and for different reverse biases of the detector. Left: Results obtained with a I_{FEED} = 100 nA. Right: Results obtained for a I_{FEED} = 280 nA.

From Figure 5.15, it can be observed that the fast decay presents a falling time of about 20 ns for the different biases. The slow components (signal tails) observed in the signals strongly depend on the applied bias. These tails can be explained first by the signal induced by holes generated by the laser pulse, which strongly varies with the electric field. However, for a bias > 180 V, no significant tail is observed in these measurements.

Measurements performed on the 32 µm thick TFA detector based on the AFP (section 5.2, Figure 5.8) show that for a 200 V reverse voltage applied to the sensor a long signal tail is observed (~ µs range). For a similar bias of 200 V, close signals induced by the movement of the generated holes would be expected for both 20 µm and 32 µm thick sensors (i.e. close signal tails). However, no tail is observed on the 20 µm thick TFA detector (Figure 5.15). This result indicates that the signal from the hole motion might not be the dominant cause of the observed signal tails. If this was the case, a long tail should be observed for 200 V on the 20 µm thick sensor. Hole transport strongly depends on electric field and is dispersive, so that variations of the deposition process might also induce variations of the signal induced by the holes. However, it seems more probable that a slowly decaying electric field at the regions between depleted and non-depleted regions might be responsible for the long signals. In that case, long tails are observed for a non-fully depleted sensor, as electrons will drift in a low slowly decaying field region near (or in) the non-depleted zone. Moreover, for a reverse bias high enough to fully deplete the sensor (as it is the case for 200 V on a 20 µm thick sensor), no such low decaying field region is expected, so that no tail should be observed. The experimental results obtained on the 20 µm and 32 µm thick sensors for a similar reverse bias of 200 V thus indicate that the signal tails observed in the different TOF measurements might be caused by low slowly decaying electric fields for non-fully depleted sensors. No tail is observed for a Vbias > 180 V on the 20 µm thick sensor, indicating thus a full depletion of the sensor for a reverse bias of about 180 to 200 V. This will be studied through another method in Chapter 6, reinforcing statements established here.

The pre-amplifier shapes the signal induced by the laser pulse, and an estimation of this induced current has been performed in order to extract the time constant τ_c that defines the speed of the signal induced by the electrons drift in the linearly decaying electric field. For the measurements performed on the TFA detectors using AFP integrated circuit, the extractions were done using HSPICE simulations of the circuit (section 5.2). A different method has been used here. One of the advantage of the pre-amplifiers integrated in the aSiHtest chip is that they can be electrically characterized even when the a-Si:H layers are deposited on the circuit surface thanks to the integrated injection capacitors. The method of extraction used to characterize the TFA detector based on an aSiHtest circuit is then based on direct measurements of the transfer function of the pre-amplifier in the same operating conditions as for the laser pulse tests. The pre-amplifier impulse response was measured during the tests, for a feedback current of 100 nA. For the biases chosen, the impulse response can be easily fitted with an adequate equation (Figure 5.16), from which the transfer function can be extracted.

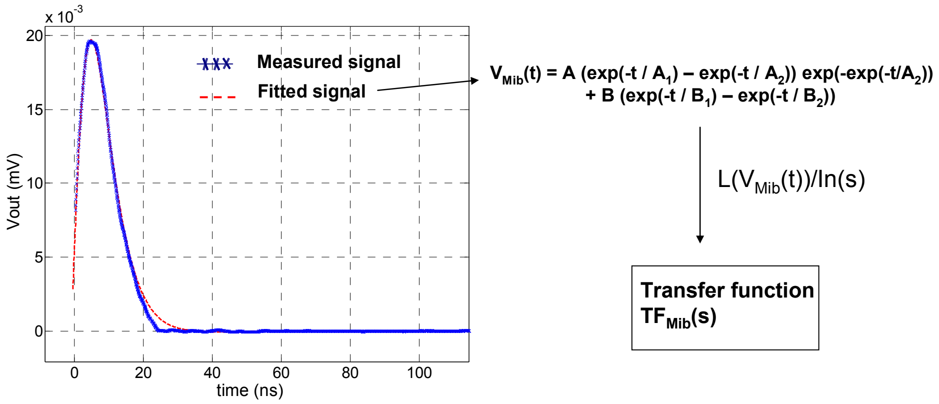

Figure 5.16. Calculation of the pre-amplifier transfer function from measurements.

The calculation of the Laplace transform of the equation defining the response to a voltage step on the injection capacitor, divided by the Laplace transform of the estimated input signal gives the transfer function of the pre-amplifier.

The current signal $I_e(t)$ induced by the electron drift was considered to vary as defined by equation 5.13, thus increasing during the laser pulse duration, and then exponentially decreasing with a time constant τ_c. The pre-amplifier output signal $V_{out}(t)$ corresponding to the defined input current $I_e(t)$ can be calculated with the extracted transfer function $TF_{Mib}(s)$. The input current is first calculated in the Laplace domain, and then multiplied by $TF_{Mib}(s)$, resulting in $V_{out}(s)$. An inverse Laplace transform of the result leads to the pre-amplifier output signal $V_{out}(t)$. Calculations were performed by using the software Mathematica. The input current parameters were varied to obtain output signals fitting the measured signals. An example of the extraction procedure and of the fitting accuracy is presented in Figure 5.17. The equivalent currents presented in Figure 5.17 left result in signals at the pre-amplifier output presented in Figure 5.17 right.

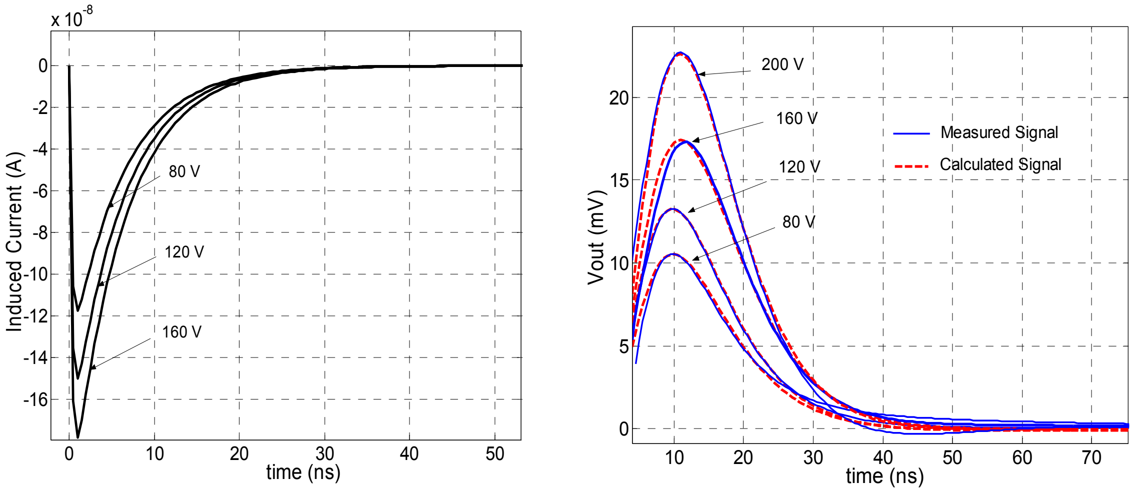

Figure 5.17. Left: Extracted equivalent induced current by the electrons drift. Right: Pre-amplifier output signals measured and calculated for the input currents defined on the left.

A good fitting was obtained between the calculated signals and the measured signals for the fast decay component of the signal. This again shows that the simple assumptions of a linear electric field and of a signal induced by the electrons defined as in equation 5.13 permit to explain the fast decays of the measured signals.

The estimation of the induced currents permits to extract the time constant τ_c that defines the signal exponential decay time. It has been calculated for different detector biases and the extracted values are listed in table 5.2 for different detector biases.

Detector bias	τ_c	Detector bias	τ_c
80 V	6.2 ns	160 V	6 ns
100 V	6.4 ns	180 V	5.4 ns
120 V	6 ns	200 V	5 ns
140V	6.4 ns		

Table 5.2. Extracted time constant for different detector biases.

A constant τ_c of ~ 6 ns is extracted, but it can be noted that at high reverse voltages, the time constant tends to decrease. A full depletion of the diode or a non-linear field for high reverse voltages could create this acceleration of the signal. The extracted time constant is in agreement with the measurements performed on the AFP chip, and leads to a product $\mu_d \cdot N_{db}^* \sim 1.1\ 10^{15}\ \mathrm{cm}^2 \cdot \mathrm{V}^{-1} \cdot \mathrm{s}^{-1}$.

The fast and long decay component of the signals can be clearly seen by integrating the measured signals (Figure 5.18). The measurements of τ_c have shown that the model of equation 5.13 is a good approximation of the signal induced by the electrons. The integral of this signal can then be calculated from equation 5.13, and leads to a charge $Q_{coll,e}$ simply defined as:

$$Q_{coll,e} = \frac{-q\,N\,d}{(d+d_2)} = \frac{-q\,N}{(d+d2)}\sqrt{\frac{2\,\varepsilon_0\,\varepsilon_{aSi}}{q\,N_{db}{}^{*}}}\sqrt{V} \qquad (5.22).$$

where d is the depleted thickness, proportional to the square root of the applied bias. N is the total number of electrons created and drifting, and $(d+d_2)$ is the total thickness of the detector i-layer. For a fully depleted diode, the total charge readout will then be equal to the total charge created.

The observation of the evolution of the integral of the signal fast component is then a good technique to estimate the bias voltage needed to fully deplete the detector. The signals fast component integrals are presented in Figure 5.18 for different detector biases.

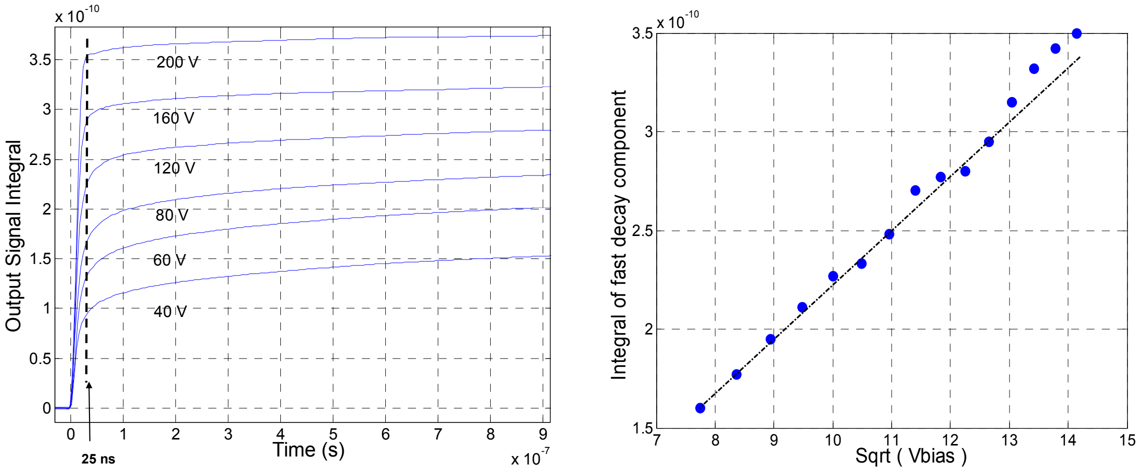

Figure 5.18. Left: Integrals of measured signals with I_{FEED} = 100 nA. Right: Integral value of the fast signal attributed to the electrons drift as a function of the square root of the applied detector bias.

The pre-amplifier output integrals correspond to a total charge of about $Q_{coll,e} = 5.13\times10^{-6}\times Q_{sig}$ C. A linear relation between the integrated signals charge and the square root of the detector bias is observed, and is in agreement with equation 5.22, as $d \propto \sqrt{V}$. The slope is equivalent to 1.28×10^{-16} C/V$^{1/2}$. The total number of electrons can be extracted from this slope and equation 5.22, and N ~ 10800 e$^-$. No saturation of the charge is observed, thus indicating that the 20 µm thick diode is not fully depleted at 200 V. However, the relation between the measured integral and the charge $Q_{coll,e-}$ is valid if the fast signal is only created by the electrons drift. The signal induced by the holes during the first 25 ns is more important for increasing biases, and might also increase the total signal readout during the fast decay. This consideration then renders more complicated the analysis of the plot in Figure 5.18 right for biases higher than 180 V. Also, the observation of a slight acceleration of the signal for a bias higher than 180 V can be an indication of a beginning of full depletion of the diode. A detail study of the depletion of the sensor will be done in Chapter 6.

5.4. Conclusions

The formation and the speed of the signal in TFA detectors have been characterized in this chapter by creating electron-hole pairs at the p-i interface vicinity with a 660 nm pulsed laser. Electrons drift down the whole depleted thickness and holes up to the p^+ layer where they are collected, and these motions induce a negative signal on the detector bottom electrode integrated in the readout integrated circuit.

Measurements have been performed on a 13 μm thick and a 32.6 μm thick a-Si:H sensor each deposited on an AFP chip, and on a 20 μm thick sensor deposited on an aSiHtest chip. The measured signals present a fast decay attributed to the electron induced current. A model based on the assumption of a linear electric field and on constant electron mobility has been developed and leads to the definition of an electron induced current exponentially decreasing in time with the time constant τ_c. After a time $t = 3\ \tau_c$, 95 % of the signal has been created. The time constant is inversely proportional to $\mu_d \cdot N_{db}^*$, so that high mobility but also high ionized defect density leads to a fast signal. The model was successful in explaining the measured signal fast decays, and time constant of 4 to 6 ns have been extracted, not varying for detector biases less than full depletion voltages. The different measurements then demonstrate that the signal induced by the electrons drifting in the linearly decaying electric field ends after a time of 12 to 18 ns. Moreover, for an over-depleted diode, one expects an even faster signal as the internal fields will be increased and the drift length will remain constant and equal to the diode thickness. This effect is observed in the aSiHtest measurements, as a time constant of 5 ns is measured for a detector bias of 200 V, while $\tau_c \sim 6$ ns for lower voltages.

The measured signals also show a slow component that can be explained by a slow and low amplitude signal induced by the hole motion or (and) by a non-linear electric field profile between depleted and non depleted zones. A qualitative model has been developed for the signal induced by the holes, taking into account their dispersive transport and their field enhanced mobility, which will serve in Chapter 6 in the calculation of charge induced by ionizing radiation. The current signal estimated by the model and the tails of the measured signals become faster as the bias voltages are increased.

For the 20 μm thick aSiHtest sample, a bias voltage of 100 V leads to a tail with a time constant of ~ 450 ns and a bias voltage of 200 V leads to a signal time constant of less than 30 ns. This signal tail is different to the one observed for a similar reverse bias on a 32 μm thick sensor (~ 1 μs). This observation indicates that a low and slowly decaying electric field in the so-called “non-depleted” region would be most probably responsible of the tails. This suggests that the zone referred to as “depleted zone” corresponds to a region with a high electric field linearly decaying, while the “non-depleted” zone corresponds to a zone with a low N_{db}^* and thus low and slowly decaying electric field.

The different studies presented in this chapter show that the 660 nm laser measurement technique has a high potential for the characterization of n-i-p a-Si:H diodes. The signal speed originating from the electron motion has been measured, and the product of the mobility and of the ionized dangling bond density has been extracted. The number of created electrons can also be extracted from the measurements, and the depletion of the diode can be studied.

In case of particle detection, the particle will create electron-hole pairs all along its path through the depleted i-layer. Electrons will drift in the internal high electric field and induce the signal. The longest contribution to the total signal induced by the electrons will then originate from electrons created at the p-i interface, as they have to drift over the whole depleted thickness. This maximum signal time is the time measured and determined in this chapter, and is about 12 ns to 18 ns. Hole mobility is field dependent, so that the amplitude and the time of the signal induced by a hole will depend on the position of its creation in the depleted region, i.e. in the linearly decaying electric field. The evolution of the signal tails observed with the field variations are thus an image of the difference of signal that will be induced by a hole if created at the p-i interface or at lower field regions in the depleted zone. Only a fraction of the total signal induced by the created holes will then be readout in a 20 ns time. The measurements and analysis presented in this chapter demonstrate that for particle detection applications of a TFA detector the created electron signal and only a fraction of the created holes signal will be obtained in less than 18 ns, and that full or over-depletion regimes of the n-i-p diodes are required for an optimum detection.

6. Ionizing radiation detection with TFA detectors

Ionizing radiation detection efficiency of Thin Film on ASIC detectors has been studied and results are presented in this chapter. Detectors based on a n-i-p a-Si:H sensor deposited on either an AFP or an aSiHtest integrated circuit have been characterized. Free carriers created by charged particles or electromagnetic radiations in the i-layer depleted region induce a signal on the sensor bottom electrode which is amplified by the integrated fast transimpedance pre-amplifiers (from 5 ns to 25 ns peaking time) so that fast detection with an a-Si:H sensor has been tested. First detection of low-energy and high-energy electrons emitted from radioactive Beta sources has been performed on a detector based on an AFP integrated circuit and the results are presented in section 6.1. The interaction of radiation with the a-Si:H sensor and the signal generation are presented in section 6.2 and permit to understand the detection limitations of the TFA technology. Full depletion of the a-Si:H sensor is an important condition for an optimized detection. However, it cannot be studied using standard semiconductor characterization techniques such as measuring the sensor capacitance-voltage characteristics (C-V [Lut99]) as the high resistivity of the non-depleted a-Si:H i-layer induces a constant capacitance of the a-Si:H diode for varying applied biases. A measurement technique is proposed and is presented in section 6.3 with results obtained on TFA detectors based on an aSiHtest integrated circuit. Detection efficiency has then been tested on these detectors and results obtained with low and high energy electrons and soft X-rays are also presented in section 6.3.

6.1. Preliminary results obtained on a detector based on the AFP integrated circuit

Preliminary characterization of particle detection with TFA detectors has been performed on the 32.6 μm thick n-i-p a-Si:H sensor deposited on an AFP circuit [Jar04]. An important limitation of the detector performance turned out to originate from the elevated leakage current, which has been presented in sections 4.1 and 4.2. The high leakage current induces a risk of breakdown of the a-Si:H sensor at high reverse voltages so that the detector has only been tested with a maximum reverse voltage of 300 V. Calculations presented in section 2.3 lead to an estimated full depletion voltage V_d defined by $V_d \sim 0.45 \times d^2$ (d being the sensor thickness in μm). A reverse voltage of about 480 V is needed for full depletion of this sensor, and tests could only be performed on an under-depleted sensor (300 V corresponding to an estimated 26 μm thick depleted region). The first detection of charged particles using a TFA detector has been performed by measuring signals created by electrons emitted from radioactive Beta sources.

We employed in a first time a Ni^{63} source. The radioactive Ni^{63} nuclei have a $Beta^{-}$ decay emitting low-energy electrons with an energy distribution presented in Figure 6.1.

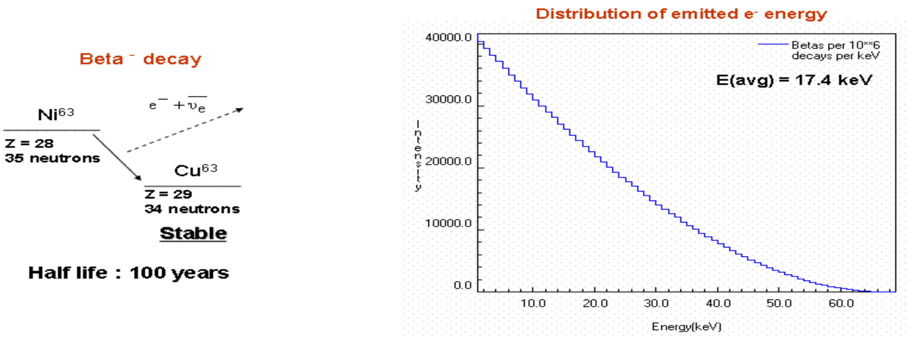

Figure 6.1. Left: $Beta^{-}$ decay of Ni^{63} nuclei. Right: Electrons energy distribution [Ber].

The radioactive source is placed above the TFA detector. The emitted Beta electrons create electron-hole pairs in the sensor depleted region and the generated carriers are separated and accelerated by the internal electric field. As it has been presented in Chapter 5, their motion induce a signal on the a-Si:H sensor bottom electrode located at the position of the electron track through the sensor. The induced signal is amplified by the integrated Active Feedback Pre-amplifier connected to the bottom electrode. A further 25 dB inverting voltage amplifier was connected at the output of the channel under test. It also limits the bandwidth and permits to improve the noise resolution of the readout system (an ENC of about 350 e^{-} rms was obtained).

Output signal waveforms created by Beta electrons were recorded with an oscilloscope in self-triggering mode. Figure 6.2 left displays 5 output signals each induced by a Beta electron and each recorded in single shot, showing the TFA detector sensitivity to low-energy Beta electrons.

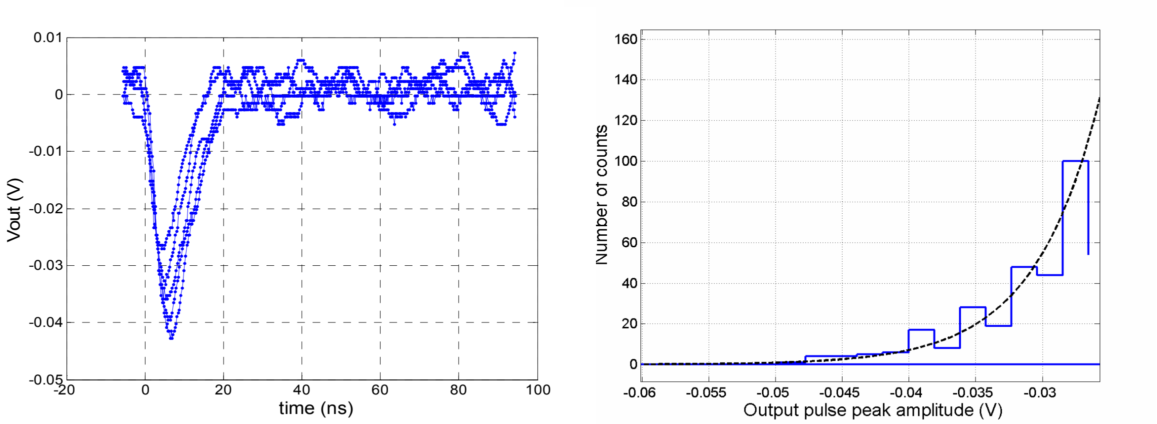

Figure 6.2. Left: 5 output signals each created by an incident electron in the TFA detector. Negative signals are readout after the 25 dB inverting amplifier, thus corresponding to a negative signal induced on the sensor bottom electrode. Right: Pulse height distribution of output signals readout with a self-trigger at ~ -25 mV.

The signal shape follows the fast processing of the integrated Active Feedback Pre-amplifier (~ 6 ns), demonstrating the feasibility of detecting low-energy Beta electrons with a 5-10 ns shaping time. The electron induced signal time constant τ_c has been extracted for this sample (Chapter 5) and $\tau_c \sim 5.6$ ns. The signal induced by holes is expected to be much slower so that the signals readout with the TFA detector based on the AFP circuit can mostly be attributed to the generated electrons.

Peak amplitudes of the output signals created by Beta electrons were recorded and the distribution of the signal heights is displayed in Figure 6.2. Incident electrons are for the most totally absorbed in the depleted layer so that the signal peak amplitude scales with the Beta electron energy. The generation of carriers in the a-Si:H sensor and the signal induced by the motion of the free carriers will be presented in detail in section 6.2.

Part of the energy of the electrons emitted from the source is lost in the air separating the source from the detector surface and in the Transparent Conductive Oxide last layer of the a-Si:H sensor (which defines the sensor top electrode). The source was placed at about 1 mm from the detector surface. Indium Tin Oxide (ITO) was used as top electrode for the tested sample, with a thickness of about 200 nm. The energy-loss of electrons has been estimated from the stopping powers, densities and compounds of air and ITO using the database ESTAR [STAR05]. This energy loss increases for decreasing electron speed (and so energy). Calculations for 10 and 50 keV electrons are presented in Table 6.1.

Material	Density (g/cm^3)	e^- energy (keV)	Stopping power (MeV/cm)	Thickness t	Energy Lost in t:
Air	1.205×10^{-3}	10	0.0238	1 mm	2.3 keV
		50	0.007		0.7 keV
ITO (In_2O_3 90% / SnO_3 10%)	7.14	10	112	200 nm	2.22 keV
		50	34.7		0.66 keV

Table 6.1. Estimated energy lost in Air and in the ITO layer [STAR05].

Electron-hole pairs generated in the p-doped layer will not participate to the signal formation because of the high density of defects associated to the doping (cf. section 2.1). This layer is therefore designed very thin and is usually ~ 30-60 nm thick.

Very few studies have been performed on the electron generation function and on electron range in a-Si:H. The electron range corresponds to the average total thickness of material an electron travels before losing all its energy. This quantity represents an average as electrons suffer multiple scattering effects along their tracks into the material, resulting in very tortuous paths. It has been shown that the extrapolated range R of an electron with energy E (in keV) in intrinsic a-Si:H is linear with $E^{1.75}$ [Naj91, Naj92]. This result is in agreement with the range dependence on the material density ρ and on the electron energy (in keV) E defined by [Eve71, Mat74]:

$$R(\mu m) = \frac{A}{\rho} E^{1.75}(keV) \tag{6.1}$$

A is a constant which has been extracted by different authors and equals 0.045 [Eve71] to 0.052 [Mat74]. The only work performed on the electron range in a-Si:H shows a factor A/ρ = 0.0204 [Naj92], equivalent to A ~ 0.045, and this value will be used in our calculations. From equation 6.1, one can calculate the range of the Beta electrons emitted by the Ni^{63} source. A 58 keV electron presents a range equivalent to the estimated thickness depleted with a reverse voltage of 300 V on the 32.6 µm thick diode. One can then consider that all electrons will be totally absorbed in the sensor active thickness (see Figure 6.1). It can be assumed that the maximum signal observed at the AFP output corresponds to a Beta electron with energy in the range ~ 45-55 keV. The ITO and p-doped layers have a high stopping power for low-energy electrons and limit the detection of few keV electrons. Tests have been performed on the same TFA detector using the electron beam of a Scanning Electron Microscope (SEM) and results have been presented in section 4.2. During these tests, the electron beam energy was varied to observe the lowest energies the detector could sense. For electron beam energy less than 10 keV, no significant signal was created in the detector, so that this energy can be considered as the lower limit of electrons that can be detected.

The spectrum corresponding to the output signal height distribution (Figure 6.2 right) can be plotted as distribution of the charge readout, which can be estimated from the electrical tests performed on the AFP (cf. section 3.1). Figure 6.3 displays such distribution for 3 different applied reverse voltages.

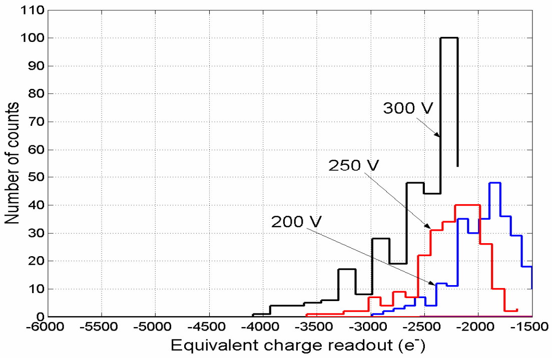

Figure 6.3. Distribution of charges generated by low-energy electrons in the TFA detector, for a reverse bias of 200 V, 250 V and 300 V.

The maximum charge readout is of about 3250 e^-, 3750 e^- and 4400 e^- for reverse biases of 200 V, 250 V and 300 V. The signal increases for increasing biasing voltages as the sensitive thickness of the sensor increases and as the signal induced by the free carrier motions is increased. This will be better explained in section 6.2.

The energy loss rate dE/dx of a particle in a detector depends on the interacting ionizing radiation and on its energy (Chapter 1). A minimum dE/dx is reached for a given energy of a given radiation. The particle with energy corresponding to this minimum dE/dx is referred to as Minimum Ionizing Particle (MIP) as this particle will create the smaller signal in the detector. In a first approximation one can consider that the energy loss in a-

Si:H will be comparable to that in crystalline silicon, so that a MIP corresponds to an electron with an energy around 1 MeV. The sensitivity of the TFA detector to MIPs can be studied by using a Sr^{90} radioactive source. The radioactive Sr^{90} nuclei have a Beta^{-} decay emitting electrons with energies up to ~ 500 keV, while the daughter nuclei Y^{90} also have a Beta^{-} decay emitting electrons with energies up to ~ 2.2 MeV. Nuclear decays and energy distributions of the emitted electrons are presented in Figure 6.4.

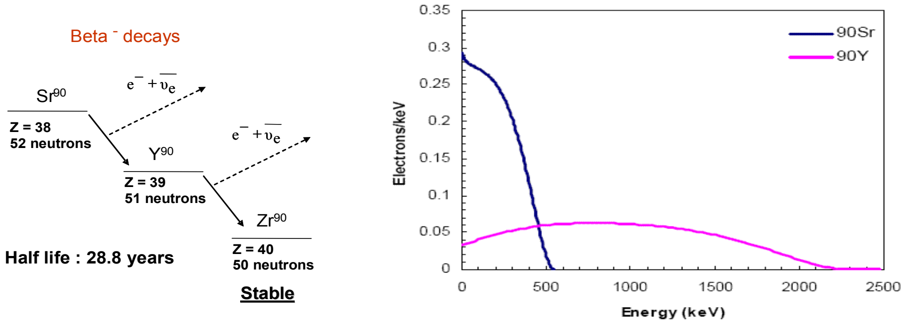

Figure 6.4. Left: Beta- decay of Sr^{90}. Right: Distribution of emitted electrons (right) [Ber].

A Sr^{90} source was placed on top of the TFA detector and first measurements were taken with self triggering of the output signals. The distribution of the output pulse heights measured is shown in Figure 6.5 left together with the noise level (which corresponds to the spectrum obtained for the same duration of data acquisition but without the source). An amplifier was used to filter the output signal to keep frequencies only in the range 20 kHz – 500 MHz in order to enhance the noise performance of the readout system. A linear relation links the output pulse amplitude to the induced charge and a 100 mV output peak corresponds to a charge of about 5000 e^{-}, so that signals were readout with a minimum at about 1300 e^{-}.

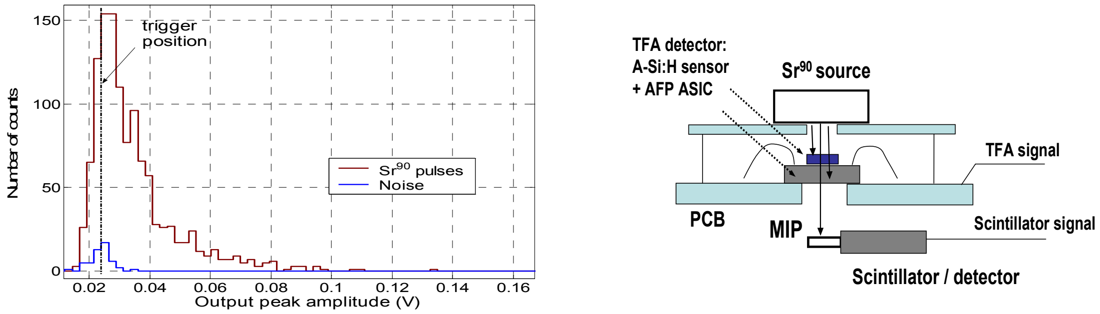

Figure 6.5. Left: TFA detector response to Sr^{90} source, output pulse amplitude distribution. Right: Measurement set up for MIP detection.

The obtained spectrum does not show a peak as it would be expected from the detection of electrons in the range of 500 keV to 2 MeV (MIPs). These signals might be covered by the electronic readout noise. A measurement technique presented in Figure 6.5 right has been used to conclude about the MIP sensitivity of the TFA detector. A detector able to sense low or high energy electrons was placed below the TFA detector. High energy electrons only are able to go through the ASIC thickness (~ 600 μm). Measurements were then performed by triggering on the detector placed below the test sample. Clear pulses were observed from this detector corresponding to MIPs going through the TFA detector but no signal was observed on the TFA detector. On the contrary, by triggering with signals from the TFA detector, no signal was observed on the detector below. This measurement proves that no MIP has been detected with a 300 V reverse bias applied to a 32.6 µm thick a-Si:H sensor deposited on top of the AFP integrated circuit. The observed spectrum corresponds to the low energy Beta electrons, similar to the tests performed with the Ni^{63} source. A maximum output pulse corresponding to signals of about 4600 e^- were readout, which corresponds to the maximum signal obtained using the Ni^{63} source.

These first measurements performed on the TFA detector based on an AFP circuit have demonstrated the possibility to detect low-energy electrons with a fast shaping time of 5 to 10 ns. However, signals created by MIPs were also shown to be below 1300 e^- so that no MIP was sensed by the detector. These preliminary measurements also permitted to first introduce the electron range in a-Si:H.

6.2. Signal generation: performance and limitations of a TFA detector

The mechanisms involved in the creation of a signal by ionizing radiations going through an a-Si:H sensor have been studied to understand the performance and limitations of a TFA detector. The signal induced on the a-Si:H sensor electrodes depends on:

- The ionizing radiation interaction with the sensor: creation of electron-hole pairs in the sensor depleted region.
- The signal induced on the sensor electrodes by the generated free carrier motion in the depleted region and on their collection (as it has been presented in section 5.1).

6.2.1. Radiation interaction in a-Si:H

First of all the signal depends on the interaction of the ionizing radiation with the sensor: it depends on the number of electron-hole pairs created and on the location of their creation in the sensor (this is explained later in detail). The interaction of a radiation in the sensor can be defined by:

- The energy deposited in the a-Si:H sensor depleted region and its distribution:
  - Charged Particles: interactions occur all along the particle track into the sensor. The integrated path length defines the average total distance travelled by a particle. The distribution of the energy loss by the particle in the depleted region is given by the generation function.
  - Electromagnetic radiation: interactions are localized. The probability that a photon interacts after travelling a distance d is an exponential function of d, defined by the absorption coefficient. The location of interaction in the sensor is then statistic.
- The mean electron-hole pair creation energy W in a-Si:H

The mean energy loss rate of a charged particle dE/ dx can be calculated from the Bethe-Bloch formula presented in Chapter 1. Depending on the particle type and energy, corrections have to be made to the formula for better accuracy. For non-relativistic charged particles (speed << c), it can be approximated by [Leo94]:

$$-\frac{dE}{dx} = 2\,\pi\, e^4 z^2 \,\frac{N_A\,\rho}{A}\,\frac{Z}{E}\,\ln\left(\xi\,\frac{E}{W}\right) \qquad (6.2).$$

N_A is Avogadro's number, A and ρ the atomic mass and the density of the absorber, so that $N_A \times \rho / A$ defines the number of target atom per unit of volume. E is the particle energy, z its charge in units of electron charge, e the electronic charge, W the mean ionisation energy and ξ a constant. This equation shows the necessity of determining the mean energy loss distribution in the sensor: dE/dx depends on the particle energy and the interacting particle slows down and loses energy during its travel through the depleted region of the sensor. dE/dx will then not be constant in the thickness of interaction.

For a compound material, dE/dx is the sum of the mean rate of energy loss in each element. a-Si:H can be considered as a compound with 15 % Hydrogen (H) and 85 % Silicon (Si). Their respective contributions can be estimated from equation 6.2 neglecting the logarithmic term. It is equivalent to the ratio of number of target atom (concentration) multiplied by the ratio of atomic charge. The H contribution with respect to the Si one is given by 15/85×1/14 = 0.01 and can be neglected. Its main effect in the energy loss is linked to the induced change in material density. The energy loss in a-Si:H can then be estimated using Z and A of Silicon, and the differences in the energy loss with respect to crystalline silicon originates principally from the different density and mean ionisation energy.

Models of mean energy loss distribution in a-Si:H have been developed for low-energy electrons by Najar et al. [Naj91]. The generation profile, also called depth-dose curve, can well be represented by third-degree polynomials in a-Si:H [Naj91], as it is presented for other materials in [Eve71]. The profile g(x,E) can be expressed as a function of the mean range R (proportional to $E^{1.75}$) of the particle in a-Si:H (defined in equation 6.1) and:

$$g(x,E) = \frac{1}{R}\left(\frac{x}{R} - b\right)\left(a_0 + a_1\frac{x}{R} + a_2\left(\frac{x}{R}\right)^2\right) \quad (6.3); \qquad \frac{dE}{dx}(x) \approx E \cdot g(E,x) \quad (6.4).$$

Parameters b, a_0, a_1 and a_2 have been found in [Naj91] close to Everhatt-Hoff fit [Eve71]: $b = 1.21$, $a_0 = -0.784$, $a_1 = -3.98$, $a_2 = 4.19$. Depth-dose curves have been calculated for low-energy electrons from equation 6.4 and are presented in Figure 6.6 left. A calculation performed for a 500 keV electron is also shown on Figure 6.6 left, even though the model might not be accurate for high energies. However, the energy loss distribution for a MIP will follow the same behaviour, i.e. it will vary very little in the thin sensor layer. Typical mean dE/dx at energies corresponding to MIPs can be estimated from equation 6.2 or from

Silicon data obtained via ESTAR calculations [STAR05] weighted with a-Si:H density and W. For a 1 MeV electron, $dE/dx \sim 0.36$ keV/µm in a-Si:H.

As it has been presented in Chapter 1, photon interaction is localized so that the location of the created electron-hole pairs is statistic. The attenuation of photons is expressed by the ratio of the intensity of a beam at the depth x over the original intensity I0: $I/I0 = \exp(-\mu \cdot x)$. Photon mass attenuation coefficient μ/ρ of Silicon can be obtained from databases as [XCOM] and a-Si:H attenuation coefficient can be estimated using the density $\rho = 2.15$ g/cm^3. X-rays with energy lower than 60 keV have a μ determined by the photo-electric effect. A 6 keV X-ray has a $\mu \sim 3.1\times10^2$ cm^{-1} so that 95 % of a 6 keV X-ray beam would be absorbed in 96 µm of a-Si:H. Attenuations of X-rays in a-Si:H can be estimated. Results are presented in Figure 6.6 right and the probability of interaction of an X-ray at a distance d in the material can be found from the exponential relation.

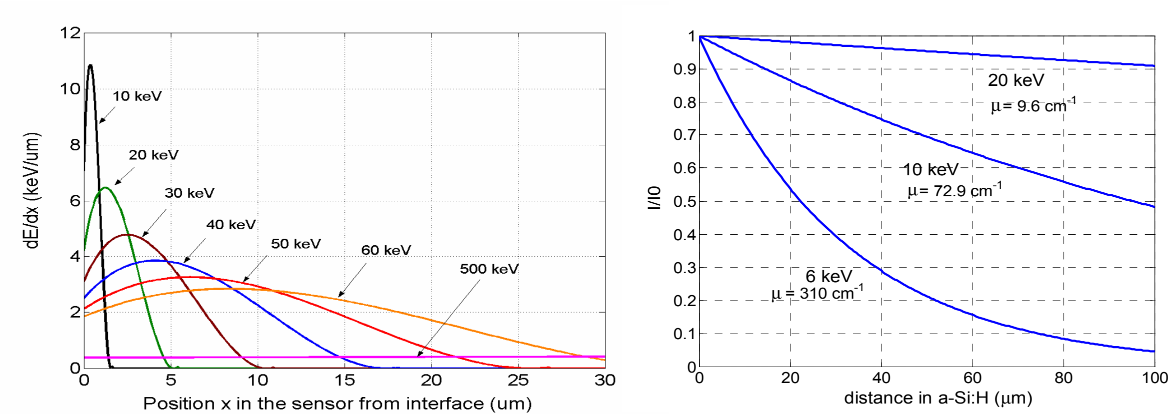

Figure 6.6. Left: Simulated distribution of mean rate of energy loss of Beta electrons in a 30 µm thick a-Si:H sensor. Right: Soft X-ray photons attenuation in a-Si:H.

Only part of the energy loss in the a-Si:H sensor is used for the creation of e^--h^+ pairs. The mean pair creation energy W has been shown to depend on the material bandgap and calculations from Klein's relation [Kle68] lead for a 1.8 eV bandgap (a-Si:H mobility bandgap) to W = 6 eV. However, the notion of gap in a-Si:H is not precisely defined because of the distribution of states in the bandgap forming conduction and valence band tails. A different gap is then considered for optical absorption and is equal to ~ 1.5 eV. From this so-called cubic gap we find W ~ 4.7 eV. This quantity has been poorly studied and some studies have shown a W in the range of 4.8 eV [Naj91] to 6 eV [Per86]. A value of 6 eV can be considered as maximum in our studies.

6.2.2. Signal induced by free carriers generated in the sensor

A current is induced on the sensor electrodes directly after the creation of e^-/h^+ pairs by interactions of particles or photons in the sensor. The signal depends on the motion of the free charges created in the depleted region (section 5.2). I have established a simplified model to calculate the current induced by an electron-hole pair created at a position x_0 in the sensor, for an under-depleted a-Si:H sensor. The interaction and the x-axis defining the position in the sensor are presented in Figure 6.7.

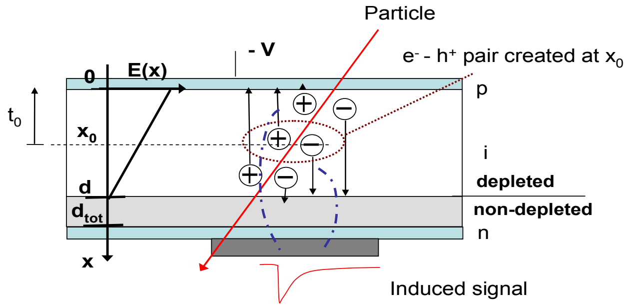

Figure 6.7. Schematic cross section of the a-Si:H sensor. Electron-hole pairs are generated at x_0 in the depleted region by a particle. Generated electrons (holes) drift to $x = d$ ($x = 0$) where they are collected. Their motion determines the signal amplitude.

Electrons created at x_0 are accelerated by the electric field down to the non-depleted region and their position in time can be calculated from equation 5.8 derived in section 5.2:

$$x(t) = d - (d - x_0)\exp(-t/\tau_c) \qquad (6.5)$$

d is the depleted thickness and τ_c is the electron transient time constant (equation 5.9). The induced current was presented in detail in section 5.2 (equation 5.11). The drift velocity of the moving charge $q \cdot N$ is obtained by derivation of equation 6.5, the weighting potential can be approximated as the inverse of the sensor thickness d_{tot} so that the current induced on the bottom electrode can be expressed as:

$$I(t) = \frac{-q\,N}{d_{tot}}(d - x_0)\frac{1}{\tau_c}\exp(-t/\tau_c) \qquad (6.6).$$

Signals induced by 1000 electrons created at the same position x_0 in a 20 µm thick sensor biased with a reverse voltage of 200 V have been simulated and results are presented in Figure 6.8 for different positions x_0.

The total charge Qe induced by N electrons created at a position x_0 can then be calculated by integrating equation 6.6, and for a time $t > 3\times\tau_c$:

$$Qe = \frac{q\,N}{d_{tot}}(d - x_0) \qquad (6.7).$$

The charge created depends on the total drift length of the electrons. This relation is illustrated by the simulations presented in Figure 6.8 right. A total charge Qe will be integrated in about 20 ns. The signal induced by the created electrons decreases linearly increasing the depth at which they are created in the a-Si:H sensor.

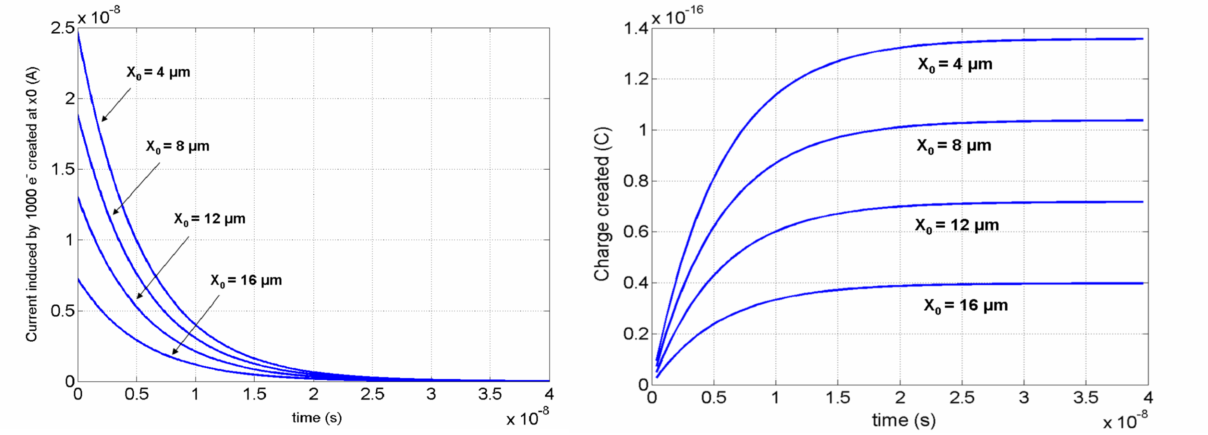

Figure 6.8. Left: absolute current created on sensor electrode by 1000 e⁻ created at a position x_0 in the sensor depleted region, for a 20 µm thick diode with a reverse bias of 200 V, and for different x_0. Right: Signal integrals showing the total charge integrated.

The signal induced by holes generated at the position x_0 has also been studied, though its calculation is more complicated. The hole drift mobility μ_d is dispersive and depends on the electric field (section 5.1) so that it varies both with time and with the position x inside the sensor. The expression defining the hole drift mobility is reminded in equation 6.8. Its variations with the electric field are taken into account by considering an attempt-to-escape frequency ω varying with the electric field as extracted by Gu in [Gu95]:

$$\mu_d(t,x)=\alpha(1-\alpha)\mu_0\,\omega[E(x)]^{(\alpha-1)}\,t^{(\alpha-1)} \quad (6.8); \qquad \omega[E(x)]=\omega_0\exp(-E(x)/E_0) \quad (6.9).$$

where E(x) is the electric field at the position x in the sensor (equation 5.5). $\alpha = 0.65$ at room temperature, $\mu_0 \approx 1$ cm²/(V·s) [Sch04], $\omega_0 = 10^{11}$-10^{12} s^{-1} and $E_0 \approx 5.7\times10^4$ V/cm [Gu95]. The position at a time t of a hole created at x_0 then depends on x and on time. A direct calculation as it has been performed for electrons cannot be done but the calculation of the position and time can be carried out from the following relations:

$$dt=-\frac{dx}{\mu_d(t,E(x))\,E(x)} \qquad (6.10)$$

$$\int_0^t \alpha(1-\alpha)\mu_0\,t^{(\alpha-1)}\cdot dt=\int_{x_0}^{x}\frac{-1}{E(x)\cdot(\omega(E(x)))^{(\alpha-1)}}\cdot dx \qquad (6.11).$$

The negative relation originates from the fact that the field and the x-axis have an inverse direction (Figure 6.7). Time and position of holes are described by equation (6.11) but the integral on the right side cannot be expressed in a simple form. Calculations have been performed on Mathematica and the resolution of equation 6.11 involves the use of an exponential integral function: $\mathrm{Ei}(z)=\int_{-z}^{\infty}(\exp(-x)/x)\,dx$.

Position variation with time x(t) cannot be obtained analytically as it has been done for electrons, but the time t(x) needed to reach a position x can be expressed from resolution of equation 6.11 and:

$$t(x)=\left[\frac{1}{(1-\alpha)\,\mu_0\,\omega_0^{(\alpha-1)}}\,\frac{\varepsilon_0\,\varepsilon_{aSi}}{q\,N_{db}^{*}}\left(\mathrm{Ei}\left(\frac{qN_{db}^{*}(\alpha-1)}{E_0\varepsilon_0\varepsilon_{aSi}}(d-x)\right)-\mathrm{Ei}\left(\frac{qN_{db}^{*}(\alpha-1)}{E_0\varepsilon_0\varepsilon_{aSi}}(d-x_0)\right)\right)\right]^{1/\alpha} \quad (6.12).$$

The time t_0 needed to reach $x = 0$ defines the full drift time of holes created at x_0, if the carriers do not suffer any recombination. This drift time can be analytically calculated from equation 6.12 ($t(x = 0)$). Drift velocity has been extracted as a function of x from equation 6.12 as: $v_{drifth}(x) = 1/(t'(x))$. Variation of the velocity in time $v_{drifth}(t)$ can be numerically represented by a parametric plot of $v_{drifth}(x)\times\mathrm{UnitStep}(x)$ versus $t(x)$. The UnitStep function equals 1 for $x > 0$ and 0 for $x < 0$, so that the global function takes into account the fact that holes drift until the position $x = 0$ and are then collected, so that they do not contribute anymore to the signal induced on the bottom electrode of the sensor. The current induced on the bottom electrode by N holes created at x_0 is then equivalent to:

$$I(t)=\frac{-qN}{d_{tot}}\cdot v_{drifth}(t) \quad (6.13).$$

The different equations have been integrated in Mathematica permitting simulations of the signals induced by hole motion. Simulations of the signal created by 1000 holes generated at a position x_0 in a 20 µm thick sensor biased with a reverse voltage of 200 V are presented in Figure 6.9.

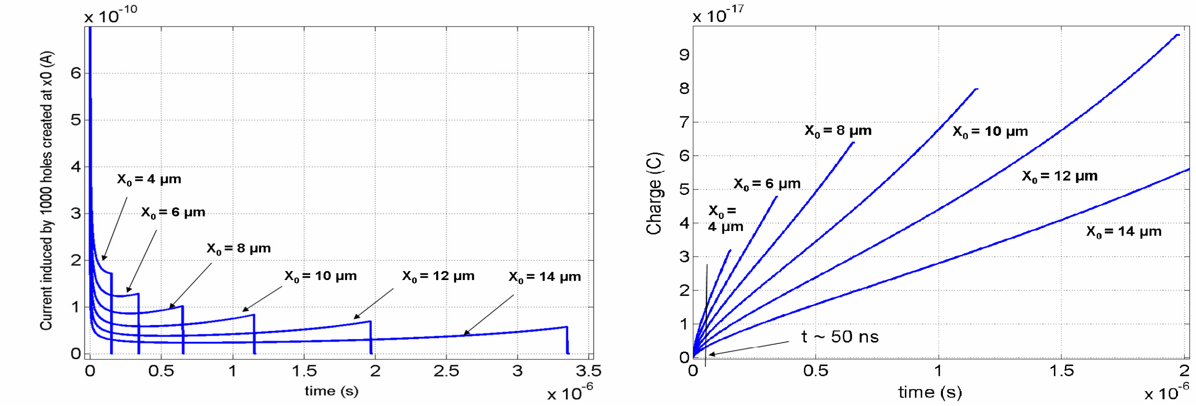

Figure 6.9. Left: current induced on sensor electrodes by 1000 holes created a position x_0 in the sensor depleted region, for a 20 µm thick diode with a reverse bias of 200 V and for different x_0. Right: Signal integrals showing the total charge induced as a function of time.

The induced current presents a sharp peak in the first ns. This signal corresponds to the highest drift mobility (close to μ_0) of holes just after their creation. The hole motion is then characterized by a mobility decreasing with time but increasing with electric field, and by an increasing electric field along the hole drift path. This results in a first decrease of the signal and in an increase of the signal for the highest fields (Figure 6.9 left). The abrupt transition corresponds to $t = t_0$ and is due to the rough approximation of the hole collection in the p^+-layer.

The total charge created by N holes generated at x_0 can be calculated by integrating equation 6.13. If no trapping or recombination occurs so that holes drift until their collection, the charge Qh induced by holes and the total charge Qsignal induced after a time t higher than t_0 correspond to:

$$\mathrm{Qh} = \frac{q \cdot N \cdot x_0}{d_{tot}} \quad (6.14); \qquad \mathrm{Qsignal} = \mathrm{Qe} + \mathrm{Qh} = \frac{q \cdot N \cdot d}{d_{tot}} \quad (6.15).$$

The charge induced by the motion of holes is represented in Figure 6.9 right and is obtained by integrating the simulated induced currents (Figure 6.9 left). The charge at time t_0 (which corresponds to the end of curves in Figure 6.9 right) is in agreement with equation 6.14. This relation holds true only for a time $t > t_0$ and for a time $t < \tau_{tr}$, τ_{tr} being the hole trapping time. However, as it can be observed in Figure 6.9, the hole drift time t_0 becomes very long as the hole drift distance increases, and $t_0 > 1$ µs for $x_0 > 9$ µm. At such time, trapping is expected to have an important impact.

The pre-amplifiers integrated in the TFA detectors we have developed have shaping times t_{shape} lower than 50 ns in order to perform fast detection. This time resolution of the electronic readout is much lower than the expected drift time of holes t_0, and also lower than the hole trapping time τ_{tr}. No trapping of holes is expected to influence the signal created by holes during this short time t_{shape} and only a small part of the current created by holes is seen during this time. The signal created by holes during the time t_{shape} is equivalent to a charge that can be expressed as $\mathrm{Qh}_{eff} = (q \cdot N/d_{tot}) \cdot (x_0 - x(t_{shape}))$.

It has been calculated that holes will travel in 50 ns a mean distance $[x_0\text{-}x(50\text{ ns})]$ of 0.3 µm (if created at $x_0 \sim 18$ µm in a 20 µm thick diode biased with a 200 V reverse voltage) to ~ 3 µm (if created at $x_0 \sim 3$ µm). Opposite variation of signal induced with the location of creation of holes is then expected in comparison to equation 6.14: the signal amplitude depends on the electric field at the position x_0, which decreases as x_0 increases. The charge Qh_{eff} created by holes then decreases increasing x_0 for low shaping times. This behaviour is represented in Figure 6.9: at 50 ns, the current induced and the total charge seen decrease increasing x_0.

This characteristic limits the detection sensitivity of the TFA detector as only a small part of the signal created by holes will contribute to the total signal amplified by the electronic readout for a shaping time lower than 50 ns. In such conditions, the hole contribution strongly depends on the sensor internal field. For an infinite shaping time the ratio Qe/Qh decreases for increasing x_0 and equals $(d\text{-}x_0)/x_0$, as it can be seen in Figures 6.8 and 6.9. However, for a shaping time of 50 ns this ratio increases for increasing x_0, and in the example of Figures 6.8 and 6.9 it equals ~ 9 for $x_0 = 4$ µm, ~ 12 for $x_0 = 8$ µm and ~ 22 for

x_0 = 12 µm. The ratio is then defined as $(d-x_0)/(x_0-x(t_{shape}))$ where $x(t_{shape})$ decreases as x_0 increases.

This model of the signal created by holes is based on the assumption of strong variations of mobility with electric field. This has been presented in [Gu95] and in [Jus95]. The total charge amplified during the readout shaping time that can be attributed to holes generated by the incident radiation thus strongly depends on the reverse bias voltage applied to the sensor and on the shaping time. It can be noted that the simulations have been performed using standard values of μ_0, ω_0 and E_0, but that even slight variations of these parameters impact on the drift time and speed of holes and induce variations of the charge readout in a time t_{shape}. The model presented then describes the basis and mechanisms of the induced signal but exact prevision of the output charge is difficult to obtain.

The signal induced by N electron-hole pairs created at a position x_0 is then defined by:

- A charge Qe induced by the generated electrons: it depends on the depleted thickness (and so on N_{db}^* and on the applied voltage) and on the position x_0. For $t_{shape} > \sim 20$ ns, $Qe = (q\cdot N/d_{tot})\cdot(d-x_0)$, and maximum signal is obtained for full depletion of the sensor.
- A charge Qh induced by the generated holes: for low shaping times of the electronic readout (< 50 ns), no trapping of holes is expected but only part of the induced signal is amplified because of the slow hole motion, and: $Qh = (q\cdot N/th)\cdot(x_0-x(t_{shape}))$. The created signal depends on the hole velocity and on the pre-amplifier shaping time. Hole mobility and velocity strongly depend on the electric field and high fields are needed to enhance the signal originating from holes. Maximum signal is obtained for a maximum reverse voltage applied to the sensor, so for over-depletion of the sensor and (or) thick diodes.

The total charge Q induced on the TFA detector bottom electrode by a particle or photon interacting in the a-Si:H sensor can be calculated with:

$$Q = \int_0^d \frac{\left[\frac{dE}{dx}\right](x_0)}{W} \left(Qe(x_0) + Qh(x_0)\right) dx_0 \qquad (6.16).$$

where $(dE/dx)(x_0)/W$ gives the number of electron-hole pairs created by the interacting radiation at a position x_0 in the sensor. $Qe(x_0)$ and $Qh(x_0)$ correspond to the charge (signal) created by an electron and by a hole generated at a position x_0 in the sensor. The integration from $x_0 = 0$ to $x_0 = d$ (depleted thickness) thus permits to calculate the total charge induced by the interacting radiation on the sensor electrodes.

6.3. Detection with TFA detectors based on an aSiHtest integrated circuit

Ionizing radiation detection characteristics of TFA detectors have been studied on detectors based on the aSiHtest integrated circuit. The developed detectors show a maximum thickness of the deposited a-Si:H sensor of 20 µm and results of some of their characterizations have been presented in the previous chapters. The limitation of the deposited thickness has been occasioned by an upgrade of the reactor dedicated to the deposition of thick sensors at the IMT. No sensors could be deposited with this reactor on aSiHtest circuits because of long installation and optimization phases of the reactor. The 1st serie of deposition on aSiHtest circuits has been done using a reactor with a lower deposition rate so that sensors with a maximum thickness of 20 µm could have been deposited and tested.

Ionizing radiation detection characterization of the developed detectors has been performed on pixel or strip structures integrated in the aSiHtest circuit (section 3.2) and each connected to aSiScope pre-amplifiers. The signal created by particles or photons is characterized by equation 6.16, which shows that full depletion of the sensor is needed to optimise the detector performance. The depletion condition of the n-i-p a-Si:H diodes has been studied and results are presented in 6.3.1. The TFA detectors were then characterized with low energy electrons (few keV) and results are presented in 6.3.2. Finally, measurements with electromagnetic radiations have been done and results are presented in 6.3.3.

6.3.1. Characterization of the a-Si:H sensor depletion

The detection efficiency first depends on the depletion of the a-Si:H sensor, as it has been presented in section 6.2. Full depletion is needed to optimise the detection as it allows maximum effective thickness of interaction in the sensor and as it ensures the induction of the maximum charge from the generated electrons (equation 6.7).

The capacitance of the a-Si:H sensor does not vary with the applied voltage because of the high resistivity of the non depleted i-layer, as it has been measured and presented in section 5.3. The depletion cannot be studied via standard C-V measurements as it is usually done for crystalline silicon detectors [Lut99]. We propose a method to estimate the depletion based on the pulsed laser measurement technique presented in Chapter 5. A 660 nm pulsed laser is used to generate in a short time (~ 3 ns) electron-hole pairs close to the p-i interface of the sensor. The signal readout on the bottom electrode will then be mainly determined by the motion of the generated electrons (Chapter 5) and also by the small current induced by the motion of the generated holes. Signal from electrons and part of the small signal from holes will be created in less than ~ 18 ns. Tests have been carried out on structures connected to integrated aSiScope pre-amplifiers which have a 25 ns peaking time. The charge readout can be calculated from the model established in section

6.2, and as $x_0 \approx 1$ µm (corresponding to the mean free path of 660 nm photons in a-Si:H), it can be approximated as:

$$Q_{laser} \cong \frac{q \cdot N \cdot d}{d_{tot}} \qquad (6.17).$$

The charge induced on the bottom electrode by the short laser pulse directly depends on the depleted thickness d, on the sensor thickness d_{tot} and on the total moving charge q·N. The observation of the output response peak amplitudes of the TFA detector to 660 nm laser pulses for different detector biases would then provide a direct insight into the depletion condition of the sensor.

Tests have been performed on the 20 µm thick sensors deposited on aSiHtest chips. Test structures are 2070 µm^2 octagonal pixels and strips with an area of 6.6 µm × 282.4 µm with an inter-strip distance of 4 to 13.4 µm. These structures are connected to the integrated pre-amplifiers aSiScope. Metal structures and pre-amplifiers are presented in detail in section 3.2. For high reverse bias voltages (> 160 V), the pre-amplifier impulse response is varied. The effective feedback current I_{feed} flowing through the active feedback is set to about 10 nA, so that at high reverse biases leakage current reduces the effective value of I_{feed} (a detailed explanation can be found in section 4.1, Figure 4.3). During the tests with laser and for particle detection, the pre-amplifier feedback current bias was increased for increasing sensor reverse voltages in order to compensate the leakage current and to have always similar current in the active feedback for the different measurements. This was done by fitting for each bias the pre-amplifier impulse response to a reference response recorded for a low detector bias, thus ensuring similar transfer function of the pre-amplifier for the different tests. An electrical characterization is thus first performed varying the detector bias to find the adequate increment of feedback current needed for each reverse voltage of the detector. An estimation of the leakage current can be done from these measurements and results are presented in Figure 6.10 left for a 20 µm thick sensor.

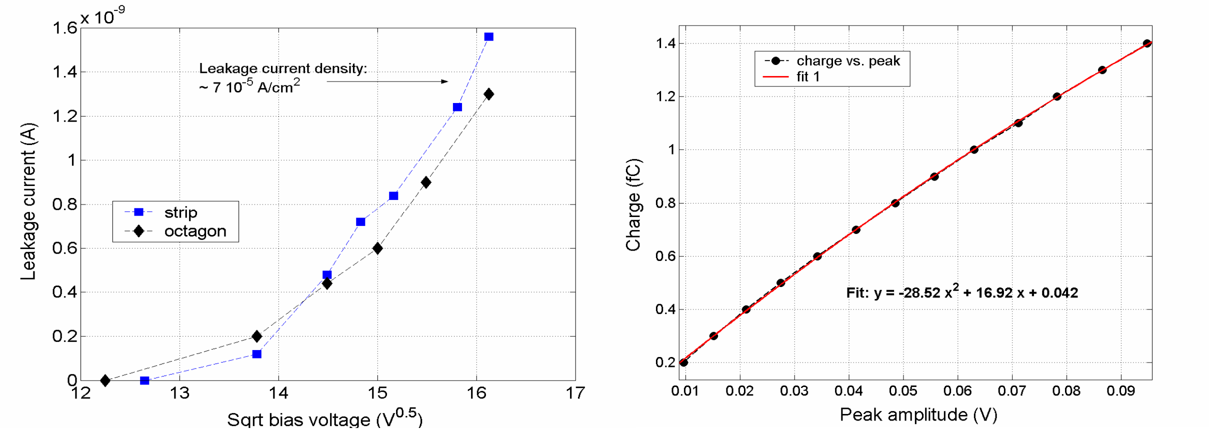

Figure 6.10. Left: Leakage current measured on a 20 µm thick sample on a 2070 µm^2 structures. Right: Electrical characterization of the pixel electronic readout.

The relation between input charge and output voltage peak is also measured because of a non linearity of the response. Results are presented in Figure 6.10 right and are similar for each detector bias with the adequate variation of I_{feed}.

Pre-amplifier output responses to 2 ns FWHM pulses of a 660 nm laser have been measured on 2 different 20 µm thick samples for different sensor biases. The output pulse shape shows a 25 to 30 ns peaking time, and results obtained on the first sample are presented in Figure 6.11.

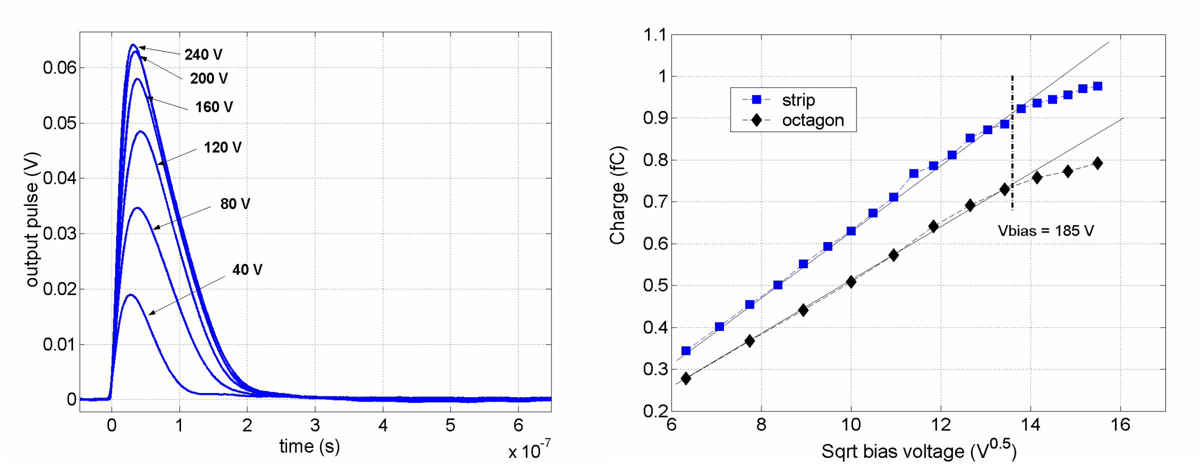

Figure 6.11. Left: Pre-amplifier output response to 660 nm laser pulses for different sensor biases. Right: Saturation of the charge readout corresponding to the output pulse peak for increasing sensors biases.

The charge corresponding to the output pulse peak amplitudes can be considered as equivalent to the charge presented in equation 6.17 as the pre-amplifier peaking time is higher than $3\times\tau_c$. A linear relation is first observed in Figure 6.11 right between the charge readout and the square root of the bias voltage, as expected from equation 6.17. The slope can be defined by equation 6.18. For a depleted thickness d equal to the sensor thickness d_{tot}, a saturation of the charge created is expected. This is observed in the measurements performed on both the octagonal pixel and a strip (Figure 6.11 right). For reverse biases higher than $V_d = 185$ V the charge created does not follow the relation of equation 6.17 and starts to saturate, so that V_d can be approximated as the full-depletion voltage. The density of ionised dangling bonds can be extracted from V_d and the number of electron-hole pairs created N can also be extracted from the measurements:

$$\frac{dQ_{laser}}{d\sqrt{V}} = \frac{q\,N}{d_{tot}}\sqrt{\frac{2\varepsilon_0\,\varepsilon_{aSi}}{q\,N_{db}^{*}}} \quad (\text{for } V < V_d) \quad (6.18); \qquad N_{db}^{*} = \frac{2\,\varepsilon_0\,\varepsilon_{aSi}\,V_d}{q\,d^2} \quad (6.19).$$

Measurements on the first sample give $V_d = 185$ V, so that $N_{db}^{*} = 6.15\times10^{14}$ cm^{-3}. A density of dangling bonds of 2×10^{15} cm^{-3} is given by the IMT, and usually 30 % of the dangling bonds are expected to be ionized [Qur89b]. The extracted value of N_{db}^* is thus very close to the expected value of 6×10^{14} cm^{-3}.

Similar measurements have been performed on a second sample and results are presented in Figure 6.12 for different laser pulse amplitudes. The slope of the curves rises for increasing laser amplitude, as the slope directly depends on N (equation 6.17). Similar V_d is measured for the different amplitudes and $V_d = 195$ V, leading to $N_{db}^* = 6.5\times10^{14}$ cm^{-3}. The number N of electron-hole pairs created by the laser pulse can be estimated from the curve slopes and equation 6.18. The laser energy was measured with an optical to electrical converter, and the laser spot size was estimated to 100 µm × 100 µm. The total energy of the laser pulse and the expected number of photons interacting for each structure can be estimated but with low accuracy because of laser calibration uncertainties.

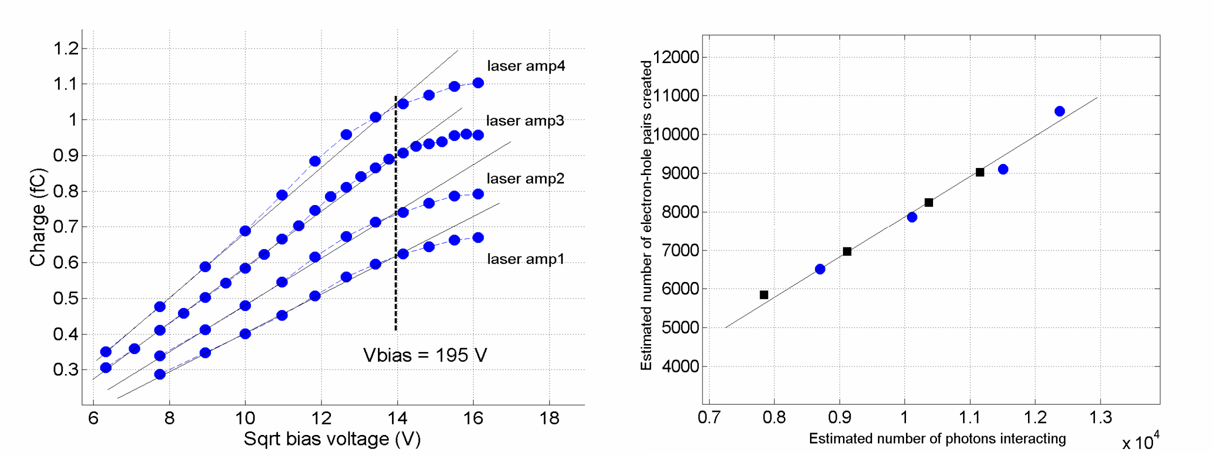

Figure 6.12. Left: Measured variations of the charge created by a laser pulse in the TFA detector on a strip structure, for different laser amplitudes. Right: Number of electrons N created extracted from the slopes of the curves in left versus estimated number of photons interacting.

From the measurements presented in Figure 6.12 right, a good linearity is observed between the charge created and the number of photons interacting. For photons with an energy of 1.88 eV (660 nm light), a pair of electron-hole is expected to be created by a single photon. Estimations of number of photons interacting have low accuracy and explain the slight deviations observed between number of pairs created and number of photons injected.

The presented measurement technique and method are thus interesting for an experimental estimation of the full-depletion voltage V_d, of the density of ionised dangling bonds N_{db}^* and of the number of electron-hole pairs created N. The extraction accuracy however depends on the sample thickness accuracy. Measurements on 20 µm thick samples have shown $V_d = 185 - 195$ V and $N_{db}^* = 6.15\times10^{14} - 6.5\times10^{14}$ cm^{-3}. This measurement technique together with a precise calibration set up for determining the laser spot size and energy could also permit a detailed study of light detection efficiency with TFA detectors.

6.3.2. Detection of electrons

First demonstrations of charged particle detection feasibility with TFA detectors using a-Si:H as sensing device have been done with samples deposited on the AFP chip. Low energy Beta electrons (in the range of few keV to about 50 keV) were detected on these samples showing an interesting potential of TFA technology for keV-electrons detection (section 6.1). Further studies have been performed on the 20 µm thick a-Si:H sensors deposited on aSiHtest integrated circuits. Tested structures are 6.6 µm × 282.4 µm strips and 2070 μm^2 octagonal pixels. Each metal structure is connected to an aSiScope pre-amplifier.

Detection of electrons emitted by a Ni^{63} radioactive source has first been studied on the strip structures. The 3 strips under test have an inter strip distance of 4 µm and 13.4 µm (Figure 6.13). EBIC measurements presented in chapter 4 have shown a very low lateral induction of signal (< 10 µm) and the deposition of the sensor on top of an integrated circuit permits the design of thin metal structures with little spacing (the limits being defined by the technology used for the development of the ASIC). The strip structures are thus integrated in order to study the potential of TFA technology for high resolution strip detection. Each strip is connected to an integrated aSiScope pre-amplifier. Some of the pre-amplifiers have an integrated injection capacitance also connected at their input to permit an electrical characterization. Cross-talk between pre-amplifiers has been tested by injecting a signal on the input of a pre-amplifier connected to one of the strip via its integrated injection capacitance and by measuring the output response of this pre-amplifier and of the neighbouring pre-amplifier connected to another strip. Results obtained are presented in Figure 6.13.

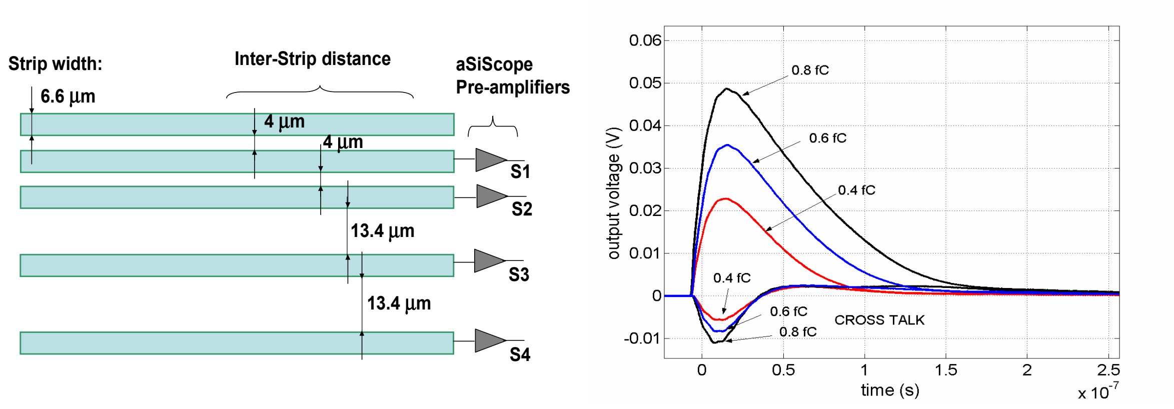

Figure 6.13. left: Schematic of the 4 strips under test. Each strip is connected to an aSiScope integrated pre-amplifier. Right: Electronic cross-talk between channels: impulse response of a pre-amplifier and signal induced on a neighbouring pre-amplifier.

Measurements with the Ni^{63} source have been performed on a 20 µm thick sample for a 240 V reverse bias applied to the sensor. Output signals of the 4 strips were directly readout on an oscilloscope in self trigger mode, the triggering being done on the strip S2 (Figure 6.14), S1 or S3 (Figure 6.15). Signals induced on the triggered strip by electron tracks through the a-Si:H sensor are readout, together with signals induced on neighbouring strips. Results obtained by triggering on S2 are presented in Figure 6.14.

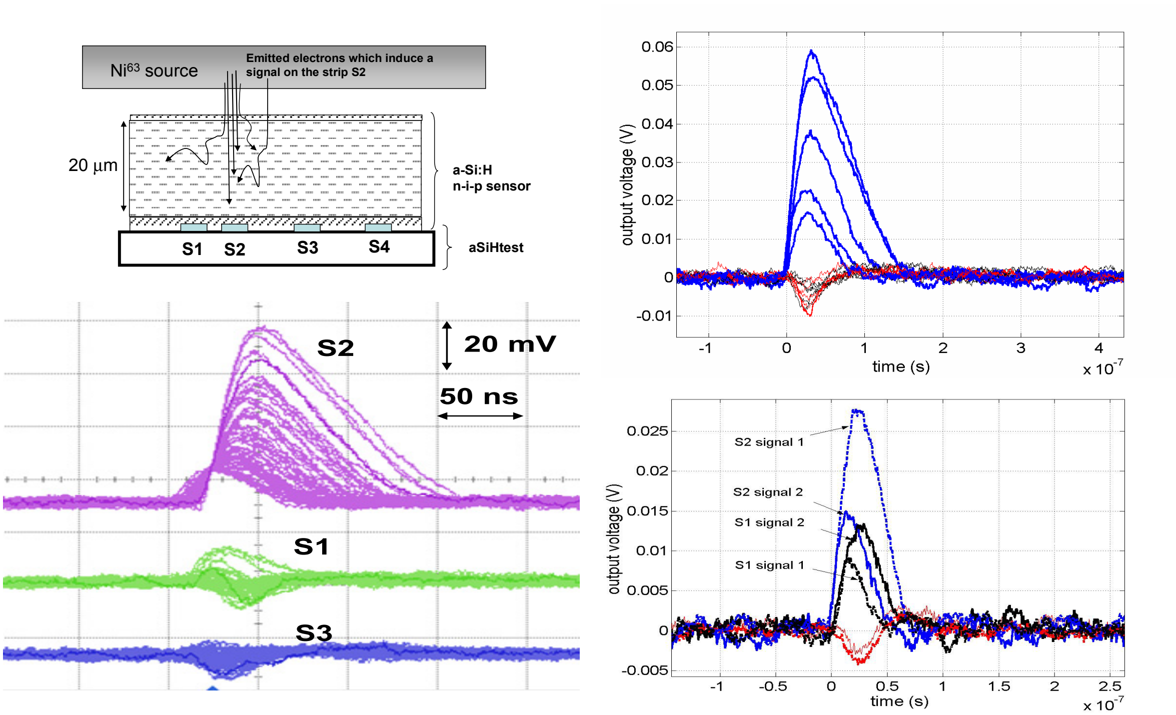

Figure 6.14. Signal created by keV electrons in a 20 µm thick a-Si:H sensor deposited on an aSiHtest circuit. The sensor is reverse biased with 240 V and readout is done on 3 strips, with trigger on S2. Left: ~ 100 superimposed signals created by electrons. S2 shows the sensor response to the distribution of electrons from few keV to ~ 50 keV, S1 and S3 show cross-talk on neighbouring strips. Right top: Cross-talk for 5 signals, representative of most of signals readout. Right bottom: representation of few signals observed with charge readout on both strips S1 and S2.

Most of the electrons which induce a signal on the strip S2 do not induce significant signal on the neighbouring strips S1 and S3. The observed signals (Figure 6.14) are in agreement with the cross-talk between the pre-amplifiers (Figure 6.13). In few cases, a signal is observed on S1 when triggering on S2. These events are rare (Figure 6.14) and correspond to signals with low amplitude induced on S2. These signals can be explained both by the non-collimated nature of the source and by the tortuous path of electrons in matter: electrons emitted from the source can have a track through the a-Si:H sensor covering the 2 strips so that a signal can be induced on the 2 strips. This effect is observed for less than 15 % of the cases, for strips separated by only 4 µm.

Similar measurements have been performed by triggering on the strip S1 or on the strip S3 and results are presented in Figure 6.15. The sensitivity of these strips to particles is demonstrated and similar signals are observed on the neighbouring strips as it has been observed in the tests done triggering on S2. High amplitude signals (V_{out} > 30 mV) induced on a strip correspond to electrons which do most of their track above S2 and signals observed on neighbouring strips are just caused by the cross-talk between the pre-amplifiers. Few signals are shared between 2 strips, and this is observed only for strips separated by 4 µm. These signals most probably correspond to electrons having a track above the two strips, and do not correspond to a lateral induction of signal.

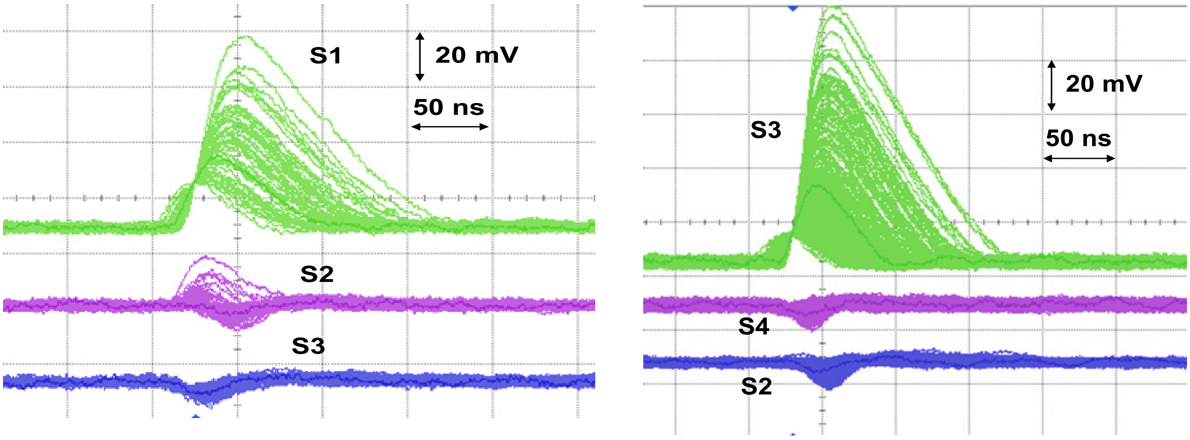

Figure 6.15. Similar tests than in Figure 6.14 but with trigger on the strip S1 (left) and on the strip S3 (right).

The movement of the generated carriers is defined by their drift under high electric field. These results obtained with low energy electrons (which even have an intrinsic property of having tortuous paths through silicon) show a low lateral induction of signal which is difficult to explain and whose causes have not been identified. These measured properties show a very interesting potential of TFA technology for high resolution strip detection.

The total signal induced on the sensor bottom electrodes by the interaction of charged particles in the a-Si:H sensor can be calculated from the simplified model presented in section 6.2. The electron-hole pair generation profile in the sensor is needed together with the signal induced by generated electrons and holes because of the low shaping time of the pre-amplifiers (~ 25 ns). For low energy electrons, a simplified model of interaction in a-Si:H has been presented in section 6.2 and the energy loss profile in the sensor can be calculated with equations 6.3 and 6.4. Signal created by electrons can be expressed as a charge in our tests, as the shaping time of the pre-amplifier is higher than $3\times\tau_c$. The signal induced by holes is difficult to calculate: no analytical expression of x(t) or $v_{drift}(t)$ can be obtained because of exponential integrals in equation 6.12, and the signal induced strongly depends on 3 parameters which have not been determined experimentally in our tests: μ_0, ω_0 and E_0 (which define the hole dispersive drift mobility presented in equations 6.8 and 6.9). However, as it has been presented in section 6.2, the signal induced by holes is slow and for shaping times of the pre-amplifiers of ~ 25 ns, only a small part of the signal from holes will participate to the total signal. This contribution is very field dependent and thus dependent on the position inside the sensor.

First estimations of the signal created by keV electrons in an a-Si:H sensor are presented in this section by neglecting the signal induced by holes and by considering only the signal created by electrons.

$$Q_E = \int_0^d \frac{E \cdot g(x,E)}{W} \frac{q \cdot (d-x)}{d_{tot}} \, dx \qquad (6.20).$$

The function g(x,E) is the generation profile of keV-electrons in a-Si:H (equation 6.3), W is the mean pair creation energy and is taken between 4.8 and 6 eV, d is the depleted thickness and d_{tot} is the total thickness of the sensor. Calculations of the charge created by low energy electrons (from 5 to 60 keV) have been performed using the charge being expressed in electrons) are presented in Figure 6.16.

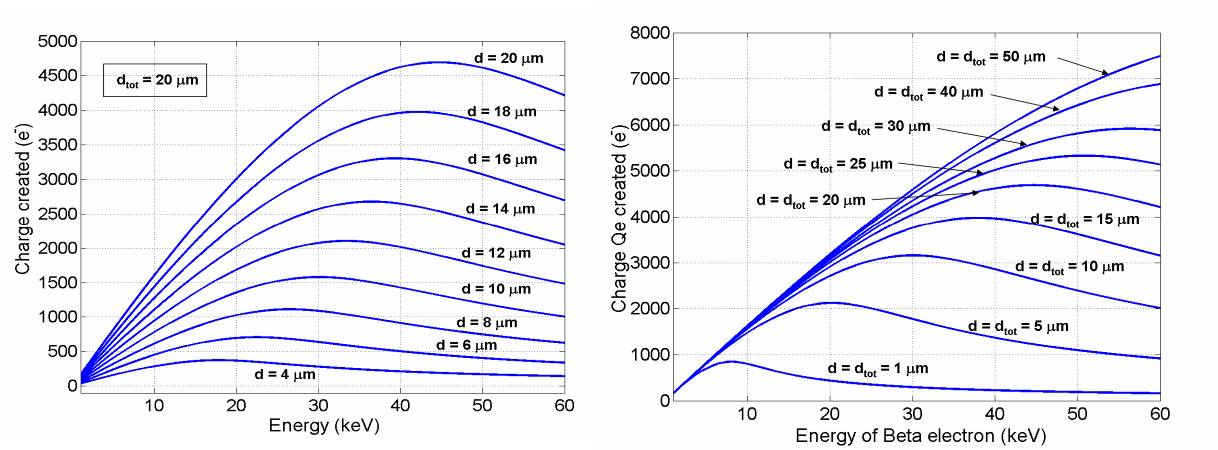

Figure 6.16. Calculated charges created by low energy electrons (5 to 60 keV). Left: For a 20 µm thick sensor with different depleted thickness. Right: For a d_{tot} µm thick sensor fully depleted.

It can first be noted that for different depleted thicknesses the maximum signal is created by electrons with different energies: a maximum of ~ 4700 e^- is created for a fully depleted 20 µm thick sensor by ~ 45 keV electrons, while ~ 2990 e^- and ~ 1580 e^- are respectively created for d = 15 µm and d = 10 µm by 38 keV and 30 keV electrons (Figure 6.16 left). Similar behaviour is observed for a fully depleted sensor with different thicknesses (Figure 6.16 right). The exact charge created corresponds to the charge calculated multiplied by W/W_{eff}, where W_{eff} is the effective mean pair creation energy. Contribution from holes must also be added. For $\mu_0 = 1$ cm^2 V^{-1} s^{-1}, $\omega_0 = 10^{11}$ to 10^{12} s^{-1} and $E_0 = 5.7\times10^4$ V/cm, a ratio of charge induced by holes over charge induced by electrons of ~ 15 to 5 % has been calculated for a 20 µm thick sensor with a 240 V reverse bias and for a pre-amplifier peaking time of 25 ns, using the model presented in section 6.2.

The peak amplitudes of the signals created by low-energy electrons in the 20 µm thick TFA detector were recorded by a customized labview program. The program displays waveforms and histograms of the distribution of peak amplitudes. The peak amplitudes are calculated and recorded with the signal baseline. Measurements were performed for different sensor reverse biases (from 60 V to 240 V) and the different distribution of equivalent charge readout are presented in Figure 6.17 (the conversion from peak amplitude to charge readout was done in the same way as it was presented in section 6.2 for the laser measurements). The maximum signal created scales with the detector reverse bias. This maximum can be compared with theoretical predictions based on the model presented before. Charge created by 5-60 keV electrons in a 20 µm thick a-Si:H sensor has been calculated for different depleted thicknesses and results are presented in Figure 6.16 left. In these calculations, W = 6 eV and using $N_{db}^{*} = 6.1\times10^{14}$ cm^{-3} (extracted value from laser measurements) the reverse bias of the sensor can be linked to the depleted thickness.

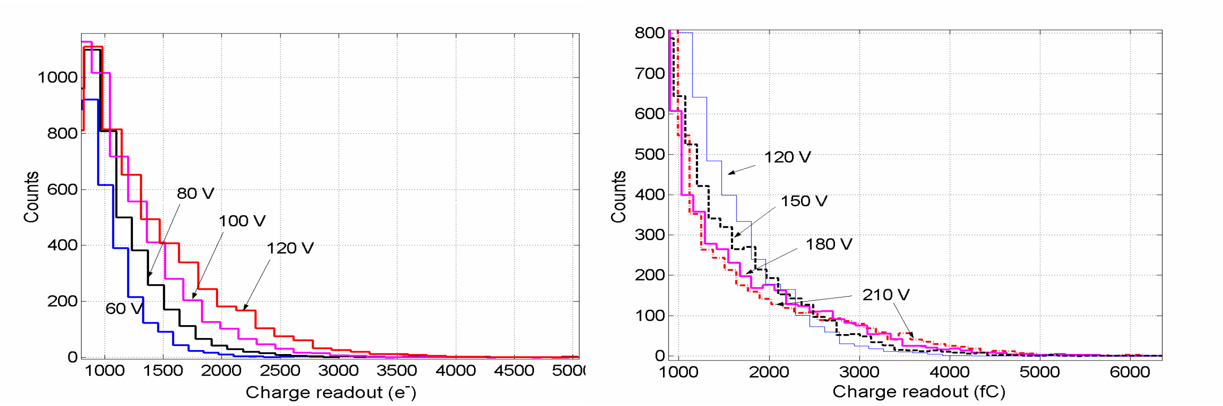

Figure 6.17. Charge created by electrons emitted from a Ni^{63} source in a 20 µm thick TFA detector. Similar acquisition time was used for all measurements presented.

The expected maximum signal created by electrons with energy ranging from few keV to 60 keV in the a-Si:H sensor under test can be calculated for the different reverse biases applied to the sensor and are listed in table 6.2. These calculations can be compared to the experimental maximum signal. The maximum cannot be measured with high accuracy and the values listed in table 6.2 have an uncertainty of ± 10 %.

Voltage	60 V	80 V	100 V	120 V	150 V	180 V	210 V	240 V
Calculated max. (e$^-$) w. W = 6 eV	1910	2410	2860	3300	3940	4540	4700	4700
Measured Max. (e$^-$)	~ 2300	~ 3200	~ 3700	~ 4200	~ 5000	~ 5900	~ 6300	~ 6600
Ratio meas./calc.	1.2	1.3	1.3	1.3	1.27	1.3	1.34	1.4

Table 6.2. Calculated and measured maximum signal created by electrons from Ni^{63}.

The ratio measured over calculated maximum is higher than 1 and globally constant until depletion voltage. The difference originates principally from the fact that holes contribute to the signal, even though their contribution is restricted because of the short shaping time of the pre-amplifiers, and from a pair creation energy W that might be lower than 6 eV. Contribution from holes is increased as the reverse voltage is increased, as their velocity is increased. In the short shaping time holes will drift on a longer distance inducing a higher signal, explaining the increase of measured maximum even if full depletion of the sensor is achieved. This contribution strongly depends on different unknown parameters and can be approximated in our case between 5 to 15 %. Measurements and calculations then lead to a mean pair creation energy $W = 5.4 \pm 0.8$ eV which corresponds to the broad distribution of the value found in the literature (W = 4-6 eV). The extraction of W from measurements with low energy electrons is then difficult, moreover because of the tortuous paths of keV electrons in matter. It can also be noted that the pixel under study has an opening inside the metal pad, so that particles which hit the sensor on the pixel edges might induce different signals.

Another Beta source emitting electrons from few keV to few MeV (Sr^{90}) has been used to study the detection feasibility of MIPs on the 20 µm thick samples. Spectrum obtained is presented in Figure 6.18. No peak is observed thus in a first time indicating a non-complete detection of MIPs (a peak is expected at low charges corresponding to electrons with energies ranging from 500 keV to few MeV). Most of the signals readout can then be attributed to low energy electrons.

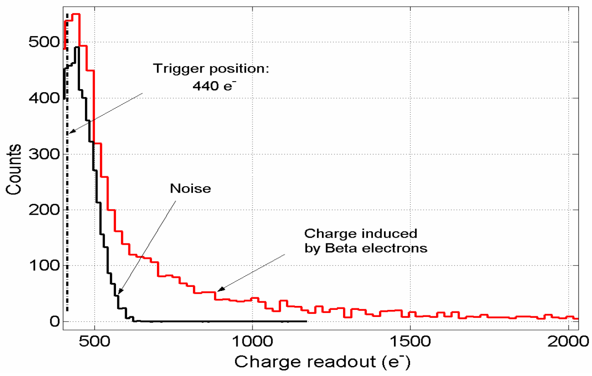

Figure 6.18. Distribution of charge induced on a 2070 μm^2 pixel by electrons from a Sr^{90} source in a 20 μm thick sensor reverse biased with 240 V.

Calculations performed in section 6.2 lead to an estimated dE/dx for a MIP of about 0.36 keV/µm. A MIP is thus expected to lose about 7.2 keV in a 20 µm thick sensor. A MIP leads to a constant distribution of the generated electrons in the sensor, so that the signal induced by the movement of these electrons will be exactly of half the total number of generated electrons. For W = 6 eV the signal created by generated electrons corresponds thus to ~ 600 e^-. Such signals could be sensed with the detector tested, even though close to the noise resolution of the pre-amplifier. Signals created by MIPs might be covered by low amplitude signals created by low energy electrons. The pixel under test has an area of 2070 μm^2 and has an opening in the passivation layers inside the metal pad. This can lead to a high proportion of low signals (around 600 e$^-$) induced by electrons having part of their track above the pixel active area or at the pixel periphery. Unfortunately, there was no possibility to perform a triggering of signals from the back as it has been performed on the AFP sample (section 6.1) as test samples were mounted on a PCB without the hole needed for such tests. It is then difficult to conclude about MIP detection from the measurements performed on the 1st serie of samples deposited on aSiHtest integrated circuits. These samples were deposited using a reactor not dedicated to the deposition of thick layers so that maximum layers of 20 μm have been deposited. A second serie of samples that could be deposited using the new reactor system still under optimization at the IMT would permit to deposit thicker layers. The study of charge readout for a MIP necessitates samples with different thicknesses ranging from 30 μm to 50 μm (giving rise to an expected charge of more than 900 e$^-$ to 1500 e$^-$).

6.3.3. Detection of 5.9 keV X-rays

The 1st series of sensors deposited on aSiHtest integrated circuits have also been characterized for electromagnetic radiation detection. Contrary to charged particles, the interaction is in this case localized. The probability of a photon to interact at a position x in the sensor has been presented in section 6.2. Tests have been performed using a Fe^{55} radioactive source. The source emits 5.9 keV X-rays [Ber] which have a $\mu \sim 3\times10^2$ cm^{-1} in a-Si:H so that its probability of interaction in the 20 μm thick sensor decreases with the depth x in the sensor. 10 % of the emitted X-rays are absorbed in the first 3 μm of the sensor and 50 % is absorbed in the 20 μm. At such energy, a photon is completely absorbed by photoelectric absorption in the sensor and generates an electron-hole pair. The electron is released with an energy given by the difference between the primary photon energy and the energy needed to create the electron-hole pair. The photo-electron subsequently loses its kinetic energy in the detector by phonon excitation and ionisation, and the mean pair creation energy W can thus be used to determine the mean number of electron-hole pairs created. A 5.9 keV X-ray is then expected to create in a localized space from 1230 to 980 electron-hole pairs for W = 4.8 to 6 eV.

Results obtained with the Fe^{55} source on the 20 μm thick sensors deposited on aSiHtest circuits are illustrated in Figure 6.21. No signal is observed for a reverse bias lower than 200 V as created signals are too small. For a reverse bias of 240 V, signals are observed with a maximum induced charge of about 1000 e$^-$. The distribution of charges readout is covered by the noise of the system, but from the extrapolation shown in Figure 6.19 one can expect a peak of created charge at about 600 e$^-$.

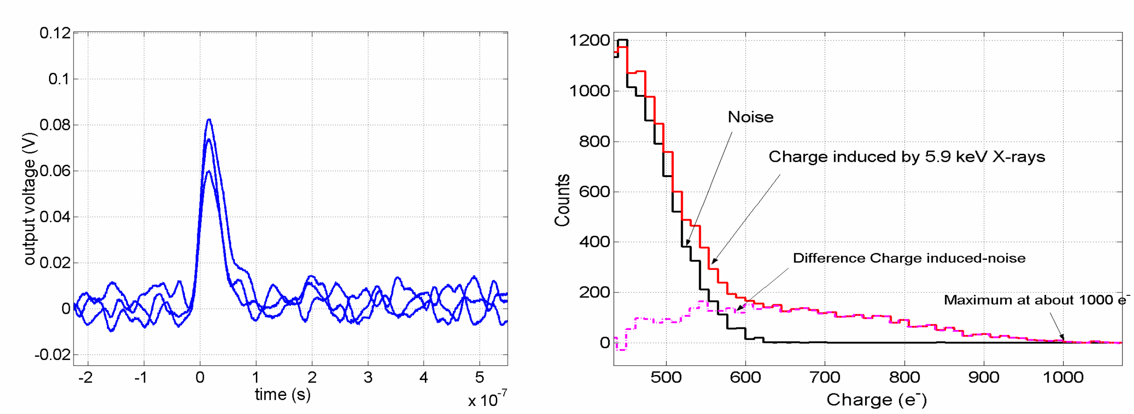

Figure 6.19. Signals created by 5.9 keV X-rays in a 20 µm thick sensor deposited on an aSiHtest circuit. Left: 3 signals created recorded in single shot. Right: Distribution of induced charge and distribution of noise acquired with and without source in a similar duration of data acquisition, and extrapolated peak.

The charge induced by the interaction of an X-ray in the TFA detector depends on the depleted thickness of the sensor and on W, and would be constant for a long shaping time and no trapping of holes. However, the pre-amplifier used has a short shaping time in comparison to the hole drift time, so that the signal at the output of the pre-amplifier depends on the location of interaction and on signals induced by electrons and by holes. Given the fact that electrons are expected to drift on the entire depleted thickness during the pre-amplifier shaping time and that holes drift on a small distance during that time, maximum signals will be created in the case of a photon interacting close to the p-i interface. As the photon interacts further into the sensor, lower signals will be induced. The maximum signal readout of 900 to 1000 e^- is then created by 5.9 keV X-rays interacting close to the p-i interface. The signal is in this case for the most determined by the motion of the generated electrons and a charge close to q·N (N being the number of electron-hole pairs created) is expected. This is confirmed by our measurements, and the measured maximum of about 1000 e^- is in agreement with the expected N of 980 to 1200. The signal induced by the motion of the generated electrons can be defined by equation 6.7. The peak charge, if neglecting signal from holes, corresponds to X-rays interacting at $x_0 \sim 7$ µm (calculated from expected N and from the 600 e^- charge corresponding to the peak). This is in agreement with the average location of creation of X-rays.

Similar measurements have been performed on a TFA detector based on a different integrated circuit called MACROPAD developed at CERN. The MACROPAD circuit consists of 48 octagonal pads with about 140 µm width and 380 µm pitch, each pad being connected to a transimpedance amplifier followed by a shaper stage. The circuit has a peaking time of about 160 ns and an ENC down to 27 e^- rms can be achieved [Mor04]. Measurements have been performed on a 15 µm thick sensor deposited on top of a MACROPAD circuit, for a 145 V reverse bias applied to the sensor [Mor04]. For such bias, the sensor leakage current increases the detecting device noise and the TFA detector presents then an equivalent noise charge of about 42 e^- rms. A clear peak distribution of charges created by 5.9 keV X-rays from a Fe^{55} source into this TFA detector has been observed (Figure 6.20). A maximum signal at about 1000 e^- and a peak at about 660 e^- were observed [Mor04], which are in agreement with results obtained in this thesis work with TFA detectors based on aSiHtest circuit. The higher value of the peak is consistent with the reduced thickness of the sample as the average distance at which interact X-rays in the sensor is reduced.

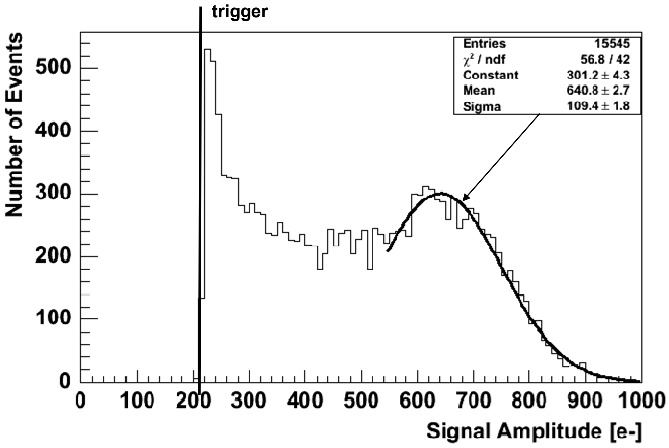

Figure 6.20. Distribution of charges induced by 5.9 keV X-rays in a 15 μm thick sensor deposited on a MACROPAD circuit, reverse biased with 145 V [Mor04]. The measurement threshold is at 200 e^-.

Results obtained show the feasibility of detecting low energy X-rays with TFA detectors. However, an important characteristic of the a-Si:H sensor for X-ray detection is that the created signal depends on the location of creation of the electron-hole pairs. As X-rays have a localized deposition of energy, the amplitude of the signal induced depends on where the photon interacts. Photons interacting in the first microns of the sensor (i.e. close to the p-i interface) will create higher signals than photons interacting further into the sensor because of shaping times faster than the slow transport of holes.

6.4. Conclusions

Radiation detection with TFA detectors has been characterized on different detectors and the mechanisms involved in the creation of a signal have been studied in detail in order to understand the performance and limitations of TFA detectors. The feasibility of detecting charged particle has been first demonstrated by preliminary measurements performed on detectors based on the AFP integrated circuit. Beta electrons with energies of 10 to 50 keV have been detected with a shaping time of 5 to 10 ns.

The signal created by the interaction of a radiation in the a-Si:H sensor first depends on the radiation energy loss profile in the sensor and on the mean pair creation energy W, i.e.

it depends on the distribution of the generated electron-hole pairs in the sensor. The total charge generated is equivalent to the sum of the charge created by the motion of electrons and by the motion of holes. For pre-amplifiers with a shaping time of few tens of ns, the charge induced by the generated electrons is expected to be complete. However, only part of the charge induced by the generated holes is integrated because of the slow transport of holes. This represents a first important limitation of the detection.

Measurements have been performed with low energy electrons (10 to 50 keV) on 20 µm thick sensors deposited on aSiHtest integrated circuits. Characterizations performed on 6.6 µm wide strips with a minimum inter-distance of 4 µm show a low lateral induction of signal in this detector. Electrons having a track above the strip under test induce a clear signal on this strip (charge of few thousands electrons) while no signal is induced on neighbouring strips. These results show an interesting potential of the technology for the detection of low energy electrons and for building high resolution strip detectors.

The samples tested had a maximum thickness of 20 µm and no MIP detection has been proven on these samples. Thicker sensors are needed for an optimized detection. Signal induced by generated electrons is maximum for full depletion of the sensor, while the signal induced by generated holes for a short shaping time of the electronic readout will be maximum for a maximum reverse voltage applied to the sensor. The low hole mobility is strongly field dependent, so that the use of thicker sensors first enhances the detection efficiency by an increase of the interaction volume, but also permits to apply higher reverse voltages and to increase the signal induced by holes.

Finally, 5.9 keV X-rays detection has been demonstrated, with a peak at about 600 e^- and with a maximum signal created at about 1000 e^-.

7. Preliminary studies on the radiation effects on a-Si:H sensors

The radiation tolerance of a detector is a crucial parameter for its application in high energy physics experiments, where requirements become more and more challenging. a-Si:H could offer radiation hard alternatives to silicon devices. Its radiation hardness has been studied in the past in the context of testing solar cells for space applications (i.e. on sensors with a thickness of about 1 μm). It has been shown that proton irradiations [Kun03] or photon irradiations (involving the Staebler Wronski effect [Sta77, Bra98]) lead to a creation of metastable deep defects that can be annealed out, resulting in a good radiation hardness of the material in comparison to crystalline silicon.

Thick a-Si:H sensors (~ 30 μm) deposited either on a glass substrate or on an ASIC have been characterized in this thesis. It must be noted that the radiation resistance of thick a-Si:H sensors is a very deep, specific and complicated topic, and it has been little studied in the past. The objectives of the measurements performed in the frame of this thesis were to extract basic properties of radiation effects on an a-Si:H sensor. This study can thus be considered as preliminary and does not constitute a systematic study of the subject. This is further explained in section 7.1. Tests have been performed on sensors deposited on a glass substrate under a 24 GeV/c proton beam and results are presented in section 7.2. The radiation effects and their impact on the sensor performance are also discussed in this section. A TFA detector based on an AFP integrated circuit has also been tested under a 26 keV electron beam. Degradation and thermal annealing of the sensor have been studied and results are presented in section 7.3.

7.1. Radiation effects on detecting devices

In the Large Hadron Collider (LHC) experiments at CERN, particle detectors will be operated in a harsh radiation environment, characterized by the machine luminosity which is expected to be about 10^{34} $cm^{-2}\cdot s^{-1}$. The radiation environment in the experiments will be composed of neutrons, photons and charged hadrons, the proportion of the different particle species depending on the distance and on the angle with respect to the interaction point. The potential and the challenges of an upgrade of the LHC machine (Super-LHC or SLHC) to a luminosity of 10^{35} $cm^{-2}\cdot s^{-1}$ have been studied at CERN [Gia05, Mol05]. The radiation level that detectors will have to withstand is expected to be 10 times higher than predicted for the LHC and the inner tracking detectors will face fluences of fast hadrons up to 1.6×10^{16} cm^{-2} for a total accumulated dose of about 5 MGy assuming a five years operation [Mol05].

Radiation damages of a detecting device can be caused both by the Non Ionizing Energy Loss (NIEL) or the Ionizing Energy Loss (IEL) of the radiation traversing the device.
In NIEL interactions, the traversing particle displaces atoms of the detector from their lattice position, leading to the creation of defects in the structure which can affect the device properties. These effects are referred to as displacement damages and are responsible for the radiation damage suffered by silicon detectors [Mol99, Bat05]. This displacement damage will depend on the interacting particle type and energy, and on the accumulated fluence (i.e. number of interactions). These mechanisms have been studied in detail for silicon detectors and are usually normalised to the displacement damage caused by 1 MeV neutrons. The displacement damage cross-sections D in silicon of different particles, normalised with respect to 1 MeV neutrons (for which D = 95 MeVmb), are displayed in Figure 7.1. Silicon detector degradation can for most of the cases be linked to the displacement damage cross-section following NIEL hypothesis [Mol99, Bat05].

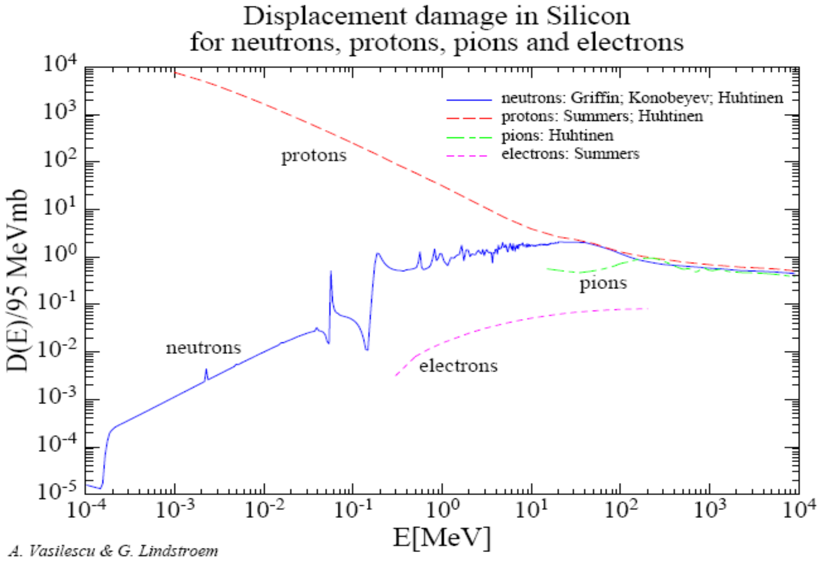

Figure 7.1. The scaling of the displacement damage in silicon with energy for neutrons, protons, pions and electrons [Vas00].

IEL interactions might also lead to a degradation of the device, as it has been presented for MOS transistors in section 3.1. The damage will depend on the ionization of the radiation which traverses the device and on the total dose deposited.

The radiation resistance of a TFA detector will depend on the resistance of the a-Si:H sensor, of the integrated circuit and of the global system. Radiation effects on integrated circuits have been widely studied and have been shortly presented in Chapter 3. The use of technologies with thinner and thinner gate oxides together with the use of specific design rules permits to obtain an improved radiation resistance of CMOS circuits (see section

3.1). The integrated circuits developed for this thesis work were designed with these specific design rules and in a 0.25 µm CMOS technology. These circuits are “test” circuits and aim to the characterization of the technology. They do not constitute circuits for TFA pixel detector prototypes and have thus not been tested under very harsh radiation environment in the frame of this work. However, the AFP integrated circuit has been tested up to 300 kGy and no degradation of the circuit response was observed [Ane03]. Resistance to 10 times higher doses seems realistic for such circuits, certainly more with the use of 0.13 µm CMOS technology that might be used in the future high energy physics experiments [Fac05].

Radiation effects on a-Si:H sensors have been little studied in the past and even less for sensors with a thickness higher than 10 µm. The tests performed in the frame of this work and presented in this chapter, and even though they do not represent a complete systematic study of the subject they contribute to the general knowledge on the radiation effects on a-Si:H sensor. The first tests have been done with irradiation of a-Si:H diodes with 23 GeV protons up to fluences of 10^{16} cm^{-2}. As it can be seen in Figure 7.1, these protons will create less displacement damages than protons with a lower energy, but their effect is relatively close to the reference 1 MeV neutrons in crystalline silicon. Results are presented in section 7.2. Tests have been performed with a scanning electronic microscope on a TFA detector in order to study the detector pixel segmentation. However, during these tests, degradation of the a-Si:H sensing device under 10 to 30 keV electrons has been observed, suggesting a degradation linked to IEL. Results obtained are presented in section 7.3. Moreover, the measurements performed show interesting localization and metastability of the defects created. These different experimental results presented in this chapter permit to extract the basic properties of radiation effects on an a-Si:H sensor.

7.2. 24 GeV/c proton irradiation

The evolution of the performance of an a-Si:H sensor in a high radiation environment has thus been studied by first testing sensors with a fast proton beam up to fluences of 10^{16} cm^{-2}, equivalent to the expected fluences after 5 years of operation of SLHC. The test structures characterized are n-i-p a-Si:H layers deposited on a Chromium coated glass substrate and are presented in detail in section 4.1. Radiation results obtained on a 32 µm and on a 20 µm thick sensor are presented in this section. Both samples have 2 mm × 2 mm square pixels, the active area being defined by the patterned transparent conductive oxide top electrode.

The a-Si:H sensors have been characterized at the CERN IRRAD 1 irradiation facility [Gla99] with a primary proton beam of the CERN Proton Synchrotron (PS). The protons have a momentum of 24 GeV/c (energy of about 23 GeV) and are directed to the irradiation area on the a-Si:H sensor. A remote controlled shuttle permits to move the sample to be tested from the counting room into the irradiation area. The PS proton beam is characterized by a 16.8 seconds supercycle, during which proton bursts are delivered in 1 to 3 spills of about 400 ms, with a maximal beam intensity of about 2×10^{11} protons per spill. A defocusing-scanning system is used to spread out the beam so that a uniform irradiation is achieved over a surface of about 2 cm × 2 cm [Rav04]. The proton fluence was measured during the tests by 2 different techniques. First, the total fluence corresponding to a test period was measured by evaluating the Na^{24} activity of aluminium foils that were introduced in the irradiation area during a fixed period of the irradiation. During the tests, several aluminium foils with an area of 5 mm × 5 mm were successively placed in the irradiation area in alignment with the pixel under test and then removed and measured, thus permitting to have an estimation of the total fluence of different periods of the irradiation with an accuracy of ± 7 % [Rav04]. Moreover, the proton fluence was measured by a Secondary Emission Chamber (SEC), giving a measurement of the fluence for each proton burst based on the whole beam size. The SEC data permits an online observation of the whole beam fluence and of its evolution, while the different aluminium foils permit a precise calibration of the proton fluence at the position of the pixel under study.

One of the two structures tested is presented in Figure 7.2, together with the measurement set up.

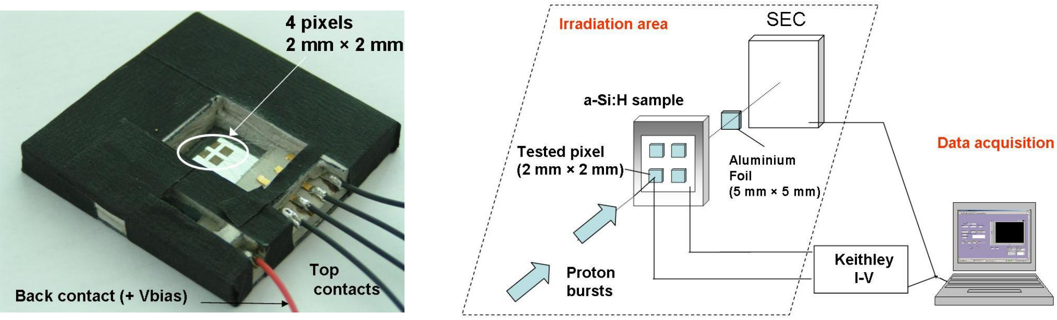

Figure 7.2. Left: Picture of an a-Si:H test structure used for the proton irradiation. Right: Test set up: each proton burst going through the a-Si:H sensor creates a current acquired by a custom labview program. The proton burst fluence is measured by both an aluminium foil and a SEC.

A Keithley 2410 source-meter permits both the application of a reverse voltage on the tested 2 mm × 2 mm pixel (a positive voltage is applied to the diode back contact connected to the n-layer) and the readout of the currents generated in the tested diode. A custom Labview program controls the Keithley and the SEC and permits the acquisition for each spill of the currents readout and of the SEC data.

The first sample tested is a 32 μm thick n-i-p a-Si:H diode. The pixel under test has an active area of 4 mm^2 and was tested under proton fluence up to 7×10^{14} protons/cm^2. The diode was reverse biased with 300 V and in dark condition at room temperature during the irradiations. The signal induced in the diode by a proton spill was measured for each spill and will be referred to as Proton Spill Induced Current (PSIC). The diode leakage current was also measured after different irradiations. The SEC count (proportional to the number of protons hitting it) was measured for each spill. The SEC data for 2500 spills is shown in Figure 7.3 left. The SEC data provides the information on the stability of the beam for each spill during the irradiation. The SEC data is then calibrated with the different fluences measured from the aluminium foils that were successively placed in the irradiation zone during the tests. The fluence versus spill number can then be extracted and is presented in Figure 7.3 right. In these first tests, the proton beam fluence was stable at about 10^{11} protons/cm^2 per spill. The irradiation tests were then done with a very high fluence rate of about 4.5×10^{13} protons/(cm^2·h).

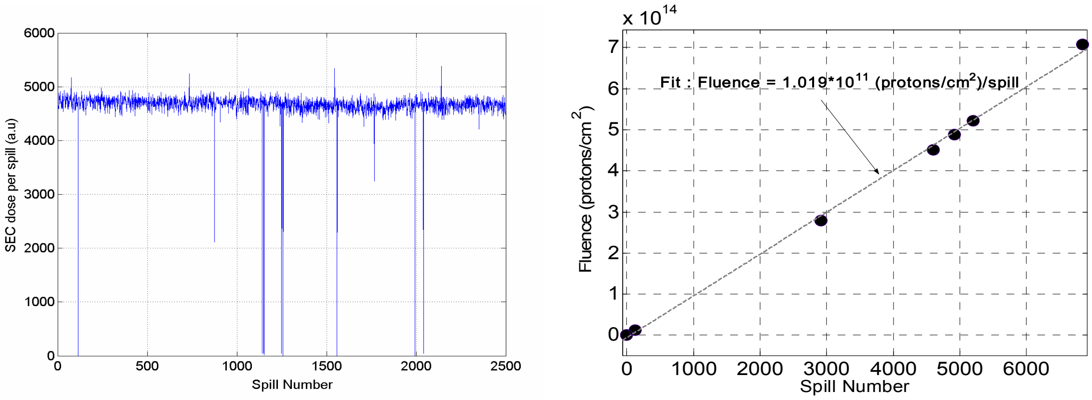

Figure 7.3. Proton fluence measurement. Left: example of SEC data, a stable SEC data for the different spills indicates a stable beam. Right: Fluence measured with the activation of 7 aluminium foils placed in the irradiation area and removed at different times versus the number of spills measured by the SEC.

The Keithley current meter was triggered by signals from the SEC, so that few points were acquired for each proton burst, corresponding to the signal induced in the detector. The PSIC was first analysed by averaging for each proton spill the currents induced in the sensor. The obtained results are presented in Figure 7.4 as a function of the fluence (the spill number being translated to the fluence via the relation shown in Figure 7.3 right).

An average PSIC of about 10 μA is measured for the first spills. The detector response decreases in a first time but an increase in the average PSIC is then observed up to a fluence of about 6×10^{13} protons/cm^2. For higher fluences, the average PSIC decreases with a log-log linearity (Figure 7.4 left). For a fluence of 5×10^{14} protons/cm^2, the average PSIC corresponds to about 50 % of the initial PSIC. At this stage, as it is indicated in Figure 7.4, the sample was placed out of the beam and kept under bias for 20 hours at room temperature. It was then placed back into the irradiation area where the average beam fluence per spill was similar. We observe that the average PSIC is back to about 60 % of its initial value, suggesting a self-annealing effect on the sample during the annealing time.

The diode leakage current was also measured after different irradiations, and results are presented in Figure 7.4 right. Proton irradiation leads to an increase of the leakage current of the tested diode (a factor 2 difference is measured for a fluence of 5×10^{14} protons/cm^2), which is consistent with an increased density of dangling bonds as leakage current is determined by field enhanced thermal generation. After the irradiation, thermal annealing tests have been performed on the irradiated sample while keeping it under bias. A reduction of the leakage current is clearly observed after 12 hours of annealing at 100 °C. After 24 hours of annealing, the sample is back to the pre-irradiation condition.

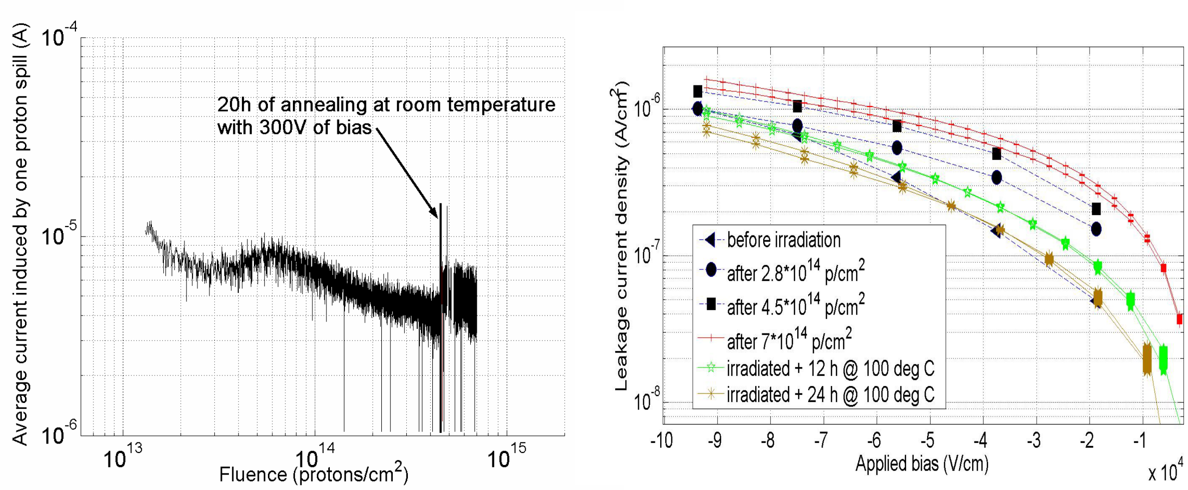

Figure 7.4. Left: Average PSIC induced by each spill versus the received fluence. Right: Leakage current of the irradiated diode after 3 steps of irradiation and after thermal annealing.

Variations of the average PSIC and of the leakage current are caused by variations of the density of dangling bonds. Deep defects are created by the irradiation and are metastable, i.e. their density is not fixed and can be varied by an external perturbation. Both decrease and increase of signal depend on this metastable defect density and will be discussed later.

The noise observed in Figure 7.4 left is caused by the fluctuations of the beam and mainly by the fact that only few points were acquired for each signal. The rate at which the data acquisition system can take data is limited, and only a few points (~ 50) can be taken during each spill. A typical signal shape during a spill is shown in Figure 7.5 left. The 50 acquired points are clearly not enough to sample accurately the signal shape. Fortunately, the labview program has a random time of acquisition, so that for each spill the different points acquired are separated by different times. Moreover, the first point acquired is defined by the trigger originating from the SEC, so that this first point is always the same for each spill data. The signals recorded for each spill have thus a similar starting point while the other points are separated from the triggering time by different times. This different time separation between acquired points permit to increase the number of points defining the PSIC by using data from several consecutive spills, the PSIC being considered constant within 100 to 200 spills. A PSIC can then be reconstructed more precisely by using several signals. A routine has been done on Matlab for this reconstruction and permits to reconstruct a precise signal from about 100 spills. It permits to have about 500 points per signal instead of 50 (Figure 7.5). The induced signal shape is presented in Figure 7.5 right, together with its integral.

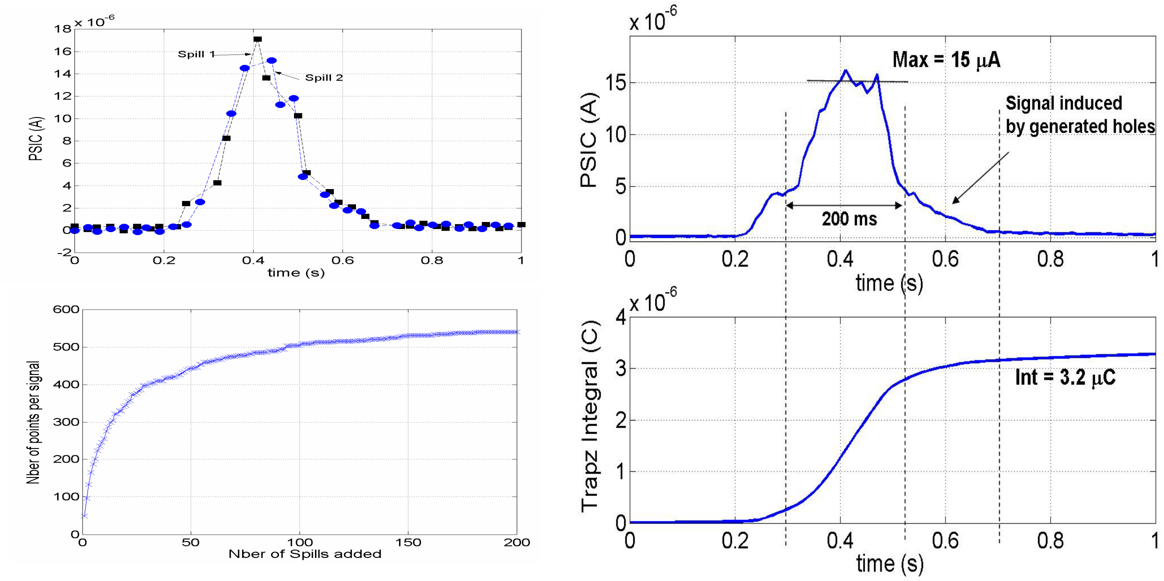

Figure 7.5. Reconstruction of Proton Spill Induced Signal. Left top: PSIC of 2 spills, showing the few points defining the PSIC. Left bottom: Number of points per reconstructed average PSIC as a function of the number of spills used for the signal reconstruction. Right: PSIC estimated using 100 spills (top) and its integral (bottom).

Analysis of the irradiation data has then been done by extracting the PSIC plateau (maximum) and integral, as presented in Figure 7.5, after different irradiations. Results are presented in Figure 7.6 left. The current induced in the diode has also been measured for different applied reverse voltages and results are presented in Figure 7.6 right.

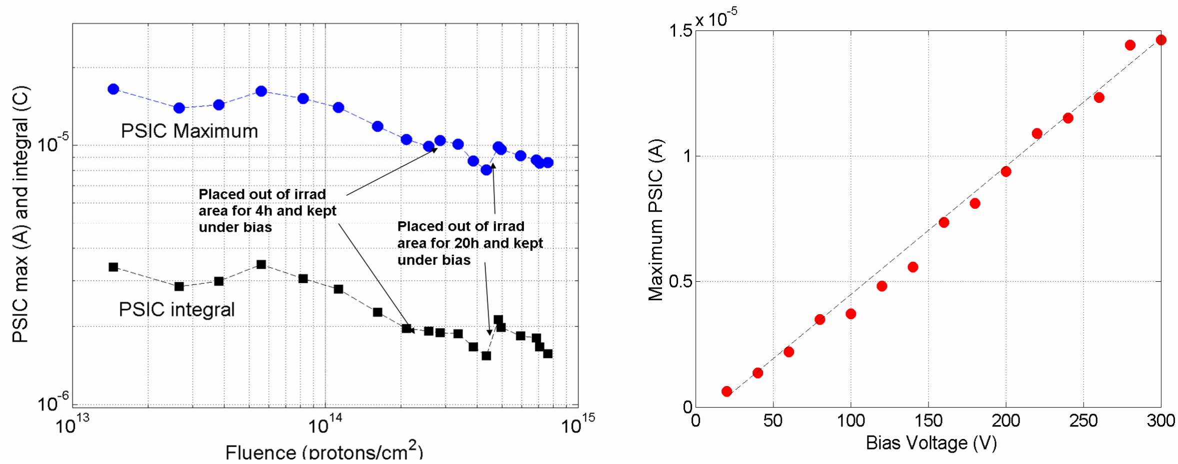

Figure 7.6. Left: Evolution of the PSIC signal plateau (maximum) and integral with the proton fluence. Right: Variation of the created current by the proton spill with respect to the applied reverse voltage (after a fluence of ~ 10^{14} protons/cm^2).

The obtained results are similar to the results presented in Figure 7.4 left. The proton irradiation induces first a slight increase of the PSIC up to about 6×10^{13} protons/cm^2, and then a log-log linear decrease so that at a fluence of 7×10^{14} protons/cm^2 the PSIC is about 2 times lower than after a fluence of 10^{13} protons/cm^2. The sample is removed twice from the irradiation area, and kept under bias, and presents an increased PSIC when it is placed back in the proton beam, showing an interesting self-annealing behaviour.

The observed variations of the created current with the applied reverse bias (Figure 7.6 right) are consistent with the model presented in section 6.2. The 23 GeV protons will go through the entire sensor without losing much of their energy. Their dE/dx can be estimated from the database [STAR05] by weighting the value for Silicon by the a-Si:H density. A dE/dx of about 0.38 keV/µm is estimated (corresponding to Minimum Ionizing Particles), so that an energy of about 10 keV is deposited in the sensor per proton. The signal created in the sensor will depend on the number of pairs generated by the protons and on the generated carrier velocity. The velocity depends on the electric field and so on the square root of the applied voltage. Moreover, the number of created pairs linearly depends on the depleted thickness which varies with the square root of the applied voltage. A signal varying linearly with the applied voltage is then expected for an under-depleted sensor and is observed in Figure 7.6 right, showing that at 300 V full depletion was not achieved. This measurement shows the variation of the PSIC for varying depleted thicknesses. The irradiation leads to a higher density of ionized dangling bonds which will lead to a lower depleted thickness of the sensor (this will be explained later) so that the PSIC will be reduced in the same way as it is shown in Figure 7.6 right.

A second sample has been characterized with the 23 GeV proton beam up to a fluence of 1.6×10^{16} protons/cm^2, and with a very high rate of 8×10^{13} protons/(cm^2·h). The a-Si:H sensor is 25 µm thick and a 4 mm^2 pixel has been tested with an applied reverse voltage of 250 V. An average fluence of the proton beam of 1.5×10^{11} protons/cm^2 was measured per spill from the SEC and aluminium foils data. The PSIC has been reconstructed from 100 spills measured at different fluences and results obtained are presented in Figure 7.7. The observed variations of the PSIC with the proton fluence are consistent with the results obtained on the first sample. A first slight increase in the PSIC is also observed here up to 3×10^{14} protons/cm^2. The signal degradation is then log-log linear with the fluence and the PSIC is reduced by a factor 5 after 1.6×10^{16} protons/cm^2. The sample was always kept in the proton beam without any annealing.

The self-annealing effect observed in the first sample suggests strongly different behaviour of the sensor degradation depending on the fluence dose rate of the irradiation. It must therefore be noted that the fluence rate during these irradiation tests were extremely high, as the expected accumulated fluence for 5 years of operation of tracking detectors for the Super-LHC was reached in less than 10 days.

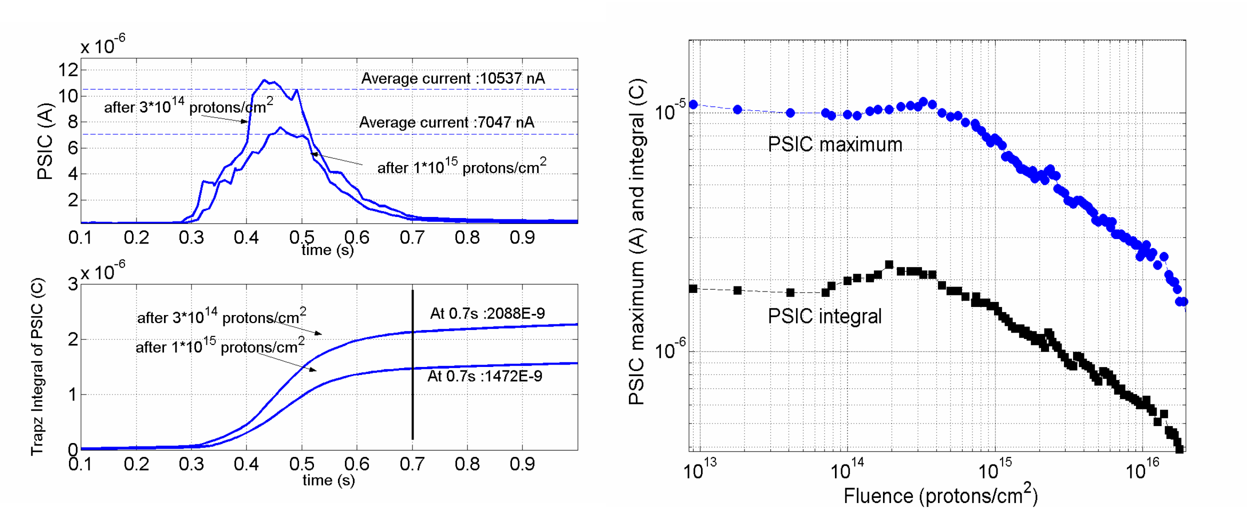

Figure 7.7. Left: Proton Spill Induced Signals after different irradiations. Right: Evolution of the PSIC maximum and integral with the proton fluence.

The variations of the signal induced by a proton burst with the accumulated fluence can be explained by the variation of defect density associated to the irradiation and by the metastability of this density.

Defects are created by the non-ionizing energy loss of the incoming particles (displacement of atoms) and by the ionization associated to the track of the particle in the sensor. In a-Si:H, some studies have shown that a creation of defects is attributed to ionization [Sro98]. Strong degradation of a-Si:H properties to light irradiation has been observed and characterized in the past 20 years and show an important creation of deep defects associated to the ionization. This effect (so-called Staebler Wronski effect) still presents controversial issues. It is nowadays associated to local breaking of “weak” Si-Si bonds and to changes in the short-range order of the material due to Si-Si bonds broken close to Si-H bonds [Gra01, Kol04]. The bond breaking appears to be linked to the energy released by the non radiative recombination of electron-hole pairs at spatially correlated tail states. To prevent the two neighbouring dangling bonds created from recombining, a neighbouring hydrogen atom moves and separates the two dangling bonds. The defect creation appears thus linked to ionization and recombination processes and hydrogen seem to play an important role.

The structural metastability of the material also leads to a possible reincorporation of the displaced atoms in the lattice by collective rearrangements of atoms. Some studies presented in [Kis98] have proposed that in the case of a proton irradiation, the proton produces a highly excited region around its track in the material which could cause the relaxation of the collisionnal displacements by causing structural rearrangements. This theory suggests a highly metastable property of the displacement damages in a-Si:H and that the energy associated to a proton track might be sufficient to recover locally some of the defects leading to a new metastable state. This can explain the surprising rise in the

PSIC we have measured on the two tested samples for fluences up to about 10^{14} protons/cm^2. Similar behaviour has been observed in measurements performed by Kishimoto where an increase of the irradiated detector photoconductivity was measured for fluences up to about 6×10^{13} protons/cm^2 [Kis98]. This can be explained by the fact that the incoming proton high electronic excitation might lead to local rearrangements of the structure and could lead to a reduction of the defect density at these fluences.

Radiation effects in a-Si:H are thus different from effects in crystalline silicon. IEL leads to an important creation of defects while in the case of proton irradiation, some of the displacement damages might be incorporated in the amorphous structure. Our results show a degradation of the a-Si:H sensor PSIC for fluences higher than 10^{15} protons/cm^2, which can thus be for the most linked to a metastable creation of deep defects from ionization.
Fluence was measured during the tests and can be linked to the deposited dose using the formula [Rav04]:

$$\text{Dose} = 1.6\times10^{-10}\times(\text{dE/dx})_m\times\Phi \qquad (7.1).$$

Φ is the proton fluence expressed in particles/cm^2, $(\text{dE/dx})_m$ is the mass stopping power expressed in MeV·cm^2/g and the dose is obtained in Gy (J/kg). For 23 GeV protons in a-Si:H, $(\text{dE/dx})_m \sim 1.8$ MeV·cm^2/g so that the dose is about $2.9\times10^{-10}\times\Phi$ Gy. Measurements have been performed up to a fluence of 1.6×10^{16} protons/cm^2 so up to a dose of 4.6 MGy (460 MRad). The pixel under study is 25 μm thick with an active area of 4 mm^2 so that the dose can be linked to the number of electron-hole pairs created (assuming W = 6 eV) and in our tests we have about 1.3×10^{15} e-h pairs/Gy.

Metastable deep defects are created by the irradiation, giving rise to enhanced densities of dangling bonds N_{db} and of ionized dangling bonds N_{db}^*. The sensor leakage current depends on both N_{db} and N_{db}^*, as it is mainly caused by field enhanced thermal generation. Higher N_{db} leads to a higher number of released trapped charges (i.e. to higher thermal generation), while higher N_{db}^* leads to higher internal electric fields in the sensor and at the p-i interface, thus increasing the leakage current by Poole-Frenkel mechanisms (section 4.3).
The current or charge created by a particle in the sensor also strongly depends on N_{db} and N_{db}^*. The defect density first determines the trapping time τ of the generated carriers, and τ has been observed to decrease linearly with the defect density [Ase99]. Moreover, the density of ionized dangling bonds determines the depleted thickness d of the sample and the internal electric field profile E(x):

$$E(x) = \frac{-q\,N_{db}^*}{\varepsilon_0\,\varepsilon_{aSi}}\,x + \sqrt{\frac{2\,q\,N_{db}^*}{\varepsilon_0\,\varepsilon_{aSi}}}\,\sqrt{V} \qquad (7.2); \qquad d = \sqrt{\frac{2\,\varepsilon_0\,\varepsilon_{aSi}}{q\,N_{db}^*}}\,\sqrt{V} \qquad (7.3).$$

An increase of the density of ionized dangling bonds then leads to a thinner depleted region if keeping similar biasing voltage V, but in higher electric fields in the depleted region. This increase in the electric field depends on the square root of N_{db}^*. The carrier drift length can be expressed for electrons as $L = \mu \cdot E \cdot \tau$, and electron mobility has been shown to be constant under irradiation [Wyr05]. L will depend on the inverse of square root of N_{db}^* and so does d (equation 7.3), so that irradiation should not increase electron trapping in dangling bonds as the trapping time is decreased and as the drift velocity is increased. The situation for holes is different because of the dispersive mobility and because of the higher defect density in the valence band tail, so that hole trapping should be enhanced by irradiation. A very important effect of the irradiation is then the decrease of the depleted thickness, which leads to a signal linearly decreasing for increasing N_{db}^*, the variations being similar to the linear variations of the PSIC for varying detector bias presented in Figure 7.6 and explained before. The inverse of the dangling bond density might thus vary with the proton fluence in a similar way than the PSIC because of the depleted thickness reduction for increased N_{db}^*.

Important thermal annealing effects have also been demonstrated in the studies presented in this section. After thermal annealing most of the created defects can be recovered while some observations suggest an annealing effect even at room temperature. In the thermal annealing process, the hydrogen atoms might move and revert back to their pre-irradiation positions. Hydrogen is thus most probably involved both in the defect creation and annealing [Kol04].

7.3. EBIC measurements: keV electron irradiation

The mono-energetic keV electron beam from a Scanning Electron Microscope (SEM) has been used to characterize a-Si:H sensors and TFA detectors. The homogeneity and the edge effects of a 32 µm thick a-Si:H sensor deposited on a glass substrate have been studied together with the pixel segmentation of a TFA detector based on a 32 µm thick a-Si:H sensor and on an AFP integrated circuit. The measurement technique and the results are presented in chapter 4. During these characterizations, an important degradation of the sensor response to the electron beam has been observed after a prolonged time of the sensors under the beam, reinforcing the idea of a dominant defect creation linked to ionization. The scanning area can be varied and scans on different areas of the sensors with different intensities of the beam have been performed.

A first characterization has been done on a 4 mm^2 pixel of the test structure. A prolonged scan of about 10 minutes has been performed on a corner of the pixel with a 26 keV electron beam with an intensity of about 6300 pA, so that this area of the pixel suffered an irradiation with about 2×10^{13} electrons (corresponding to about 1.6×10^{15} electrons/cm^2). A zoom out was then done so that the electron beam was scanning the whole pixel and an

EBIC image has been taken, the different colours showing the detector response amplitude to the injected electrons. The EBIC image is shown in Figure 7.8 left. Without irradiation, homogeneity of the detector response has been shown in section 4.2. Here, a grey region is clearly observed corresponding exactly to the irradiated area.
The pixel edge has been studied and the EBIC image obtained by scanning a small part of the pixel has been presented in section 4 (Figure 4.10). The beam was then kept in this position for a prolonged time and a zoom out was performed after around the scanned zone. The EBIC image obtained is presented in Figure 7.8 right and shows a strong degradation of the detector at the place where the prolonged scan was performed (black region in comparison to white region around).

These studies demonstrate a strong degradation of the signal creation in a-Si:H after 26 keV electron beam irradiation. All electron energy is deposited in the sensor (section 6.2) so that a mean number of 4300 electron-hole pairs are created by an injected electron for mean pair creation energy of 6 eV. The irradiation of the corner of the pixel corresponds to about 10^{17} pairs created and to an accumulated dose estimated at about 1.6 MGy (160MRad). The degradation is very localized as it can be seen from the EBIC images of the pixel edge. The signal decreases because of the creation of a high quantity of metastable defects linked to the ionization process. This leads to a decrease of the depletion region and to increased recombination of the generated carriers.

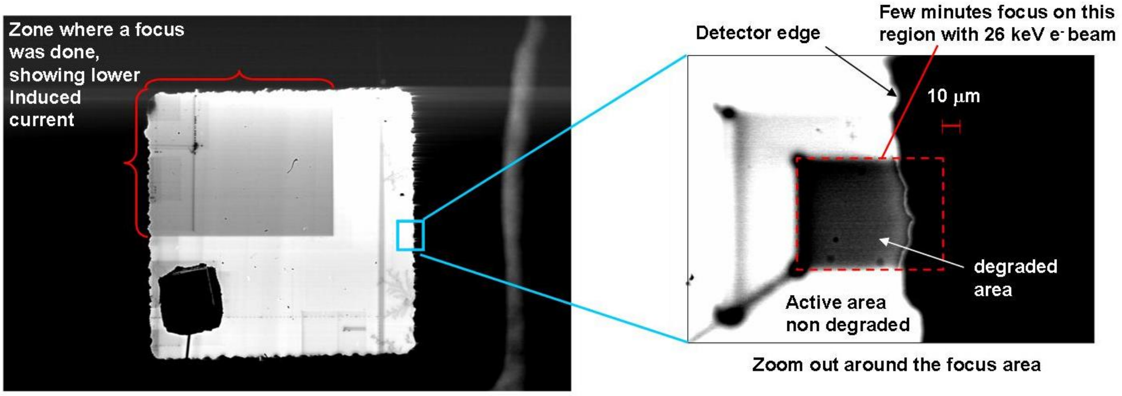

Figure 7.8. EBIC images of a 32 μm thick a-Si:H sensor deposited on a glass substrate, obtained with a 26 keV electron beam for a 250 V reverse bias applied on the sensor. Left: Full pixel with the top left corner which suffered an irradiation with about 2×10^{13} electrons. Right: Zoom out of the pixel edge after a closer prolonged zoom on the area indicated, for which strong degradation is observed.

Similar measurements have been performed on the TFA detector based on an AFP integrated circuit. 32 pixels are located in the center of the circuit, and the electron beam scanning area can be well defined (tens of nm precision), so that only few pixels were irradiated by the electron beam during this study (Figure 7.9 left). This permits to have on the same detector irradiated and non-irradiated pixels. The EBIC image obtained before irradiation on 2 pixels is shown in Figure 7.9 right, where the enhanced currents created at the pixel edges and corners can be seen.

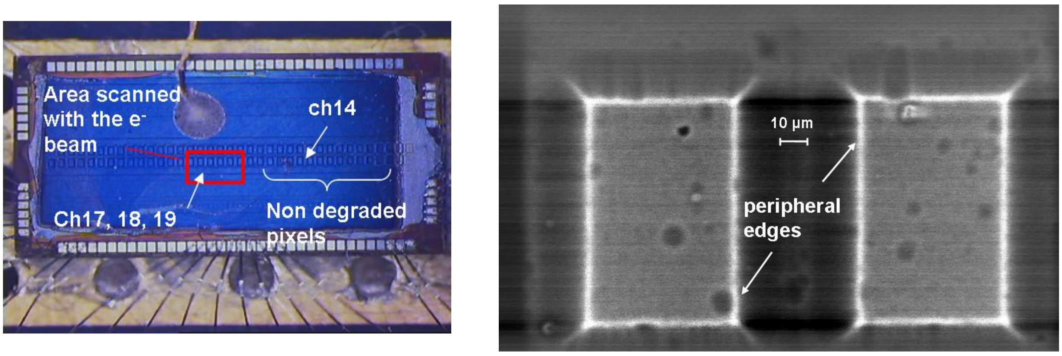

Figure 7.9. Left: TFA detector which consists in a 32 µm thick a-Si:H sensor deposited on an AFP circuit. Only 6 of the 32 pixels of the detector were placed under the e^- beam during the study. Right: EBIC image obtained before prolonged irradiation on 2 pixels.

The electron beam was then focused on a 135 µm × 105 µm area, covering one pixel and the sides of the neighbouring pixels. The beam was set to an amplitude of 1750 pA for electrons with 26 keV energy and was kept for 8 minutes on the selected area. This corresponds to an irradiation with about 5×10^{12} electrons and to a fluence of about 3×10^{16} electrons/cm^2. Scans of the 2 pixels were then performed and the 2 EBIC images obtained are presented in Figure 7.10.

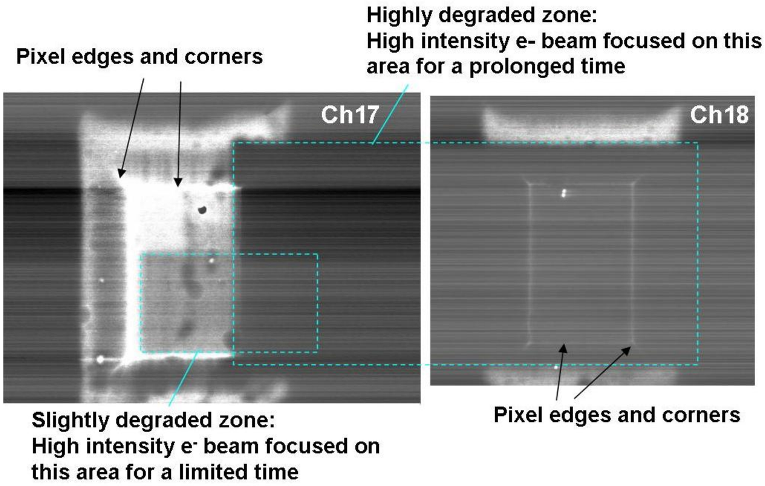

Figure 7.10. EBIC images of 2 pixels (Ch17 and Ch18) after a prolonged scan of the 26 keV electron beam in the area indicated in the images. The estimated fluence of the electron irradiation is of 3×10^{16} electrons/cm^2.

The area corresponding to the irradiated zone of the pixels shows a very high degradation, with a reduction of induced signal (and thus of colour) of more than an order of magnitude. Here again, the location of the degraded area exactly corresponds to the area scanned for the prolonged time. A very high creation of defects is associated to the irradiation with keV electrons. The observed degradation of the signal induced is higher than the degradation observed with the 23 GeV protons for close fluences. The ionization energy deposited per particle is different in the two cases, as a 26 keV electron deposit about 4.3 keV while a 23 GeV proton deposits about 1.8 keV for a similar sensor. The observed differences show a strong creation of deep defects linked to the ionization in a-Si:H. The observed differences might also be explained by the effects associated to the proton irradiation presented by Kishimoto and mentioned in section 7.2. The proton could provide along its track a sufficient energy to recover some of the created defects, while electrons do not provide sufficient energy to the lattice for these structural rearrangements.

The tested TFA detector was then characterized after the irradiation with a 660 nm pulsed laser in order to compare the signals created in the irradiated pixels, namely Ch17, Ch18 and Ch19, and in one of the non-irradiated pixels, Ch14. It must be noted that most of the damages created by the electron beam are located close to the p-i interface, as 20 keV electrons have a mean range of 5 µm (ionizations occurred close to the interface, section 6.2). The 660 nm laser has a mean free path of 1 µm in a-Si:H, so that electron-hole pairs will be generated close to the p-i interface, i.e. at the same location where were created the defects by the irradiation. The laser measurement set up is presented in section 5.1, and the laser was successively oriented on the 4 pixels. The degraded pixels show a much lower response to the laser pulse than the non irradiated pixel (Ch14). In order to observe significant signals from the irradiated pixels, the laser pulse width and amplitude were increased. Responses of the 4 channels to a similar laser pulse are shown in Figure 7.11, for a detector bias of 250 V. A high current is created from Ch14 so that the output pulse saturates, while lower signals can be seen from channels 17, 18 and 19. Ch18 is the most damaged pixel and the integral of the signal induced on this pixel corresponds to about 1 % of the integral of the signal readout on Ch14.

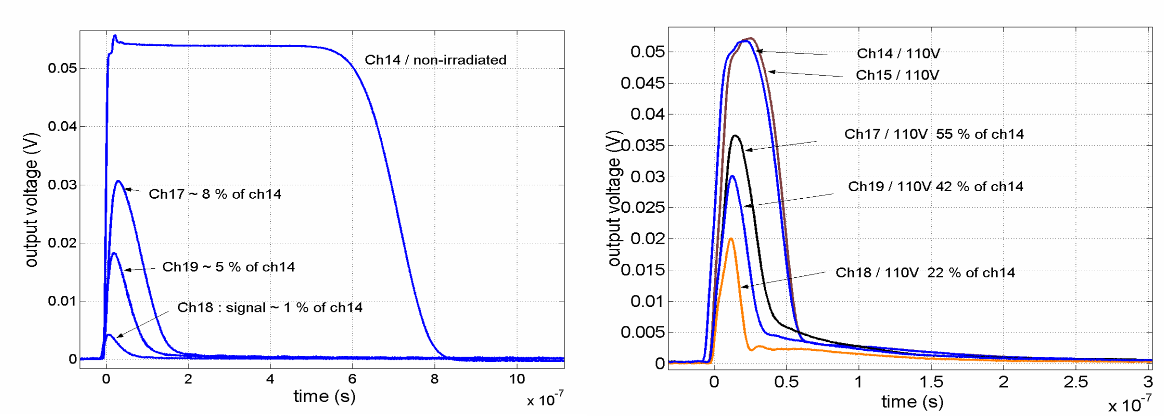

Figure 7.11. 660 nm pulsed laser response of the TFA detector for a 250 V reverse bias. Ch14 and Ch15 are non-irradiated pixels, and Ch17, Ch18 and Ch19 are irradiated pixels. The percentage indicated corresponds to the ratio of the integral of the signal created in the pixel under study over the integral of the signal created in Ch 14. Left: Results after the irradiation. Right: Results after an annealing of 2 hours at 100 °C.

The defects created by the irradiation lead to a complex internal electric field because of the induced non-uniformity of the distribution of dangling bonds and ionized dangling bonds in the sensor (as most of the defects are created close to the p-i interface). A complex distribution of the space charge in the sensor has been caused by the irradiation. The deep defects limit the depletion region of the sensor and also enhance the recombination probability of the carriers during their drift, moreover because the pairs are created close to the p-i interface. These effects lead to the strong reduction of signal observed.

The metastability of the created defects has been tested. The sample was placed for different times at a temperature of 100 °C and then tested again with the 660 nm laser. Pulse responses observed on Ch14, Ch17, Ch18 and Ch19, for a detector reverse bias of 250 V and after an annealing of 2 hours at 100 °C are shown in Figure 7.11 right. The response of Ch15 is also displayed. This pixel has not been irradiated and the pulse response is similar to that of Ch14. Significant increase of the signals created by the laser pulse on the irradiated pixels is observed after the thermal annealing. The laser conditions were changed for the different studies and signals were always compared with the response of Ch14. Tests were done after different times of annealing by varying the detector bias, by measuring the integral of the created signal and by dividing it by the signal created on Ch14. Results obtained for Ch17 and Ch18 are shown in Figure 7.12.

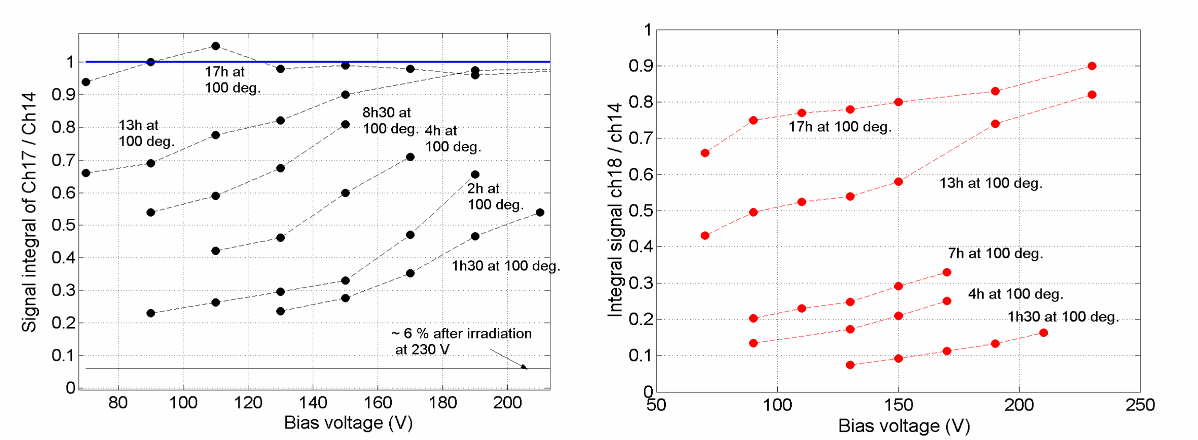

Figure 7.12. Ratio of the integral of the signal created by the laser pulse in an irradiated pixel over the signal created in a non-irradiated pixel. Left: Ch17, right: Ch18.

A very interesting recovery of signal is observed for all the irradiated pixels by thermal annealing. These results demonstrate that a recovery process of the defects can be achieved by thermal excitation, showing the metastability of the defects created by an irradiation in a-Si:H. A full recovery has been obtained for Ch17 after 17 hours of annealing at 100 °C while the signal created in Ch18 was back to 90 % of the signal created on non-irradiated pixels. Differences in the signal recovery are observed with the detector reverse bias. The higher is the detector reverse bias the faster is the signal recovery. For example, for Ch17, full recovery of signal for biases higher than 180 V is achieved after 13 hours of annealing, while the signal at 70 V corresponds to about 70 % of the signal induced in Ch14. This can be explained by the fact that higher reverse biases lead to higher electric fields in the sensor and at the p-i interface, where recombination of the generated carriers should occur. The enhanced electric field leads to a decreased recombination by increasing the generated carriers drift velocity. The application of high reverse biases on the detector is thus a way of reducing the degradation of the signal induced by the irradiation in a-Si:H. The annealing effects are presented in Figure 7.13 for a detector reverse bias of 150 V.

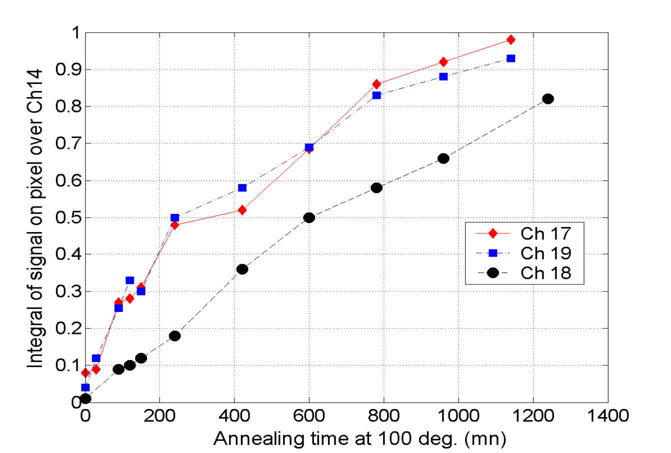

Figure 7.13. Recovery of the signal created by the laser pulse in the irradiated pixels as a function of the annealing time at 100 °C.

The TFA detector was then tested again with the electron beam of a SEM to observe the EBIC images of the irradiated pixels after the thermal annealing. The EBIC image taken after the irradiation of Ch17 is presented in Figure 7.14 left, on which different degraded areas can be observed. The EBIC images obtained on the same pixel after thermal annealing, and for 3 reverse biases are shown in Figure 7.14 right.

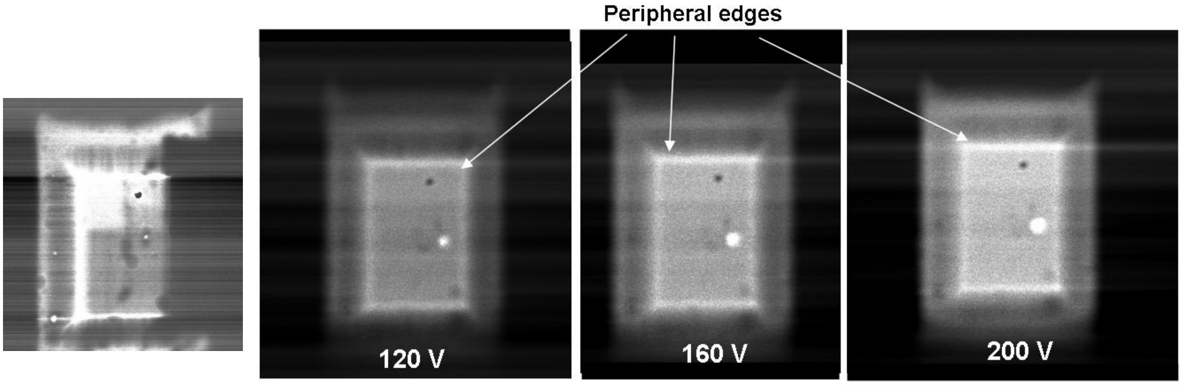

Figure 7.14. Recovery of the signal created by the electron in the irradiated pixel Ch1. Left: EBIC image after irradiation. Right: EBIC images after thermal annealing.

Clear homogeneity of the pixel response is observed for each detector bias after the thermal annealing. The irradiated areas of the pixel have after thermal annealing a similar response than the non-irradiated areas of the pixel. These results are a clear visual proof of a very effective annealing effect, and that full recovery of signal can be achieved.

7.4. Conclusions

Radiation effects on the electrical properties of a-Si:H have been studied in a first time by irradiating test structures deposited on glass with high energy protons (23 GeV) and in a second time by irradiating a TFA detector with keV electrons.

The signal induced by a 23 GeV proton burst was measured for different fluences. Reductions of the signal by a factor 2 after about 10^{15} protons/cm^2 (equivalent to a dose of 300 kGy) and by a factor 4 after about 10^{16} protons/cm^2 (equivalent to a dose of 3 MGy) have been measured. An increase in the leakage current by also a factor 2 has been measured for a 10^{15} protons/cm^2 irradiation. These variations are due to a creation of deep defects associated to the irradiation which lead to an enhanced thermal generation, to a decrease of the depleted thickness and to enhanced recombination of generated charges.
Tests were carried out with an intense beam and with a high fluence rate of 4 to 8×10^{13} protons/(cm^2·h). The total fluence corresponding to 5 years of operation of tracking detectors for Super-LHC has been obtained in less than 10 days. Measurements performed suggest self-annealing of the sensor while kept under bias at room temperature, so that radiation resistance of an a-Si:H sensor must strongly depend on the fluence rate. The annealing of one sensor at 100 °C after irradiation, for about 24 hours, leads to a decrease of the leakage current which was then measured similar to pre-irradiation.

Strong degradation of signal created by radiation has been measured on a TFA detector irradiated with 26 keV electrons from a Scanning Electron Microscope. For fluences close to the fluences achieved in the proton irradiation, higher degradation was observed as a reduction of 1 to 2 orders of magnitude in the signal created by a laser pulse has been measured between an irradiated and a non-irradiated pixel. In this irradiation, the creation of defects was localized in the first microns close to the p-i interface, at the position where the photons injected for the laser test interact, and the fluence rate was even higher than for the proton irradiation, as similar fluences were reached in about 10 minutes.

A creation of deep defects in an a-Si:H sensor is thus linked to the IEL of a particle, degrading the sensor electrical properties. However, a clear metastability of the created defects has been demonstrated: the defects can be recovered by structural rearrangement caused by an external energy. A thermal excitation provides enough energy to allow a passivation of the created defects. After subsequent thermal annealing at 100 °C, full recovery of the created signals by particles has been measured in most of the cases.

The radiation resistance of a-Si:H is then caused by the metastability and reversibility of the radiation effects. Irradiation leads to an increase of the deep defect density, inducing a higher thermal generation and higher internal electric fields, both leading to an increased leakage current. Moreover, it also leads to the decrease of the depleted thickness and to an increase of the recombination probability, so that signal created by radiations will be reduced. The depleted thickness reduction might be the dominant effect because the internal electric field is also increased leading to faster collection of the charges and reducing the recombination probability.

Thermal excitation permits structural rearrangements and decrease of the defect density. The radiation resistance of a-Si:H for any application is thus strongly dependent on the fluence or dose rate and temperature of operation of the sensor for the application.

Conclusions

First characterization tests of the performance and limitations of a radiation detector based on Thin Film on ASIC technology have been presented in this thesis. This work has been motivated by the interesting potential this technology could offer for High Energy Physics experiments and for other detection applications. Hydrogenated amorphous silicon sensors with a thickness higher than usual a-Si:H devices (~ 1 µm) but at the same time limited by the deposition possibilities have been deposited on processed Application Specific Integrated Circuits. a-Si:H sensor with a thickness higher than 1 µm and the details of its operation represent a field with many different open questions. Moreover, the TFA technology involves the conception of ASIC able to readout small signals created by particles in the a-Si:H sensor and the definition of the detector sensing element at the ASIC level. The work presented contributes to an evolution into further understanding of the detection particularities of an a-Si:H sensing device and to the definition of the detection limitations and of the specific segmentation of TFA detectors. In the following, I will draw the main conclusions coming from my contributions to these fields.

- **Developed TFA detectors**

TFA detectors characterized in this work were built by depositing n-i-p a-Si:H sensors on top of two different integrated circuits (all depositions were done at the institute of micro-technology of Neuchatel [IMT]). The circuits designed in this work are:

- the AFP
- the aSiHtest

We have first demonstrated the feasibility of the TFA concept by the characterizations of sensors deposited on an AFP circuit. Usable a-Si:H sensors with thickness up to 32 µm can be deposited without affecting the integrated electronic readout, and first direct detection of single particles (electrons with energy ranging from 15 to 55 keV) with TFA detectors have been shown. The AFP chip pixels are defined by 68 µm × 94 µm metal pads while the integrated trans-impedance pre-amplifiers have a 5 ns peaking time for an equivalent noise charge (ENC) of about 450 e^- rms.

One of the main contributions of the work presented in this thesis is the design of the aSiHtest IC, which is dedicated to the characterization of sensors able to be deposited on its surface. It permits the characterization of the deposited sensor leakage current, of the detector system segmentation and of the signal induction and speed in the sensor. The central area of the chip integrates different metal pads on top of which is deposited the sensor. The metal structures present different shapes, sizes and different openings in the passivation layers. The passivation layers and the openings turned out to have a major role in the detector performance because of their impact on the interface ASIC/a-Si:H. Each metal structure is connected to one of the three electronic readouts integrated in the circuit. Current mirrors allowing a current amplification from 10^2 to 10^5 and Active feedback pre-amplifiers called respectively MiBeDo and aSiScope are integrated. The designed pre-amplifiers respectively have a peaking time of 5 ns and 25 ns and an ENC of 160 e^- rms and 70 e^- rms. Different TFA detectors based on this aSiHtest circuit and with a maximum thickness of 20 μm of the deposited sensor have been characterized in the presented work.

- **TFA detector leakage current and segmentation**

In order to construct a signal from the passage of a particle through the sensor which can be readout by the integrated electronic processing, a sufficient interacting and active sensor thickness is required. In other words, a "thick" sensor fully-depleted is needed for an optimized detection efficiency. The n-i-p a-Si:H sensors characterized in this thesis present a maximum thickness of about 32 μm. Depletion of the intrinsic layer is achieved by applying a reverse voltage (about 200 V for 20 μm) to the n-i-p structure. The internal electric field (about 10^4-10^5 V/cm) extends from the p-i interface as part of the deep defects present in a-Si:H (dangling bonds) are ionized and lead to a positive space charge.

We demonstrated that a first important limitation of a TFA detector performance originates from elevated leakage currents preventing a full-depletion of the sensor. The work presented in the thesis has permitted to make significant progress in the understanding of the mechanisms governing the dark currents in TFA detectors, and in the solutions to reduce them. We have shown that the physical mechanism causing the leakage current is a field enhanced thermal generation, explaining the strong field and temperature dependencies observed. Thermal generation depends on the deep defect density (N_{db}) and is enhanced by electric field through Poole-Frenkel mechanisms. Most of the current is expected to originate from the p-i interface which exhibits a higher defect density and higher electric fields. For TFA detectors, we have identified two important additional currents. Characterizations performed in this work on an AFP detector with a scanning electron microscope and on different aSiHtest detectors demonstrate that high additional currents arise from the pixel edges and corners. High fields are induced in these regions by the ASIC uneven surface caused by the openings in the passivation layers. In standard CMOS technologies, integrated circuits are protected with a passivation layer which covers its surface. Openings in these layers are made to contact metal pads and are normally made "inside" a metal pad. This means that the opening is smaller than the metal pad and that only metal is visible where openings were done in the passivation layers. The different pixels of the AFP detectors are made in this standard way. However, some metal structures integrated in the aSiHtest circuit have openings made all around the metal pads (on top of silicon dioxide layer separating metal pads). We have shown that these structures present a factor 3 to 10 lower current density than structures with an opening inside the metal pad and that the current reduction scales with the distance from the metal pad to the opening location. Characterizations presented in Chapter 4 thus prove that the deposition of the a-Si:H sensor on top of the ASIC leads to increased leakage currents of the sensor because of the ASIC unevenness. The reduction of the dark current of the detecting device has thus to be taken into account during the design phase of the integrated circuit. Large openings in the passivation layers around the metal pads have to be performed to permit the full-depletion of the a-Si:H sensor without increasing too much leakage currents.

- **Radiation detection**

The signal induction and speed in a TFA detector have been studied with a 660 nm laser photo-generating in about 2 ns free carriers close to the p-i interface of the sensor. Different conclusions arise from the measurements performed on TFA detectors based on AFP and aSiHtest circuits. For an under-depleted a-Si:H sensor, the electron collection time constant τ_c has been shown to be constant and equal to about 5 to 6 ns. This time is inversely proportional to the electron mobility and to the density of ionized dangling bonds. Over-depletion leads to faster signals. A full signal from electron motion in the sensor is thus created in less than 20 ns. A small and long signal induced by the motion of generated holes has also been observed. Measurements show a strong electric field dependence of hole transport and therefore of the induced signal.

We measured that the signal induction in a-Si:H is different from the case of crystalline silicon. The non-depleted layer of the a-Si:H sensor has a high resistivity and affects the signal induction. The charge induced by $q \cdot N$ electrons created at the p-i interface and drifting through the depleted region d is thus given by $Q_e = q \cdot N \cdot d / d_{tot}$ (d_{tot} being the total sensor thickness). Up to full depletion, this charge thus varies with the square root of the applied voltage. A partial depletion of an a-Si:H sensor has thus a double detrimental effect on the signal creation efficiency. It first limits the interacting active volume but it also reduces the total charge induced by the ratio depleted thickness over total thickness of the sensor.

Depletion of the a-Si:H sensor is thus of primary importance. However, the depleted thickness of the detector cannot be studied through capacitance measurements as an a-Si:H sensor capacitance does not vary with the applied voltage. We propose an experimental method to determine the depletion based on the laser technique and details are presented in Chapter 6. Measurements performed on TFA detectors based on 20 μm thick sensors deposited on an aSiHtest circuit have demonstrated the need of a minimum reverse voltage of about 180 V to 195 V to achieve full depletion. Measurements confirm the expected value of average density of ionized dangling bonds of $N_{db}^* \sim 6\times10^{14}$ cm^{-3}. They also confirm that full depletion voltage can be estimated as $V \sim 0.45\times d_{tot}^2$ (with d_{tot} in μm).

The signal creation has been studied in detail in Chapter 6. Electrons generated by the incoming radiation will create a signal in a maximum time of 20 ns, while holes generated will drift during a time strongly varying with the electric field driving their motion. The dispersive and slow hole transport leads to a partial signal from holes strongly depending on the applied reverse voltage and on the electronic readout shaping time. For a shaping time of 25 ns, the signal from holes represents only about 5 to 15 % of the total signal expected from holes. Full depletion of the a-Si:H sensor is thus needed to optimize the detection and to optimize the signal created by the generated electrons. High electric fields (over-depletion) are required to optimize the signal created by holes in the fast shaping time. Full depletion of 20 μm thick sensors on aSiHtest circuits has been achieved, and radiation detection has been characterized with these sensors.

An efficient detection of low energy electrons (from ~ 15 keV to 50 keV) has been demonstrated, with a signal of few thousand electrons created in a 20 μm thick sensor. Such detection has been carried out on pixels with an area of 2070 μm^2 and on 6.6 μm wide strips separated by a minimum distance of 4 μm, showing a mean pair creation energy W of 5.4 ± 0.8 eV. Very low lateral induction of signal has been observed with these strip structures, as electrons having a track on top of a strip were not inducing any significant signal on the neighboring strips. These measurements together with EBIC measurements presented in Chapter 4 suggest a very low edge effect and low charge sharing in hydrogenated amorphous silicon detectors. This represents a very interesting property for the design of high resolution detectors.

However, no clear Minimum Ionizing Particle (MIP) detection has been demonstrated. The test set up used to characterize aSiHtest detectors permitted to measure with a signal over noise ratio of 10 minimum charges of about 700 electrons. No signals that can be clearly attributed to MIPs have been measured with this set-up, thus demonstrating that a MIP creates a signal inferior to 700 electrons in a 20 μm thick depleted sensor connected to an electronic readout with a shaping time of 25 ns. However, calculations lead to an expected charge of about 600 electrons, so that signals originating from a MIP might be close to the set-up noise limit. The weak signal created a MIP represents a strong limitation of the TFA technology for high energy physics applications.

We have successfully demonstrated X-ray detection with TFA detectors. 6 keV X-rays have been detected, with a maximum signal created at about 1000 electrons and a peak charge at about 660 electrons in a fully depleted 15 μm thick sensor.

Evolutions of the a-Si:H sensor electrical properties under a harsh radiation environment have also been studied and results have been detailed in Chapter 7. Radiation effects have been shown to be linked to ionization which leads to an increase of the dangling bond density. Principal consequences are a reduced depleted thickness and increased leakage currents, leading to a reduced signal from the track of a particle. Tests with a 23 GeV proton beam up to fluences of 10^{16} protons/cm^2 have shown a reduction of the signal created by a proton spill by a factor 4, for high fluence rate of 4 to 8×10^{13} protons/(cm^2·h).

A very interesting self annealing effect at room temperature has also been shown, demonstrating that radiation resistance of the a-Si:H sensor strongly depends on the irradiation rate. Irradiations with a 26 keV electron beam and post irradiation measurements have shown that even after strong degradation of the material, full recovery of signal can be obtained after consequent thermal annealing at 100 °C. The created defects are metastable and can thus be annealed out through thermal treatment of the sensor. Their density can be varied by irradiation but can be brought back to a value around 10^{15} cm^{-3} after annealing. TFA technology thus presents an interesting radiation resistance linked to the material metastability, so that detector degradation depends on the dose rate.

- **Perspectives**

The work carried out in this thesis has thus first demonstrated the feasibility of the TFA radiation detector concept. A signal can be constructed in less than 20 ns by the motion of the electrons and by part of the motion of the holes generated by an incoming ionizing radiation. We have shown that the sensing elements are defined by the metal pads integrated in the ASIC with μm precision (very low lateral induction has been measured). We have identified a strong dependence of a sensing element leakage current on the pad definition at the ASIC level. A flat substrate is required for a fully optimized sensor.

For the construction of a pixel or a strip detector based on the TFA technology, a first method can consist in the design of metal pads at the ASIC level with minimal separation (for minimal dead area) and with openings in the passivation layer made all around the full active area. A second technique can consist in a further process step on the ASIC. Metal pads smaller than the desired sensing element area can be designed at the ASIC level with standard openings in the passivation layers inside the metal pads. The construction of the detector electrodes can then be done by first filling with metal the different openings to obtain a rather flat surface with metal connections to the different integrated pre-amplifiers. The second step could consist in extending and patterning metal pads on top of this flat surface, each designed electrode being connected to its electronic readout through the passivation openings filled by metal. This second method even though asking for a further process step would lead to much lower parasitic capacitances than the first method, allowing the design of lower noise electronic readout.

In order to use the TFA technology for future High Energy Experiments, MIP detection has to be performed. The low signals created by particles in the thin sensor represent an important limitation of the technology. MIP detection could be achieved by an increase of the sensor thickness. Lower leakage currents of the a-Si:H sensor can be obtained with the different segmentation techniques presented before, so that 40 μm thick sensors could be deposited and depleted. Reduction of the leakage current and of the depletion voltage could also be achieved by reducing the dangling bond density. However, this turns out to be limited as the densities obtained by different institutes and after annealing of irradiated samples always show a stable value of about 10^{15} cm^{-3}, indicating a stable metastability of hydrogenated amorphous silicon. A thicker sensor of 40 µm fully depleted could lead to an estimated charge of about 1400 electrons.

The technology radiation resistance has been shown to be dependent on the annealing mechanisms of the material, so that further detailed characterizations are necessitated to conclude about the radiation damage a TFA detector would suffer in a given radiation environment.

Finally, TFA technology presents a very interesting potential for high resolution low energy electron detection, as it has been presented in Chapter 6. Sensors with a thickness of 15 µm requiring a biasing voltage of about 100 V appear as the optimal detector solution for such application.

Performance of TFA technology in the context of particle detectors has been assessed for the first time, and the results have been presented in this thesis. Due to the innovative nature of this work, we have inevitably revealed various weaknesses and limitations of this application. The thesis has resolved some of the difficulties encountered during development. The results are promising regarding the use of TFA technology for radiation detection, though several problems need to be addressed if this is to become a viable solution for particle detection in high energy physics.

Appendix

Calculation of the transient response of a second order feedback system

The Active Feedback Preamplifier can be approximated as a second order feedback system. The structure of its transient behavior is calculated is this appendix to obtain simple equations defining the rise time and the gain of the AFP circuit response to a delta of Dirac current pulse of total charge Q. The transfer function in the frequency domain can be expressed as:

$$H_{AFP}[s] \cong \frac{-A_{buf}}{gmsf} \frac{\omega_0{}^2}{s^2 + 2\,\xi\,\omega_0\,s + \omega_0{}^2} \qquad (A.1);$$

where ξ is the damping ratio and ω_0 the natural resonant frequency of the system. For $\xi \geq 1$, the poles are real, and for $\xi < 1$, the poles are complex conjugates:

$$\omega_1 = -\xi\,\omega_0 + \omega_0\sqrt{\xi^2 - 1}\ ; \qquad \omega_2 = -\xi\,\omega_0 - \omega_0\sqrt{\xi^2 - 1}\ ; \qquad \text{for } \xi \geq 1 \qquad (A.2);$$

$$\omega_{1,2} = -\xi\,\omega_0 \pm i\,\omega_0\sqrt{1 - \xi^2} \qquad \text{for } \xi < 1 \qquad (A.3).$$

Calculating the Inverse Laplace Transform of the frequency response, we obtain the transient response to a Dirac current impulse, and for a total input charge Q:

$$V_{out}(t) = L^{-1}\left\{Q.H_{AFP}[s]\right\} \qquad (A.4)\ ;$$

$$V_{out}(t) = \frac{-\omega_0\,Q\,A_{buf}}{2\ gms_f\sqrt{\xi^2 - 1}}\left(\exp\left[t\,\omega_0\left(\sqrt{\xi^2 - 1} - \xi\right)\right] - \exp\left[-t\,\omega_0\left(\sqrt{\xi^2 - 1} + \xi\right)\right]\right) \qquad \text{for } \xi \geq 1 \qquad (A.5);$$

$$V_{out}(t) = \frac{-\omega_0\,Q\,A_{buf}}{gms_f\sqrt{1 - \xi^2}}\exp\left(-t\ \omega_0\xi\right)\sin\left(\omega_0\sqrt{1 - \xi^2}\ t\right) \qquad \text{for } \xi < 1 \qquad (A.6).$$

The transient response to a 4 fC input charge is illustrated in Figure A.1, for $gms_f = 7\ \mu S$, $\omega_0 = 2.2\ 10^8$ rad/s and $\xi = 0.8$. The derivative of the transient response is nil at the pulse extreme and the rise time can be calculated:

$$dV_{out}(t_{max})/dt = 0 \qquad t_{max} = \frac{1}{\omega_0} F_1(\xi) \qquad (A.7);$$

$$F_1(\xi) = \frac{-1}{2\sqrt{\xi^2-1}} \ln\left(-\frac{(\sqrt{\xi^2-1}-\xi)}{(\sqrt{\xi^2-1}+\xi)} \right) \quad \text{for } \xi > 1 \qquad \text{(A.8);}$$

$$F1_{comp}(\xi) = \frac{1}{\sqrt{1-\xi^2}} \text{ Arctan}\left(\frac{\sqrt{1-\xi^2}}{\xi} \right) \quad \text{for } \xi < 1 \qquad \text{(A.9).}$$

Or for every ξ:

$$F_1(\xi) = \left| F1_{comp}(\xi) \right| \qquad \text{(A.10).}$$

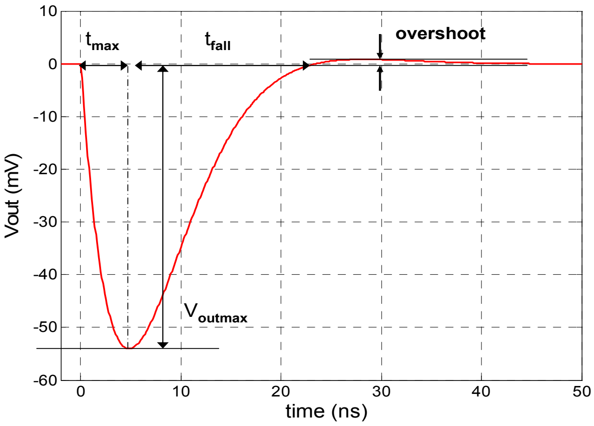

Figure A.1. Transient pulse response for a second order feedback system with gmsf = 7 µS, ω_0 = 2.2 10^8 rad/s, ξ = 0.8 and Q = 4 fC. Illustration the different pulse parameters calculated analytically: peaking time, return to zero time, pulse amplitude, overshoot amplitude.

The pulse response gain can then be calculated and expressed as:

$$V_{outmax} = V_{out}(t_{max}) = \frac{-\omega_0 \, Q \, A_{buf}}{gms_f} F_2(\xi) \qquad \text{(A.11)}$$

The damping ratio function F2 can be expressed for every ξ as:

$$F_2(\xi) = \exp\left(-\xi \left| \frac{1}{\sqrt{1-\xi^2}} \text{Arctan}\left(\frac{\sqrt{1-\xi^2}}{\xi} \right) \right| \right) \qquad \text{(A.12)}$$

The two functions F1[1/ξ] and F2[1/ ξ] are decreasing functions of the damping ratio (Figure A.1.2). Evolutions of the maximum voltage and of the peaking time of the output pulse response to a negative input charge of 4 fC are illustrated in Figures A.2 and A.3.

For $\xi < 1$, the poles are complex conjugate and the transient pulse response presents an overshoot V_{ov} at the time t_{ov}:

$$t_{ov} = \frac{\pi}{\omega_0 \sqrt{1-\xi^2}} \qquad \text{and} \qquad V_{ov} = V_{outmax} \exp\left(\frac{-\pi\,\xi}{\sqrt{1-\xi^2}}\right) \tag{A.13}$$

The pulse returns to zero at t_{ov} and the fall time can be defined as: $t_{fall} = t_{ov} - t_{max}$

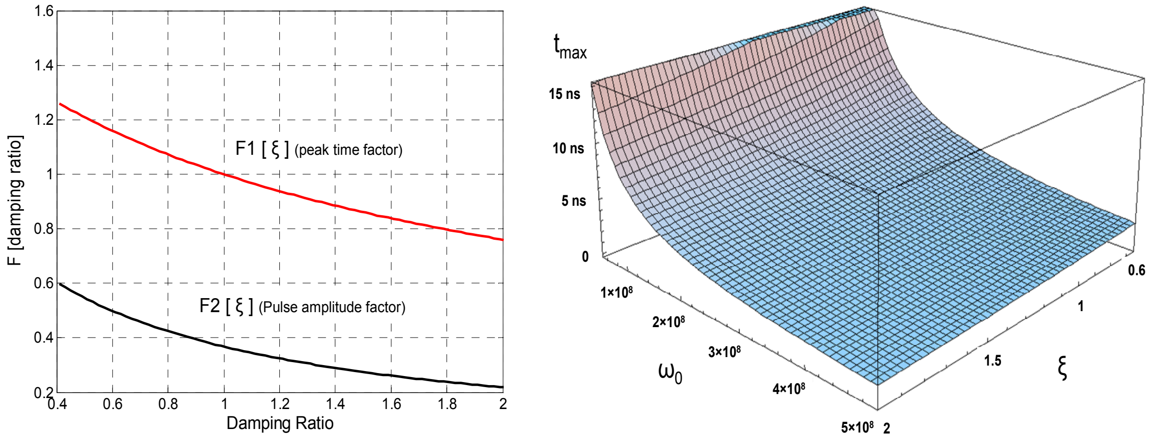

Figure A.2. Evolution of the damping ratio functions defining the peak time and the pulse amplitude (left). Evolution of the output response peaking time for a 4 fC input charge and for gms$_f$ = 7 µS varying ω$_0$ and ξ (right).

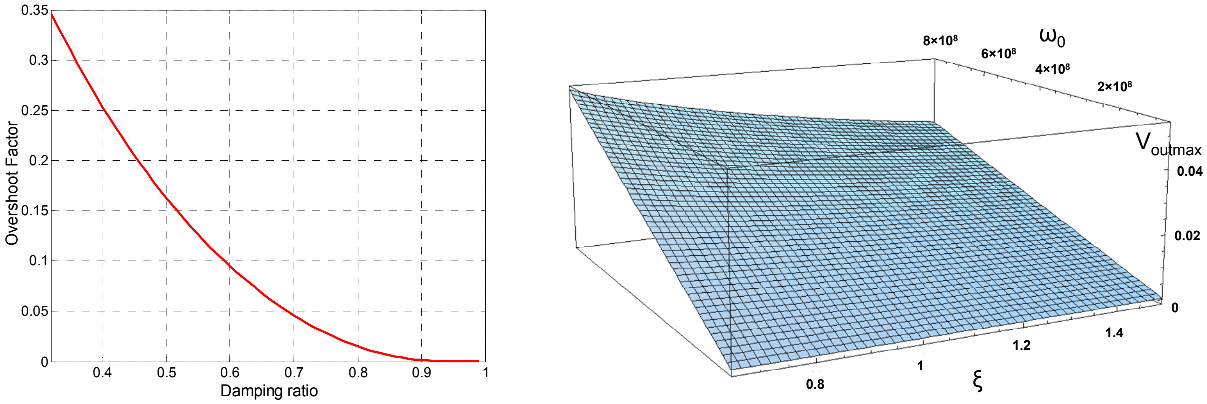

Figure A.3. Evolution of the pulse response overshoots with the damping ratio (left). Evolution of the maximum voltage of the output response for a 4 fC input charge and for gms$_f$ = 7 µS varying ω$_0$ and ξ (right).

Bibliography

The references for all the chapters of the thesis are in alphabetical order by the first author name. The referencing system adopted uses the first three letters of the first author surname followed by the last two digits of the publication year. This system has been chosen because it provides to the reader an immediate idea (without having to go and search in the reference list) about when the reference was published. A list of the different references directly related to the thesis work is also presented separately at the end.

[Abr79] ABRAHAMS E., ANDERSON P.W., LICCIARDELLO D.C, et al. Scaling theory of localization: absence of quantum diffusion in two dimensions. Physical Review Letters, 1979, vol. 42, pp. 673-676.

[Ale91] ALEKSAN R., BOLOGNESE T., EQUER B., et al. Observation of single minimum ionizing particles with amorphous silicon diodes. Nuclear instruments and methods in physics research A, 1991, vol. 305, pp. 512-516.

[Alv04] ALVAREZ-GAUME I., BLAIZOT J.P, CVETIC M., et al. Review of particle physics. Physics letters B, 2004, vol. 592, issues 1-4, pp. 262-263.

[Ane99] ANELLI G., CAMPBELL M., DELMASTRO M., et al. Radiation tolerant VLSI circuits in standard deep submicron CMOS technologies for the LHC experiments: practical design aspects. IEEE Transactions on Nuclear Science, 1999, vol. 46, n° 6, pp. 1690-1696.

[Ane01] ANELLI G. Conception et Caractérisation de Circuits Intégrés Résistants aux radiations pour les détecteurs de particules du LHC en technologies submicroniques profondes. Thèse Electronique, Electrotechnique, Automatique, Télécommunications, Signal. Grenoble: INPG, 2000, 214 p.

[Ane03] ANELLI G., BORER K., DESPEISSE M., et al. A high speed low noise transimpedance amplifier in a 0.25 μm CMOS technology. Nuclear instruments and methods in physics research A, 2003, vol. 512, pp. 117-128.

[Ase99] ASENSI J.M, MERTEN J., VOZ C., et al. Analysis of the role of mobility-lifetime products in the performance of amorphous silicon p-i-n solar cells. Journal of applied physics, 1999, vol. 85, n° 5, pp. 2939-2951.

[ATLAS] ATLAS. The ATLAS experiment **[en ligne]**. Disponible sur: http://atlas.ch/ (consulté le 12.12.2005).

[Att04] ATTA-FYNN R., BISWAS P., DRABOLD D.A. Electron-phonon coupling is large for localized states. Physical Review B, 2004, vol. 69, p. 245204.

[Bat05] BATES A. Developments in silicon detectors and their impact on LHCb physics measurements. Thèse. Glasgow: University of Glasgow, 229 p.

[Bei90] BEINSTINGL W., SAWADCITANG P., HOPFEL R.A., et al. Drift time limited hydrogenated amorphous silicon detectors with picosecond response times. Journal of applied physics, 1990, vol. 67, n° 8, pp. 3888-3890.

[Ber] BERKELEY LABORATORY. Berkeley Laboratory Isotopes Project **[en ligne]**. Disponible sur : http://ie.lbl.gov/education/isotopes.htm (consulté le 05.12.2005).

[Bra94] BRANZ H.M., YELON A., MOVAGHAR B. Physics of the Meyer-Neldel rule in amorphous silicon. Material research society symposium proceedings, 1994, vol. 336, p. 159.

[Bra98] BRANZ H.M. Hydrogen collision model of light-induced metastability in hydrogenated amorphous silicon. Solid state communications, 1998, vol. 105, n° 6, pp. 387-391.

[Car76] CARLSON D. E., WRONSKI C. R. Amorphous silicon Solar Cell. Applied physics letters, 1976, vol. 28, n° 11, pp. 671-673.

[Cas98] CASSE G. The effect of hadron irradiation on the electrical properties of particle detectors made from various silicon materials. Thèse Physique. Grenoble, France: Université Joseph Fourier, 1998, 182 p.

[Cav71] CAVALLERI G., GATTI E., FABRI G., et al. Extension of Ramo's theorem as applied to induced charge in semiconductor detectors. Nuclear instruments and methods, 1971, vol. 92, pp. 137-140.

[CERN] CERN. Le plus grand laboratoire de physique des particules du monde **[en ligne]**. Disponible sur : http://public.web.cern.ch/public/Welcome-fr.html (consulté le 10.11.2005).

[Cha91] CHANG Z.Y., SANSEN W.M.C. Low-noise wide-band amplifiers in bipolar and CMOS technologies. Boston, Dordrecht, London: Kluwer Academic Publishers, 1991, 211 p.

[Cha96] CHABLOZ P. Les couches épaisses en silicium amorphe, application comme détecteur de rayons X. Thèse Microtechnique n° 1485. Lausanne, Suisse : Ecole Polytechnique Fédérale de Lausanne, 1996, 88 p.

[Che94] CHEVRIER J.B., EQUER B. High electric-field amorphous silicon p-i-n diodes: Effect of the p-layer thickness. Journal of applied physics, 1994, vol. 76, n° 11, pp. 7415-7422.

[Chi69] CHITTICK R.C., ALEXANDER J.H., STERLING H.F. The preparation and properties of amorphous silicon. Journal of the electrochemical society, 1969, vol. 116, n° 1, pp. 77-81.

[Das03] DASH R.K., VOYLES P.M., GIBSON J.M., et al. A quantitative measure of medium-range order in amorphous materials from transmission electron micrographs. Journal of physics: condensed matter, 2003, vol. 15, pp. S2425-S2435.

[DaV03] DA VIA C., ANELLI G., HASI J., et al. Advances in silicon detectors for particle tracking in extreme radiation environment. Nuclear instruments and methods in physics research A, 2003, vol. 509, pp. 86-91.

[Dep02] DEPTUCH G., BERST J.D., CLAUS G., et al. Design and testing of monolithic active pixel sensors for charged particle tracking. IEEE Transactions on nuclear science, 2002, vol. 49, n° 2, pp. 601-610.

[Des03] DESPEISSE M., ANELLI G., COMMICHAU S., et al. Characterization of 13 and 30 µm thick hydrogenated amorphous silicon diodes deposited over CMOS integrated circuits for particle detection application. Nuclear instruments and methods in physics research A, 2004, vol. 518, pp. 357-361.

[Din04] DINAPOLI R. A radiation tolerant pixel detector system for the ALICE and LHCb experiments at CERN. Thèse Electronique et micro-optoélectronique. Montpellier, France: Université Montpellier II, 2004, 284 p.

[Dod03] DODD P.E., MASSENGILL L.W. Basic mechanisms and modeling of single-event upsets in digital microelectronics. IEEE Transactions on Nuclear Science, 2003, vol. 50, n° 3, pp. 583-602.

[Dub91] DUBEAU J., POCHET T., HAMEL L.A., et al. Response of amorphous p-i-n detectors to ionizing particles. Nuclear instruments and methods in physics research B, 1991, vol. 54, pp. 458-471.

[Equ89] EQUER B., KARAR A. Amorphous semiconductors for particle detection: physical and technical limits and possibilities. Nuclear instruments and methods in physics research A, vol. 275, 1989, pp. 558-563.

[ESRF] ESRF. European Synchrotron Radiation Facility **[en ligne]**. Disponible sur : http://www.esrf.fr/ (consulté le 08.12.2005).

[Eve71] EVERHART T.E., HOFF P.H. Determination of kilovolt electron energy dissipation vs penetration distance in solid materials. Journal of applied physics, 1971, vol. 42, n° 13, pp. 5837-5846.

[Fac05] FACCIO F., CERVELLI G. Radiation induced edge effects in deep-submicron CMOS transistors. IEEE transactions on nuclear science, 2005, vol. 52, no. 6, pp. 2413-2420.

[Fen85] FENZ P., MULLER H., OVERHOF H., et al. Activated transport in amorphous semiconductors: II Interpretation of experimental data. Journal of physics C: solid state physics, 1985, vol. 18, pp. 3191-3199.

[Fis92] FISCHER H., SCHULTE J., GIEHL J., et al. Thin Film on ASIC – A novel concept for intelligent image sensors. Material research society symposium proceedings, 1992, vol. 285, pp. 1139-1145.

[Fis94] FISCHER D. Electric Field and photocarrier collection in amorphous silicon p-i-n solar cells, effects of light-induced degradation and of low-level i-layer doping. Thèse Microtechnique. Neuchatel, Suisse : Universite de Neuchatel, 1994, 131 p.

[Fis03] FISCHBACH F., FREUND T., PECH M. et al. Comparison of indirect CsI/a:Si and direct a:Se digital radiography. Acta Radiologica, 2003, vol. 44, pp. 616-621.

[Fou01] FOULON F., HORDEQUIN C., BRAMBILLA A., et al. Nuclear radiation detectors using thick amorphous silicon MIS devices. Nuclear instruments and methods in physics research A, 2001, vol. 456, pp. 284-289

[Fre38] FRENKEL J. On pre-breakdown phenomena in insulators and electronic Semi-conductors. Physical Review, 1938, vol. 54, pp. 647-648.

[Fri77] FRITZSCHE H. Electrons in disordered systems, scaling near the mobility edge. **In:** SPEAR W.E. eds. Proceedings of the 7th International Conference on Amorphous and Liquid Semiconductors, Edinburgh, 1977, p. 301.

[Gat86] GATTI E., MANFREDI P. F. Processing the signals from solid state detectors in elementary-particle physics. Rivista del nuovo cimento, 1986, vol. 9, n° 1, 146 p.

[Gay05] GAY A., CLAUS G., COLLEDANI C.,et al. High-resolution CMOS sensors for a vertex detector at the Linear Collider. Nuclear instruments and methods in physics research A, 2005, vol. 549, pp. 99-102.

[Gia05] GIANOTTI F., MANGANO M.L., VIRDEE T., et al. Physics Potential and Experimental Challenges of the LHC Luminosity Upgrade. The European physical journal C, 2005, vol. 39, pp. 293-333.

[Gib97] GIBSON J.M., TREACY M.M.J. Diminished Medium-Range Order observed in Annealed amorphous Germanium. Physical review letters, 1997, vol. 78, n°6, pp. 1074-1077.

[Gir00] GIRALDO A., PACCAGNELLA A., MINZONI A. Aspect ratio calculation in n-channel MOSFETs with a gate-enclosed layout. Solid-state electronics, 2000, vol. 44, pp. 981-989.

[Gla99] GLASER M., DURIEU L., LEMEILLEUR F. New irradiation zones at the CERN-PS. Nuclear instruments and methods in physics research A, 1999, vol. 426, pp. 72-77.

[Goe03] GOETZBERGER A., HEBLING C., SCHOCK H-W. Photovoltaic materials, history, status and outlook. Material science and engineering, 2003, vol. 40, n° 1, 46p..

[Gra01] GRACIN D., BORJANOVIC V., VLAHOVIC B., et al. Selective bond breaking in amorphous hydrogenated silicon by using Duke FEL. Nuclear instruments and methods in physics research A. 2001, vol. 475, pp. 635-639.

[Gro05] GROSSE-KNETTER J. The ATLAS pixel detector. Nuclear Instruments and Methods in Physics Research A, 2005, vol. 549, pp. 70-74.

[Gu95] GU Q., SCHIFF E.A., CHEVRIER J-B., et al. High-field electron-drift measurements and the mobility edge in hydrogenated amorphous silicon. Physical Review B, 1995, vol. 52, n° 8, pp. 5695-5707.

[Gu96] GU Q., SCHIFF E.A, GREBNER S., et al. Non-gaussian transport measurements and the Einstein relation in amorphous silicon. Physical review letters, 1996, vol. 76, n° 17, pp. 3196-3199.

[Ham97] HAMEL L-A., CHAO CHEN W., YELON A. Monte-Carlo simulations of Meyer-Neldel effect on carrier time-of-flight in a-Si:H. Journal of Non-Crystalline Solids, 1997, Vol. 220, pp. 254-260.

[Ham99] HAMEL L-A., CHAO CHEN W., YELON A. Multiple-trapping model with field-dependent effects on carrier time of flight in a-Si:H. Journal of Non-Crystalline Solids, 1999, vol. 258, pp. 223-233.

[Hei03] HEIJNE E.H.M. Semiconductor detectors in the low countries. Nuclear instruments and methods in physics research A. 2003, vol. 509, pp. 1-6.

[Hon95] HONG W.S., MIRESHGI A., DREWERY J.S., et al. Charged Particle Detectors based on high quality amorphous silicon deposited with hydrogen or helium dilution of Silane. IEEE Transactions on nuclear science, 1995, vol. 42, n° 4, pp. 240-246.

[IMT] Institute of Micro-technology of Neuchatel. PV-LAB, Photovoltaics and thin-film electronics **[en ligne]**. Disponible sur: http://www-micromorph.unine.ch/Welcome.htm (consulté le 06.12.2005).

[Jar96] JARRON P., ANGHINOLFI F., DELAGNE E., et al. A transimpedance amplifier using a novel current mode feedback loop. Nuclear instruments and methods in physics research A, 1996, vol. 377, pp. 435-439.

[Jar04] JARRON P., ANELLI G., DESPEISSE M., et al. A New concept of monolithic silicon pixel detectors: hydrogenated amorphous silicon on ASIC. Nuclear instruments and methods in physics research A, 2004, vol. 518, pp. 366-372.

[Jin95] JING T., GOODMAN A., DREWERY J., et al. Detection of charged particles and X-rays by scintillator layers coupled to amorphous silicon photodiode arrays. Nuclear instruments and methods in physics research A, 1996, vol. 368, pp. 757-764.

[Jus95] JUSKA G., ARLAUSKAS K., KOCKA J., et al. Hot Electrons in Amorphous Silicon. Physical review letters, 1995, vol. 75, n° 16, pp. 2984-2987.

[Kap86] KAPLAN S.N., MOREL J.R., MULERA T.A. Detection of charged particles in amorphous silicon layers. IEEE Transactions on nuclear science, 1986, vol. NS-33, p. 351.

[Kap04] KAPLON J. Fast bipolar and CMOS rad-hard front end electronics for silicon strip detectors. Thèse “Electrical engineering, automatics, computer science and electronics”. Cracow, Poland: AGH University of science and technology of Cracow, 2004, 124 p.

[Kel88] KELIRES P.C., TERSOFF J. Glassy quasithermal distribution of local geometries and defects in quenched amorphous silicon. Physical review letters, 1988, vol. 61, n° 5, pp. 562-565.

[Kim02] KIM H.J., CHO G. Analysis of the transient leakage current of an a-Si:H P-I-N diode. Journal of the Korean Physical Society, 2002, vol. 40, n° 5, pp. 908-912.

[Kim03] KIM H.J., KIM H.K., CHO G., et al. Construction and characterization of an amorphous silicon flat-panel detector based on ion-shower doping process. Nuclear instruments and methods in physics research A, 2003, vol. 505, pp. 155-158.

[Kis98] KISHIMOTO N., AMEKURA H., KONO K., et al. Stable photoconductivity in metastable a-Si:H under high-energy proton irradiation. Journal of non-crystalline solids, 1998, vol. 227-230, pp. 238-242.

[Kla82] KLAZES R.H., VAN DEN BROEK M.H.L.M., BEZEMER J., et al. Determination of the optical bandgap of amorphous silicon. Philosophical magazine B, 1982, vol. 45, p. 377.

[Kle68] KLEIN C. A. Bandgap dependence and related features of radiation ionizing energies in semiconductors. Journal of applied physics, 1968, vol. 39, n° 4, pp. 2029-2038.

[Kno99] KNOLL G. F. Radiation detection and measurement. Third edition. New York: John Wiley and sons, 1999, 802 p.

[Kok05] KOK A. Signal Formation and active edge studies of 3D silicon detector technology. Thèse. Middlessex, West London, England: Brunel University, 2005, 244 p.

[Kol04] KOLODZIEJ A. Staebler-Wronski effect in amorphous silicon and its alloys. Opto-Electronics review, 2004, vol. 12, pp. 21-32.

[Kra00] KRAMBERGER G., CINDRO V., MANDIC I., et al. Determination of effective trapping times for electrons and holes in irradiated silicon. Nuclear instruments and methods in physics research, 2002, vol. 476, pp. 645-651.

[Kun03] KUNDIG J. Cellules solaires en couches minces de silicium: Résistance aux radiations et applications spatiales. Thèse sciences et techniques de l'ingénieur, Microtechnique, n° 2874. Lausanne : Ecole Polytechnique Fédérale de Lausanne, 2003, 121 p.

[Laa99] LAAZIRI K., KYCIA S., ROORDA S. et al. High Energy X-ray diffraction study of pure amorphous silicon. Physical Review B, 1999, vol. 60, n° 19, pp. 13520-13533.

[Lai99] LAISSUE J.A. et al. Microbeam radiation Therapy. **In:** Proceedings of SPIE Conference on Medical Applications of Penetrating radiation, July 1999, Denver, USA. Bellingham : SPIE, 1999, vol. 3770, pp. 38-45.

[Lea82] LEAMY H.J. Charge collection scanning electron microscopy. Journal of applied physics, 1982, vol. 53, pp. R51-R80.

[Leo94] LEO W.R. Techniques for nuclear and particle physics experiments : a how-to approach. 2nd edition. Berlin : Springer, 1994, 378 p.

[Lut99] LUTZ G. Semiconductor Radiation Detectors. Berlin: Springer-Verlag, 1999, 378 p.

[Mal87] MALEY N., LANNIN J.S. Influence of hydrogen on vibrational and optical properties of a-$Si_{1-x}H_x$ alloys. Physical Review B, 1987, vol. 36, n° 2, pp. 1146-1152.

[Mat74] MATSUKAWA T., SHIMIZU R., HARADA K., et al. Investigation of kilovolt electron energy dissipation in solids. Journal of applied physics, 1974, Vol. 45, n° 2, pp. 733-740.

[MED] MEDIPIX. Medipix2, a single photon counting chip to improve X-ray and gamma-ray imaging **[en ligne]**. Disponible sur: http://medipix.web.cern.ch/MEDIPIX/ (consulté le 10.12.2005).

[Mei04] MEILLAUD F., SHAH A., DROZ C., et al. Efficiency limits for single-junction and tandem solar cells. Solar Energy and Materials To be published .Si vous avez l'année, vous pouvez la noter

[Mey37] MEYER W., NELDEL H. A relation between the energy constant ε and the quantity constant a in the conductivity-temperature formula for oxide. Zeitschrift fuer Technische Physik, 1937, ol. 18, pp. 588-593.

[Mir94] MIRESHGHI A., CHO G., DREWERY J.S., et al. High efficiency neutron Amorphous Silicon Pixel detectors. IEEE Transactions on nuclear science, 1994, vol. 1, n° 4, pp. 915-921.

[Moh01] MOHAN N. Multiplexer Design in Amorphous Silicon technology. Thèse, electrical and computer engineering. Waterloo, Canada: University of Waterloo, 2001, 106 p.

[Mol99] MOLL M. Radiation damage in silicon particle detectors. Thèse. Hamburg: Universitat Hamburg, 251 p.

[Mol05] MOLL M., et al. Development of radiation tolerant semiconductor detectors for the super-LHC. Nuclear instruments and methods in physics research A, 2005, vol. 546. pp. 99-107.

[Mor04] MORAES D., ANELLI G., DESPEISSE M., et al. A Novel Low Noise Hydrogenated Amorphous Silicon Pixel Detector. Journal of non-crystalline solids, 2004, vol. 338-340, pp. 729-731.

[Mos69] MOSS S.C., GRACZYK J.F. Evidence of voids within the as-deposited structure of glassy silicon. Physical Review Letters, 1969, vol. 23, n° 20, pp. 1167-1170.

[Mot79] MOTT N.F., DAVIS E.A. Electronic processes in Non-crystalline Materials. Oxford, England: Clarendon press, 1979, 590 p.

[Naj91] NAJAR S., EQUER B., LAKHOUA N. Electronic transport analysis by electron-beam-induced current at variable energy of thin-film amorphous semiconductors. Journal of applied physics, 1991, vol. 69, n° 7, pp. 3975-3985.

[Naj92] NAJAR S., EQUER B., CHEVRIER J-B. Electron range and electron generation function in a-Si:H. Material research society symposium proceedings, 1992, vol. 258, pp. 1157-1162.

[Oco01] O'CONNOR P., DE GERONIMO G. Prospects for charge sensitive amplifiers in scaled CMOS. Nuclear instruments and methods in physics research A, 2002, vol. 480, pp 713-725.

[Old03] OLDHAM T.R., MCLEAN F.B. Total ionizing dose effects in MOS oxides and devices. IEEE Transactions on Nuclear Science, 2003, vol. 50, n° 3, pp. 483-499.

[Ove89] OVERHOF H., THOMAS P. Electronic transport in Hydrogenated amorphous semiconductors. Berlin, Germany: Springer 1989, 174 p.(Springer tracts in modern physics ; vol.114)

[Pan86] PANTELIDES S.T. Defects in amorphous silicon : a new perspective. Physical Review Letters, 1986, vol. 57, n° 23, pp. 2979-2982.

[Par97] PARKER S.I., KENNEY C.J., SEGAL J. 3D – A proposed new architecture for solid-state radiation detectors. Nuclear instruments and methods in physics research A, 1997, vol. 395, pp. 328-343.

[Per86] PEREZ-MENDEZ V., MOREL J., KAPLAN S.N, et al. Detection of charged particles in amorphous silicon layers. Nuclear instruments and methods in physics research, 1986, vol. 252, pp. 478-482.

[Per87] PEREZ-MENDEZ V., HONG W.S., DREWERY J.S., et al. Thick (~ 50 μm) amorphous silicon p-i-n dioses for direct detection of minimum ionizing particles. Nuclear instruments and methods in physics research A, 1995, vol. 365, pp. 239-247.

[Per00] PERESSI M., FORNARI M., DE GIRONCOLI S., et al. Coordination defects in amorphous silicon and hydrogenated amorphous silicon: a characterization from first-principles calculations. Philosophical Magazine B, 2000, vol. 80, n° 4, pp. 515-521.

[Poc96] POCHET T., EQUER E., ILIE A., et al. Sensitivity measurements of Thick amorphous silicon p-i-n Nuclear Detectors. IEEE transactions on nuclear science, 1996, vol. 43, n° 3, pp. 1452-1457.

[Pop02] POPOV A. Structural Characteristics and structural modifications of non-crystalline semiconductors. Journal of optoelectronics and advanced materials, 2002, vol. 4, n° 3, pp. 481-488.

[Qur89a] QURESHI S., PEREZ-MENDEZ V., KAPLAN S.N., et al. Signal generation in a hydrogenated amorphous silicon detector. IEEE Transactions on nuclear science, 1989, vol. 36, n° 1, pp. 194-198.

[Qur89b] QURESHI S., PEREZ-MENDEZ V., KAPLAN S.N., et al. Material parameters in a thick hydrogenated amorphous silicon detector and their effect on signal collection. Material research society symposium proceedings, vol. 149, pp. 649-654.

[Rad88] RADEKA V. Low-noise techniques in detectors. Annual review of Nuclear Particle Science, 1988, vol. 38, pp. 217-277.

[Ram39] RAMO S. Currents Induced by Electron Motion. Proc. I.R.E, 1939, vol. 27, p. 584.

[Rav04] RAVOTTI F., GLASER M., DUSSEAU L., et al. Conception of an Integrated Sensor for the Radiation Monitoring of the CMS Experiment at the Large Hadron Collider. IEEE Transactions on nuclear science, 2004, vol. 51, pp. 3642-3648.

[Raz01] RAZAVI B. Design of analog CMOS integrated circuits. New York: McGraw-Hill, 2001, 684 p.(McGraw-Hill series in electrical and computer engineering)

[Rie04] RIEGLER W. Extended theorems for signal induction in particle detectors VCI 2004. Nuclear instruments and methods in physics research A, 2004, vol. 535, pp. 287-293.

[Sch94] SCHWANK J.R. Basic mechanisms of radiation effects in the natural space environment. **In:** Short course notes of the IEEE Nuclear and Space Radiation Effects Conference, 1994, Tucson, USA. Section II, pp. 1-109.

[Sch96] SCHIFF E.A., STREET R.A., WEISFIELD R.L. Reverse bias currents in amorphous silicon nip sensors. Journal of non-crystalline solids, 1996, vol. 198-200, pp. 1155-1158.

[Sch99] SCHNEIDER B., RIEVE P., BOHM M. Image sensors in TFA (Thin Film on ASIC) technology. Handbook of Computer Vision and applications, 1999, vol. 1, pp. 237-270.

[Sch04] SCHIFF E.A. Drift-mobility measurements and mobility edges in disordered silicons. Journal of physics: condensed matter, 2004, vol. 16, pp. S5265-S5275.

[Sed01] SEDKY S., WITVROUW A., BENDER H., et al. Experimental Determination of the maximum post-process annealing temperature for standard CMOS wafers. IEEE Transactions on electron devices, 2001, vol. 48, n° 2, pp. 377-385.

[Sel06] SELLIN P.J., VAITKUS J. New materials for radiation hard semiconductor detectors. Nuclear instruments and methods in physics research A, 2006, vol. 557, pp. 479-489.

[Sha95] SHAH A. Matériaux Electroniques amorphes. Neuchatel, Switzerland: Ecole polytechnique fédérale de Lausanne, 1995, vol. 1, 152 p.

[Sha05] SHAH A., BAILAT J., BALLIF C., et al. Microcrystalline and “micromorph” solar cells and modules: status and potential. Proceedings of IEEE Photovoltaic Specialist, 2005, pp. 1353-1358.

[Shi81] SHIMIZU I., SHIRAI S., INOUE E. Photoreceptor of a-Si:H with diode like structure for electro photography. Journal of applied physics, 1981, vol. 52, p. 2776.

[Sho38] SHOCKLEY W. Currents to conductors induced by a moving point charge. Journal of applied physics, 1938, vol. 9, pp. 635-636.

[SIAM] SIAM-CERN. A novel concept of monolithic silicon detector **[en ligne]**. Disponible sur: http://asi-hdet-project.web.cern.ch/asi-hdet-project/default.htm (consulté le 08.12.2005).

[Sne81] SNELL A. J., MACKENZIE K. D., SPEAR W. E., et al. Application of amorphous silicon field effect transistors in addressable liquid crystal display panels. Applied Physics, 1981, vol. 24, p. 357.

[Sno00] SNOEYS W., ANELLI G., CAMPBELL M., et al. Integrated circuits for particle physics experiments. IEEE Journal of solid-state circuits, 2000, vol. 35, no. 12, pp. 2018-2030.

[Spe75] SPEAR W.E., LECOMBER P.G. Substitutionnal doping of amorphous silicon. Solid state communications, 1975, vol. 17, pp. 1193-1196.

[Sro98] SROUR J.R., VENDURA G.J., LO D.H., et al.. Damage Mechanisms in radiation-tolerant Amorphous Silicon Solar Cells. IEEE Transactions on nuclear science, 1998, vol. 45, n° 6, p. 2624.

[Sta77] STAEBLER D., WRONSKI C. Reversible conductivity changes in discharge-produced amorphous Si. Applied physics letters, 1977, vol. 31, p. 292.

[Sta05] STALLINGA P., GOMES H.L. Trap states as an explanation for the Meyer-Neldel rule in semiconductors. Organic electronics, 2005, vol. 6, pp. 137-141.

[STAR05] BERGER M.J., COURSEY J.S., ZUCKER M.A., et al. ESTAR, PSTAR, and ASTAR: Computer Programs for Calculating Stopping-Power and Range Tables for Electrons, Protons, and Helium Ions (version 1.2.3) **[en ligne]**. Disponible sur: http://physics.nist.gov/PhysRefData/Star/Text/contents.html (consulté le 24.11.2005).

[Str83] STREET R.A. Measurements of depletion layers in hydrogenated amorphous silicon. Physical Review B, 1983, vol. 27, n° 8, pp. 4924-4932.

[Str90] STREET R.A. Thermal generation currents in hydrogenated amorphous silicon p-i-n structures. Applied physics letter, 1990, vol. 57, n° 13, pp. 1334-1336.

[Str91] STREET R.A. Hydrogenated Amorphous Silicon. New York: Cambridge university press, 1991.

[Str00] STREET R.A. Large area image sensor arrays. **In:** Street R. A. ed. Technology and Application of Amorphous Silicon,.., New York : Springer, 2000, p. 147. (Series in Materials Sciences, vol.37),.

[Sze81] SZE S.M. Physics of Semiconductor Devices. 2nd edition. New York: John Wiley & Sons, 1981, 564 p.

[Tau72] TAUC J. Chapter 5. **In:** Abelès F. Optical Properties of solids. Amsterdam, the Netherlands North Holland.publisher, 1972, p. 277.

[Ter04] TERRAZZONI-DAUDRIX V., GUILLET J., NIQUILLE X., et al. Enhanced light trapping in thin film silicon solar cells deposited on PET and glass. Proceedings of the 3rd world conference on photovoltaic energy conversion, 2004, pp. 1596-1600.

[The02] THEIL J.A., SNYDER R., HULA D., et al. a-Si:H photodiode technology for advanced CMOS active pixel sensor imagers. Journal of non-crystalline solids, 2002, vol. 299-302, p. 1234.

[Tie80] TIEDJE T., ROSE A. A physical interpretation of dispersive transport in disordered semiconductors. Solid state communications, 1980, vol. 37, p. 49.

[Tur01] TURCHETTA R., BERST J.D., CASADEI B., et al. A monolithic active pixel sensor for charged particle tracking and imaging using standard VLSI CMOS technology. Nuclear Instruments and Methods in Physics Research A, 2001, vol. 458, pp. 677-689.

[Vai86] VAILLANT F., JOUSSE D. Recombination at dangling bonds and steady-state photoconductivity in a-Si :H. Physical Review B, 1986, vol. 34, n° 6, pp. 4088-4098.

[Van86] VAN DER ZIEL A. Noise in solid state devices and circuits. New York,: John Wiley & sons, 1986, 306 p.

[Van02] VAN SARK W. Methods of deposition of Hydrogenated Amorphous silicon for device applications. Thèse. Utrecht, Netherlands: Debye Institute, Utrecht University, 2002, 204 p.

[Van92] VAN DEN BOOGAARD M.J., et al. The influence of the void structure on deuterium diffusion in a-Si:H. Material research society symposium proceedings, 1992, vol. 258, p. 407.

[Vas00] VASILESCU A., LINDSTROEM G. Displacement damage in silicon [**en ligne**]. Disponible sur: http://sesam.desy.de/members/gunnar/Si-dfuncs.html (consulté le 12.12.2005)

[Wea71] WEAIRE D., THORPE M.F. Electronic properties of an amorphous solid. I. A simple tight binding theory. Physical Review B, 1971, vol. 4, p. 2508.

[Wer05] WERMES N. Pixel detectors for tracking and their spin-off in imaging applications. Nuclear Instruments and Methods in Physics Research A, 2005, vol. 541, pp. 150-165.

[Woo85] WOOTEN F., WINER K., WEAIRE D. Computer generation of structural models of amorphous Si and Ge. Physical Review Letters, 1985, vol. 54, n° 13, pp. 1392-1395.

[Wyr03] WYRSCH N., MIAZZA C., DUNAND S., et al. Development of vertically integrated imaging and particle sensors. Material research society symposium proceedings, 2003, vol. 762, pp. 205-210.

[Wyr04] WYRSCH N., MIAZZA C., DESPEISSE M., et al. Vertically Integrated Amorphous Silicon Particle Sensors. Material research society symposium proceedings, 2004, vol. 808, pp. 441-446.

[Wyr05] WYRSCH N., DUNAND S., BALLIF C., et al. Radiation hardness of amorphous silicon particle sensors. Journal of Non-Crystalline Solids, 2005, accepté pour publication.

[XCOM] BERGER M.J., HUBBELL J.H., SELTZER S.M., et al. XCOM: photon cross section database.Online:
http://physics.nist.gov/PhysRefData/Xcom/Text/XCOM.html
(consulté le 10/12/05).

[Zac32] ZACHARIASEN W. H. The atomic arrangement in glass, Journal of american chemical society, 1932, vol. 54, pp. 3841-3851.

[Zho94] ZHOU J-H. Estimation of the Mobility-Lifetime Products in Amorphous Silicon in the Presence of Dispersive Transport. Journal of applied physics, 1994, vol. 33, pp. 1655-1658.

[Zhu03] ZHU S., RAU E.I., YANG F.H. A novel method of determining semiconductor parameters in EBIC and SEBIV modes of SEM. Semiconductor science technology, 2003, vol. 18, n° 4, pp. 361-366.

List of the different references and publications directly related to the thesis work:

[Ane03] ANELLI G., BORER K., DESPEISSE M., et al. A high speed low noise transimpedance amplifier in a 0.25 µm CMOS technology. Nuclear instruments and methods in physics research A, 2003, vol. 512, pp. 117-128.

[Des04a] DESPEISSE M., JARRON P., ANELLI G., et al. Characterization of 13 µm and 30 µm thick hydrogenated amorphous silicon diodes deposited over CMOS integrated circuits for particle detection applications. Nuclear instruments and methods in physics research A, 2004, vol. 518, pp. 357-361.

[Des04b] DESPEISSE M., JARRON P., MORAES D., et al. Preliminary radiation tests of 32 µm thick hydrogenated amorphous silicon films. Nuclear instruments and methods in physics research A, 2005, vol. 552, pp. 88-92.

[Des05b] DESPEISSE M., SARAMAD S., JARRON P., et al. Characterization of a Thick Layer a-Si:H Pixel Detector with TFA Technology Using a Scanning Electron Microscope. Journal of non-crystalline solids, 2005, to be published.

[Des05b] DESPEISSE M., MORAES D., JARRON P., et al. Hydrogenated amorphous silicon sensors based on thin film on ASIC technology. **In:** Proceedings of the IEEE Nuclear Science Symposium and Medical Imaging conference, 2005, Porto-Rico.

[Jar04] JARRON P., DESPEISSE M., ANELLI G., et al**.** A New concept of monolithic silicon pixel detectors:hydrogenated amorphous silicon on ASIC. Nuclear instruments and methods in physics research A, 2004, vol. 518, pp. 366-372.

[Jar05] JARRON P., MORAES D., DESPEISSE M., et al. TFA Pixel Sensor Technology for Vertex Detectors. Nuclear instruments and methods in physics research A, 2005, to be published.

[Mia05] MIAZZA C., WYRSCH N., DESPEISSE M., et al. Influence of pixel configuration on dark current of vertically integrated a-Si:H diodes. Proceedings of the MRS Spring Meeting, 2005, vol. 869, to be published.

[Mor04] MORAES D., ANELLI G., DESPEISSE M., et al. A Novel Low Noise Hydrogenated Amorphous Silicon Pixel Detector. Journal of non-crystalline solids, 2004, vol. 338-340, pp. 729-731.

[Sar05] SARAMAD S., JARRON P., DESPEISSE M., et al. A realistic model for hydrogenated amorphous silicon p-i-n diodes. Nuclear Instruments and Methods in Physics Research A, 2005, to be published.

[Wyr03] WYRSCH N., MIAZZA C., DESPEISSE M., et al. Development of vertically integrated imaging and particle sensors. Material research society symposium proceedings, 2003, vol. 762, pp. 205-210.

[Wyr04a] WYRSCH N., MIAZZA C., DESPEISSE M., et al. Vertically Integrated Amorphous Silicon Particle Sensors. Material research society symposium proceedings, 2004, vol. 808, pp. 441-446.

[Wyr04b] WYRSCH N., DESPEISSE M., ANELLI G., et al. Thin-Film Silicon Detectors for particle detection. Physica Status Solidi (c), 2004, vol. 1n°5, pp. 1284-1291.

[Wyr05a] WYRSCH N., SHAH A., DESPEISSE M., et al. Radiation hard amorphous silicon particle sensors. Proceedings of the MRS Spring Meeting, 2005, Vol. 862, to be published.

[Wyr05b] WYRSCH N., DUNAND S., DESPEISSE M., et al. Radiation hardness of amorphous silicon particle sensors. Journal of Non-Crystalline Solids, 2005, accepté pour publication.

THESE SOUTENUE DEVANT L'INSTITUT NATIONAL DES SCIENCES APPLIQUEES DE LYON

NOM : DESPEISSE Matthieu DATE de SOUTENANCE : 03 Mars 2006

TITRE : **Etude et caractérisation d'un capteur en silicium amorphe hydrogéné déposé directement sur circuit intégré pour la détection de particules et de rayonnements.**

TITRE en anglais : **Characterization of a hydrogenated amorphous silicon sensor deposited on integrated circuit for particle detection**

NATURE : Doctorat Ecole doctorale : Electronique, Electrotechnique, Automatique (EEA)

RESUME :

Pour les futures expériences de physique des hautes énergies au laboratoire européen de physique des particules (CERN), des technologies de détection alternatives aux détecteurs silicium actuels seront nécessaires. Le travail effectué dans cette thèse présente les performances et les limitations d'une nouvelle technologie de détection. Celle-ci est basée sur la déposition d'un capteur en silicium amorphe hydrogéné directement sur circuit intégré, présentant ainsi un haut degré d'intégration. Le travail présenté comprend l'optimisation et le développement de circuits intégrés pour la caractérisation de cette technologie dite « Thin-Film on ASIC ». L'interface entre le capteur déposé et le circuit intégré a été caractérisée pour comprendre en détail la méthode de segmentation du détecteur. L'induction d'un signal par le passage d'une particule chargée ou d'un rayonnement au travers du capteur a été démontrée et étudiée. La vitesse et l'amplitude du signal induit, ainsi que la résistance à de hauts niveaux de radiations ont été particulièrement appréciées. Le travail présenté démontre la faisabilité du concept de détection proposé et d'intéressantes propriétés de cette technologie pour diverses applications de détection, mais révèlent cependant différentes limitations pour d'éventuelles applications pour la physique des particules.

RESUME EN ANGLAIS :

Next generation experiments at the European laboratory of particle physics (CERN) require particle detector alternatives to actual silicon detectors. This thesis presents a novel detector technology, which is based on the deposition of a hydrogenated amorphous silicon sensor on top of an integrated circuit. Performance and limitations of this technology have been assessed for the first time in this thesis in the context of particle detectors. Specific integrated circuits have been designed and the detector segmentation, the interface sensor – chip and the sensor leakage current have been studied in details. The signal induced by the track of an ionizing particle in the sensor has been characterized and results on the signal speed, amplitude and on the sensor resistance to radiation are presented. The results are promising regarding the use of this novel technology for radiation detection, though limitations have been shown for particle physics application.

MOTS-CLES : détection, capteur, silicium amorphe hydrogéné, TFA, AFP, courants de fuite, signal induit, déplétion, résistance aux radiations.

Laboratoire (s) de recherche : Laboratoire de Physique de la Matière (LPM) // Centre européen de recherche nucléaire (CERN)

Directeur de thèse: Christian Gontrand

Président de jury : Gérard Guillot

Composition du jury : Laurent Dusseau (rapporteur), Christophe Ballif (rapporteur), Wladyslaw Dabrowski (rapporteur), Giovanni Anelli (superviseur CERN), Christian Gontrand et Gérard Guillot